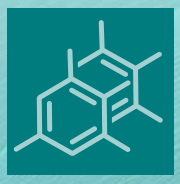

molecules

Smart and Functional Polymers

Edited by
Jianxun Ding, Yang Li, and Mingqiang Li

Printed Edition of the Special Issue Published in *Molecules*

www.mdpi.com/journal/molecules

Smart and Functional Polymers

Smart and Functional Polymers

Special Issue Editors

Jianxun Ding
Yang Li
Mingqiang Li

MDPI • Basel • Beijing • Wuhan • Barcelona • Belgrade

Special Issue Editors
Jianxun Ding
Changchun Institute of Applied
Chemistry, Chinese Academy of Sciences
China

Mingqiang Li
Sun Yat-sen University
China

Yang Li
Boston Children's Hospital
USA

Editorial Office
MDPI
St. Alban-Anlage 66
4052 Basel, Switzerland

This is a reprint of articles from the Special Issue published online in the open access journal *Molecules* (ISSN 1420-3049) from 2018 to 2019 (available at: https://www.mdpi.com/journal/molecules/special_issues/SFP)

For citation purposes, cite each article independently as indicated on the article page online and as indicated below:

LastName, A.A.; LastName, B.B.; LastName, C.C. Article Title. *Journal Name* **Year**, *Article Number*, Page Range.

ISBN 978-3-03921-590-4 (Pbk)
ISBN 978-3-03921-591-1 (PDF)

Contents

About the Special Issue Editors . . . . . **vii**

Preface to "Smart and Functional Polymers" . . . . . **ix**

Xiangru Feng, Mingqiang Li, Yang Li and Jianxun Ding
Special Issue: "Smart and Functional Polymers"
Reprinted from: *Molecules* **2019**, *24*, 2976, doi:10.3390/molecules24162976 . . . . . **1**

Meishan Chen, Xiangru Feng, Weiguo Xu, Yanqiao Wang, Yanan Yang, Zhongyu Jiang and Jianxun Ding
PEGylated Polyurea Bearing Hindered Urea Bond for Drug Delivery
Reprinted from: *Molecules* **2019**, *24*, 1538, doi:10.3390/molecules24081538 . . . . . **5**

Jorge M. Guerrero, Amanda Carrillo, María L. Mota, Roberto C. Ambrosio and Francisco S. Aguirre
Purification and Glutaraldehyde Activation Study on HCl-Doped PVA–PANI Copolymers with Different Aniline Concentrations
Reprinted from: *Molecules* **2019**, *24*, 63, doi:10.3390/molecules24010063 . . . . . **19**

William Ndugire, Bin Wu and Mingdi Yan
Synthesis of Carbohydrate-Grafted Glycopolymers Using a Catalyst-Free, Perfluoroarylazide-Mediated Fast Staudinger Reaction
Reprinted from: *Molecules* **2019**, *24*, 157, doi:10.3390/molecules24010157 . . . . . **36**

Yomaira L. Uscátegui, Luis E. Díaz, José A. Gómez-Tejedor, Ana Vallés-Lluch, Guillermo Vilariño-Feltrer, María A. Serrano and Manuel F. Valero
Candidate Polyurethanes Based on Castor Oil (*Ricinus communis*), with Polycaprolactone Diol and Chitosan Additions, for Use in Biomedical Applications
Reprinted from: *Molecules* **2019**, *24*, 237, doi:10.3390/molecules24020237 . . . . . **47**

Liying Guo, Xianchao Jin, Xin Wang, Longzhu Yin, Yirong Wang and Ying-Wei Yang
Immobilizing Polyether Imidazole Ionic Liquids on ZSM-5 Zeolite for the Catalytic Synthesis of Propylene Carbonate from Carbon Dioxide
Reprinted from: *Molecules* **2018**, *23*, 2710, doi:10.3390/molecules23102710 . . . . . **77**

Juan Li, Guimei Wu, Cuiying Qin, Wuhai Chen, Gang Chen and Lu Wen
Structure Characterization and Otoprotective Effects of a New Endophytic Exopolysaccharide from Saffron
Reprinted from: *Molecules* **2019**, *24*, 749, doi:10.3390/molecules24040749 . . . . . **89**

Lili Xu, Man Wang, Qing Chen, Jiajia Yang, Wubin Zheng, Guanglei Lv, Zewei Quan and Chunxia Li
Rare Earth Hydroxide as a Precursor for Controlled Fabrication of Uniform β-$NaYF_4$ Nanoparticles: A Novel, Low Cost, and Facile Method
Reprinted from: *Molecules* **2019**, *24*, 357, doi:10.3390/molecules24020357 . . . . . **102**

Julia Kredel, Christian Dietz and Markus Gallei
Fluoropolymer-Containing Opals and Inverse Opals by Melt-Shear Organization
Reprinted from: *Molecules* **2019**, *24*, 333, doi:10.3390/molecules24020333 . . . . . **112**

Bo Tang, Yu Qian, Yi Gou, Gang Cheng and Guihua Fang
VE-Albumin Core-Shell Nanoparticles for Paclitaxel Delivery to Treat MDR Breast Cancer
Reprinted from: *Molecules* **2018**, *23*, 2760, doi:10.3390/molecules23112760 . . . . . **129**

Haiming Fan, Po Li, Wei Li, Hui Li and Xiaonan Huang
Ultrasensitive (Co)polymers Based on Poly(methacrylamide) Structure with Fining-Tunable pH Responsive Value
Reprinted from: *Molecules* **2018**, *23*, 1870, doi:10.3390/molecules23081870 . . . . . **139**

Jiandong Han, Xingyu Zhao, Weiguo Xu, Wei Wang, Yuping Han and Xiangru Feng
Effect of Hydrophobic Polypeptide Length on Performances of Thermo-Sensitive Hydrogels
Reprinted from: *Molecules* **2018**, *23*, 1017, doi: **148**

Qi Lu, Wen Jiao Han and Hyoung Jin Choi
Smart and Functional Conducting Polymers: Application to Electrorheological Fluids
Reprinted from: *Molecules* **2018**, *23*, 2854, doi:10.3390/molecules23112854 . . . . . **159**

Houliang Tang, Yi Luan, Lu Yang and Hao Sun
A Perspective on Reversibility in Controlled Polymerization Systems: Recent Progress and New Opportunities
Reprinted from: *Molecules* **2018**, *23*, 2870, doi:10.3390/molecules23112870 . . . . . **183**

Jiayi Pan, Kobra Rostamizadeh, Nina Filipczak and Vladimir P. Torchilin
Polymeric Co-Delivery Systems in Cancer Treatment: An Overview on Component Drugs' Dosage Ratio Effect
Reprinted from: *Molecules* **2019**, *24*, 1035, doi:10.3390/molecules24061035 . . . . . **199**

Houliang Tang, Weilong Zhao, Jinming Yu, Yang Li and Chao Zhao
Recent Development of pH-Responsive Polymers for Cancer Nanomedicine
Reprinted from: *Molecules* **2019**, *24*, 4, doi:10.3390/molecules24010004 . . . . . **231**

Chenyu Wang, Bozhong Lin, Haopeng Zhu, Fei Bi, Shanshan Xiao, Liyan Wang, Guangqing Gai and Li Zhao
Recent Advances in Phenylboronic Acid-Based Gels with Potential for Self-Regulated Drug Delivery
Reprinted from: *Molecules* **2019**, *24*, 1089, doi: **255**

Radhika Narayanaswamy and Vladimir P. Torchilin
Hydrogels and Their Applications in Targeted Drug Delivery
Reprinted from: *Molecules* **2019**, *24*, 603, doi:10.3390/molecules24030603 . . . . . **276**

About the Special Issue Editors

Jianxun Ding received his B.S. degree in Polymer Chemistry from University of Science and Technology of China in 2007 and obtained his Ph.D. degree at Changchun Institute of Applied Chemistry (CIAC), Chinese Academy of Sciences (CAS), in 2013 under the supervision of Dr. Xuesi Chen. During 2017–2019, he worked with Dr. Omid C. Farokhzad and Dr. Jinjun Shi from Brigham and Women's Hospital, Harvard Medical School, as a Postdoctoral Research Fellow. During his study, he was awarded over 10 awards, such as the Tang Aoqing Chemistry Scholarship in 2011, and the Graduate National Scholarship and the President Excellence Award of Chinese Academy of Sciences in 2012. He works now as an Associate Professor at CIAC, CAS. His research focuses on the synthesis of functional biodegradable polymers, the development of smart polymer platforms for controlled drug delivery, the exploitation of polymer-based adjuvants for immunotherapy, and the preparation of polymer scaffolds for regenerative medicine. He was invited to serve as the Editorial Board Members of *Molecules*, *Current Pharmaceutical Design*, *Medicine*, *Current Molecular Pharmacology*, *Sci*, and *Heliyon*, and as a Young Editorial Board Member of *Journal of Functional Polymers*. In addition, he served as a Guest Editor for several journals, including *Frontiers in Pharmacology*, *Current Pharmaceutical Design*, *Current Pharmaceutical Biotechnology*, *Polymers*, and *Journal of Nanomaterials*. Heretofore, he has published more than 160 academic articles in mainstream journals, including *Advanced Materials*, *Nano Letters*, *ACS Nano*, *Nature Communications*, *Advanced Functional Materials*, *Advanced Sciences*, *Biomaterials*, *Journal of Controlled Release*, and so forth, with over 6000 citations. Moreover, he has applied for over 70 patents in China, of which over 60 have been authorized. Among them, two patents were awarded the Invention Contest of Jilin Province and the Excellence Award of Chinese Patent Award in 2013. Meanwhile, owing to his significant accomplishments, he has won more than 10 awards, such as the Natural Science Award of Jilin Province, the Science and Technology Progress Award of Jilin Province, and the Natural Science Academic Achievement Award of Jilin Province. He was selected for the Fifth Batch Outstanding Innovative Talents in Jilin Province in 2015. He was selected in the Young Talents Promotion Project of Jilin Province and joined the CIAC Yinghua Young Innovation Promotion Association, CAS, in 2018, and joined the CAS Young Innovation Promotion Association in 2019. Based on previous studies and accomplishments, he has undertaken more than 10 grants for groups, such as the National Natural Science Foundation of China and the Science and Technology Development Program of Jilin Province.

Yang Li obtained his B.S. degree (2011) in Polymer Chemistry from University of Science and Technology of China. He earned his Ph.D. degree (2017) in Biomedical Science from University of Texas Southwestern Medical Center under the supervision of Dr. Jinming Gao. Currently, he works as a postdoctoral research fellow in the research group of Dr. Daniel Kohane at Boston Children's Hospital, Harvard Medical School. His research interest focuses on developing stimuli-responsive nanomaterials for biological sensing and drug delivery. He is also interested in the mechanistic investigation of supramolecular self-assembly.

Mingqiang Li received his B.S. degree in Polymer Chemistry from University of Science and Technology of China in 2009. He carried out his graduate studies under Dr. Xuesi Chen at Changchun Institute of Applied Chemistry, Chinese Academy of Sciences, and postdoctoral training with Dr. Kam W. Leong at Columbia University. His current research is mainly focused on biomaterials, nanomedicines, and microfluidics.

Preface to "Smart and Functional Polymers"

Smart and functional polymers have attracted increasing interest in recent years thanks to their full range of applications in various fields, such as industry, bioengineering, and medicine. Polymers with different physicochemical properties can be synthesized through the polymerization of functional monomers or the modification of different active groups after polymerization. Compared with small molecules, these polymers have relatively large surface-to-volume ratio, adjustable size and surface, enhanced sensitivity and specificity, excellent targeting binding affinity, and stimuli-responsive ability. With the development of synthesis and characterization techniques, a series of smart and functional polymer materials, including shape memory polymers, drug release polymer nanosystems, polymer gels, polymer films, polymer fibers, and so forth, have been successfully designed and achieved rapid progress. However, the synthesis technology, structure and performance, stability, and biosafety of smart and functional polymers need to be further improved to meet the increasing needs of different fields.

This book is based on the Special Issue of the journal Molecules on "Smart and Functional Polymers". The collected research and review articles focus on the synthesis and characterizations of advanced functional polymers, polymers with specific structures and performances, current improvements in advanced polymer-based materials for various applications, and the opportunities and challenges in the future. The topics cover the emerging synthesis and characterization technologies of smart polymers, core–shell structure polymers, stimuli-responsive polymers, anhydrous electrorheological materials fabricated from conducting polymers, reversible polymerization systems, and biomedical polymers for drug delivery and disease theranostics.

In summary, this book provides a comprehensive overview of the latest synthesis approaches, representative structures and performances, and various applications of smart and functional polymers. It will serve as a useful reference for all researchers and readers interested in polymer sciences and technologies.

Jianxun Ding, Yang Li, and Mingqiang Li

Special Issue Editors

molecules

MDPI

Editorial

Special Issue: "Smart and Functional Polymers"

Xiangru Feng [1], Mingqiang Li [2,*], Yang Li [3,*] and Jianxun Ding [1,*]

1 Key Laboratory of Polymer Ecomaterials, Changchun Institute of Applied Chemistry, Chinese Academy of Sciences, Changchun 130022, China
2 Department of Biomedical Engineering, Columbia University, 116th and Broadway, New York, NY 10027, USA
3 Laboratory for Biomaterials and Drug Delivery, Boston Children's Hospital and Harvard Medical School, 300 Longwood Ave., Boston, MA 02115, USA
* Correspondence: limq567@mail.sysu.edu.cn (M.L.); yang.li2@childrens.harvard.edu (Y.L.); jxding@ciac.ac.cn (J.D.)

Received: 14 August 2019; Accepted: 15 August 2019; Published: 16 August 2019

Keywords: polymerization or post-polymerization modification methods; polymer-based supramolecular chemistry; stimuli-responsive polymers; shape memory polymers; self-healing polymers; polymers for industrial catalysis; polymers for water or effluent treatment; polymers for sensing, separation, and purification; polymers for fabrication; renewable polymer materials used for agriculture; functional polymers used in food science; polymers for information storage, electronics, and energy conversion; functional polymers for diagnosis, imaging, drug delivery, and tissue engineering; polymers with biological activity (e.g., antitumor, antidiabetic, and antimicrobial activity); polymer-based medical devices

Polymerization provides an efficient strategy for synthesizing macromolecules with versatile functionality [1,2]. Smart and functional polymers with various active groups have attracted increasing interest as they hold considerable promise for a variety of applications [3,4]. The advanced polymers can be constructed via the polymerization of functional monomers or post-polymerization modification [5–7]. These polymers possess a combination of the physical properties of nanoscale or microscale architectures and the physiochemical reactivities of the attached functional groups [8]. Moreover, their ability to form microscopic and macroscopic assemblies in response to external targets or signals gives them unique physiochemical properties (e.g., a large surface-to-volume ratio, variable composition and size, dynamic association, and reversible phase separation) and tailored functionalities (e.g., enhanced sensitivity and specificity, extraordinary target binding affinity, and tunable surface chemistry), which are absent in small molecules [9,10].

Eleven original research articles and six review papers have been collected in this Special Issue. These articles focus on functional polymers with specific structures and performances.

Six original research articles focus on the synthesis and characterization of advanced functional polymers. Chen et al. synthesized an amphiphilic polyurea consisting of cyclohexyl-*tert*-butyl polyurea and poly(ethylene glycol) (PEG) for the encapsulation of chemotherapeutic drug paclitaxel (PTX) [11]. The PEGylated polyurea micelle showed more efficient delivery of PTX into 4T1 cells, with enhanced antitumor efficacy. Guerrero et al. proposed a method to purify poly(vinyl alcohol)−polyaniline (PVA−PANI) copolymers at different aniline concentrations [12]. After activation with glutaraldehyde exposure, reduction of the polymer was detected, along with an increase of the benzenoid section of PANI. Ndugire et al. developed carbohydrate-grafted glycopolymers via a catalyst-free perfluorophenyl azide-mediated Staudinger reaction [13]. Using this method, they successfully conjugated maltoheptaose and mannose onto poly(lactic acid). Valero and co-workers prepared different polyurethanes with castor oil and isophorone diisocyanate by adding polycaprolactone diol and chitosan [14]. The change of polyols from using castor oil significantly increased the mechanical

properties of interest. Guo et al. immobilized three polyether imidazole ionic liquids onto ZSM-5 zeolite to acquire three immobilized catalysts [15]. The prepared catalysts maintain excellent stability and high catalytic activity after eight cycles. Wen, Chen, and co-workers reported the purification and characterization of a water-soluble exopolysaccharide (EPS-2) from the fermentation culture of endophytic fungus CSL-27 of saffron [16]. It was found that EPS-2 could protect cochlear hair cells from ototoxicity exposure.

Five original research articles report polymers with specific structures and performances, including core−shell structure and stimuli-responsive properties. Nanoparticles with a core−shell structure have shown advantageous performance. Xu et al. used cheap rare earth hydroxide as a precursor to develop a monodisperse hexagonal $NaYF_4$:Yb^{3+}/Ln^{3+} core and $NaYF_4$:Yb^{3+}/Ln^{3+}@$NaGdF_4$ core−shell nanoparticles with well-controlled shapes [17]. The sizes of the nanocrystals were tunable, and the core−shell nanoparticles showed intense emission under 980-nm laser excitation. Kredel et al. prepared core−shell particles with highly fluorinated shell materials [18]. The incorporation of fluoropolymers into core−shell particle structures can be used for the melt/shear organization technique, which produced free-standing fluoropolymer opal and inverse films with different hydrophobic properties and reflection colors. Tang et al. used bovine serum albumin to fabricate vitamin E (VE)-albumin core−shell nanoparticles for the delivery of PTX and VE [19]. Owing to the existence of VE as an oil core, the nanoparticles achieved higher PTX-loading efficiency and also overcame the P-gp-mediated drug efflux. Stimuli-responsive (e.g., pH, temperature, and light) polymers have shown great promise in the design of smart materials for various biomedical applications, such as drug delivery and molecular imaging. Fan and co-workers developed reversible pH-responsive copolymers by using tertiary amine-based monomers, 2-(dibutyl amino)ethyl methacrylate, and 2-(dimethylamino)ethyl methacrylate [20]. These polymers were pH-sensitive and could be responsively fine-tuned in aqueous solution. At low pH, the polymers were in unimer state, while a high pH would lead to polymer aggregation. The pK_a values of these polymers fall into the physiological pH range, making them ideal carriers for therapeutic drugs and imaging contrast agents to the tumor microenvironment or cytosol. Han and co-workers synthesized a series of methoxy poly(ethylene glycol)−poly(L-alanine) thermosensitive hydrogels with different degrees of polymerization (DPs) [21]. They found that hydrogels with higher DPs had better gelation ability than those with lower ones.

In addition, six review articles summarize the current improvements in advanced polymer-based materials for various applications. Lu et al. introduced anhydrous electrorheological materials, fabricated from conducting polymers and nanocomposites [22]. They mainly focused on the study of the electrical conductivity and thermal or mechanical stability of nanocomposites. Due to the emergence of various reversible materials bearing reversible-covalent linkages, reversible sol−gel transition, or reversible bonds, there has been a rapid development in reversible polymerization in recent years. In this context, Tang et al. summarized recent progress made in this area and provided insight into future reversible polymerization systems [23]. In order to investigate the effect of drug ratios used in polymer nanoparticles, Pan et al. reviewed polymer-based co-delivery systems and drug combinations for synergistic antitumor efficacy [24]. They pointed out that understanding the drug ratio of therapeutic agents and heterogeneity of tumors helped with optimizing the therapeutic effect. In another review, Tang et al. highlighted recent advances in pH-responsive nanomaterials in cancer diagnosis and treatment [25]. They summarized the recent advances in polymer design, mechanistic investigation, drug delivery, and bioimaging applications. Wang et al. reviewed the recent development of phenylboronic acid-based glucose-sensitive gels for self-regulated drug delivery, which might promote a drug delivery system for diabetes therapy [26]. In another review article, Narayanaswamy and Torchilin discussed methods of manipulating hydrogels for targeted drug delivery in diverse diseases [27].

Smart and functional polymer materials represent an interdisciplinary field that integrates physics, chemistry, material science, engineering, and biology. Over the past decade, the field has experienced rapid progress as a result of unmet needs in various areas. This Special Issue aims to provide

a comprehensive collection of the latest advances in the development of synthetic approaches, the mechanisms underlying structure-property correlations, and the current and emerging applications of smart and functional polymers. The issue covers smart and functional polymers for a diverse range of applications, involving synthetic chemistry, materials science, and biomedical technology. It mentions state-of-the-art breakthroughs that will provide guidance and references for interested readers.

Acknowledgments: The editors appreciate the contributions of all authors to the Special Issue, the constructive comments of all the reviewers, and the editorial support from Genie Lu and other editorial staff members of MDPI.

Conflicts of Interest: The authors declare no conflict of interest.

References

1. Ding, J.; Shi, F.; Xiao, C.; Lin, L.; Chen, L.; He, C.; Zhuang, X.; Chen, X. One-step preparation of reduction-responsive poly(ethylene glycol)-poly(amino acid)s nanogels as efficient intracellular drug delivery platforms. *Polym. Chem.* **2011**, *2*, 2857–2864. [CrossRef]
2. Wang, Y.; Jiang, Z.; Xu, W.; Yang, Y.; Zhuang, X.; Ding, J.; Chen, X. Chiral polypeptide thermogels induce controlled inflammatory response as potential immunoadjuvants. *ACS Appl. Mater. Interfaces* **2019**, *11*, 8725–8730. [CrossRef]
3. He, L.; Liu, J.; Li, S.; Feng, X.; Wang, C.; Zhuang, X.; Ding, J.; Chen, X. Polymer nanoplatforms at work in prostate cancer therapy. *Adv. Ther.* **2019**, *2*, 1800122. [CrossRef]
4. Jiang, Z.; Liu, Y.; Feng, X.; Ding, J. Functional polypeptide nanogels. *J. Funct. Polym.* **2019**, *31*, 13–27.
5. Ding, J.; Xiao, C.; Tang, Z.; Zhuang, X.; Chen, X. Highly efficient "grafting from" an α-helical polypeptide backbone by atom transfer radical polymerization. *Macromol. Biosci.* **2011**, *11*, 192–198. [CrossRef] [PubMed]
6. Xu, W.; Ding, J.; Chen, X. Reduction-responsive polypeptide micelles for intracellular delivery of antineoplastic agent. *Biomacromolecules* **2017**, *18*, 3291–3301. [CrossRef] [PubMed]
7. Ding, J.; Xiao, C.; Li, Y.; Cheng, Y.; Wang, N.; He, C.; Zhuang, X.; Zhu, X.; Chen, X. Efficacious hepatoma-targeted nanomedicine self-assembled from galactopeptide and doxorubicin driven by two-stage physical interactions. *J. Controlled Release* **2013**, *169*, 193–203. [CrossRef] [PubMed]
8. Feng, X.; Ding, J.; Gref, R.; Chen, X. Poly(β-cyclodextrin)-mediated polylactide-cholesterol stereocomplex micelles for controlled drug delivery. *Chin. J. Polym. Sci.* **2017**, *35*, 693–699. [CrossRef]
9. Chen, J.; Ding, J.; Wang, Y.; Cheng, J.; Ji, S.; Zhuang, X.; Chen, X. Sequentially responsive shell-stacked nanoparticles for deep penetration into solid tumors. *Adv. Mater.* **2017**, *29*, 1701170. [CrossRef]
10. Chen, J.; Ding, J.; Xu, W.; Sun, T.; Xiao, H.; Zhuang, X.; Chen, X. Receptor and microenvironment dual-recognizable nanogel for targeted chemotherapy of highly metastatic malignancy. *Nano Lett.* **2017**, *17*, 4526–4533. [CrossRef]
11. Chen, M.; Feng, X.; Xu, W.; Wang, Y.; Yang, Y.; Jiang, Z.; Ding, J. PEGylated polyurea bearing hindered urea bond for drug delivery. *Molecules* **2019**, *24*, 1538. [CrossRef] [PubMed]
12. Guerrero, J.M.; Carrillo, A.; Mota, M.L.; Ambrosio, R.C.; Aguirre, F.S. Purification and glutaraldehyde activation study on HCl-doped PVA–PANI copolymers with different aniline concentrations. *Molecules* **2018**, *24*, 63. [CrossRef] [PubMed]
13. Ndugire, W.; Wu, B.; Yan, M. Synthesis of carbohydrate-grafted glycopolymers using a catalyst-free, perfluoroarylazide-mediated fast staudinger reaction. *Molecules* **2019**, *24*, 157. [CrossRef] [PubMed]
14. Uscátegui, Y.L.; Díaz, L.E.; Gómez-Tejedor, J.A.; Vallés-Lluch, A.; Vilariño-Feltrer, G.; Serrano, M.A.; Valero, M.F. Candidate polyurethanes based on castor oil (Ricinus communis), with polycaprolactone diol and chitosan additions, for use in biomedical applications. *Molecules* **2019**, *24*, 237. [CrossRef]
15. Guo, L.; Jin, X.; Wang, X.; Yin, L.; Wang, Y.; Yang, Y.W. Immobilizing polyether imidazole ionic liquids on ZSM-5 zeolite for the catalytic synthesis of propylene carbonate from carbon dioxide. *Molecules* **2018**, *23*, 2710. [CrossRef]
16. Li, J.; Wu, G.; Qin, C.; Chen, W.; Chen, G.; Wen, L. Structure characterization and otoprotective effects of a new endophytic exopolysaccharide from Saffron. *Molecules* **2019**, *24*, 749. [CrossRef]
17. Xu, L.; Wang, M.; Chen, Q.; Yang, J.; Zheng, W.; Lv, G.; Quan, Z.; Li, C. Rare earth hydroxide as a precursor for controlled fabrication of uniform β-$NaYF_4$ nanoparticles: A novel, low cost, and facile method. *Molecules* **2019**, *24*, 357. [CrossRef]

18. Kredel, J.; Dietz, C.; Gallei, M. Fluoropolymer-containing opals and inverse opals by melt-shear organization. *Molecules* **2019**, *24*, 333. [CrossRef]
19. Tang, B.; Qian, Y.; Gou, Y.; Cheng, G.; Fang, G. VE-albumin core-shell nanoparticles for paclitaxel delivery to treat MDR breast cancer. *Molecules* **2018**, *23*, 2760. [CrossRef]
20. Fan, H.; Li, P.; Li, W.; Li, H.; Huang, X. Ultrasensitive (co)polymers based on poly(methacrylamide) structure with fining-tunable pH responsive value. *Molecules* **2018**, *23*, 1870. [CrossRef]
21. Han, J.; Zhao, X.; Xu, W.; Wang, W.; Han, Y.; Feng, X. Effect of hydrophobic polypeptide length on performances of thermo-sensitive hydrogels. *Molecules* **2018**, *23*, 1017. [CrossRef] [PubMed]
22. Lu, Q.; Han, W.J.; Choi, H.J. Smart and functional conducting polymers: Application to electrorheological fluids. *Molecules* **2018**, *23*, 2854. [CrossRef] [PubMed]
23. Tang, H.; Luan, Y.; Yang, L.; Sun, H. A perspective on reversibility in controlled polymerization systems: Recent progress and new opportunities. *Molecules* **2018**, *23*, 2870. [CrossRef] [PubMed]
24. Pan, J.; Rostamizadeh, K.; Filipczak, N.; Torchilin, V.P. Polymeric co-delivery systems in cancer treatment: An overview on component drugs' dosage ratio effect. *Molecules* **2019**, *24*, 1035. [CrossRef] [PubMed]
25. Tang, H.; Zhao, W.; Yu, J.; Li, Y.; Zhao, C. Recent development of pH-responsive polymers for cancer nanomedicine. *Molecules* **2018**, *24*, 4. [CrossRef] [PubMed]
26. Wang, C.; Lin, B.; Zhu, H.; Bi, F.; Xiao, S.; Wang, L.; Gai, G.; Zhao, L. Recent advances in phenylboronic acid-based gels with potential for self-regulated drug delivery. *Molecules* **2019**, *24*, 1089. [CrossRef] [PubMed]
27. Narayanaswamy, R.; Torchilin, V.P. Hydrogels and their applications in targeted drug delivery. *Molecules* **2019**, *24*, 603. [CrossRef] [PubMed]

molecules

MDPI

Article

PEGylated Polyurea Bearing Hindered Urea Bond for Drug Delivery

Meishan Chen [1,2], Xiangru Feng [2,3], Weiguo Xu [2,3], Yanqiao Wang [2,3], Yanan Yang [1,*], Zhongyu Jiang [2,3,*] and Jianxun Ding [2,3]

1 Chemical Engineering Institute, Changchun University of Technology, 2055 Yan'an Street, Changchun 130012, China; mschen@ciac.ac.cn
2 Key Laboratory of Polymer Ecomaterials, Changchun Institute of Applied Chemistry, Chinese Academy of Sciences, 5625 Renmin Street, Changchun 130022, China; xrfeng@ciac.ac.cn (X.F.); wgxu@caic.ac.cn (W.X.); candyqiao77@jlu.edu.cn (Y.W.); jxding@ciac.ac.cn (J.D.)
3 Jilin Biomedical Polymers Engineering Laboratory, 5625 Renmin Street, Changchun 130022, China
* Correspondence: yangyanan@ccut.edu.cn (Y.Y.); zyjiang@ciac.ac.cn (Z.J.)

Received: 6 March 2019; Accepted: 13 April 2019; Published: 18 April 2019

Abstract: In recent years, polyureas with dynamic hindered urea bonds (HUBs), a class of promising biomedical polymers, have attracted wide attention as a result of their controlled hydrolytic properties. The effect of the chemical structures on the properties of polyureas and their assemblies has rarely been reported. In this study, four kinds of polyureas with different chemical groups have been synthesized, and the polyureas from cyclohexyl diisocyanate and *tert*-butyl diamine showed the fastest hydrolytic rate. The amphiphilic polyurea composed of hydrophobic cyclohexyl-*tert*-butyl polyurea and hydrophilic poly(ethylene glycol) (PEG) was synthesized for the controlled delivery of the antitumor drug paclitaxel (PTX). The PTX-loaded PEGylated polyurea micelle more effectively entered into the murine breast cancer 4T1 cells and inhibited the corresponding tumor growth in vitro and in vivo. Therefore, the PEGylated polyurea with adjustable degradation might be a promising polymer matrix for drug delivery.

Keywords: amphiphilic copolymer; hydrolyzable polyurea; micelle; controlled drug delivery; cancer chemotherapy

1. Introduction

Polyureas bearing hindered urea bonds (HUBs) are able to be synthesized by the reaction between the monomers with diisocyanate or diamine groups [1,2]. As the orbital coplanarity of the amide bonds can be disturbed [3], HUBs are hydrolyzable, and the hydrolytic products are biologically safe [4]. Furthermore, the hydrolyzability can be regulated by changing the units of polyureas [5]. Due to their excellent hydrolyzability and biocompatibility, polyureas have been developed for biomedical applications, including drug delivery [6–8].

As drug carriers, the drug release profiles of polyureas can be adjusted by changing the hydrolytic rates [4], and the accumulation of therapeutic drugs at the desired tissues can also be enhanced by passive and active targeting. For instance, Shoaib et al. developed several polyurethane-urea elastomers with various diisocyanate groups to deliver the antitumor drug doxorubicin (DOX). The drug release could be adjusted by changing the pH of media and hard segment chemical structures of the polyureas [9]. Morral-Ruiz et al. developed the biotinylated polyurethane-urea nanoparticles for target delivery of plasmids and drugs [10]. The nanoparticles were loaded with a reporter gene containing plasmids and antitumor drugs for simultaneous theranostics of cancer cells. The nanoplatforms based on biotinylated polyurethane-ureas were potentially used for the therapy of other types of cancer. John et al. synthesized a series of polyureas with disulfide linkages in the backbone, and the antitumor

drug DOX was encapsulated by the nanocarriers [7]. The drug-loaded nanocarriers demonstrated the glutathione-responsive drug release behavior, indicating significant potential for controlled drug delivery. Although polyureas have been widely explored as a nanocarrier due to their biological safety and modifiability, the effect of the chemical structures of HUBs on the properties of hydrolyzable polyureas as a drug nanocarrier has rarely been reported.

In our study, a series of hydrolyzable polyureas with different chemical structures were synthesized through different diisocyanate monomers (i.e., cyclohexyl and benzyl diisocyanates) and diamine monomers (i.e., isopropyl, *tert*-butyl, and hydroxyethyl diamines). The polyureas were denoted as poly(**1**/**3**), poly(**1**/**4**), poly(**2**/**3**), and poly(**2**/**5**), as depicted in Scheme 1. The four polyureas showed distinct hydrolytic rates. Among the obtained polyureas, poly(**1**/**3**), with the fastest hydrolytic property, had the most ideal potential as a nanocarrier for drug release. As the amphiphilic PEGylated polyurea, methoxy poly(ethylene glycol)−poly(**1**/**3**) (mPEG−poly(**1**/**3**)), composed of hydrophilic amino-terminated mPEG ($mPEG_{113}$-NH_2) and hydrophobic poly(**1**/**3**), was synthesized according to the reaction between the amino group of mPEG and the isocyanate group of polyurea. In addition, paclitaxel (PTX), a traditional hydrophobic antitumor agent, was loaded into mPEG−poly(**1**/**3**) to obtain the drug-loaded polyurea micelle (PUM/PTX), as shown in Scheme 2. PUM/PTX could be efficiently internalized by mouse breast cancer 4T1 cells and showed noticeable cytotoxicity in vitro. Moreover, PUM/PTX was also proven to be potent in inhibiting the growth of murine breast tumor compared to PTX treatment alone in vivo. Both histopathology and immunofluorescence were further conducted to validate the enhanced antitumor effect and biological safety of PUM/PTX. In conclusion, the PEGylated polyurea with adjustable degradation might be a meaningful polymer for drug delivery.

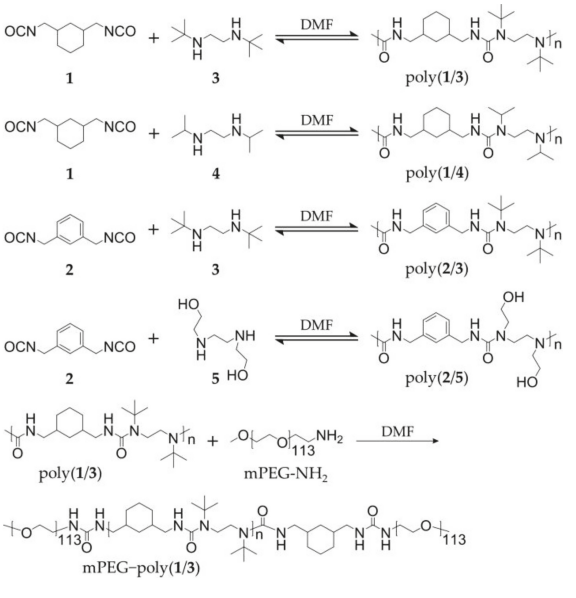

Scheme 1. Synthetic routes of hydrolyzable polyureas.

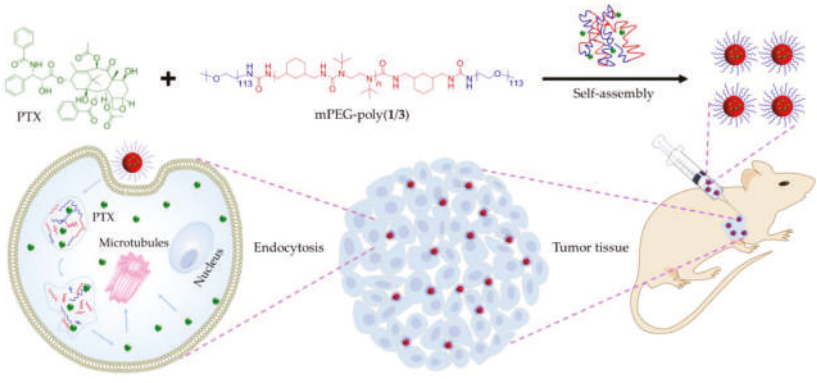

Scheme 2. Encapsulation of paclitaxel (PTX) into methoxy poly(ethylene glycol)−poly(**1**/**3**) (mPEG−poly(**1**/**3**)) micelle to obtain paclitaxel-loaded polyurea micelle (PUM/PTX), and cell uptake and intracellular PTX release of PUM/PTX after intratumoral administration.

2. Results and Discussion

2.1. Syntheses and Characterizations

Four kinds of hydrolyzable polyureas with different chemical groups were successfully synthesized. Briefly, equal amounts (1.0 mmol) of each monomer (**1** and **3**, **1** and **4**, **2** and **3**, or **2** and **5**) were mixed in deuterated chloroform ($CDCl_3$, 5.0 g). The solutions were vigorously stirred at room temperature overnight, two-fold diluted without purification, and directly characterized by proton nuclear magnetic resonance (^{1}H NMR). All peaks in the ^{1}H NMR spectra of polymers were accurately assigned (Figure 1a,b). The characteristic peaks at 5.87, 6.29, and 6.46 ppm were attributed to the hydrogen atom in HUBs. The typical resonances at 1.12–1.30 and 3.62–4.70 ppm represented the substituents on a nitrogen atom. Fourier-transform infrared (FT-IR) spectroscopy further confirmed the chemical structures of polyureas as the ^{1}H NMR results. The typical signals of ureas were at 3300–3320 cm^{-1}. The typical wavenumbers of PEG were at 1360, 1297, and 1249 cm^{-1}. These results demonstrate that the hydrolyzable polyureas were successfully synthesized (Figure 1c,d).

The number-average molecular weights (M_ns) of polyureas were obtained from gel permeation chromatography (GPC) at the scheduled time points (Figure 1e). It was observed that the hydrolytic rates of poly(**1**/**3**) and poly(**2**/**3**) in a mixed solution were faster than poly(**1**/**4**) and poly(**2**/**5**). After 48 h, M_ns reduction percentages of poly(**1**/**3**), poly(**2**/**3**), poly(**1**/**4**), and poly(**2**/**5**) were 78.4%, 74.6%, 6.4%, and 4.8%, respectively. The hydrolytic rate of poly(**1**/**3**) increased to 82.5% after incubation for 72 h. The results could be explained as the bulky substituents incorporating into one of the nitrogen atoms [11]. Urea bonds could be easily destabilized by disarranging the orbital coplanarity of the amide bonds and diminished the conjugation effect. Urea bonds with a bulky substituent could dissociate into isocyanate and amines reversibly. Isocyanates could hydrolyze into amines and carbon dioxide (CO_2) in an aqueous solution. It was an irreversible reaction that shifted the balance to aid the HUBs dissociation reaction and finally led to the complete hydrolysis of HUBs. Since poly(**1**/**3**) had a suitable hydrolytic time, it was selected for the following experiments.

In order to increase the hydrophilia of polyureas, mPEG was attached to both ends of poly(**1**/**3**). The ^{1}H NMR spectrum of mPEG−poly(**1**/**3**) dissolved in $CDCl_3$ demonstrated the successful synthesis of PEGylated polyurea (Figure 1a). In mPEG−poly(**1**/**3**), the mPEG segment was the hydrophilic segment, and the poly(**1**/**3**) moiety was the hydrophobic moiety. The amphiphilic mPEG−poly(**1**/**3**) self-assembled into micelle in phosphate-buffered saline (PBS). Observed by transmission electron microscopy (TEM; Figure 2a), the PUM showed a spherical structure with a mean radius of around 38 nm. The hydrodynamic radius (R_h) of PUM determined by dynamic laser light scattering (DLS)

was 39.6 ± 8.1 nm. The radius of PUM examined by TEM showed the similar result to that by DLS. In order to explore the hydrolytic characteristic of mPEG–poly(**1**/**3**), the M_ns were detected at the scheduled time points. PUM exhibited the desired hydrolytic rates in PBS, which was similar to poly(**1**/**3**). After incubation for 48 h, the M_n of PEGylated PUM was reduced to 71.5% (Figure 2b).

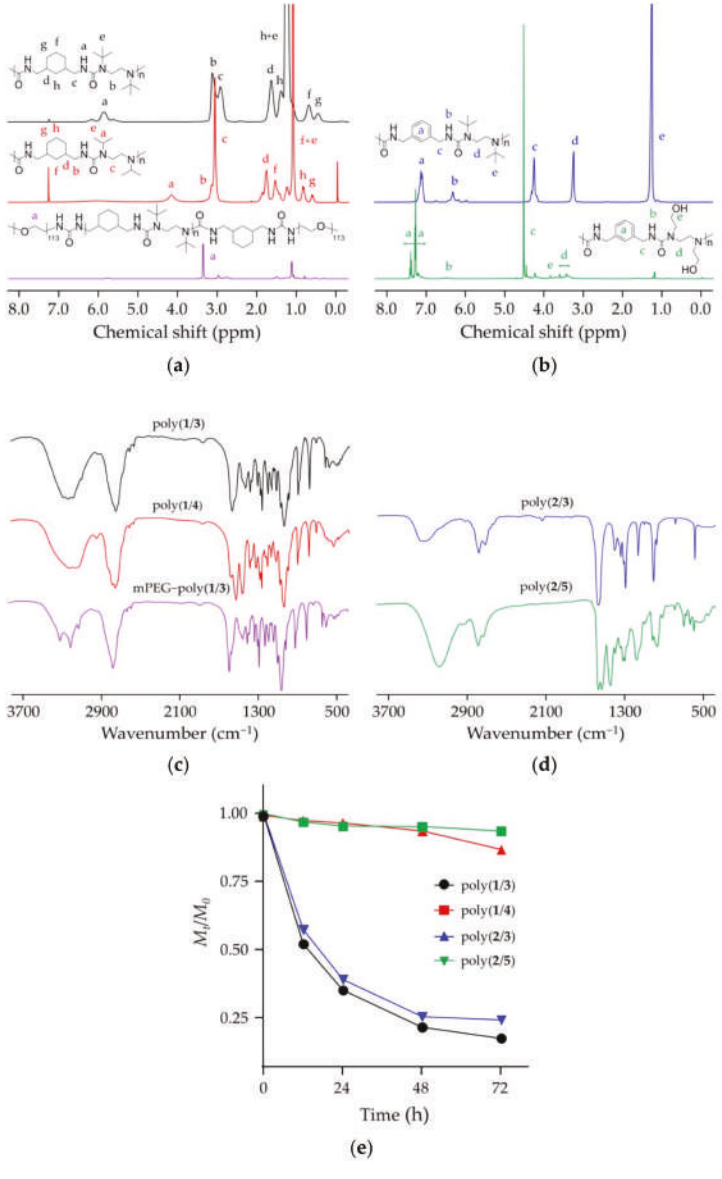

Figure 1. Characterizations of polyureas bearing hindered urea bonds (HUBs). (**a**) Proton nuclear magnetic resonance (^{1}H NMR) spectra of poly(**1**/**3**), poly(**1**/**4**), and mPEG–poly(**1**/**3**) in deuterated chloroform ($CDCl_3$); (**b**) ^{1}H NMR spectra of poly(**2**/**3**) and poly(**2**/**5**) in $CDCl_3$; (**c**) Fourier-transform infrared (FT-IR) spectra of poly(**1**/**3**), poly(**1**/**4**), and mPEG–poly(**1**/**3**); (**d**) FT-IR spectra of poly(**2**/**3**) and poly(**2**/**5**); (**e**) Changes of number-average molecular weights (M_ns) of four polyureas with different chemical groups by gel permeation chromatography (GPC).

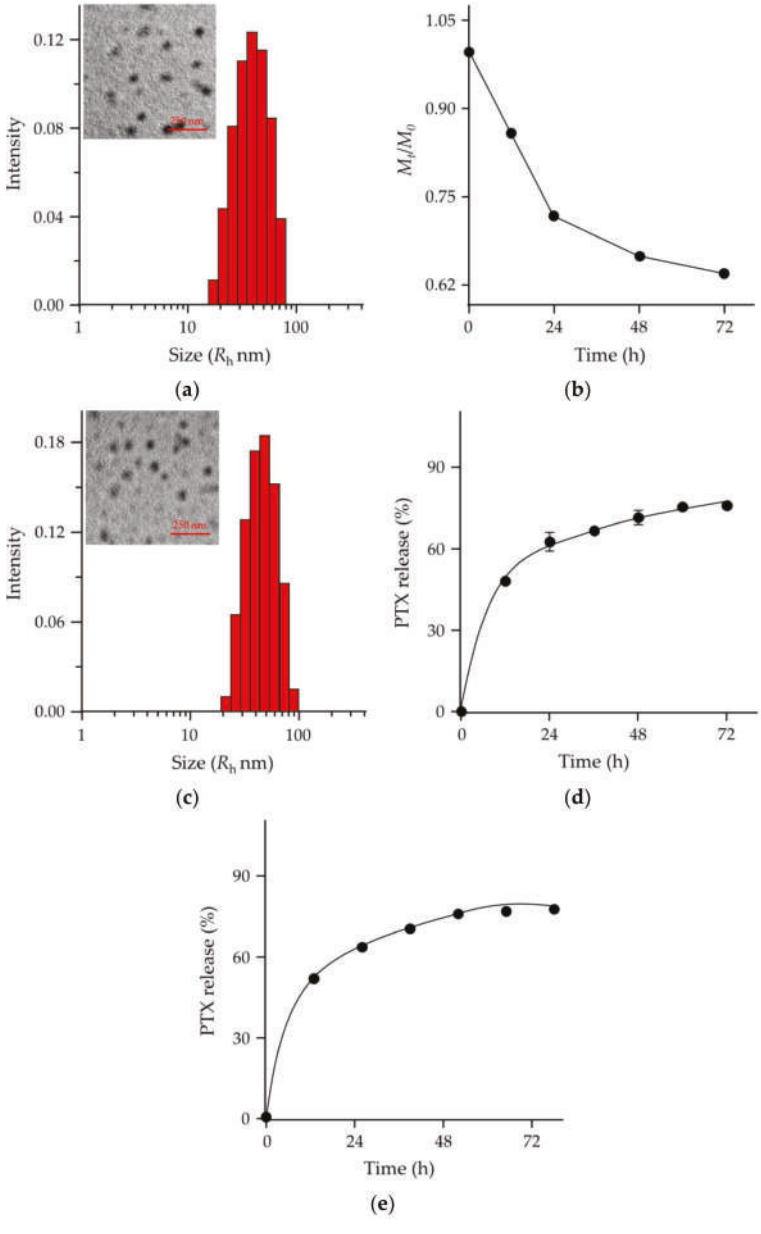

Figure 2. Characterizations of PUM and PUM/PTX. (**a**) Transmission electron microscopy (TEM) image and hydrodynamic radius (R_h) of PUM in PBS; (**b**) M_n change of PUM by GPC; (**c**) TEM image and R_h of PUM/PTX in PBS; (**d**,**e**) PTX release behavior of PUM/PTX in phosphate-buffered saline (PBS) at pH 7.4 (**d**) and pH 6.8 (**e**).

The drug encapsulation capability is another important requirement for a suitable and robust drug delivery system [12–14]. In order to explore the drug loading properties of the polymer, PTX was loaded into mPEG−poly(**1**/**3**) micelle to obtain PUM/PTX. The drug loading content (DLC) and drug loading efficiency (DLE) were computed using the following Equations (1) and (2) [15,16]:

$$\text{DLC} = \frac{\text{Weight of drug in PUM/PTX}}{\text{Weight of drug} - \text{loaded micelle}} \times 100\% \quad (1)$$

$$\text{DLE} = \frac{\text{Weight of drug in PUM/PTX}}{\text{Weight of feeding drug}} \times 100\% \quad (2)$$

PTX was successfully loaded into mPEG−poly(**1**/**3**) micelle with DLC of 8.7% and DLE of 87.5%. The morphological characteristic of PUM/PTX was observed by TEM (Figure 2c), and the average nanoparticle size was around 43 nm. The R_h was 44.7 ± 11.6 nm by the DLS test, showing a similar result with TEM. The results suggested that PUM/PTX was a monodisperse micelle and had a uniform particle size distribution.

2.2. PTX Release, In Vitro Cell Uptake, and Cell Proliferation Inhibition

The release characteristics of PTX from PUM/PTX were detected in PBS. As depicted in Figure 2d, the release profile showed no apparent burst release of PTX from PUM/PTX in PBS at pH 7.4 within 24 h. The amount of PTX released from PUM/PTX was lower than 45% during the first 12 h. At 48 h, over 65% of PTX was released. Since the tumoral microenvironment is more acidic, the PTX release behavior was also tested in PBS at pH 6.8 (Figure 2e). The amount of PTX released from PUM/PTX was 46% in the first 12 h. At 60 h, about 69% of PTX was released. These two release rates indicated that the hydrolytic rate of PUM was faster in the acidic condition. This controlled release pattern indicated that polyurea could be used as a suitable drug delivery system.

Drug release was a complicated process [13]. To just explain the nature of drug release behaviors, a classic empirical equation was established by Peppas et al. [17]. The equations were written as:

$$\frac{M_t}{M_\infty} = k\, t^n \quad (3)$$

$$\lg\left(\frac{M_t}{M_\infty}\right) = \lg k + n \lg t \quad (4)$$

In Equations (3) and (4), M_t and M_∞ were the cumulative drug release at time t and infinite time, respectively; k was the proportionality constant, and n was the release exponent that was related to the release mechanism of payloads. In the study of drug release, an increase in n indicates that the release was more influenced in a swelling-controlled way. n was calculated using the Equations (3) and (4), and the values for a pH of 6.8 and 7.4 were 0.32 and 0.21, respectively. The value of n was larger at pH 6.8 than pH 7.4, which was attributed to the faster hydrolysis of polyurea in an acidic environment.

Coumarin-6 (C_6) as a hydrophobic model fluorescence molecule was used for cell uptake study [18]. C_6 was loaded into mPEG−poly(**1**/**3**) micelle to form PUM/C_6. The internalization of PUM/C_6 by 4T1 cells was monitored through flow cytometry (FCM) and confocal laser scanning microscopy (CLSM). As shown in Figure 3a, after 1 h incubation, the control group had no fluorescence signal of C_6, while in the PUM/C_6 group the fluorescence signals were significantly increased, and fluorescence intensity was further increased at 6 h. Similarly, CLSM images in Figure 3b,c showed that the highest fluorescence intensity was detected when PUM/C_6 was incubated with 4T1 cells for 6 h. The results demonstrated that the PUM micelle could efficiently deliver PTX into 4T1 cells.

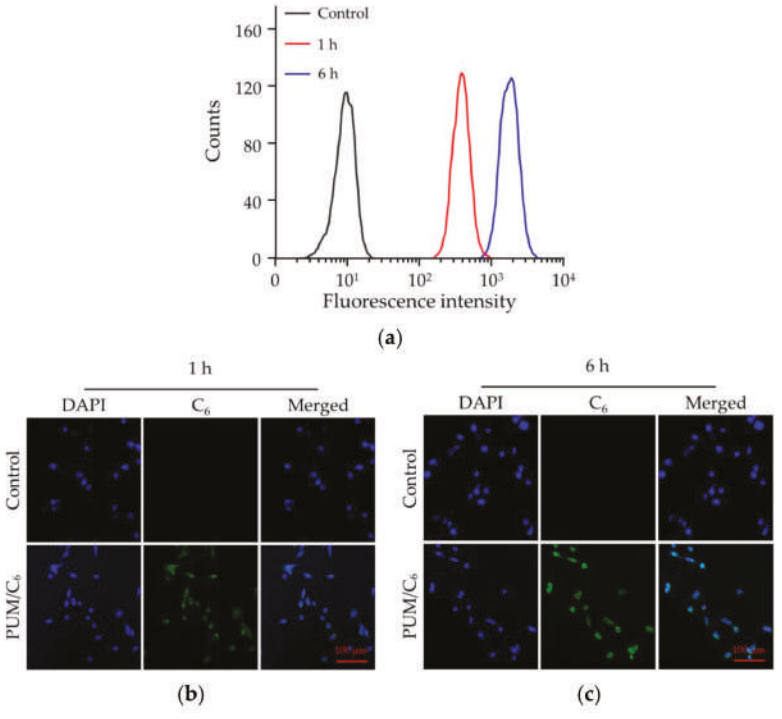

Figure 3. Cell uptake of PUM/C_6 after incubation with 4T1 cells detected by (**a**) flow cytometry (FCM) and (**b**,**c**) confocal laser scanning microscopy (CLSM) analyses in 1 h (**b**) and 6 h (**c**).

PUM with HUBs was synthesized by the reversible reaction between cyclohexyl diisocyanate and *tert*-butyl diamine. With the hydrolysis of PUM, the degradation products were cyclohexane-1,3-diyldimethanamine and *tert*-butyl diamine. The cytotoxicity of the hydrolytic products of HUBs to 4T1 and L929 cells was tested by methyl thiazolyl tetrazolium (MTT) assays (Figure 4a, b). After incubation with PUM at the concentration of 100.0 μg mL^{-1} for 72 h, the viability of L929 cells was kept around 93%, indicating negligible toxicity of PUM to normal cells. After incubation with PUM for 72 h at a concentration of 50.0 μg mL^{-1}, the cell viability of 4T1 cells was 86.97%, indicating that the polymer had little effect on the growth of tumor cells. MTT assays compared the toxicity of free PTX and PUM/PTX toward 4T1 cells. Both free PTX and PUM/PTX inhibited the growth of 4T1 cells. The cell viability was reduced to 51.9% after incubation with free PTX for 48 h at a concentration of 10.0 μg mL^{-1}, while the cells treated with an equivalent dose of PUM/PTX showed viability of 46.6% (Figure 4c). As shown in Figure 4d, the cell proliferation was further suppressed at 72 h with cell viability reduced to around 45.9%. The data above confirmed that PUM/PTX could be efficiently endocytosed by 4T1 cells and release PTX to perform the antitumor effect. In vitro experiments proved that the polymer could make a proper drug delivery vehicle.

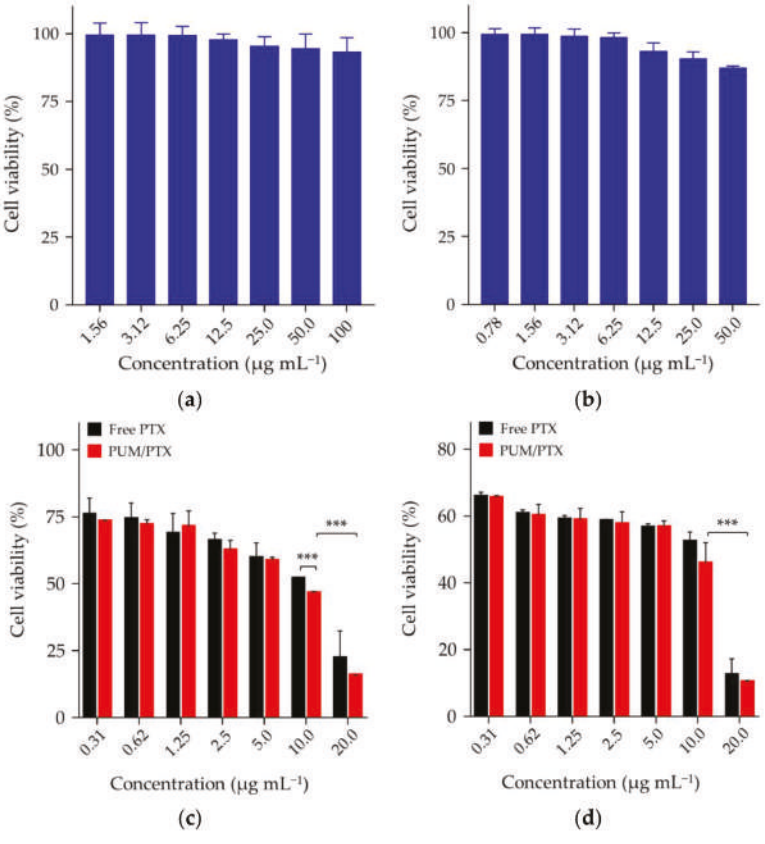

Figure 4. In vitro cytotoxicity of (**a**) L929 and (**b**) 4T1 cells in 72 h; (**c**) PUM/PTX in 48 h and (**d**) PUM/PTX in 72 h after incubation with 4T1 cells. The error bars represent the standard deviation (n = 3; * $p < 0.05$, ** $p < 0.01$, *** $p < 0.001$).

2.3. In Vivo Antitumor Efficacy

The antitumor activity was investigated in a BALB/c model of mice bearing allograft orthotopic murine 4T1 breast tumors. The antitumor efficacy of PUM/PTX was further detected in vivo. Free PTX was dissolved in the mixture of castor oil and ethanol [19], and diluted with PBS. The mice were treated with free PTX or PUM/PTX at a dosage of 5.0 mg kg^{-1} PTX, and the mice treated with PBS were set as a control group. The treatment started at the time when the tumor volumes reached approximately 200 mm^3. As shown in Figure 5a, free PTX showed modest antitumor efficacy compared with the control group within 18 days, whereas PUM/PTX showed the best inhibition rate of 32.7%. This result suggests that PUM/PTX could well inhibit tumor growth. The photograph of the tumors had a similar result (Figure 5b).

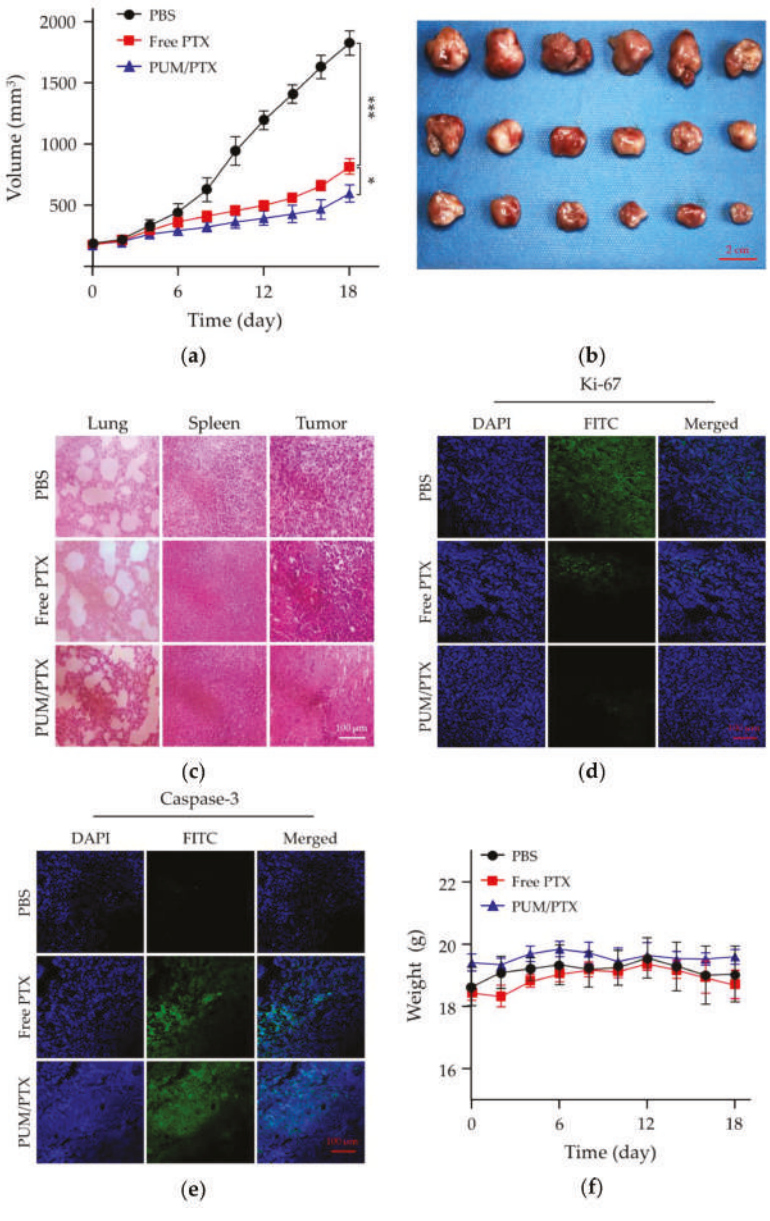

Figure 5. In vivo antitumor efficacy, safety assessment, and immunofluorescence experiments. (**a**) Tumor volumes and (**b**) photograph of the isolated tumors. Data were presented as a mean ± SD ($n = 6$; * $p < 0.05$, ** $p < 0.01$, *** $p < 0.001$); (**c**) Hematoxylin and eosin (H&E) staining of normal organs (the lungs and spleens) and tumor tissues; (**d**) Ki-67 staining of tumor tissues; (**e**) Caspase-3 staining of tumor tissues; (**f**) Changes of body weight in each group ($n = 3$).

Histopathology and immunofluorescence analyses were further conducted on the isolated tumors to evaluate the antitumor efficacies of PBS as control, free PTX, and PUM/PTX. In this work, lung metastasis, the trauma to healthy tissue, and the antitumor efficacies of all groups were evaluated

by hematoxylin and eosin (H&E) staining. As shown in Figure 5c, without the appearance of lung metastasis, intratumoral administration of PTX and PUM/PTX at a dose of 5.0 mg kg^{-1} did not cause a noticeable change in the histopathological morphologies of the lungs and spleens. In the PTX and PUM/PTX groups, tumor cells showed a decrease in volume and denser cytoplasm compared with those of the control group. A large area of apoptosis appeared in the tumor tissue. The H&E results were further verified by immunofluorescence staining of Ki-67 and caspase-3. Immunofluorescence staining of Ki-67 was used to evaluate the effect of PTX formulations on the growth of tumor [20]. As shown in Figure 5d, both PUM/PTX and free PTX-treated group showed less Ki-67-positive cells. Especially, a slightly stronger antitumor effect was observed in the PUM/PTX group. The caspase-3 analysis is a standard method to analyze the apoptosis of tumor cells [21]. The amount of caspase-3 suggests the apoptosis level of cells in different tumor tissues. Compared with the control group, more strong signals of caspase-3 were manifested in tumor tissues of the free PTX and PUM/PTX group, indicating a larger apoptosis area (Figure 5e). These results were consistent with histopathological H&E analyses.

The body weight is an essential physiological factor to assess the toxicity of drugs [22]. As exhibited in Figure 5f, mice treated with free PTX showed an apparent decrease in body weight compared with the control group, while the body weight of mice in the PUM/PTX group remained stable. This phenomenon indicates that mPEG−poly(**1**/**3**) could efficiently improve safety. All experiments validated that mPEG−poly(**1**/**3**) could act as a suitable and biological safety drug delivery vehicle.

3. Materials and Methods

3.1. Materials

1,3-Bis(isocyanatomethyl) cyclohexane (**1**) and 3-bis(isocyanatomethyl) benzene (**2**) were purchased from Tokyo Chemical Industry Co., Ltd. (Shanghai, China), *N,N′*-di-*tert*-butyl-ethylenediamine (**3**) was purchased from Biological Science and Technology Co., Ltd. (Shanghai, China), and *N,N′*-di-*iso*-propylethylenediamine (**4**) was purchased from Aladdin (Shanghai, China), and all of them were used as obtained. *N,N′*-Bis(2-hydroxyethyl)ethylenediamine (**5**) was purchased from Energy Chemical (Shanghai, China). *N,N*-dimethylformamide (DMF) and ethyl ether were bought from Tiantai Fine Chemical Co., Ltd. (Tianjin, China). DMF was stored over calcium hydride (CaH_2) and purified by vacuum distillation. C_6 and $mPEG_{113}$ were purchased from Sigma-Aldrich (Shanghai, China). $mPEG_{113}$−NH_2 was prepared as the protocol reported in our previous work [23]. PTX was purchased from Huafeng United Technology Co., Ltd. (Beijing, China). Dulbecco's modified Eagle's medium (DMEM) and newborn bovine serum (NBS) were bought from Gibco (Grand Island, NY, USA) and Every Green (Hangzhou China), respectively. Methyl thiazolyl tetrazolium (MTT) and 4′,6-diamidino-2-phenylindole dihydrochloride (DAPI) were purchased from Sigma-Aldrich (Shanghai, China). The primary antibody was purchased from Abcam Company (Cambridge, UK). The secondary antibody was purchased from ABclonal (Wuhan, China). The purified deionized water was prepared by the Milli-Q plus system (Millipore Co., Billerica, MA, USA).

3.2. Syntheses of Four Different Polyureas

The equimolar of **1** (1.94 g, 10.0 mmol) and **3** (1.72 g, 10.0 mmol), **1** (1.94 g, 10.0 mmol) and **4** (1.44 g, 10.0 mmol), **2** (1.88 g, 10.0 mmol) and **5** (1.48 g, 10.0 mmol), **2** (1.88 g, 10.0 mmol) and **3** (1.72 g, 10.0 mmol) were separately dissolved in anhydrous DMF (10.0 g). The solutions were vigorously stirred at room temperature overnight. The polymer solutions had 5% water added to them, and they were then shaken at 80 rpm in a 37 °C incubator. Then they were used for the study of hydrolysis directly [5].

3.3. Synthesis of mPEG−poly(1/3)

The **1** (1.3 g, 6.7 mmol) and **3** (1.1 g, 6.5 mmol) were dissolved in anhydrous DMF, separately, and vigorously stirred at room temperature overnight. $mPEG_{113}$-NH_2 (2.5 g, 0.5 mmol) was dissolved in toluene, and residual water in the solution was removed by azeotropic distillation. The dehydrated $mPEG_{113}$-NH_2 was dissolved in anhydrous DMF, and then added into the reaction flask. The mixture was stirred at room temperature for three days and was precipitated by anhydrous ethyl ether.

3.4. Preparation of PUM

mPEG−poly(**1**/**3**) was dissolved in dimethyl sulfoxide (DMSO) and slowly added into 0 °C PBS. The mixture solution was ultrafiltrated by an ultrafiltration tube (molecular weight cut-off (MWCO) = 10,000 Da; Millipore Co., Billerica, MA, USA). Finally, the concentration of mPEG−poly(**1**/**3**) solution was kept at 1.0 mg mL^{-1}.

To investigate the hydrolysis of mPEG−poly(**1**/**3**), PUM was shaken at 80 rpm in a 37 °C incubator, 3.0 mL of the liquid was pipetted at different time points, and the liquid was lyophilized. Finally, the lyophilized solids were dissolved in DMF, and M_ns were monitored by GPC.

3.5. Preparation of PUM/PTX

First, mPEG−poly(**1**/**3**) and PTX were dissolved in DMSO with a mass ratio of 9:1. Then, the two solutions were mixed evenly. The mixture was added into 0 °C PBS slowly while stirring quickly. Finally, the DMSO of the mixture solution was removed by ultrafiltration.

3.6. Characterizations

^{1}H NMR spectra were recorded on a Bruker AV 400 NMR spectrometer in $CDCl_3$. FT-IR spectra were recorded on a Bio-Rad Win-IR instrument (Cambridge, MA, USA). GPC analyses of polymers were conducted on a Waters 2414 system (Waters Co., Milford, MA, USA) equipped with Ultrahydrogel™ linear columns and a Waters 2414 refractive index detector (injection volume: 30.0 μL, column temperature: 50 °C, eluant: DMF through 0.45 and 0.22 μm filters, flow rate: 1.0 mL min^{-1}). TEM measurements were performed on a JEOL JEM-1011 transmission electron microscope with an accelerating voltage of 100 kV. DLS measurements were performed with a vertically polarized He−Ne laser (DAWN EOS, Wyatt Technology Co., Santa Barbara, CA, USA). The high-performance liquid chromatography (HPLC) analyses of PTX were performed with a Symmetry® C18 column connected to a Waters 2487 (Waters Co., Milford, MA, USA) at a flow rate of 1.0 mL min^{-1}. The DLC and DLE of PUM/PTX were determined according to the following protocol. A volume of 200.0 μL of the PUM/PTX sample was mixed into 800.0 μL of acetonitrile, and the detection wavelength was 227 nm.

3.7. In Vitro PTX Release

The PUM/PTX solution was placed into dialysis bags (MWCO = 3500 Da). The dialysis bags were transferred into PBS at pH 6.8 and 7.4, 37 °C with 80 rpm. HPLC tests detected the amount of released PTX.

3.8. Cell Cultures

4T1 cells were cultured in complete DMEM, supplemented with 10% (*V*/*V*) NBS, penicillin (50.0 IU mL^{-1}), and streptomycin (50.0 IU mL^{-1}) at 37 °C in a 5% (*V*/*V*) CO_2 atmosphere.

3.9. Cell Uptakes

PUM/C_6 was used for the cell uptake study. Both CLSM and FCM investigated the cell uptake of PUM/C_6 toward 4T1 cells.

3.9.1. FCM

The cell uptake study was conducted with C_6, which was used as a hydrophobic model fluorescence probe. The cells were seeded in 6-well plates at a density of 2.0×10^5 cells to each well and cultured for 12 h. Then, 100.0 μL of PUM/C_6 was added into the wells, and the cells were further incubated at 37 °C for 1 or 6 h. Next, the harvested cells were suspended in PBS and centrifuged at 1,000 rpm for 5 min. All the cells were washed with PBS. Finally, the cells were resuspended with 500.0 μL of PBS. Data were analyzed by FCM on a Guava® easyCyte™ flow cytometer (Merck Millipore, Darmstadt, Germany).

3.9.2. CLSM

The cells were seeded on the coverslips in 6-well plates with a density of 2.0×10^5 cells/well. A volume of 2.0 mL of DMEM was added into the cells per well and cultured for 12 h. Then 100.0 μL of PUM/C_6 was added to each well. After incubation for 1 or 6 h, the cells were fixed with 4% (*W*/*V*) formaldehyde for 15 min. Then, the fixed cells were incubated with DAPI for 3 min and washed with PBS. The images of cell localization were observed under LSM 780 CLSM (Carl Zeiss, Jena, Germany) with 10× eyepiece and 40× objective.

3.10. Cytotoxicity Assays

The MTT assays evaluated the cytotoxicity of PUM/PTX. 4T1 cells with a density of 5.0×10^3 cells/well were seeded in 96-well plates in 180.0 μL of DMEM and incubated for 24 h. A volume of 20.0 μL of free PTX or PUM/PTX was added in each well with a maximum PTX concentration of 200.0 μg mL^{-1}. The cells were subjected to MTT assay after being incubated for another 48 or 72 h. The absorbance of the above solution was measured on a Bio-Rad 680 microplate reader (Hercules, CA, USA) at 490 nm. The cells viability was calculated based on the following Equation (5):

$$\text{Cells viability } (\%) = \frac{A_{\text{sample}}}{A_{\text{control}}} \times 100\% \quad (5)$$

In Equation (5), A_{sample} was denoted as the absorbance of the sample, and A_{control} was denoted as the absorbance of the control.

The cytotoxicity of PUM to 4T1 and L929 cells was also tested at 72 h. The specific steps were the same as above.

3.11. Animal Procedures

Female BALB/c mice at five weeks of age were obtained from Vital River Laboratory Animal Technology Co., Ltd. (Beijing, China). The body weight of the mice was kept between 18 to 20 g before the start of the experiment. The experiments on the animals were carried out according to the guidelines outlined in the Guide for the Care and Use of Laboratory Animals, provided by Jilin University (Changchun, China) and the procedures were approved by the Animal Care and Use Committee of Jilin University (Protocol No. 2017-154).

3.12. In Vivo Antitumor Efficacy

BALB/c mice were inoculated with 4T1 cells to develop the breast tumor xenograft model. The breasts were injected with 1.0×10^6 cells in 0.1 mL of PBS. The mice were treated with PBS, PUM/PTX, or free PTX on day 0, 4, 8, 12, and 16 through intratumoral injections. The tumor volumes (V, mm^3) were estimated using the following Equation (6) [24],

$$V\ (\text{mm}^3) = \frac{a \times b^2}{2} \quad (6)$$

In Equation (6), a and b (mm) were the largest and the smallest axes of the tumor, measured by a caliper.

3.13. Histopathological and Immunofluorescence Analyses

The mice were sacrificed two days after the last injection. According to the protocol reported in previous studies, the lung is the most common organ for breast cancer metastasis, while the spleen is the primary immune organ that should be observed at the end of the experiments [25]. The tumors and major organs (i.e., the lungs and spleens) were collected, fixed in 4% (*W*/*V*) PBS-buffered paraformaldehyde overnight, and then embedded in paraffin. The paraffin-embedded tissues were cut into ~5 μm slices for H&E staining and ~3 μm sheets for immunofluorescence analyses (i.e., Ki-67 and caspase-3). The histological and immunofluorescence alterations were detected by a microscope (Nikon Eclipse Ti, Optical Apparatus Co., Ardmore, PA, USA).

4. Conclusions

In this study, we synthesized four kinds of hydrolyzable polyureas with different hydrolytic rates by changing the chemical groups on the polyureas. Among them, poly(**1/3**) from cyclohexyl diisocyanate and *tert*-butyl diamine showed the fastest hydrolytic rate. After modification by hydrophilic mPEG, the amphiphilic mPEG−poly(**1/3**) was synthesized for delivery of PTX. The PTX was successfully encapsulated by mPEG−poly(**1/3**) micelle with a DLC and DLE of 8.75% and 87.5%, respectively. PUM/PTX could be efficiently internalized by murine breast cancer 4T1 cells and released PTX along with the hydrolysis of polyurea. The results showed that PUM/PTX drastically suppressed the proliferation of tumor cells in vitro and significantly inhibited tumor growth in an orthotopic 4T1 breast tumor model in vivo. Therefore, the hydrolyzable PEGylated polyureas with adjustable degradation might become a promising platform for controlled drug delivery.

Author Contributions: J.D., W.X. and Y.Y. conceived and designed the experiments; M.C. performed the experiments; M.C., X.F. and Z.J. analyzed the data; M.C. wrote the draft manuscript; X.F., Z.J., Y.W. and J.D. revised the manuscript. All the authors confirmed the content of the manuscript and approved the submission.

Funding: This research was financially supported by the National Natural Science Foundation of China (Grant Nos. 51873207, 51803006, 51833010, 51673190, 51603204, 51673187, and 51520105004), the Science and Technology Development Program of Jilin Province (Grant No. 20190201068JC), and the National Key Research and Development Program of China (Grant No. 2016YFC1100701).

Conflicts of Interest: The authors declare no conflict of interest.

References

1. Cai, K.M.; Ying, H.Z.; Cheng, J.J. Dynamic ureas with fast and pH-independent hydrolytic kinetics. *Chem. Eur. J.* **2018**, *24*, 7345–7348. [CrossRef] [PubMed]
2. Ying, H.Z.; Zhang, Y.F.; Cheng, J.J. Dynamic urea bond for the design of reversible and self-healing polymers. *Nat. Commun.* **2014**, *5*, 3218–3226. [CrossRef] [PubMed]
3. Hutchby, M.; Houlden, C.E.; Ford, J.G.; Tyler, S.N.G.; Gagne, M.R.; Lloyd-Jones, G.C.; Booker-Milburn, K.I. Hindered ureas as masked isocyanates: Facile carbamoylation of nucleophiles under neutral conditions. *Angew. Chem. Int. Ed.* **2009**, *48*, 8721–8724. [CrossRef]
4. Rocas, P.; Cusco, C.; Rocas, J.; Albericio, F. On the importance of polyurethane and polyurea nanosystems for future drug delivery. *Curr. Drug Delivery* **2018**, *15*, 37–43. [CrossRef]
5. Ying, H.Z.; Cheng, J.J. Hydrolyzable polyureas bearing hindered urea bonds. *J. Am. Chem. Soc.* **2014**, *136*, 16974–16977. [CrossRef]
6. Florez-Grau, G.; Rocas, P.; Cabezon, R.; Espana, C.; Panes, J.; Rocas, J.; Albericio, F.; Benitez-Ribas, D. Nanoencapsulated budesonide in self-stratified polyurethane-polyurea nanoparticles is highly effective in inducing human tolerogenic dendritic cells. *Int. J. Pharm.* **2016**, *511*, 785–793. [CrossRef] [PubMed]
7. John, J.V.; Seo, E.J.; Augustine, R.; Jang, I.H.; Kim, D.K.; Kwon, Y.W.; Kim, J.H.; Kim, I. Phospholipid end-capped bioreducible polyurea micelles as a potential platform for intracellular drug delivery of doxorubicin in tumor cells. *ACS Biomater. Sci. Eng.* **2016**, *2*, 1883–1893. [CrossRef]

8. Valerio, A.; Feuser, P.E.; Bubniak, L.D.; Dos Santos-Silva, M.C.; de Araujo, P.H.H.; Sayer, C. In vitro biocompatibility and macrophage uptake assays of poly(urea-urethane) nanoparticles obtained by miniemulsion polymerization. *J. Nanosci. Nanotechnol.* **2017**, *17*, 4955–4960. [CrossRef]
9. Shoaib, M.; Bahadur, A.; Rahman, M.S.U.; Iqbal, S.; Arshad, M.I.; Tahir, M.A.; Mahmood, T. Sustained drug delivery of doxorubicin as a function of pH, releasing media, and NCO contents in polyurethane urea elastomers. *J. Drug Deliv. Sci. Tec.* **2017**, *39*, 277–282. [CrossRef]
10. Morral-Ruiz, G.; Melgar-Lesmes, P.; Lopez-Vicente, A.; Solans, C.; Garcia-Celma, M.J. Biotinylated polyurethane-urea nanoparticles for targeted theranostics in human hepatocellular carcinoma. *Nano Res.* **2015**, *8*, 1729–1745. [CrossRef]
11. Zhang, Y.F.; Ying, H.Z.; Hart, K.R.; Wu, Y.X.; Hsu, A.J.; Coppola, A.M.; Kim, T.A.; Yang, K.; Sottos, N.R.; White, S.R.; et al. Malleable and recyclable poly(urea-urethane) thermosets bearing hindered urea bonds. *Adv. Mater.* **2016**, *28*, 7646–7651. [CrossRef] [PubMed]
12. Jiang, Z.Y.; Chen, J.J.; Cui, L.G.; Zhuang, X.L.; Ding, J.X.; Chen, X.S. Advances in stimuli-responsive polypeptide nanogels. *Small Methods* **2018**, *2*, 307–321. [CrossRef]
13. Gao, S.; Tang, G.; Hua, D.; Xiong, R.; Han, J.; Jiang, S.; Zhang, Q.; Huang, C. Stimuli-responsive bio-based polymeric systems and their applications. *J. Mater. Chem. B* **2019**, *7*, 709–729. [CrossRef]
14. Jiang, Z.; Liu, Y.; Feng, X.; Ding, J. Functional polypeptide nanogels. *J. Funct. Polym.* **2019**, *32*, 13–27.
15. Tang, B.Q.; Zaro, J.L.; Shen, Y.; Chen, Q.; Yu, Y.L.; Sun, P.P.; Wang, Y.Q.; Shen, W.C.; Tu, J.S.; Sun, C.M. Acid-sensitive hybrid polymeric micelles containing a reversibly activatable cell-penetrating peptide for tumor-specific cytoplasm targeting. *J. Controlled Release* **2018**, *279*, 147–156. [CrossRef] [PubMed]
16. Wang, J.; Xu, W.; Li, S.; Qiu, H.; Li, Z.; Wang, C.; Wang, X.; Ding, J. Polylactide-cholesterol stereocomplex micelle encapsulating chemotherapeutic agent for improved antitumor efficacy and safety. *J. Biomed. Nanotechnol.* **2018**, *14*, 2102–2113. [CrossRef] [PubMed]
17. Shi, F.H.; Ding, J.X.; Xiao, C.S.; Zhuang, X.L.; He, C.L.; Chen, L.; Chen, X.S. Intracellular microenvironment responsive PEGylated polypeptide nanogels with ionizable cores for efficient doxorubicin loading and triggered release. *J. Mater. Chem.* **2012**, *22*, 14168–14179. [CrossRef]
18. Chu, B.Y.; Qu, Y.; Huang, Y.X.; Zhang, L.; Chen, X.X.; Long, C.F.; He, Y.Q.; Ou, C.W.; Qian, Z.Y. PEG-derivatized octacosanol as micellar carrier for paclitaxel delivery. *Int. J. Pharm.* **2016**, *500*, 345–359. [CrossRef]
19. Cheng, Y.L.; He, C.L.; Ding, J.X.; Xiao, C.S.; Zhuang, X.L.; Chen, X.S. Thermosensitive hydrogels based on polypeptides for localized and sustained delivery of anticancer drugs. *Biomaterials* **2013**, *34*, 10338–10347. [CrossRef]
20. Zhang, Y.; Cai, L.L.; Li, D.; Lao, Y.H.; Liu, D.Z.; Li, M.Q.; Ding, J.X.; Chen, X.S. Tumor microenvironment-responsive hyaluronate-calcium carbonate hybrid nanoparticle enables effective chemotherapy for primary and advanced osteosarcomas. *Nano Res.* **2018**, *11*, 4806–4822. [CrossRef]
21. Wang, Y.P.; Gao, W.Q.; Shi, X.Y.; Ding, J.J.; Liu, W.; He, H.B.; Wang, K.; Shao, F. Chemotherapy drugs induce pyroptosis through caspase-3 cleavage of a gasdermin. *Nature* **2017**, *547*, 99–103. [CrossRef]
22. Chen, J.J.; Ding, J.X.; Wang, Y.C.; Cheng, J.J.; Ji, S.X.; Zhuang, X.L.; Chen, X.S. Sequentially responsive shell-stacked nanoparticles for deep penetration into solid tumors. *Adv. Mater.* **2017**, *29*, 170–177. [CrossRef]
23. Wang, Y.; Jiang, Z.; Xu, W.; Yang, Y.; Zhuang, X.; Ding, J.; Chen, X. Chiral Polypeptide Thermogels Induce Controlled Inflammatory Response as Potential Immunoadjuvants. *ACS Appl. Mater. Interfaces* **2019**, *11*, 8725–8730. [CrossRef] [PubMed]
24. Xu, W.G.; Ding, J.X.; Xiao, C.S.; Li, L.Y.; Zhuang, X.L.; Chen, X.S. Versatile preparation of intracellular-acidity-sensitive oxime-linked polysaccharide-doxorubicin conjugate for malignancy therapeutic. *Biomaterials* **2015**, *54*, 72–86. [CrossRef] [PubMed]
25. Lv, Y.; Xu, C.; Zhao, X.; Lin, C.; Yang, X.; Xin, X.; Zhang, L.; Qn, C.; Han, X.; Yang, L.; et al. Nanoplatform assembled from a CD44-targeted prodrug and smart liposomes for dual targeting of tumor microenvironment and cancer cells. *ACS Nano* **2018**, *12*, 1519–1536. [CrossRef] [PubMed]

Sample Availability: Samples of the compounds are available from the authors.

molecules

MDPI

Article

Purification and Glutaraldehyde Activation Study on HCl-Doped PVA–PANI Copolymers with Different Aniline Concentrations

Jorge M. Guerrero [1], Amanda Carrillo [2,*], María L. Mota [2,3], Roberto C. Ambrosio and Francisco S. Aguirre [1,*]

1 Centro de Investigación en Materiales Avanzados, S.C., Alianza Norte 202, Parque de Investigación e Innovación Tecnológica, Apodaca, NL C.P. 66600, Mexico; jorge.guerrero@cimav.edu.mx
2 Instituto de Ingeniería y Tecnología, Universidad Autónoma de Ciudad Juárez, Av. Del Charro 610, Ciudad Juárez, CHIH C.P. 32310, Mexico; mdllmotago@conacyt.mx
3 CONACYT, Universidad Autónoma de Ciudad Juárez, Ciudad Juárez, CHIH C.P. 32310, Mexico
4 Facultad de Electrónica, Benemérita Universidad Autónoma de Puebla, Puebla C.P 72000, Mexico; roberto.ambrosio@correo.buap.mx
* Correspondence: amanda.carrillo@uacj.mx (A.C.); servando.aguirre@cimav.edu.mx (F.S.A.); Tel.: +52-1-656-688-4800 (A.C.); +52-1-811-721-6676 (F.S.A.)

Academic Editors: Jianxun Ding, Yang Li and Mingqiang Li
Received: 30 November 2018; Accepted: 21 December 2018; Published: 25 December 2018

Abstract: In this work, we report the synthesis and purification of polyvinyl alcohol-polyaniline (PVA–PANI) copolymers at different aniline concentrations, and their molecular (^{1}H-NMR and FTIR), thermal (TGA/DTG/DSC), optical (UV–Vis-NIR), and microstructural (XRD and SEM) properties before and after activation with glutaraldehyde (GA) in order to obtain an active membrane. The PVA–PANI copolymers were synthesized by chemical oxidation of aniline using ammonium persulfate (APS) in an acidified (HCl) polyvinyl alcohol matrix. The obtained copolymers were purified by dialysis and the precipitation–redispersion method in order to eliminate undesired products and compare changes due to purification. PVA–PANI products were analyzed as gels, colloidal dispersions, and thin films. ^{1}H-NMR confirmed the molecular structure of PVA–PANI as the proposed skeletal formula, and FTIR of the obtained purified gels showed the characteristic functional groups of PVA gels with PANI nanoparticles. After exposing the material to a GA solution, the presence of the FTIR absorption bands at 1595 cm^{-1}, 1650 cm^{-1}, and 1717 cm^{-1} confirmed the activation of the material. FTIR and UV–Vis-NIR characterization showed an increase of the benzenoid section of PANI with GA exposure, which can be interpreted as a reduction of the polymer with the time of activation and concentration of the solution.

Keywords: polymerization dispersion method; polyaniline; polyvinyl alcohol; glutaraldehyde; chemical activation

1. Introduction

Conductive polymers have been studied since their discovery in 1977 [1]. Among all known conductive polymers, polyaniline (PANI) has been one of the most studied due its high environmental stability, straightforward control of its chemical and physical properties through doping, and relatively low cost of development in comparison to other conductive polymers. PANI has been the subject in numerous studies for applications such as membranes [2], anticorrosive coatings [3], biosensors [4–7], and electronic devices [8,9]. However, the implementation of PANI has been limited because of its poor mechanical properties and its poor solubility in most organic solvents. This insolubility results in heterogeneous solutions, where the presence of microparticles hinders the formation of

homogeneous PANI thin films at low cost by physical methods such as spin or dip coating. To overcome these drawbacks, several methods have been studied, such as the possibility of processing PANI in the form of mixtures with electrically insulating polymers, improving the presented deficiencies, and opening a range of potential applications. In recent years, several publications report on the use of polystyrene (PS) [10], polyvinyl chloride (PVC) [11], and polyvinyl alcohol (PVA) [12], to stabilize PANI nanoparticles and improve the processing and formation of thin films.

The preparation of PVA–PANI copolymers by polymerization dispersion has already been reported showing a stable colloidal dispersion without sedimentation [13]. Also, with the increase of PVA content the stability of the colloidal dispersion increases, improving its mechanical properties [14]. Nevertheless, PVA addition affects the conductivity of the material. Work has been done to correlate the mechanical and electrical properties of PVA–PANI as function of aniline concentration [15].

Both PANI and PVA–PANI have been activated with glutaraldehyde (GA) to obtain PANI-G and PVA–PANI-G materials that can be used as biological platforms for the detection of different analytes such as enzymes and proteins [16,17]. The biocompatibility of PVA is already known, but PVA–PANI obtained by polymerization dispersion requires further purification in order to be applied in the biomedical field because of the presence of undesired byproducts produced by the chemical polymerization of aniline [18], which can also affect the activation of the material.

The present work is focused on the study of purified PVA–PANI copolymers at different concentrations of aniline. The molecular, thermal, optical, and microstructural properties before and after PVA–PANI copolymer activation with GA have been studied. The aim of this work is to provide information about the effects of purified PANI in a PVA matrix with GA activation.

2. Results and Discussion

2.1. Molecular Structure Variation and Modification of PVA–PANI Copolymers

2.1.1. Proton Nuclear Magnetic Resonance Spectroscopy (^{1}H-NMR)

To obtain the molecular structure of PVA–PANI copolymers, ^{1}H-NMR analysis (500 MHz, TMS) was carried out using deuterium oxide (D_2O) as solvent. The obtained spectrum for PVA–PANI is shown in Figure 1 where at δ = 7.3 ppm and δ = 7.5 ppm there is evidence of a doublet of doublets (d, J = 6.5 Hz, C_6H_4) corresponding to the benzenoid and quinoid sections of PANI in emeraldine phase, then δ = 4.7 ppm (s, D_2O). The doublet located at δ = 3.9 ppm (d, J = 28.5 Hz) corresponds to the characteristic signal of α proton of oxygen binding PVA–PANI, while the multiplet located at δ = 1.5 ppm (m, J = 18.7 Hz) suggests the integration of methylene protons from the PVA backbone [19,20].

The smooth baseline of the spectrum suggests absence of impurities in the obtained material (Figure 2). After water suppression the actual PVA:PANI ratio can be calculated by integrating the signal corresponding to PVA and PANI, obtaining a 2:1 ratio (PVA:PANI). Moreover, two sharp singlets can be clearly seen at δ = 2 ppm and δ = 3.25 ppm corresponding to absorbed solvent in the copolymer. The δ = 4.7 ppm (d, J = 19 Hz), can correspond to the proton of PVA hydroxyl (–OH), pendant groups or PANI secondary amine (–NH) groups within the polymer chain. The doublet located at δ = 3.9 ppm (d, J = 28.5 Hz) corresponds to the characteristic signal of α proton of oxygen binding PVA–PANI, this completes the molecular structure of the PVA–PANI copolymers as proposed from the skeletal formula in Figure 2. Is important to mention that the signals could be clearly seen only after the water suppression and is considered to be masked by the solvent peak in Figure 1.

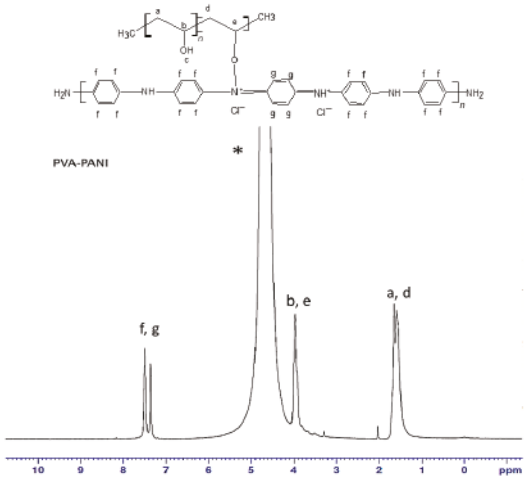

Figure 1. ^{1}H-NMR spectra for PVA–PANI in D_2O (*).

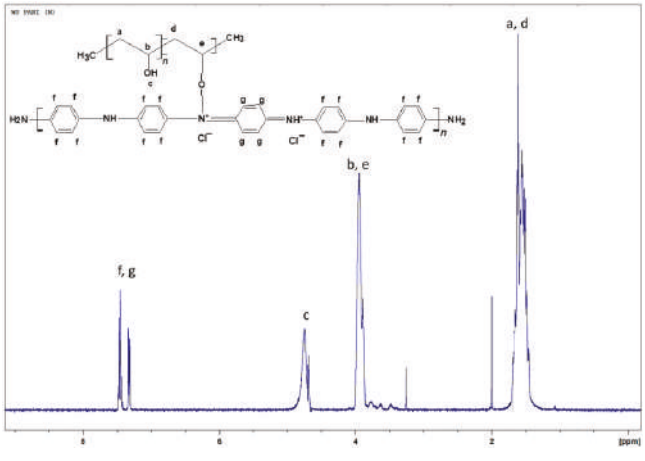

Figure 2. ^{1}H-NMR spectra for PVA–PANI with water suppression.

2.1.2. Fourier Transform Infrared Spectroscopy (FTIR)

To confirm the structure of PVA–PANI and evaluate chemical changes upon activation with GA, an FTIR analysis was carried out. First, a comparison of both purification methods was made through a study of the functional groups present (Figure 3). It was observed that PVA–PANI purified by the precipitation–redispersion method presents the characteristic bands as follows, O–H between 3600 and 3000 cm^{-1}, aliphatic groups for the PVA backbone between 2900 and 2800 cm^{-1}, and stretching of C=O and C–O acetate groups from hydrolyzed PVA in the fingerprint region [21]. The presence of the bands at 1179, 1031, 739, and 689 cm^{-1} corresponding to C–N and C–H vibrations from the benzenoid and quinoid section of PANI confirm the presence of the polymer in the PVA matrix. On the other hand, the spectrum for the dialysis purified material shows the characteristic bands for PVA–PANI at a medium–high concentration of aniline in a PVA matrix, according to previous studies [15]. The N-H, C=C, C–C, and C–N vibrations centered at 3383, 1600, 1423, and 1297 cm^{-1}, respectively, can be seen along with the C–H in plane and out of plane vibrations from the quinoid and benzenoid rings [22]. Also, from Figure 3, it is seen that both purification methods do not show any uncoupled or overlapped bands by the content of unreacted material, especially in the fingerprint region of the spectrum.

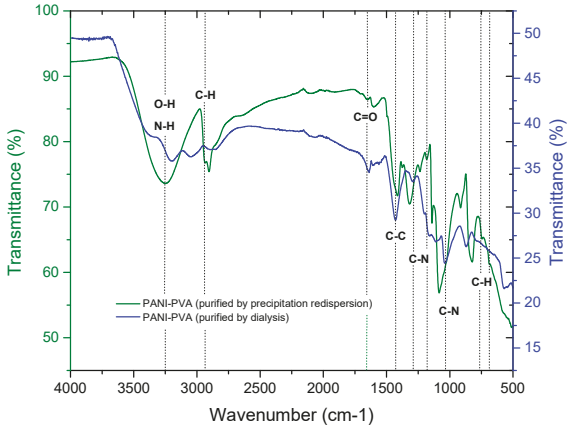

Figure 3. FTIR spectra of PVA–PANI purified by dialysis (-) and by precipitation–redispersion (-).

The implementation of dialysis has been used for the purification of PANI, since it provides a better dispersion of particles and minimizes product loss. However, filtration of the product obtained from precipitation–redispersion is highly recommended, since it takes a short time and allows the obtaining of only the desired copolymer in gel form through precipitation. Figure 4 shows the corresponding bands of PVA gels modified with PANI (ES) nanoparticles obtained by the precipitation–redispersion method with different concentrations of aniline (Table 1). An increase in the absorption bands with the increase of monomer in the PVA matrix was observed.

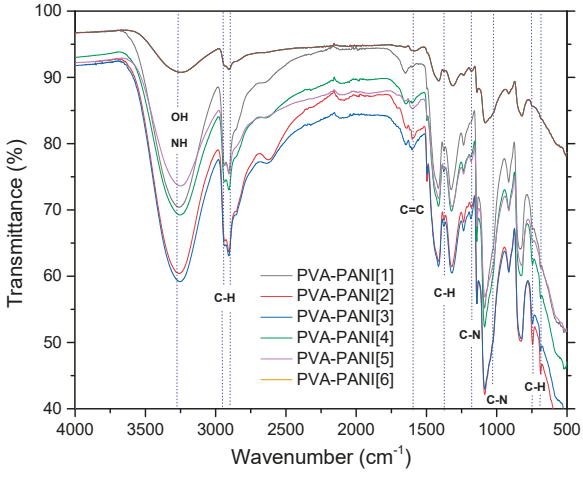

Figure 4. FTIR spectra of PVA–PANI gels at different PANI concentrations.

The absorption bands located between 3600 and 3000 cm^{-1}, attributed to O–H and N–H groups of PVA and PANI, respectively, show an intensity increase which is due to the functional groups in this range and widening due to minimum wavenumber displacements. Subsequently, in the range of 2350 to 1750 cm^{-1}, small absorption bands can be observed corresponding to the presence of overtones from PVA–PANI. These bands show an intensity decrease with increasing aniline in the polymer matrix. The latter can be attributed to chain length variation of the obtained PANI for each experiment. An increase in the absorption band located at 1586 cm^{-1} indicates an increase in C=C bonds associated to quinoid rings which can also be correlated to significant production of PANI in the

PVA matrix. The absorption bands found at 1416, 1369, and 1320 cm^{-1} correspond to the absorption of C–C stretching of the quinoid ring in PANI, the flexion of the C–H group, and the stretching vibration of the C–N bond of the amine in the aromatic ring, respectively. Absorption bands due to the vibration of the C–N bond and the stretching of the C–H group from the aromatic ring within the plane are shown at 1230 and 1130 cm^{-1}, respectively. The band located at 1090 cm^{-1} corresponds to the stretching vibration of the C–O bond which tends to be much higher in PVA–PANI composites, showing a more pronounced shoulder in 1031 cm^{-1} with the increase of monomer, demonstrating a cross-linking between the materials [23]. The FTIR spectra obtained for the activated material with 1% GA solution for an activation time of 5, 15, and 30 min can be observed in Figure 5a–c, respectively.

Table 1. Experiment of aniline concentration variation against PVA 5 wt %.

Concentration	Sample	PVA 5 wt %	Aniline	PVA–PANI (*wt*/*wt*)
Low	PVA–PANI-1	0.0202 mmol	3.5203 mmol	12.5 wt %
	PVA–PANI-2	0.0202 mmol	7.0640 mmol	25 wt %
Medium	PVA–PANI-3	0.0202 mmol	14.1281 mmol	37.5 wt %
	PVA–PANI-4	0.0202 mmol	17.6601 mmol	50 wt %
	PVA–PANI-5	0.0202 mmol	21.1921 mmol	62.5 wt %
High	PVA–PANI-6	0.0202 mmol	24.7241 mmol	75 wt %

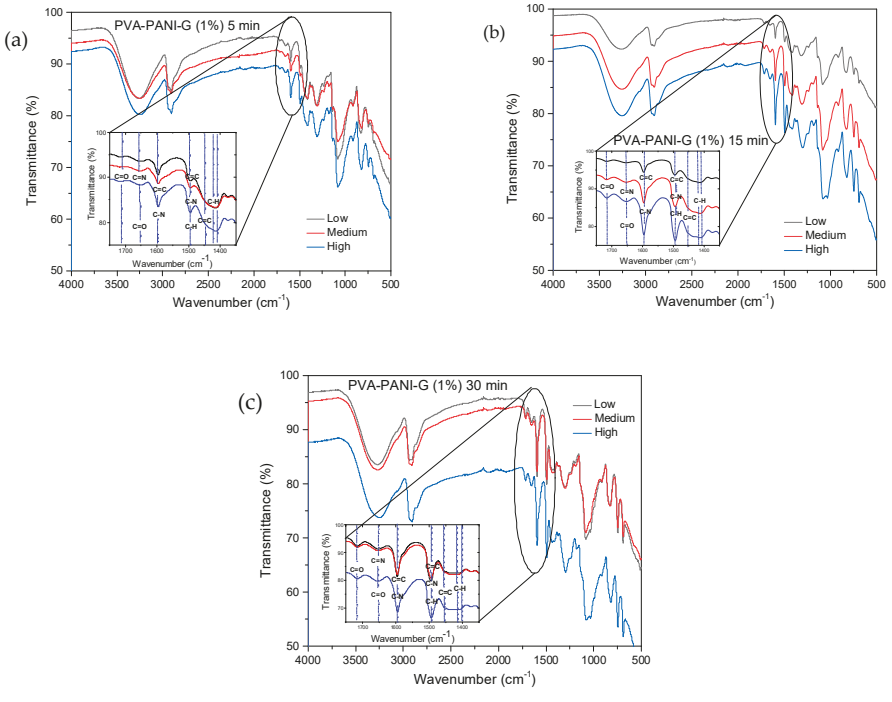

Figure 5. FTIR spectra of PVA–PANI gels at low, medium and high concentration of PANI activated with GA at 1% for: (**a**) 5 min, (**b**) 15 min, and (**c**) 30 min.

In Figure 5, a reduction in the intensity of the absorption bands corresponding to the O–H and N–H groups of PVA–PANI is shown, indicating an interaction between the activating solution and the polymer [24]. The inset shows the range from 1550 to 1750 cm^{-1}, where the presence of three absorption bands can be observed at 1595, 1650, and 1717 cm^{-1}, corresponding to the presence of C=N (Schiff base) bonds formed by the linkage of primary amines with C=O groups, and the presence of

free C=O groups [24,25]. As the activation time so does the absorption band at 1595 cm^{-1}, correlated to the vibration of the C=N (imine) bond, overlapping the vibration of the C=C bond of the quinoid section of PANI. Moreover, an increase in the absorption band located at 1490 cm^{-1} can be observed, which is associated to the benzenoid ring stretching [22], along with a reduction of the intensity of the C–C stretching from the quinoid section, which can indicate a reduction of the purified material with the increase of activation time [26]. Further activation of PVA–PANI with a more concentrated solution (2.5% GA) confirmed the reduction of the material as well as a branching between both materials (Figure S1).

2.1.3. UV–Visible-Near-Infrared Spectroscopy (UV–Vis-NIR)

UV–Vis-NIR absorption spectra and its normalized form for PVA–PANI films at low, medium, and high concentrations of PANI can be observed in Figure 6. Absorption bands corresponding to π–π^* transitions from the excitation of benzenoid segments (~330 nm), polaron-π^* transitions associated with benzenoid and quinoid ring (~430 nm), and π-polaron transitions from the excitation of quinoid rings from doped PANI (~800 nm) can be seen in each experiment [3,27]. The absorption bands corresponding to π–π^* transitions show a bathochromic effect as a function of the increase in aniline concentration in the PVA matrix, attributed to an increase in the molecular weight of the produced PANI [28]. Furthermore, a clear hyperchromic effect is observed, associated to the increase in concentration of the material, as established by Beer–Lambert's law.

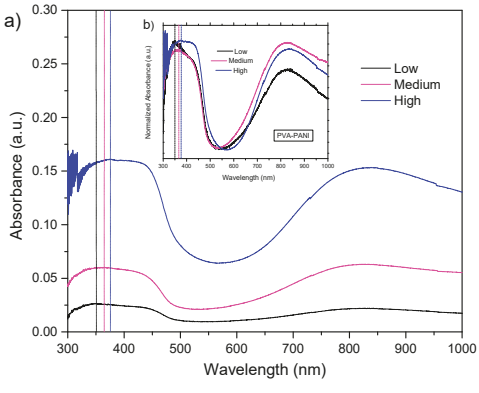

Figure 6. (**a**) UV–Vis-NIR absorbance and (**b**) normalized UV–Vis-NIR absorbance spectra of PVA–PANI thin films at low, medium, and high concentrations of PANI.

According to the results of activated PVA–PANI obtained by FTIR, an immersion time of 30 min was used for the PVA–PANI-G films. The UV–Vis-NIR absorption spectra and its normalized form for PVA–PANI-G films at low, medium, and high aniline concentrations are shown in Figure 7.

It can be seen that the absorption bands of the obtained PVA–PANI-G films present an hypsochromic effect for low and medium aniline concentrations, and a bathochromic effect for medium and high aniline concentrations, which can be attributed to a change in polarity of the molecule when interacting with the aldehyde groups of GA. The characteristic absorption bands for the electronic transitions of PANI, as well as the characteristic shift due to the increase in aniline concentration, according to the PVA–PANI experiment shown in Table 1, are also seen in Figure 7. A hyperchromic effect can be seen in the absorption band located at 380 nm, which can be related to an increase of the benzenoid section of PANI due to the activation time and concentration of GA. Comparison of bandgap variations due to concentration and activation of the material are shown in Figure S2.

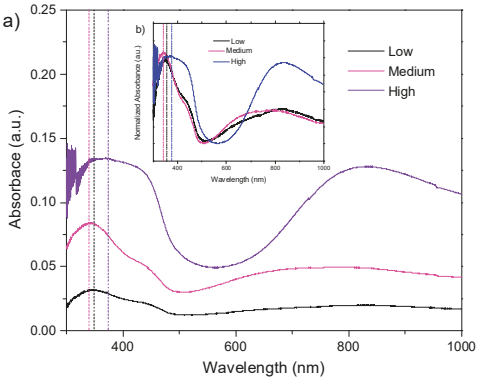

Figure 7. (**a**) UV–Vis-NIR absorbance spectra and (**b**) normalized UV–Vis-NIR absorbance spectra of PVA–PANI thin films activated with 1% GA for 30 min.

2.2. Purity, Thermal Stability and Cross-Linking of PVA–PANI Copolymers

Thermogravimetric Analysis, Derivative Thermogravimetric Analysis, and Differential Scanning Calorimetry (TGA/DTG/DSC)

In order to evaluate the thermal stability, the purity of the obtained materials by both purification methods, and to correlate an increase in hydroxyl and amine functional groups, TGA-DTG analysis were carried out. DSC study was performed to observe the cross-linking effects on PVA–PANI and PVA–PANI-G in order to evaluate the sensitivity of the material towards GA. First, to confirm purification of the material, an analysis of the transition temperatures and molecular weight for the obtained byproducts and sideproducts of the synthesis route for PVA–PANI (Figure 8) was attained as shown in Figure 9.

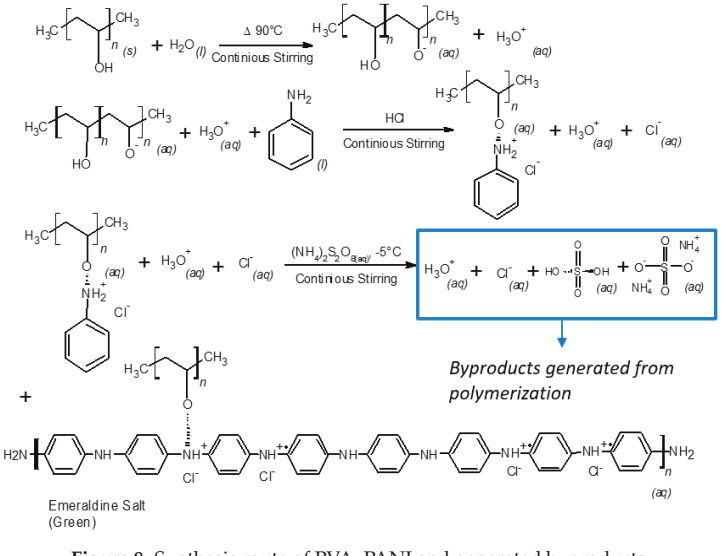

Figure 8. Synthesis route of PVA–PANI and generated byproducts.

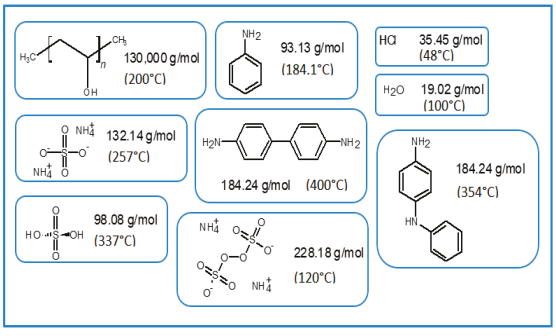

Figure 9. Molecular weight and transition temperatures of byproducts, sideproducts, and reagents present during synthesis.

We expected to observe a weight loss for each undesired product along with an exothermic peak in the temperature range of the thermograms presented in Figure 10. TGA and DTG of the material purified by precipitation–redispersion method (Figure 10a) show a loss of 8.41 wt % between 25 to 172 °C, which can be attributed to solvent and moisture loss at the surface of the material. The absence of an exothermic peak in this range and a gradual weight loss can be related to the absence of undesired products that can present a transition in this range of temperature, such as APS and HCl. Subsequently, the presence of two exothermic peaks located at 173.9 and 193.3 °C is associated to the removal of bound water, moisture, and dopant molecules inside the polymer matrix, as well as the loss of free hydroxyl functional groups due to the decomposition of PVA [29] (mass loss of 21.97 wt %). At ~250 °C an exothermic peak is shown as a shoulder corresponding to the breaking of free amine functional groups associated to the decomposition of the PANI polymeric chain, which continues to gradually decrease along with the dehydroxylation of the copolymer up to 395 °C (total mass loss of 44 wt %). In the range of 400 to 500 °C several peaks associated with the degradation of similar materials can be observed, which can be related to a variation in distribution of different molecular weights of PANI. On the other hand, PVA–PANI purified by dialysis (Figure 10b) shows a weight loss of 12.37%, which is attributed to moisture and the removal of HCl from the material [12], showing an exothermic peak at 52.94 °C. In the same way as the material purified by precipitation–redispersion, the decomposition of PVA and PANI is shown at 199.55 °C and 250.74 °C, respectively, to which the gradual loss of hydroxyl and amine functional groups can be related, having a total weight loss of 20.6% of the material. The presence of a small exothermic band at 355.25 °C can be attributed to a cross-linking reaction in the polymer matrix and not to the presence of oligomers in the material, which can be confirmed with the presence of a single exothermic peak at 489.15 °C associated with the degradation of the copolymer with a loss of 16.95 wt %. Also, from Figure 10, it can be seen that PVA–PANI purified by dialysis shows improved thermal stability and molecular integration which is evidenced by the presence of peaks correlated to decomposition and degradation of PVA and PANI only; this can be attributed to the processing of the material during the purification process.

After analyzing the thermal stability and purity of the material obtained by both purification methods, the effect of aniline concentration was studied. Figure 11 shows three weight losses. The first weight loss in the temperature range from 25 to 160 °C can be attributed to the loss of moisture and free acid, corresponding to a weight loss of 9.76%. There is another weight loss between 160 and 400 °C which is attributed to degradation of short polymer chains along with the removal of hydrogen bonds and Coulomb interactions from O–H and N–H functional groups, corresponding to a weight loss of 40.24% [30,31]. With regard to the increase of aniline, a shift to higher temperatures of 21.14 °C can be observed starting from a low concentration level to a high concentration of PANI from room temperature to 400 °C, which corresponds to a weight loss of 27%, 29%, and 30% for low, medium, and high concentrations, respectively, indicating that an increase in molecular weight of

PANI contributes to a higher thermal stability, but also a mayor weight loss because of the presence of more hydroxyl and amine functional groups in the polymer chain. The decomposition of the purified PVA–PANI gels tends to be gradual until 400 °C where there is another pronounced weight loss of 36.3% due to the degradation of the material, leaving a residue of 14.5 wt % with a variation of 1.21% between each concentration.

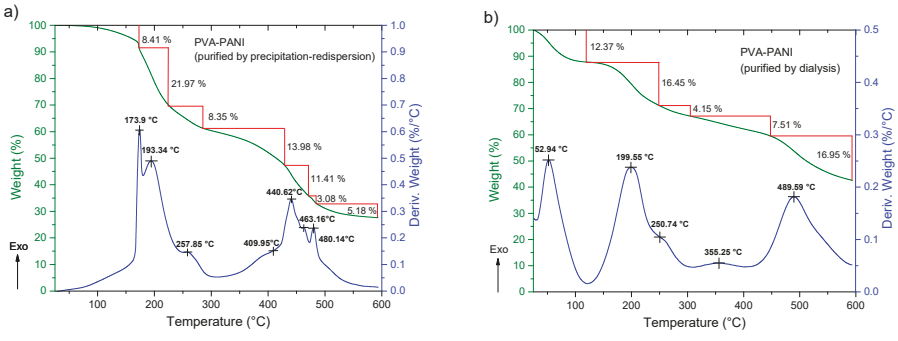

Figure 10. TGA-DTG of PVA–PANI purified by (**a**) precipitation–redispersion and (**b**) dialysis.

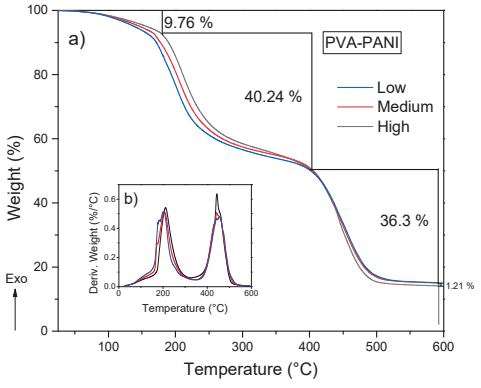

Figure 11. (**a**) TGA and (**b**) DTG of purified PVA–PANI gels at low, medium, and high concentrations of PANI.

Correlation of previously obtained thermal stability and cross-linking was studied by DSC, in order to observe energy variations associated to interactions of the polymer matrix with the PANI nanoparticles. According to the obtained DSC results (Figure 12), the presence of an endothermic peak at ~200 °C can be attributed to a cross-linking reaction between PVA and PANI at that temperature, where enthalpy changes are inversely proportional to the concentration of chemically linked PANI [32]; indicating that PVA–PANI at low concentration of monomer shows a better cross-linking between the materials. Also, it can be seen that no other prominent transition peaks are shown in the thermogram, indicating that the purified material is amorphous.

The obtained TGA-DTG results for PVA–PANI-G gels are shown in Figure 13. First, a weight loss of 6 to 9% can be observed, which corresponds to the loss of absorbed solvent and moisture. Subsequently there is a weight loss of 33 to 41% corresponding to the loss of pendant functional groups and hydroxyl and/or amino terminal groups. Starting at 400 °C, the degradation of the copolymer is seen, which no longer presents a gradual and constant decomposition as shown in Figure 11. At this range of temperature, the material shows two stages of weight loss, one with an almost linear loss with respect to the increase in temperature and another with gradual degradation, which can be attributed

to a modification in the main chain of the polymer caused by the interaction with GA. PVA–PANI at high concentration activated for 30 min showed the best thermal properties.

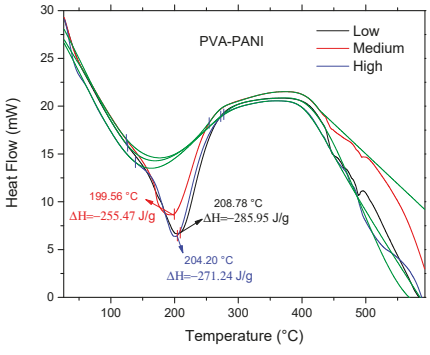

Figure 12. DSC of purified PVA–PANI gels at low, medium, and high concentrations of PANI.

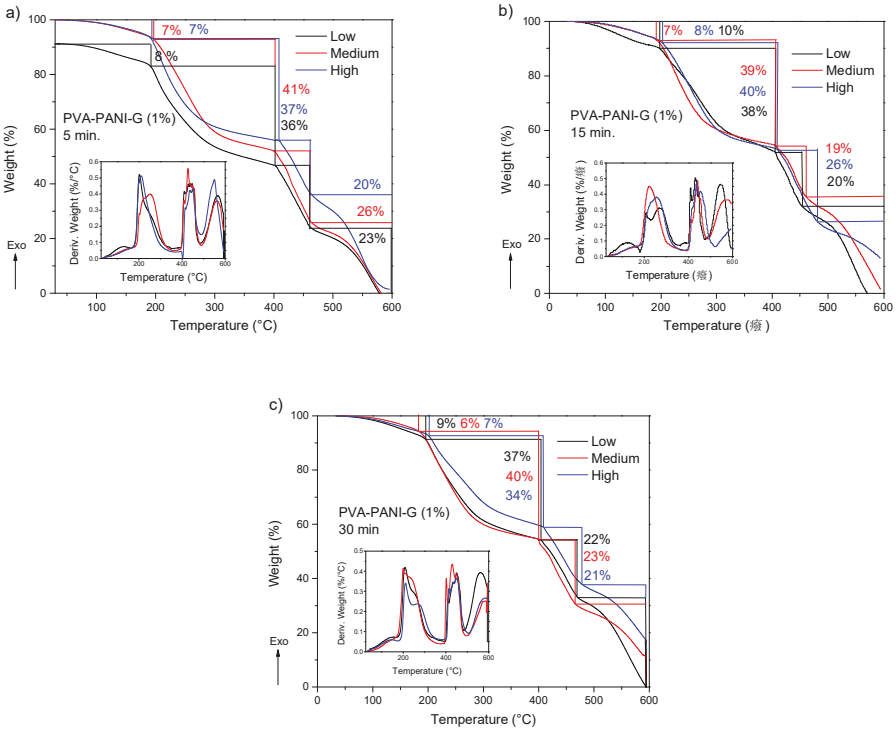

Figure 13. TGA and DTG thermograms of purified PVA–PANI-G gels, activated with 1% GA for (**a**) 5 min, (**b**) 15 min, and (**c**) 30 min.

The DSC analysis for the previous gels is shown in Figure 14. Comparing the thermogram from Figure 12 to the obtained results for the activated copolymers, it is seen that a decrease in transition temperatures is obtained for low aniline concentration along with a decrease in enthalpy from −285.95 J/g to a minimum of −320.86 J/g at 15 min of activation, which indicates that cross-linking is favored with an increase of GA for this particular concentration. However, with an increase in activation time, the material shows an increase of enthalpy up to a maximum of −56.69 J/g for a high

concentration of PANI at 30 min of activation, meaning that cross-linking between PVA–PANI and GA is disfavored, which can be related to a molecular disarrangement produced by branching of PVA–PANI, making it difficult to cross-link. Results for a higher concentration of GA are provided in Figure S3.

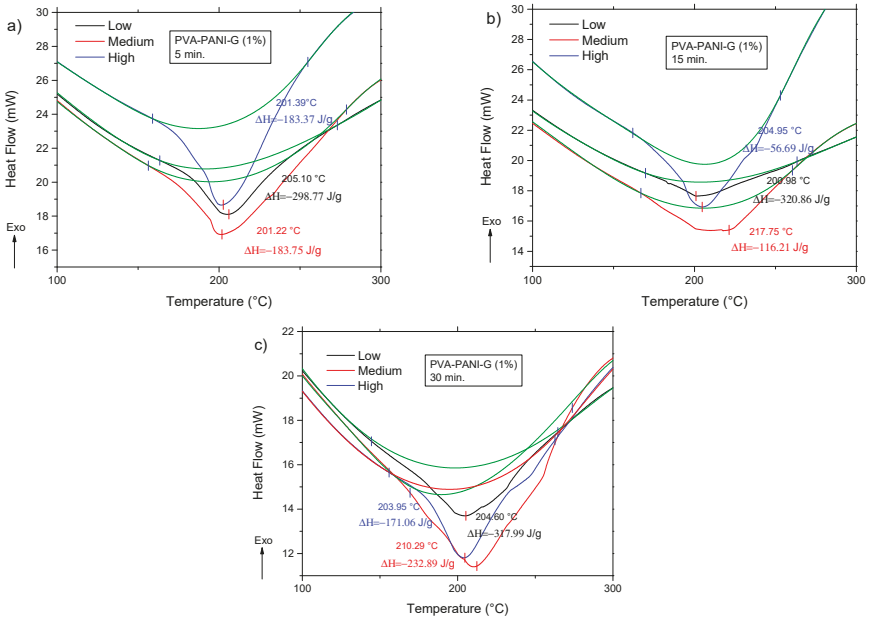

Figure 14. DSC thermograms of purified PVA–PANI-G gels, activated with 1% GA for (**a**) 5 min, (**b**) 15 min, and (**c**) 30 min.

2.3. Microstructural Variation of PVA–PANI Copolymers

2.3.1. X-ray Diffraction (XRD)

XRD analysis was carried out to observe if the material crystallinity is affected by the purification process or the concentration of PANI nanoparticles in the PVA matrix. In Figure 15, it is observed that both purification processes seem to reduce the crystallinity of the thin films showing a broad peak between 16 and 40° (2θ), where PVA–PANI thin films purified by dialysis tend to show a better molecular order than PVA–PANI purified by the precipitation–redispersion method, presenting a diffraction peak located at 2θ = 19.77° which corresponds to the (101) plane of semicrystalline PVA with d_{101} = 4.485 Å [29,33]. These results were compared to the XRD results obtained from unpurified PVA–PANI thin films with high PVA concentration, showing the discussed diffraction peak without any trace of PANI peaks at 2θ ≈ 25°, which indicates that the obtained PANI is amorphous.

From the data shown in Figure 16a, it can be observed that the purified PVA–PANI doped with HCl 1 M (pH = 1) has a low atomic order regardless of aniline concentration, showing a broad peak with a maximum intensity found at 2θ = 23.29°, which is in agreement with the reported for PANI doped with HCl [34,35]. It is expected to have a lower crystallinity of the copolymer with GA activation due to the disarrangement produced by cross-linking, increasing molecular dispersion, and broadening of the XRD peaks [36]. This behavior can be observed for PVA–PANI-G thin films at low, medium, and high concentrations of aniline (Figure 16b).

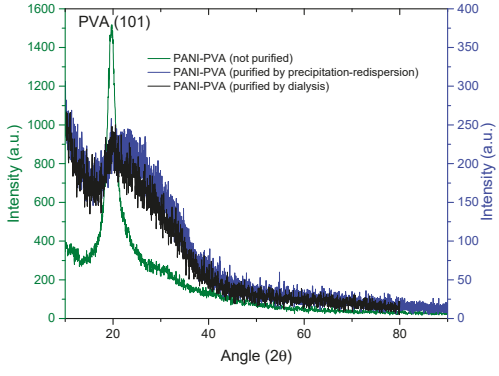

Figure 15. XRD diffractogram comparison for unpurified and purified PVA–PANI by precipitation –redispersion and dialysis.

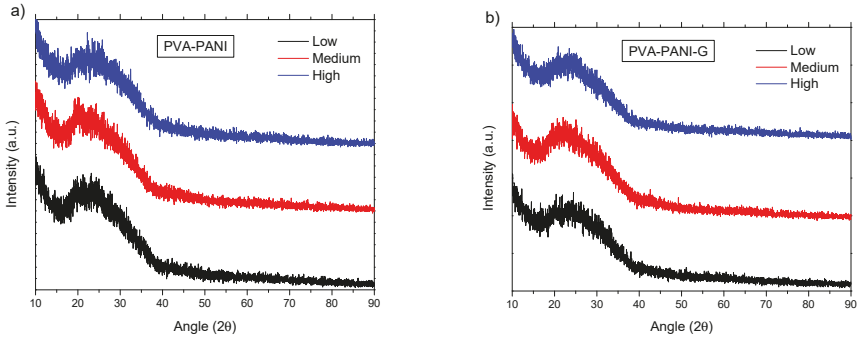

Figure 16. XRD diffractogram of (**a**) PVA–PANI thin films at different concentrations of aniline and (**b**) its comparison with PVA–PANI-G thin films.

2.3.2. Scanning Electron Microscopy (SEM)

Figure 17 shows the SEM micrographs obtained for PVA–PANI films purified by the precipitation–redispersion method for low, medium, and high aniline concentrations with respect to the PVA polymer matrix. Similar results were obtained for PVA–PANI-G thin films (Figure S4).

The morphology of the particles presents as needles which changed with increasing aniline concentration, generating particles in granular form which tend to agglomerate in different nucleation points, according to the reports of Gangopadhyay et al. [12]. On the other hand, the morphology observed for both PVA–PANI and PVA–PANI-G purified by dialysis maintained a spherical shape with an average size of 156 nm (Figure 18), which has been reported for various PANI synthesis processes [37]. This indicates that the precipitation–redispersion process (Figure 17) influences morphological changes in the material, along with pH, temperature, and solvents used.

Even though a significant difference in morphology is shown between both purification methods, we found no significant difference in the crystallinity of the material according to Figure 15, where PVA–PANI purified by dialysis tends to show a better molecular order due to the stabilizing effect of the PVA, promoting better control in the growth of nucleation sites for the obtained films.

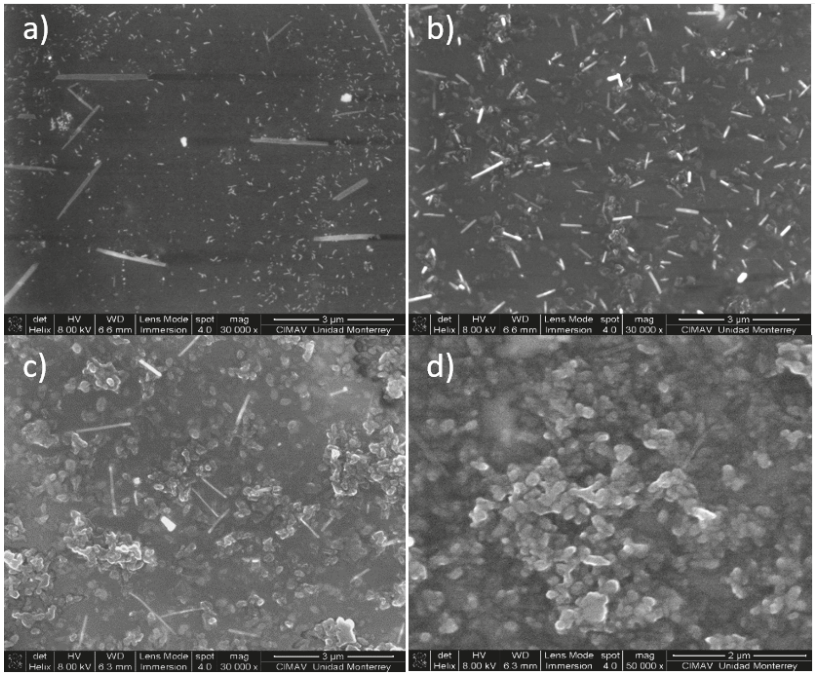

Figure 17. SEM micrographs of purified PVA–PANI thin films and its morphologic variations at (**a**) low concentration, (**b**) medium concentration, and (**c**,**d**) high concentration.

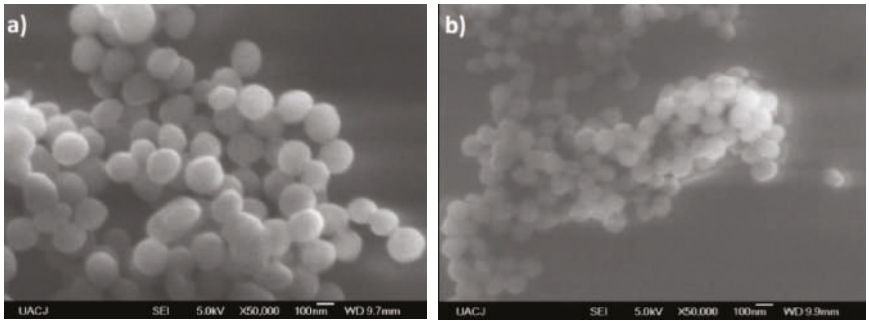

Figure 18. SEM micrographs of (**a**) PVA–PANI and (**b**) PVA–PANI-G purified by dialysis.

3. Materials and Methods

3.1. Materials

The reagents used for the synthesis of PVA–PANI copolymers are as follows. Polyvinyl alcohol (PVA) (130,000 MW, 99% hydrolyzed), high purity aniline monomer (≥99.5%), and ammonium persulfate (APS) (ACS ≥ 98%) (Sigma Aldrich Co., Toluca, Edo. Mex., Mexico). Hydrochloric acid (36–38%) (J.T. Baker, Phillipsburg, NJ, USA) and glutaraldehyde solution (50 wt % in H_2O) (Sigma Aldrich Co.) for the activation of the obtained PVA–PANI blends. Aniline was stored in a dark environment and under refrigeration, all reagents were used as acquired.

3.2. Synthesis of PVA–PANI

First a solution of PVA 5 wt % was made by dissolving 0.0202 mmol (2.6315 g) of PVA (MW = 130,000 g/mol) in 50 mL of deionized water (Milli-Q) under constant magnetic stirring at 80 °C until a clear solution was obtained. Then, the PVA 5 wt % was used as a polymer matrix for the polymerization of aniline at different ratios with respect to the PVA as shown in Table 1.

Subsequently, the pH of the matrix was adjusted to a value of $\leq$2, and it was taken immediately to an ice bath (T $\leq$ 5 °C) where ammonium persulfate was added drop wise at a ratio of 1:1 M to aniline according to Table 2. After a few minutes, the color change of the colloidal dispersion was observed, obtaining a dark green dispersion without sedimentation as reported in the literature [13].

Table 2. Monomer and intermediary molar ratios.

PVA (mmol)	Aniline (mmol)	Aniline (M)	HCl (mmol)	APS (mmol)	APS (M)
0.0202	3.532	0.070	100	3.532	0.070
0.0202	7.064	0.141	100	7.064	0.141
0.0202	10.596	0.212	100	10.596	0.212
0.0202	14.128	0.282	100	14.128	0.282
0.0202	17.660	0.353	100	17.660	0.353
0.0202	21.192	0.423	100	21.192	0.423

3.3. Purification Process

When carrying out the PVA–PANI synthesis by the polymerization dispersion method, a number of byproducts related to doping, oxidant material (APS) and oligomers are generated (Figure 8). Therefore, these byproducts must be eliminated by means of a purification process, in order to obtain the PVA–PANI material without any other product that influences the effects produced by the material in future characterizations.

The purification of PVA–PANI copolymers was carried out mainly by two methods: precipitation–redispersion based on a solvent system CH_3OH:H_2O (5:1) in which the copolymer precipitates, then this precipitate is filtered, dried in vacuum, and redispersed in deionized water (Milli-Q) under temperature and continuous agitation. As well as a dialysis process, which is based on the implementation of membranes with a cut out molecular weight (MWCO) of 12,000 Da (Obtained from Sigma Aldrich Co.), where a certain amount of PVA–PANI is placed against deionized water (Milli-Q) for 48 h so that most byproducts permeate through the membrane. Prior to its chemical and thermal characterization, the obtained PVA–PANI was vacuum-filtered and dried.

3.4. Thin Film Development

PVA–PANI thin films were obtained by dip coating (for precipitation–redispersion purification) and spin coating (for dialysis purification) physical methods using Corning glass substrates previously cleaned with acetone, isopropanol, and deionized water (Milli-Q). Once the thin films were obtained they were washed, dried with N_2 gas, and kept in a desiccator before being analyzed.

3.5. Activation of PVA–PANI Thin Films

Activation of PVA–PANI films with GA was carried out by immersing them in a 1% dilution of GA for a time of 5, 15, and 30 min at room temperature. Followed by a wash with deionized water (Milli-Q) to remove any agent that did not reacted. Later they were placed in a desiccator for storage.

3.6. Characterization Methods

Purity and molecular structure of the obtained PVA–PANI blend was confirmed by ^{1}H-NMR using a Brucker NMR equipment (Brucker, Billerica, MA., USA) at a frequency of 500 MHz, using tetramethyl silane (TMS) as standard at room temperature. To complement molecular structure and observe

the present functional groups in the material an FTIR analysis was carried out using a Thermo Scientific Nicolet iS10 FT-IR spectrometer (ATR) in the region from 400 to 4000 cm^{-1} in air atmosphere and at room temperature. Optical properties and transitions of the developed PVA–PANI thin films were analyzed using a Jenway 6850 UV–Vis-NIR spectrophotometer (Bibby Scientific, Staffs., UK) in the region from 1000 to 300 nm in absorption mode. The thermal stability, composition, purity, and cross-linking effect of the PVA–PANI gels were analyzed using a TGA/DSC SDT-Q600 implementing a temperature program from 25 °C to 600 °C with a heating speed of 10 °C/min and controlled N_2 atmosphere. Microstructural characteristics for the thin films were obtained by XRD using a Panalytical diffractometer with a Cu kα radiation with a 1.54 wavelength used at a glancing angle. And the morphological variations of the material were observed with a Nova NanoSEM 200 equipment (FEI, Tokyo, Japan) using secondary electrons.

4. Conclusions

The purification of HCl-doped PVA–PANI copolymers at different aniline concentrations and the effect of their activation with GA was studied. ^{1}H-NMR and FTIR analysis was used to confirm the molecular structure of the material as proposed from the skeletal formula before carrying out further characterizations. Regarding the activation of the material, it was observed that GA has a reduction effect on the PVA–PANI copolymer (increasing the number of benzene units of PANI), which increases proportionally with immersion time and concentration as confirmed by FTIR and UV–Vis-NIR. The activation of the material was confirmed by FTIR showing the characteristic absorption bands in the 1550 to 1750 cm^{-1} range, where the C=N (Schiff base) bond corresponding to the formation of imines can be found. Further analysis of cross-linking between PVA–PANI and GA was carried out by DSC, showing that the interaction of GA towards the material is favored at low aniline concentration, where minor variations where observed due to doping level. The purity of the material was confirmed by TGA-DTG, which showed bands corresponding to weight losses and exothermic peaks of PVA–PANI only. Moreover, it was seen that the precipitation–redispersion method seems to affect the structural and morphological properties of the PVA–PANI at different aniline concentrations, even after GA activation, as shown from the XRD and SEM results. Therefore, the dialysis purification method is recommended for upcoming experiments. We propose, as future work, to carry out experiments immobilizing an antibody on the activated material to test it as a platform for biological detection, in order to apply it as an active membrane in future in vitro diagnostic devices.

Supplementary Materials: Supplementary materials are available online.

Author Contributions: Conceptualization, J.M.G., A.C., and F.S.A.; Methodology, J.M.G., A.C., and M.L.M.; Formal Analysis, J.M.G., A.C., M.L.M., and F.S.A.; Investigation, J.M.G., A.C., M.L.M., R.C.A., and F.S.A; Resources, A.C. and F.S.A.; Data Curation, J.M.G.; Writing—Original Draft Preparation, J.M.G; Writing—Review and Editing, J.M.G., R.C.A., A.C., M.L.M., and F.S.A.; Visualization, J.M.G; Supervision, A.C., M.L.M., R.C.A., and F.S.A.; Validation, Project Administration, and Funding Acquisition, F.S.A., A.C., and CONACYT.

Funding: This research was funded by CONACYT, México, Grant Number 294690.

Acknowledgments: The authors would like to acknowledge to José Guadalupe Téllez Padilla (^{1}H-NMR), Alberto Toxqui Terán (TGA/DTG/DSC), Nayely Pineda Aguilar (SEM), and Francisco Enrique Longoria Rodríguez (XRD) for assisting in the presented characterization, and personnel from UACJ (Chihuahua, México), Biotechnology Incubator (Nuevo León, México), and CIMAV (Nuevo León, México) for technical support and for providing the infrastructure to develop this work.

Conflicts of Interest: The authors declare no conflicts of interest.

References

1. Shirakawa, H.; Louis, E.J.; Chiang, C.K.; Heeger, A.J. Synthesis of Electrically Conducting Organic Polymers: Halogene Derivatives of Polyacetylene, (CH)x. *J. C. S. Chem. Comm.* **1977**, *16*, 578–580. [CrossRef]
2. Blinova, N.V.; Stejskal, J.; Trchová, M.; Ćirić-Marjanović, G.; Sapurina, I. Polymerization of aniline on polyaniline membranes. *J. Phys. Chem. B* **2007**, *111*, 2440–2448. [CrossRef] [PubMed]

3. Gao, X.Z.; Liu, H.J.; Cheng, F.; Chen, Y. Thermoresponsive polyaniline nanoparticles: Preparation, characterization, and their potential application in waterborne anticorrosion coatings. *Chem. Eng. J.* **2016**, *283*, 682–691. [CrossRef]
4. Wang, P.; Liu, M.; Kan, J. Amperometric phenol biosensor based on polyaniline. *Sensors Actuators B Chem.* **2009**, *140*, 577–584. [CrossRef]
5. Parente, A.H.; Marques, E.T.A.; Azevedo, W.M.; Filho, J.L.L. Glucose Biosensor Using Glucose Oxidase Immobilized in Polyaniline. *Appl. Biochem. Biotechnol.* **1992**, *37*, 267–273. [CrossRef]
6. Tiwari, A.; Shukla, S.K. Chitosan-g-polyaniline: A creatine amidinohydrolase immobilization matrix for creatine biosensor. *Express Polym. Lett.* **2009**, *3*, 553–559. [CrossRef]
7. Chowdhury, A.D.; De, A.; Chaudhuri, C.R.; Bandyopadhyay, K.; Sen, P. Label free polyaniline based impedimetric biosensor for detection of *E. coli* O157:H7 Bacteria. *Sensors Actuators B Chem.* **2012**, *171–172*, 916–923. [CrossRef]
8. Sawangphruk, M.; Suksomboon, M.; Kongsupornsak, K.; Khuntilo, J.; Srimuk, P.; Sanguansak, Y.; Klunbud, P.; Suktha, P.; Chiochan, P. High-performance supercapacitors based on silver nanoparticle-polyaniline- graphene nanocomposites coated on flexible carbon fiber paper. *J. Mater. Chem. A* **2013**, *1*, 9630–9636. [CrossRef]
9. Bhadra, J.; Sarkar, D. Field effect transistor fabricated from polyaniline-polyvinyl alcohol nanocomposite. *Indian J. Phys.* **2010**, *84*, 693–697. [CrossRef]
10. Qin, Y. Alginate fibers: An overwiew of the production processes and applications in wound management. *Polym. Int.* **2008**, *57*, 171–180. [CrossRef]
11. Ameen, S.; Ali, V.; Zulfequar, M.; Mazharul, M.; Husain, M. Synthesis and characterization of polyaniline-polyvinyl chloride blends doped with sulfamic acid in aqueous tetrahydrofuran. *Cent. Eur. J. Chem.* **2006**, *4*, 565–577. [CrossRef]
12. Gangopadhyay, R.; De, A.; Ghosh, G. Polyaniline-poly(vinyl alcohol) conducting composite: Material with easy processability and novel application potential. *Synth. Met.* **2001**, *123*, 21–31. [CrossRef]
13. Bhadra, J.; Sarkar, D. Self-assembled polyaniline nanorods synthesized by facile route of dispersion polymerization. *Mater. Lett.* **2009**, *63*, 69–71. [CrossRef]
14. Mirmohseni, A.; Wallace, G.G. Preparation and characterization of processable electroactive polyaniline-polyvinyl alcohol composite. *Polymer* **2003**, *44*, 3523–3528. [CrossRef]
15. Bhadra, J.; Al-Thani, N.J.; Madi, N.K.; Al-Maadeed, M.A. Effects of aniline concentrations on the electrical and mechanical properties of polyaniline polyvinyl alcohol blends. *Arab. J. Chem.* **2015**, *10*, 664–672. [CrossRef]
16. Purcena, L.L.A.; Caramori, S.S.; Mitidieri, S.; Fernandes, K.F. The immobilization of trypsin onto polyaniline for protein digestion. *Mater. Sci. Eng. C* **2009**, *29*, 1077–1081. [CrossRef]
17. Caramori, S.S.; De Faria, F.N.; Viana, M.P.; Fernandes, K.F.; Carvalho, L.B. Trypsin immobilization on discs of polyvinyl alcohol glutaraldehyde/ polyaniline composite. *Mater. Sci. Eng. C* **2011**, *31*, 252–257. [CrossRef]
18. Stejskal, J.; Hajná, M.; Kašpárková, V.; Humpolíček, P.; Zhigunov, A.; Trchová, M. Purification of a conducting polymer, polyaniline, for biomedical applications. *Synth. Met.* **2014**, *195*, 286–293. [CrossRef]
19. Alves, M.; Young, C.; Bozzetto, K.; Poole-Warren, L.A.; Martens, P.J. Degradable, poly(vinyl alcohol) hydrogels: Characterization of degradation and cellular compatibility. *Biomed. Mater.* **2012**, *7*, 024106. [CrossRef]
20. Nagy, M.; Szollosi, L.; Keki, S.; Faust, R.; Zsuga, M. Poly(vinyl alcohol)-based amphiphilic copolymer aggregates as drug carrying nanoparticles. *J. Macromol. Sci. Part A Pure Appl. Chem.* **2009**, *46*, 331–338. [CrossRef]
21. Andrade, G.; Barbosa-Stancioli, E.F.; Piscitelli Mansur, A.A.; Vasconcelos, W.L.; Mansur, H.S. Design of novel hybrid organic-inorganic nanostructured biomaterials for immunoassay applications. *Biomed. Mater.* **2006**, *1*, 221–234. [CrossRef] [PubMed]
22. Trchová, M.; Stejskal, J. Polyaniline: The infrared spectroscopy of conducting polymer nanotubes (IUPAC Technical Report). *Pure Appl. Chem.* **2011**, *83*, 1803–1817. [CrossRef]
23. Bhadra, J.; Sarkar, D. Size variation of polyaniline nanoparticles dispersed in polyvinyl alcohol matrix. *Bull. Mater. Sci.* **2010**, *33*, 519–523. [CrossRef]
24. Mansur, H.S.; Sadahira, C.M.; Souza, A.N.; Mansur, A.A.P. FTIR spectroscopy characterization of poly (vinyl alcohol) hydrogel with different hydrolysis degree and chemically crosslinked with glutaraldehyde. *Mater. Sci. Eng. C* **2008**, *28*, 539–548. [CrossRef]
25. Lin-Vien, D.; Colthup, N.B.; Fateley, W.G.; Grasselli, J.G. *The Handbook of Infrared and Raman Characteristic Frequencies of Organic Molecules*, 1st ed.; Academic Press: San Diego, CA, USA, 1991; p. 503. ISBN 9780080571164.

26. De Melo, J.V.; Bello, M.E.; de Azevêdo, W.M.; de Souza, J.M.; Diniz, F.B. The effect of glutaraldehyde on the electrochemical behavior of polyaniline. *Electrochim. Acta* **1999**, *44*, 2405–2412. [CrossRef]
27. Gomes, E.C.; Oliveira, M.A.S. Chemical Polymerization of Aniline in Hydrochloric Acid (HCl) and Formic Acid (HCOOH) Media. Differences Between the Two Synthesized Polyanilines. *Am. J. Polym. Sci.* **2012**, *2*, 5–13. [CrossRef]
28. Yang, D.; Lu, W.; Goering, R.; Mattes, B.R. Investigation of polyaniline processibility using GPC/UV-vis analysis. *Synth. Met.* **2009**, *159*, 666–674. [CrossRef]
29. Honmute, S.; Ganachari, S.V. Studies on Polyaniline-Polyvinyl Alcohol (PANI-PVA) Interpenetrating Polymer Network (IPN) Thin Films. *Int. J. Sci. Res.* **2012**, *1*, 102–106.
30. Bhadra, J.; Madi, N.K.; Al-Thani, N.J.; Al-Maadeed, M.A. Polyaniline/polyvinyl alcohol blends: Effect of sulfonic acid dopants on microstructural, optical, thermal and electrical properties. *Synth. Met.* **2014**, *191*, 126–134. [CrossRef]
31. Mahato, M.; Adhikari, B. Vapor phase sensing response of doped polyaniline-poly (vinyl alcohol) composite membrane to different aliphatic alcohols. *Synth. Met.* **2016**, *220*, 410–420. [CrossRef]
32. Vargas, L.R.; Poli, A.K.; Lazzarini Dutra, R.; Brito de Souza, C.; Ribeiro Baldan, M.; Sarmento Goncalves, E. Formation of Composite Polyaniline and Graphene Oxide by Physical Mixture Method. *J. Aerosp. Technol. Manag.* **2017**, *9*, 29–38. [CrossRef]
33. Meftah, A.M.; Gharibshahi, E.; Soltani, N.; Mat Yunus, W.M.; Saion, E. Structural, optical and electrical properties of PVA/PANI/Nickel nanocomposites synthesized by gamma radiolytic method. *Polymers* **2014**, *6*, 2435–2450. [CrossRef]
34. Mansour, F.; Elfalaky, A.; Maged, F.A. Synthesis, Characterization and Optical properties of PANI/ PVA Blends. *IOSR J. Appl. Phys.* **2015**, *7*, 37–45.
35. Geethalakshmi, D.; Muthukumarasamy, N.; Balasundaraprabhu, R. Effect of dopant concentration on the properties of HCl-doped PANI thin films prepared at different temperatures. *Optik* **2014**, *125*, 1307–1310. [CrossRef]
36. Hu, H.; Xin, J.H.; Hu, H.; Chan, A.; He, L. Glutaraldehyde-chitosan and poly (vinyl alcohol) blends, and fluorescence of their nano-silica composite films. *Carbohyd. Polym.* **2013**, *91*, 305–313. [CrossRef] [PubMed]
37. Zhang, L.; Ma, H.; Cong, C.; Su, Z. Nonaqueos synthesis of uniform polyaniline nanospheres via cellulose acetate template. *J. Polym. Sci. Part A Polym. Chem.* **2012**, *50*, 912–917. [CrossRef]

Sample Availability: Samples of the compounds are not available from the authors.

molecules

MDPI

Article

Synthesis of Carbohydrate-Grafted Glycopolymers Using a Catalyst-Free, Perfluoroarylazide-Mediated Fast Staudinger Reaction

William Ndugire, Bin Wu and Mingdi Yan *

Department of Chemistry, University of Massachusetts Lowell, 1 University Ave., Lowell, MA 01854, USA; William_Ndugire@student.uml.edu (W.N.); Bin_Wu1@student.uml.edu (B.W.)

* Correspondence: mingdi_yan@uml.edu; Tel.: +978-934-3647

Received: 5 December 2018; Accepted: 30 December 2018; Published: 3 January 2019

Abstract: Glycopolymers have gained increasing importance in investigating glycan-lectin interactions, as drug delivery vehicles and in modulating interactions with proteins. The synthesis of these glycopolymers is still a challenging and rigorous exercise. In this regard, the highly efficient click reaction, copper (I)-catalyzed alkyne-azide cycloaddition, has been widely applied not only for its efficiency but also for its tolerance of the appended carbohydrate groups. However, a significant drawback of this method is the use of the heavy metal catalyst which is difficult to remove completely, and ultimately toxic to biological systems. In this work, we present the synthesis of carbohydrate-grafted glycopolymers utilizing a mild and catalyst-free perfluorophenyl azide (PFPA)-mediated Staudinger reaction. Using this strategy, mannose (Man) and maltoheptaose (MH) were grafted onto the biodegradable poly(lactic acid) (PLA) by stirring a PFAA-functionalized PLA with a phosphine-derivatized Man or MH in DMSO at room temperature within an hour. The glycopolymers were characterized by ^{1}H-NMR, ^{19}F-NMR, ^{31}P-NMR and FTIR.

Keywords: Glycopolymer; post-polymerization functionalization; perfluoroaryl azides; Staudinger reaction

1. Introduction

Carbohydrates are not only the core of metabolism in many biological systems, but are also integral in many cells as structural [1], communication [2], and recognition [3] elements. Synthetic carbohydrate-functionalized polymers, i.e., glycopolymers, has become an important tool in fundamental glycobiology research, and in biomedical applications such as sensing [4,5], drug delivery [6], and cryopreservation [7,8]. Synthetic glycopolymers can be categorized broadly into two types based on the mode of synthesis: (1) polymerization of carbohydrate-derivatized monomers (such as allyl [9], acrylamide [10] and acrylate [11]), and (2) grafting of carbohydrates onto a polymer backbone [12–17]. The latter technique, typically referred to as post-polymerization modification, allows facile synthesis of the polymer backbone and control over carbohydrate grafting density. To successfully graft carbohydrates onto the polymer, the conjugation reaction must be highly efficient, of high yield, and tolerant of the functional groups on the polymer. The popular 'click' type of reactions, particularly the copper(I)-catalyzed alkyne-azide cycloaddition (CuAAC), meet these requirements and have been applied in the synthesis of glycopolymers by post-polymerization and in glycosylation of surfaces [18–20]. This reaction tolerates a wide variety of carbohydrate side groups. Analytically, it offers the advantage in the form of the distinct chemical shift of the triazole proton in ^{1}H-NMR that facilitates straightforward characterization [21,22]. However, a drawback of this reaction is the necessity of Cu (I) catalyst that has proved difficult to be removed completely from the products. While at least 2–5 mol% of Cu (I) is required to achieve a respectable reaction rate, even

small amounts of residual metal in the final product has been shown to denature proteins and cause oxidative damage to cells [21,23,24]. Other click-type reactions that do not require metal catalysts include SPAAC (strain-promoted azide-alkyne cycloaddition), azide-aryne based "benzyne click" reaction, and iEDDA (inverse electron demand Diels–Alder) reaction [25–27], but these have not been applied directly in the synthesis of glycopolymers.

Another click-type reaction is the phosphine-azide Staudinger reaction [28]. The recent improvement by Bertozzi via the introduction of an ester trap [29] rendered this bioorthogonal reaction suitable for in vivo conjugations [30,31] and in oligosaccharide metabolic engineering for cell-surface labelling [29,32]. Despite its versatility, the Staudinger ligation suffers from a slow reaction rate. To overcome this issue, we have recently shown that by using an electron-deficient perfluoroaryl azide (PFPA), the rate of reaction can be increased up to four orders of magnitude to give an iminophosphorane product [33]. The rate enhancement can be attributed to the highly electronegative F atoms lowering the LUMO of PFPA thus accelerating the reactions with dienophiles and nucleophiles [34–37]. In addition, the PFPA-iminophosphorane formed in this reaction was stable and not readily hydrolyzed in vivo, as demonstrated in the metabolic labeling of A549 cells [33].

The fast reaction rate and high yield make this PFPA-Staudinger reaction an excellent candidate for polymerization. In an earlier work, we demonstrated that the reaction of bis-PFPA and a bisphosphene occurred at room temperature in 30 min to yield poly(iminophosphorane) having molecular weight of over 59,000 and a narrow dispersity of 1.1–1.2 [38]. In this work, we applied this reaction in the post-polymerization synthesis of carbohydrate–grafted glycopolymers. By taking advantage of the fast reaction rate, mild reaction conditions, and high chemoselectivity of the PFPA-Staudinger reaction, we conjugated maltoheptaose and mannose onto poly(lactic acid) (PLA), a biocompatible and biodegradable glycopolymer.

2. Results and Discussion

While the availability of pendant functional groups like the hydroxyl on the polymer would be suited for condensation with a carboxyl-modified sugar, this strategy is less desirable as it requires the use of coupling agents that can be difficult to remove like DCC/DMAP [39] or strong acid [40] that would hydrolyze the polymer.

Our design for grafting carbohydrates to PLA was to functionalize PLA with PFPA followed by reaction with a phosphine-derivatized carbohydrate. A PLA-*co*-PLA-PFPA copolymer is synthesized so that the density of PFPA and the carbohydrate can be varied and controlled. A hydroxy-functionalized polylactide copolymer **4** (Scheme 1A) was synthesized to conjugate PFPA and subsequently graft the carbohydrate. The benzyl-derivatized lactide monomer **1** was synthesized according to Scheme 1B. Ring-opening copolymerization of lactide **1** and lactide **2** in toluene using stannous octoate as the catalyst gave polylactide copolymer **4** in 74% yield [5]. The ratio of the two monomers can be varied so as to control the grafting density of carbohydrate on the PLA polymer. In this work, the polymer obtained had a monomer ratio (m:n) of 1:22 for **1** and **2** after copolymerization. Deprotection of the benzyl group on **3** gave the hydroxy-functionalized polylactide copolymer **4** in 63% yield [5]. The m:n ratio was calculated from the ^{1}H-NMR spectrum of **4** (Figure 1A) by taking the ratio of the methine protons (H-a and H-c) that overlap at 5.2 ppm. The integral value of the H-a is equivalent to methylene protons H-b/2. Subtraction of this value from the overlapped (H-a + H-c) gives the integration of H-c and therefore H-a/H-c can be calculated.

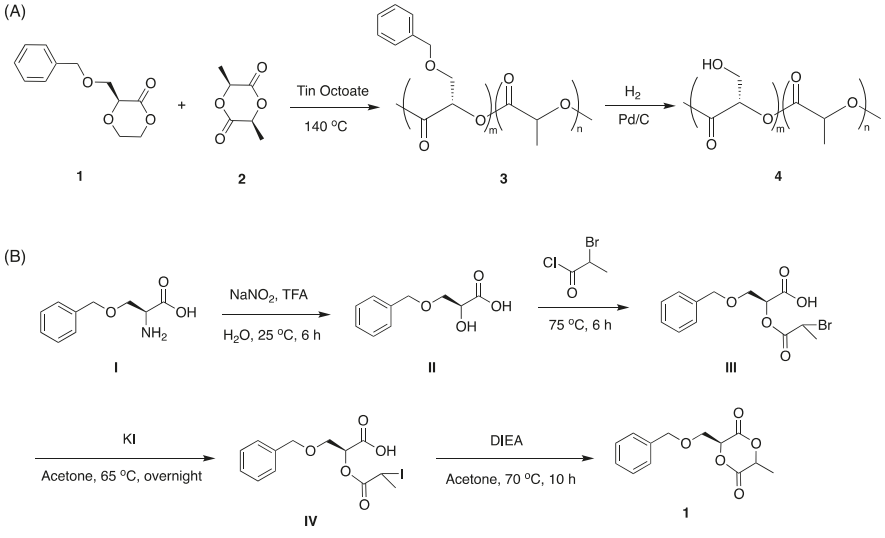

Scheme 1. Synthesis of (**A**) hydroxy-functionalized polylactide copolymer **4**, and (**B**) lactide monomer **1**.

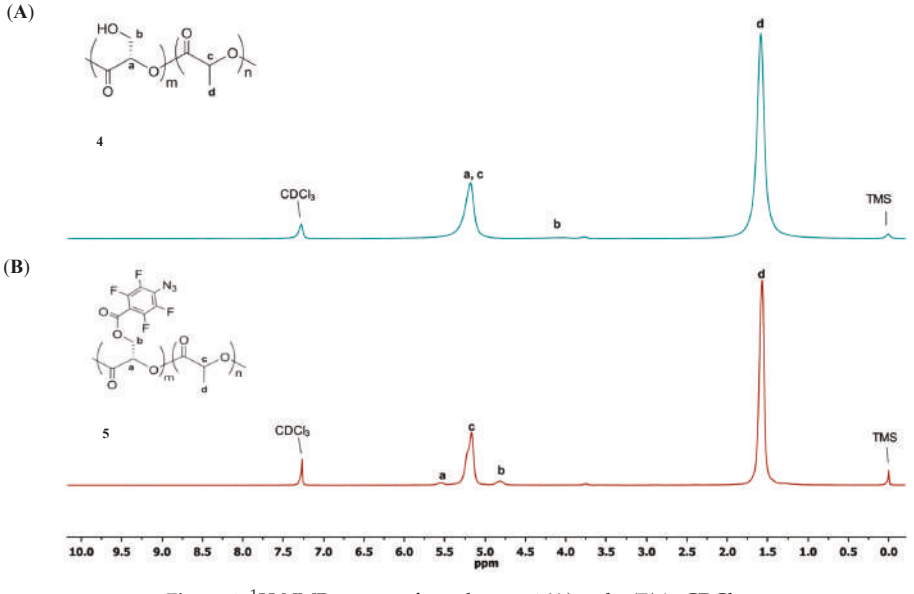

Figure 1. ^{1}H-NMR spectra of copolymers **4** (**A**) and **5** (**B**) in $CDCl_3$.

PFPA-functionalized PLA copolymer **5** was prepared by esterification of **4** with carboxy-derivatized PFPA using DCC and a catalytic amount of DMAP giving **5** in 86% yield (Scheme 2).

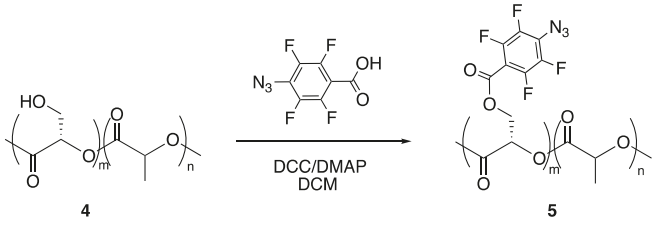

Scheme 2. Synthesis of PFPA-PLA copolymer **5**.

The ^{1}H-NMR spectrum of **5** showed a near complete reaction as demonstrated by a marked shift of the methylene proton H-b from 4.05 ppm to 4.83 ppm (Figure 1). No degradation of the copolymers to the free lactic acid monomer was observed during the reaction, as evidenced by the absence of peaks at ~1.2 ppm which belongs to the free lactic acid. In addition, the characteristic azide peak at 2133 cm^{-1} appeared in the Fourier transform-infrared spectroscopy (FTIR) spectrum of copolymer 5 (Figure 2).

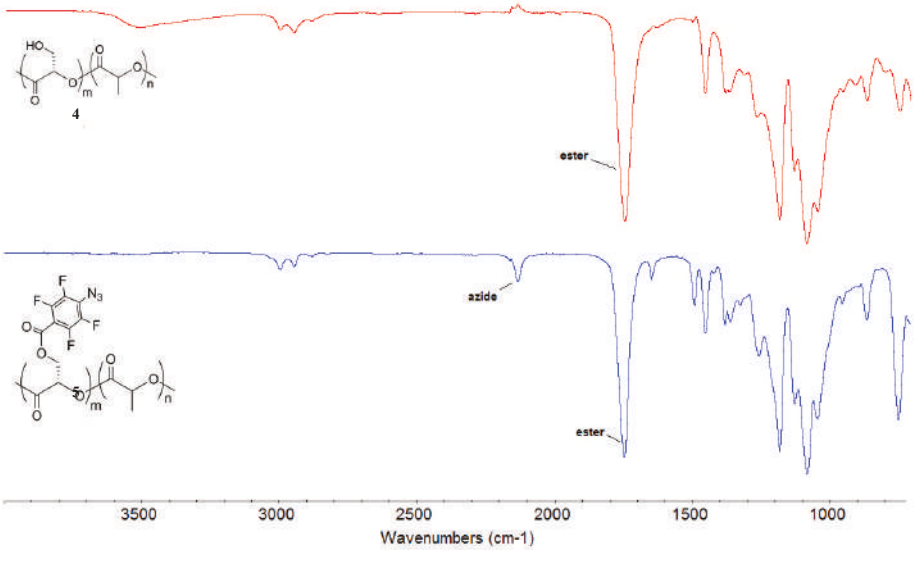

Figure 2. FTIR spectra of PLA copolymers **4** and **5.**

The phosphine-derivatized carbohydrates were prepared from an amine-derivatized carbohydrate and the NHS-functionalized phosphine (Scheme 3). A monosaccharide, D-mannose (Man), and an oligosaccharide, D-maltoheptaose (MH), were used as model carbohydrates in this study. The amine-Man **6** was synthesized according to previously reported procedure (see Scheme S2 and detailed procedures in SI) [41]. The amine-MH **7** was synthesized following the procedure in Scheme S1 (see detailed procedures in SI). Reaction of NHS-functionalized triphenylphosphine with excess of **6** or **7** in DMSO at room temperature gave the triphenylphosphine-derivatized Man (**8**) or MH (**9**).

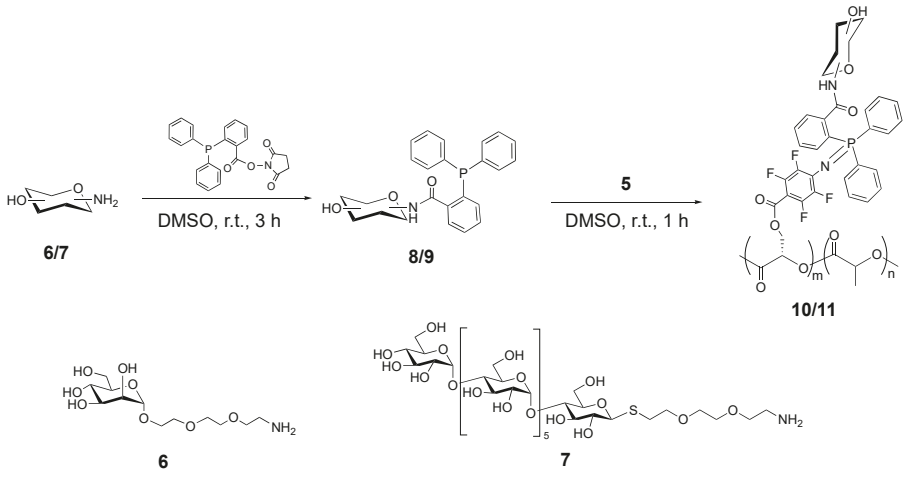

Scheme 3. Synthesis of phosphine-derivatized mannose **8** and maltoheptaose **9**, and subsequent grafting to PFPA-PLA copolymer **5** to yield mannose-polymer **10** and maltoheptaose-polymer **11**, respectively.

To prepare Man- or MH-grafted PLA **10** and **11**, copolymer **5** was added directly to the reaction mixture of **8** or **9** in DMSO and stirred at room temperature for 1 h. The products were purified by dialysis for 48 h and dried by lyophilization. After the carbohydrate was grafted, the aromatic and the carbohydrate peaks appeared in the ^{1}H-NMR spectra of **10** and **11** at 7.5–7.7 ppm and 3.0–6.0 ppm, respectively (Figure 3). In the ^{31}P-NMR spectra of the products (Figure 4), a new peak was observed at 13 ppm after conjugation of the phosphine onto the copolymer. The absence of any peaks higher than 13 ppm confirmed the absence of byproducts resulting from the oxidation of phosphine.

The yield of conjugation was obtained from the ^{1}H-NMR spectrum by taking the ratio of peak integration of the phenyl protons (Ph) at 7.5–7.7 ppm and the methyl protons H-b at 1.48 ppm, together with the previously calculated monomer ratio of m:n = 1:22 to give the formula:

$$(\%)coupling\ yield = \left(\frac{\frac{Ph}{14} \times 22}{\frac{H-b}{3}} \right) \times 100 \quad (1)$$

Using this equation, the yields were calculated to be 25% and 35% for the Man-grafted PLA copolymer **10** and MH-grafted PLA copolymer **11**, respectively (see Figures S5 and S6 for peak integrations).

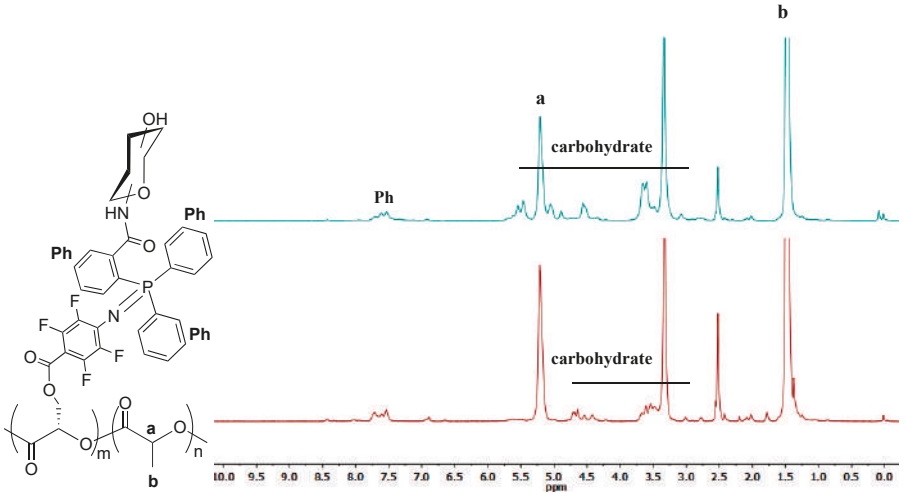

Figure 3. ^{1}H-NMR spectra of Man- and MH-grafted copolymers **10** (**top**) and **11** (**bottom**) in DMSO-d_6.

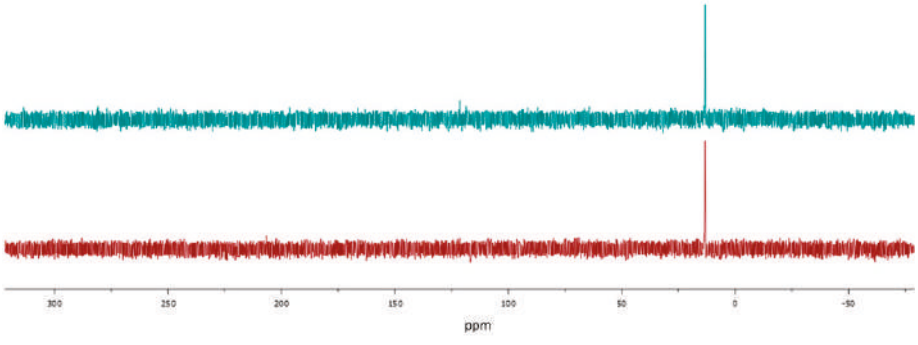

Figure 4. ^{31}P-NMR spectra of copolymer **10** (**top**) and **11** (**bottom**) in DMSO-d_6.

3. Conclusions

In this work, we utilized an electron-deficient perfluorophenyl azide-mediated fast Staudinger reaction to efficiently synthesize carbohydrate grafted-polylactide glycopolymers by post-polymerization modification. A polylactide copolymer was synthesized by stannous octoate-catalyzed cationic ring-opening copolymerization, which was subsequently modified with PFPA. Conjugation with a phosphine-derivatized carbohydrate yield mannose- and maltoheptaose-grafted polylactide glycopolymers in 35% and 25% yields. These yields are comparable to those obtained by other groups in post-polymerization synthesis of glycopolymers using other techniques [42,43]. The main limiting factor of efficient grafting being steric hindrance between ligands and the polymer backbone restricting access to the reactive sites. In our work, this occurs between carbohydrate-phosphines reaction with the pendant PFPA groups, which is further complicated by the difference in polarity between the PLA and D-mannose/maltoheptaose. However, the grafting reaction is fast, carried out under mild conditions without the use of any catalyst. This metal catalyst-free approach to glycopolymer synthesis is significant as it eliminates the concerns over the potential toxicity of heavy metals, making these glycopolymers attractive for biomedical applications.

4. Experimental Procedures

4.1. Materials and Instruments

All chemicals and solvents were purchased from Sigma-Aldrich (St. Louis, MO, USA), TCI America (Portland, Oregon, USA) or Fisher Scientific (Hampton, NH, USA), and were used without further purification unless otherwise noted. Dichloromethane (DCM), dimethylformamide (DMF), ethyl acetate (EtOAc) and dimethyl sulfoxide (DMSO) were purified by distillation over CaH_2. Deuterated solvents were acquired from Cambridge Isotope Lab., Inc. (Tewksbury, MA, USA). Amberlite IRC-120H$^+$ resin was activated by washing with NaOH and HCl, followed by water, ethanol and toluene.

Nuclear magnetic resonance spectroscopy data were collected on either a Bruker 500 MHz spectrometer (^{1}H-NMR) or a Bruker 200 MHz spectrometer (^{19}F- and ^{31}P-NMR) (Bruker Corporation, Billerica, MA, USA). FT-IR spectra were recorded on a Nicolet 6700 FT-IR spectrometer (Thermo Fisher Scientific, Waltham, MA, USA).

4-Azido-2,3,5,6-tetrafluorobenzoic acid (PFPA-COOH) was synthesized following our previously developed protocol [44,45]. The detailed synthesis of 1-(2-(2-(2-aminoethoxy)ethoxy)ethoxy-α-D-mannopyranoside (**6**, Scheme S2) [41,46] and 1-(2-(2-(2-aminoethoxy)ethoxy)ethoxy-maltoheptaoside (**7**, Scheme S1) can be found in the Supporting Information.

*4.2. Synthesis of 3-benzyloxy-2-hydroxypropionic acid (***II***)*

Synthesized according to literature procedure [47]. To a 200 mL of 0.7 M aqueous solution of trifluoroacetic acid, H-Ser(benzyl)-OH (**I**, 10.0 g, 52 mmol) was added, and the mixture was stirred at room temperature until all solids were dissolved. Then, 50 mL of aqueous $NaNO_2$ (5.3 g, 77 mmol) was added dropwise with a syringe pump under Ar protection and the reaction was stirred for another 3 h. After confirming of the consumption of starting material by TLC, NaCl (10 g) was added and the mixture was extracted with ethyl acetate three times followed by washing with brine and dried over $MgSO_4$. After passing through a flash column using CH_2Cl_2/MeOH/AcOH (*v*/*v*/*v* 100:8:1), compound **II** was obtained (7.2 g, 72%).[3] ^{1}H-NMR (500 MHz, DMSO-d_6) δ 7.35–7.26 (m, 5H, Ar-H), 4.60 (s, 2H, PhCH_2O-), 4.38 (s, 1H, -OCH$_2$C*H*(COOH)O-) 3.83 (d, *J* = 15 Hz, 2H, -OCH_2CH-). IR: 3324, 3070, 3032, 2925, 2871, 2645, 2537, 1693, 1495, 1455, 1412, 1379, 1274, 1225, 1202, 1161, 1019, 1001, 973, 926, 827, 791, 732, 610, 529 cm^{-1}.

*4.3. Synthesis of 3-(benzyloxy)-2-(2-bromopropanoyloxy)propanoic acid (***III***)*

Synthesized per literature [47]. Compound **II** (10.0 g, 51 mmol) and 2-bromopropionyl chloride (6.3 mL, 61.2 mmol) were mixed in a 50-mL round-bottom flask backfilled with Ar. The reaction mixture was heated to 70 °C and stirred for 6 h. Upon the completion of the reaction, the crude product was heated at 60 °C under reduced pressure to remove unreacted 2-bromopropionyl chloride and 2-bromopropionyl acid. After cooling to room temperature, the residue was washed with water and extracted with ethyl acetate 3 times. The combined organic phase was washed with brine and dried over $MgSO_4$. Compound **III** was obtained as a brown oil after further purification by flash column CH_2Cl_2/MeOH/AcOH (*v*/*v*/*v* 100:2:0.5) (12.6 g, 75%). ^{1}H-NMR (500 MHz, $CDCl_3$): 7.35–7.25 (m, 5H, Ar-H), 5.34–5.32 (m, 1H, -OCH$_2$C*H*(COOH)O-), 4.62–4.38 (m, 3H, PhCH_2O- and -OCC*H*(Br)CH$_3$), 3.97–3.85 (m, 2H, -OCH_2CH-), 1.88–1.83 (m, 3H, -CH(Br)CH_3). IR: 3442, 3031, 2928, 2871, 1732, 1452, 1362, 1211, 1155, 1097, 1070, 985, 910, 738, 697, 610 cm^{-1}.

*4.4. Synthesis of 3-(benzyloxy)-2-(2-iodopropanoyloxy)propanoic acid (***IV***)*

Prepare following literature procedures [47]. Compound **III** (8.0 g, 24 mmol) and potassium iodide (40 g, 0.24 mol) were mixed with 100 mL of anhydrous acetone. The mixture was heated at 60 °C overnight under Ar. The solid salt was removed by passing through a layer of Celite® and the

filtrate was concentrated under vacuum. Ethyl acetate was added to the oily residue and the solution was filtered again to remove trace potassium iodide/potassium bromide. The organic phase was washed with 2 M aq. $Na_2S_2O_3$ for 3 times and dried over $MgSO_4$. After removing the solvent from the filtrate, the product **IV** was obtained and used directly in the next step without purification (7.5 g, 82%). ^{1}H-NMR (500 MHz, $CDCl_3$): δ 10.26 (s, 1H, -COO*H*), 7.50–7.16 (m, 5H, Ar-H), 5.39 (m, 1H, -OCH$_2$C*H*(COOH)O-), 4.84–4.41 (m, 3H, PhCH_2O- and –OCC*H*(Br)CH_3), 3.94 (dd, J = 48.3, 10.4 Hz, 2H, -OCH_2CH-), 2.29–1.87 (m, 3H, -CH(I)CH_3). IR: 2923, 1728, 1496, 1452, 1362, 1197, 1124, 1094, 1043, 1026, 977, 909, 737, 697, 633, 603, 582, 570, 563, 554, 548, 538, 529, 526 cm^{-1}.

4.5. Synthesis of 3-(benzyloxymethyl)-6-methyl-1,4-dioxane-2,5-dione (Monomer **1***)*

Synthesized as described in literature [7]. A solution of compound **IV** (10.0 g, 26.8 mmol) in dry CH_2Cl_2 (100 mL) was added dropwise to refluxing dry acetone (1 L) containing DIEA (8.8 mL, 53.6 mmol) under Ar. It took 10 h to finish the addition and the reaction was refluxed for another hour. The solvents were removed under reduced pressure and ether was added to dissolve the crude product. Insoluble ammonium iodide was filtered and the filtrate was concentrated. After purification by flash column chromatography using hexanes/ethyl acetate (*v*/*v* 4:1), the title compound **1** was obtained as a yellow oil (2.1 g, 31%). The diastereomers were used directly without separation. ^{1}H-NMR (500 MHz, $CDCl_3$): (SS) δ 7.34–7.26 (m, 5H, Ar H), 5.24–5.04 (2H; -OCC*H*(CH$_2$O-)O- and - OCC*H*(CH$_3$)O-), 4.61–4.56 (2H; ArCH_2O-), 3.97 (2H; -OCH_2CH-), 1.63 (3H; -CHCH_3). IR: 2993 (w, ν_s(aromatic C-H)), 2942 (w, ν_{as}(-CH$_2$- and –CH$_3$)), 2872 (w, ν_s(-CH$_2$- and aliphatic -CH-)), 1748 (vs, ν_s(ester C=O)), 1453 (m, δ_s(-CH$_2$-)), 1365 (w), 1268 (w), 1182 (s), 1084 (vs), 1046 (m), 865 (w), 739 (m, ω(aromatic C-H)), 698 (m, τ(aromatic ring)) cm^{-1}.

4.6. Synthesis of PLA copolymer **3**

Monomer **1** (1.0 g, 4.0 mmol), recrystallized L-lactide (**2**, 1.0 g, 6.9 mmol) and Sn(Oct)$_2$ (10 mg in 1 mL anhydrous toluene) were added into a 5-mL round-bottom flask. The mixture was heated to 70 °C under vacuum for 1 h. Ar was filled in the flask and the temperature was increased to 140 °C. The mixture was stirred until the stir bar stopped moving. After cooling to room temperature, the solid was dissolved in CH_2Cl_2 and hexanes was added. The precipitate was re-dissolved in CH_2Cl_2, and this dissolution/precipitation was repeated three times, and the precipitate was finally dried under vacuum to give copolymer **1c** as a dark brown solid (1.48 g, 74%). ^{1}H-NMR (500 MHz, $CDCl_3$) δ 5.20 (-OCH$_2$C*H*(COOH)O- and -OC*H*(CH$_3$)CO-), 4.59 (PhCH_2O-), 3.90 (-OCH_2CH-), 1.56 (-CHCH_3). IR (ATR) 2942, 1747, 1497, 1452, 1365, 1192, 1084, 1046, 865, 739, 698 cm^{-1}.

4.7. Synthesis of PLA copolymer **4**

Following literature synthesis [47]. Copolymer **3** (1.0 g) was dissolved in 50 mL ethyl acetate/methanol (3:1), and catalytic amount of Pd/C was added. The mixture was purged with Ar for 20 min and filled with H_2 under vigorous stirring. After 12 h, the solution was passed through a pile of Celite to remove Pd/C and the filtrate was dried under vacuum to give copolymer **4** as a light brown solid (630 mg, 63%). ^{1}H-NMR (500 MHz, $CDCl_3$): δ 5.0–5.5 (-OC*H*(CH$_2$OH)CO- and -OC*H*(CH$_3$)CO-), 3.78 (HOCH_2CH-), 1.49 (-CHCH_3). IR (ATR): ~3500 (br, w), 2995 (m), 2945 (m), 1744 (s), 1452 (m), 1380 (w), 1182 (s), 1129 (s), 1084 (s), 864 (m), 743 (m) cm^{-1}.

4.8. Synthesis of PFPA-grafted PLA copolymer **5**

Copolymer **4** (100 mg) and PFPA-COOH (20 mg, 0.09 mmol) were added together with DCC (41 mg, 0.2 mmol) and DMAP (2.4 mg, 0.02 mmol) to 10 mL anhydrous dichloromethane under Ar, and the mixture was stirred at room temperature overnight. The solution was then concentrated to 3 mL and was poured into 50 mL of hexane/methanol (*v*/*v* 9:1) to precipitate the crude product. The yellow precipitate was dissolved in dichloromethane and was precipitated in hexane/methanol. This dissolution/ precipitation was repeated for a total of 3 times. Finally, the precipitate was

dried under vacuum to give PFPA-grafted PLA copolymer **5** as a bright yellow solid (104 mg, 86%). ^{1}H-NMR (500 MHz, $CDCl_3$): δ 5.56 (-OC*H*(-CH_2OCOPFPA)CO-), 5.19 (-OC*H*(CH_3)CO), 4.83 (-OCH_2(OCOPFPA)CH-), 1.59 (-CHCH_3). ^{19}F-NMR (188 MHz, $CDCl_3$): δ −137.5 (doublet), −149.62 (singlet). FTIR (ATR): 2995 (m), 2945 (m), 2133 (m), 1747 (s), 1648 (w), 1563 (m), 1490 (s), 1381 (m), 1363 (m), 1258 (s), 1182 (s), 1128 (s), 1082 (s), 1044 (s), 957 (w), 865 (m), 751 (s), 667 (m) cm^{-1}.

4.9. Synthesis of Man- or MH-grafted PLA glycopolymers **10** *or* **11**

General Procedures

The mole ratio of *N*-succinimidyl 2-(diphenylphosphanyl)benzoate:amine-carbohydrate: PFPA in polymer **10** or **11** was set as 4:6:1. *N*-Succinimidyl 2-(diphenylphosphanyl) benzoate and amine-Man **6** or amine-MH **7** were added to 5 mL anhydrous DMSO, and the solution was stirred for 3 h. Then, the mixture was added to a DMSO solution containing copolymer **5**. Afterwards, the mixture was stirred for another hour. The mixture was transferred into a dialysis tube (molecule cutoff: 3500) and dialyzed in water for 2 days. Finally, the product was obtained after lyophilization.

Polymer **10**: yellow powder (yield: 92%). ^{1}H-NMR (500 MHz, DMSO-d_6): δ 7.70–7.20 (Ar-H), 5.21 (-OCH(CH_3)CO-), 5.80–3.00 (carbohydrate), 1.48 (-CHCH_3); IR (ATR): 3362, 2945, 1747, 1651, 1489, 1451, 1381, 1515, 1184, 1082, 1043, 865, 749, 695 cm^{-1}.

Polymer **11**: a white powder (yield: 94%). ^{1}H-NMR (500 MHz, DMSO-d_6): 7.75–7.40 (Ar-H), 5.21 (-OCH(CH_3)CO-), 4.90–3.00 (carbohydrate), 1.48 (-CHCH_3); IR (ATR): 3371, 2945, 1748, 1651, 1503, 1452, 1381, 1133, 1084, 865, 752, 695 cm^{-1}.

Supplementary Materials: Supporting information including detailed synthetic protocols, ^{1}H, ^{19}F and ^{31}P NMR and IR spectra are available online.

Author Contributions: The authors contributed as follows M.Y., B.W. and W.N. in conceptualization, visualization and methodology and synthesis, W.N. and M.Y. in writing—original draft preparation, M.Y., B.W. and W.N. in writing—review and editing; supervision, project administration, and funding acquisition, M.Y.

Funding: This study was supported in part by the National Institute of Health (R15GM128164) and National Science Foundation (CHE-1808671).

Acknowledgments: The authors thank Xuan Chen for his help in the synthesis.

Conflicts of Interest: The authors declare no conflict of interest.

References

1. Caroff, M.; Karibian, D. Structure of bacterial lipopolysaccharides. *Carbohydr. Res.* **2003**, *338*, 2431–2447. [CrossRef] [PubMed]
2. Ramon, M.; Rolland, F.; Sheen, J. Sugar sensing and signaling. *Arabidopsis Book* **2008**, *6*, e0117. [CrossRef] [PubMed]
3. Brandley Brian, K.; Schnaar Ronald, L. Cell—Surface Carbohydrates in Cell Recognition and Response. *J. Leukocyte Biol.* **1986**, *40*, 97–111. [CrossRef]
4. Jin, Y.; Wong, K.H.; Granville, A.M. Enhancement of Localized Surface Plasmon Resonance polymer based biosensor chips using well-defined glycopolymers for lectin detection. *J. Colloid Interface Sci.* **2016**, *462*, 19–28. [CrossRef] [PubMed]
5. Chen, X.; Wu, B.; Jayawardana, K.W.; Hao, N.; Jayawardena, H.S.N.; Langer, R.; Jaklenec, A.; Yan, M. Magnetic Multivalent Trehalose Glycopolymer Nanoparticles for the Detection of Mycobacteria. *Adv. Healthc. Mater* **2016**, *5*, 2007–2012. [CrossRef] [PubMed]
6. Zhou, W.-J.; Kurth, M.J.; Hsieh, Y.-L.; Krochta, J.M. Synthesis and thermal properties of a novel lactose-containing poly(N-isopropylacrylamide-co-acrylamidolactamine) hydrogel. *J. Polym. Sci. A Polym. Chem.* **2000**, *37*, 1393–1402. [CrossRef]
7. Newman, Y.M.; Ring, S.G.; Colaco, C. The Role of Trehalose and Other Carbohydrates in Biopreservation. *Biotechnol. Genet. Eng. Rev* **1993**, *11*, 263–294. [CrossRef] [PubMed]

8. Beattie, G.M.; Crowe, J.H.; Lopez, A.D.; Cirulli, V.; Ricordi, C.; Hayek, A. Trehalose: A Cryoprotectant That Enhances Recovery and Preserves Function of Human Pancreatic Islets After Long-Term Storage. *Diabetes* **1997**, *46*, 519. [CrossRef]
9. Roy, R.; Tropper, F. Syntheses of copolymer antigens containing 2-acetamido-2-deoxy-α-orβ-d-glucopyranosides. *Glycoconjugate J.* **1988**, *5*, 203–206. [CrossRef]
10. Cao, S.; Roy, R. Synthesis of glycopolymers containing GM3-saccharide. *Tetrahedron Lett.* **1996**, *37*, 3421–3424. [CrossRef]
11. Desport, J.; Moreno, M.; Barandiaran, M. Fructose-Based Acrylic Copolymers by Emulsion Polymerization. *Polymers* **2018**, *10*, 488. [CrossRef]
12. Spain, S.G.; Gibson, M.I.; Cameron, N.R. Recent advances in the synthesis of well-defined glycopolymers. *J. Polym. Sci. A Polym. Chem.* **2007**, *45*, 2059–2072. [CrossRef]
13. Varma, A.J.; Kennedy, J.F.; Galgali, P. Synthetic polymers functionalized by carbohydrates: A review. *Carbohydr. Polym.* **2004**, *56*, 429–445. [CrossRef]
14. Wang, Q.; Dordick, J.S.; Linhardt, R.J. Synthesis and Application of Carbohydrate-Containing Polymers. *Chem. Mater.* **2002**, *14*, 3232–3244. [CrossRef]
15. Yang, L.; Sun, H.; Liu, Y.; Hou, W.; Yang, Y.; Cai, R.; Cui, C.; Zhang, P.; Pan, X.; Li, X.; et al. Self-Assembled Aptamer-Grafted Hyperbranched Polymer Nanocarrier for Targeted and Photoresponsive Drug Delivery. *Angew. Chem. Int. Ed.* **2018**, *57*, 17048–17052. [CrossRef] [PubMed]
16. Tang, H.; Tsarevsky, N.V. Preparation and functionalization of linear and reductively degradable highly branched cyanoacrylate-based polymers. *J. Polym. Sci. A Polym. Chem.* **2016**, *54*, 3683–3693. [CrossRef]
17. Ding, J.; Xiao, C.; Li, Y.; Cheng, Y.; Wang, N.; He, C.; Zhuang, X.; Zhu, X.; Chen, X. Efficacious hepatoma-targeted nanomedicine self-assembled from galactopeptide and doxorubicin driven by two-stage physical interactions. *J. Control. Release* **2013**, *169*, 193–203. [CrossRef] [PubMed]
18. Dondoni, A. Triazole: The Keystone in Glycosylated Molecular Architectures Constructed by a Click Reaction. *A. Chem. Asian J.* **2007**, *2*, 700–708. [CrossRef]
19. Pérez-Balderas, F.; Ortega-Muñoz, M.; Morales-Sanfrutos, J.; Hernández-Mateo, F.; Calvo-Flores, F.G.; Calvo-Asín, J.A.; Isac-García, J.; Santoyo-González, F. Multivalent Neoglycoconjugates by Regiospecific Cycloaddition of Alkynes and Azides Using Organic-Soluble Copper Catalysts. *Org. Lett.* **2003**, *5*, 1951–1954. [CrossRef] [PubMed]
20. Fazio, F.; Bryan, M.C.; Blixt, O.; Paulson, J.C.; Wong, C.-H. Synthesis of Sugar Arrays in Microtiter Plate. *J. Am. Chem. Soc.* **2002**, *124*, 14397–14402. [CrossRef]
21. Aragão-Leoneti, V.; Campo, V.L.; Gomes, A.S.; Field, R.A.; Carvalho, I. Application of copper(I)-catalysed azide/alkyne cycloaddition (CuAAC) 'click chemistry' in carbohydrate drug and neoglycopolymer synthesis. *Tetrahedron* **2010**, *66*, 9475–9492. [CrossRef]
22. Slavin, S.; Burns, J.; Haddleton, D.M.; Becer, C.R. Synthesis of glycopolymers via click reactions. *Eur. Polym. J.* **2011**, *47*, 435–446. [CrossRef]
23. Baskin, J.M.; Prescher, J.A.; Laughlin, S.T.; Agard, N.J.; Chang, P.V.; Miller, I.A.; Lo, A.; Codelli, J.A.; Bertozzi, C.R. Copper-free click chemistry for dynamic in vivo imaging. *Proc. Natl. Acad. Sci. USA* **2007**, *104*, 16793–16797. [CrossRef] [PubMed]
24. Wu, P.; Feldman, A.K.; Nugent, A.K.; Hawker, C.J.; Scheel, A.; Voit, B.; Pyun, J.; Fréchet, J.M.J.; Sharpless, K.B.; Fokin, V.V. Efficiency and Fidelity in a Click-Chemistry Route to Triazole Dendrimers by the Copper(I)-Catalyzed Ligation of Azides and Alkynes. *Angew. Chem. Int. Ed.* **2004**, *43*, 3928–3932. [CrossRef]
25. Becer, C.R.; Hoogenboom, R.; Schubert, U.S. Click Chemistry beyond Metal-Catalyzed Cycloaddition. *Angew. Chem. Int. Ed.* **2009**, *48*, 4900–4908. [CrossRef]
26. Chang, P.V.; Prescher, J.A.; Sletten, E.M.; Baskin, J.M.; Miller, I.A.; Agard, N.J.; Lo, A.; Bertozzi, C.R. Copper-free click chemistry in living animals. *Proc. Natl. Acad. Sci. USA* **2010**, *107*, 1821–1826. [CrossRef]
27. Campbell-Verduyn, L.; Elsinga, P.H.; Mirfeizi, L.; Dierckx, R.A.; Feringa, B.L. Copper-free 'click': 1,3-dipolar cycloaddition of azides and arynes. *Org. Biomol. Chem.* **2008**, *6*, 3461–3463. [CrossRef]
28. Staudinger, H.; Meyer, J. Über neue organische Phosphorverbindungen III. Phosphinmethylenderivate und Phosphinimine. *Helv. Chim. Acta* **1919**, *2*, 635–646. [CrossRef]
29. Saxon, E.; Bertozzi, C.R. Cell Surface Engineering by a Modified Staudinger Reaction. *Science* **2000**, *287*, 2007. [CrossRef]

30. Köhn, M.; Breinbauer, R. The Staudinger Ligation—A Gift to Chemical Biology. *Angew. Chem. Int. Ed.* **2004**, *43*, 3106–3116. [CrossRef]
31. Lin, F.L.; Hoyt, H.M.; van Halbeek, H.; Bergman, R.G.; Bertozzi, C.R. Mechanistic Investigation of the Staudinger Ligation. *J. Am. Chem. Soc.* **2005**, *127*, 2686–2695. [CrossRef] [PubMed]
32. Prescher, J.A.; Dube, D.H.; Bertozzi, C.R. Chemical remodelling of cell surfaces in living animals. *Nature* **2004**, *430*, 873–877. [CrossRef] [PubMed]
33. Sundhoro, M.; Jeon, S.; Park, J.; Ramström, O.; Yan, M. Perfluoroaryl Azide Staudinger Reaction: A Fast and Bioorthogonal Reaction. *Angew. Chem.* **2017**, *129*, 12285–12289. [CrossRef]
34. Xie, S.; Ramström, O.; Yan, M. N,N-Diethylurea-Catalyzed Amidation between Electron-Deficient Aryl Azides and Phenylacetaldehydes. *Org. Lett.* **2015**, *17*, 636–639. [CrossRef] [PubMed]
35. Xie, S.; Zhang, Y.; Ramström, O.; Yan, M. Base-catalyzed synthesis of aryl amides from aryl azides and aldehydes. *Chem. Sci.* **2016**, *7*, 713–718. [CrossRef] [PubMed]
36. Xie, S.; Lopez, S.A.; Ramström, O.; Yan, M.; Houk, K.N. 1,3-Dipolar Cycloaddition Reactivities of Perfluorinated Aryl Azides with Enamines and Strained Dipolarophiles. *J. Am. Chem. Soc.* **2015**, *137*, 2958–2966. [CrossRef] [PubMed]
37. Xie, S.; Fukumoto, R.; Ramström, O.; Yan, M. Anilide Formation from Thioacids and Perfluoroaryl Azides. *J. Org. Chem.* **2015**, *80*, 4392–4397. [CrossRef]
38. Sundhoro, M.; Park, J.; Wu, B.; Yan, M. Synthesis of Polyphosphazenes by a Fast Perfluoroaryl Azide-Mediated Staudinger Reaction. *Macromolecules* **2018**, *51*, 4532–4540. [CrossRef]
39. Duchateau, J.; Lutsen, L.; Guedens, W.; Cleij, T.J.; Vanderzande, D. Versatile post-polymerization functionalization of poly(p-phenylene vinylene) copolymers containing carboxylic acid substituents: Development of a universal method towards functional conjugated copolymers. *Polym. Chem.* **2010**, *1*, 1313–1322. [CrossRef]
40. Ting, S.R.S.; Chen, G.; Stenzel, M.H. Synthesis of glycopolymers and their multivalent recognitions with lectins. *Polym. Chem.* **2010**, *1*, 1392–1412. [CrossRef]
41. Kong, N.; Shimpi, M.R.; Park, J.H.; Ramström, O.; Yan, M. Carbohydrate conjugation through microwave-assisted functionalization of single-walled carbon nanotubes using perfluorophenyl azides. *Carbohydr. Res.* **2015**, *405*, 33–38. [CrossRef] [PubMed]
42. Peng, K.-Y.; Hua, M.-Y.; Lee, R.-S. Amphiphilic polyesters bearing pendant sugar moieties: Synthesis, characterization, and cellular uptake. *Carbohydr. Polym.* **2014**, *99*, 710–719. [CrossRef] [PubMed]
43. Disney, M.D.; Zheng, J.; Swager, T.M.; Seeberger, P.H. Detection of Bacteria with Carbohydrate-Functionalized Fluorescent Polymers. *J. Am. Chem. Soc.* **2004**, *126*, 13343–13346. [CrossRef]
44. Liu, L.; Yan, M. A General Approach to the Covalent Immobilization of Single Polymers. *Angew. Chem.* **2006**, *118*, 6353–6356. [CrossRef]
45. Wang, X.; Ramström, O.; Yan, M. Dynamic light scattering as an efficient tool to study glyconanoparticle–lectin interactions. *Analyst* **2011**, *136*, 4174–4178. [CrossRef] [PubMed]
46. Deng, L.; Norberg, O.; Uppalapati, S.; Yan, M.; Ramström, O. Stereoselective synthesis of light-activatable perfluorophenylazide-conjugated carbohydrates for glycoarray fabrication and evaluation of structural effects on protein binding by SPR imaging. *Org. Biomol. Chem.* **2011**, *9*, 3188–3198. [CrossRef] [PubMed]
47. Gerhardt, W.W.; Noga, D.E.; Hardcastle, K.I.; García, A.J.; Collard, D.M.; Weck, M. Functional Lactide Monomers: Methodology and Polymerization. *Biomacromolecules* **2006**, *7*, 1735–1742. [CrossRef]

Sample Availability: Samples of the compounds are not currently available from the authors.

molecules

MDPI

Article

Candidate Polyurethanes Based on Castor Oil (*Ricinus communis*), with Polycaprolactone Diol and Chitosan Additions, for Use in Biomedical Applications

Yomaira L. Uscátegui [1,2], Luis E. Díaz [3], José A. Gómez-Tejedor [4,5], Ana Vallés-Lluch [4], Guillermo Vilariño-Feltrer [4], María A. Serrano [4] and Manuel F. Valero [2,*]

1 Doctoral Program of Biosciences, Universidad de La Sabana, Chía 140013, Colombia; yomairausma@unisabana.edu.co
2 Energy, Materials and Environment Group, Faculty of Engineering, Universidad de La Sabana, Chía 140013, Colombia
3 Bioprospecting Research Group, Faculty of Engineering, Universidad de La Sabana, Chía 140013, Colombia; luis.diaz1@unisabana.edu.co
4 Centre for Biomaterials and Tissue Engineering, Universitat Politècnica de València, Camino de Vera, s/n, 46022 Valencia, Spain; jogomez@fis.upv.es (J.A.G.-T.); avalles@ter.upv.es (A.V.-L.); guivifel@upv.es (G.V.-F.); mserranj@fis.upv.es (M.A.S.)
5 Biomedical Research Networking Center in Bioengineering, Biomaterials, and Nanomedicine (CIBER-BBN), 46022 Valencia, Spain
* Correspondence: manuelvv@unisabana.edu.co; Tel.: +57-1-8615555 (ext. 25224)

Received: 14 December 2018; Accepted: 4 January 2019; Published: 10 January 2019

Abstract: Polyurethanes are widely used in the development of medical devices due to their biocompatibility, degradability, non-toxicity and chemical versatility. Polyurethanes were obtained from polyols derived from castor oil, and isophorone diisocyanate, with the incorporation of polycaprolactone-diol (15% *w*/*w*) and chitosan (3% *w*/*w*). The objective of this research was to evaluate the effect of the type of polyol and the incorporation of polycaprolactone-diol and chitosan on the mechanical and biological properties of the polyurethanes to identify the optimal ones for applications such as wound dressings or tissue engineering. Polyurethanes were characterized by stress-strain, contact angle by sessile drop method, thermogravimetric analysis, differential scanning calorimetry, water uptake and in vitro degradation by enzymatic processes. In vitro biological properties were evaluated by a 24 h cytotoxicity test using the colorimetric assay MTT and the LIVE/DEAD kit with cell line L-929 (mouse embryonic fibroblasts). In vitro evaluation of the possible inflammatory effect of polyurethane-based materials was evaluated by means of the expression of anti-inflammatory and proinflammatory cytokines expressed in a cellular model such as THP-1 cells by means of the MILLIPLEX® MAP kit. The modification of polyols derived from castor oil increases the mechanical properties of interest for a wide range of applications. The polyurethanes evaluated did not generate a cytotoxic effect on the evaluated cell line. The assessed polyurethanes are suggested as possible candidate biomaterials for wound dressings due to their improved mechanical properties and biocompatibility.

Keywords: castor oil; biomedical devices; polyurethanes; polycaprolactone-diol; chitosan

1. Introduction

Polyurethanes (PUs) are widely used in the preparation of medical devices due to their biocompatibility, degradability, and non-toxicity when compared to polymers such as polylactic

acid (PLA), polycarbonate, polycaprolactone, among others [1–4]. Examples of PU applications in the biomedical field are implants, artificial heart valves, sutures, catheters, artificial heart, vascular prostheses, wound coatings, blood compatible coatings, drug delivery systems, porous supports for tissue regeneration, among others [5–9].

Since the mechanical, thermal, chemical and biological properties of PUs can be varied during the synthesis process [10–14], the addition of polymers, such as polycaprolactone diol (PCL) or chitosan (Ch) can modify the properties of PUs such as biocompatibility [15] and the antimicrobial activity. PCL is an attractive polymer for the development of biomaterials due to its properties such as biocompatibility, biodegradability, ease in the processing of biomaterials, among others [16]. Ch is a polysaccharide that is obtained from renewable sources because it is part of the structure of some crustaceans. Ch is mainly characterized by being biocompatible, biodegradable, bioadhesive, non-the toxic, and has antimicrobial properties, among others [15,17,18]. These properties have allowed PCL and Ch to be used in some applications such as wound dressings, surgical sutures, scaffolds in tissue engineering, among others [19]. The use of Ch and PCL is expected to increase the biocompatibility of the PUs synthesized with polyols derived from castor oil. Additionally, the filler effect is expected to increase the mechanical properties such as tensile strength. And when using the mixture of chitosan with polycaprolactone, it is sought to evaluate if there is a possible synergistic effect or not to obtain biocompatible materials with antimicrobial properties, or if both mechanical and biological properties are affected.

Biocompatibility is interpreted as a series of interactions that occur at the tissue/material interface, allowing the identification of those materials with surface characteristics and/or more biocompatible polymer chemistry; these interactions are influenced by the intrinsic characteristics of the material. Some biocompatibility tests involve analytical tests or observations of physiological phenomena, reactions or surface properties attributable to a specific application [12].

Cell cultures are ideal systems for the study and observation of a specific cell type under specific conditions since these systems do not have the complexity that an in vivo system entails, due to a large number of variables that interact. In vitro tests assess the morphology, cytotoxicity and secretory functions of different cell types. The tests can be by direct contact of the cells and the material or indirect, adding an extract of the material to the cell culture [20,21].

Monocytes and macrophages are part of the innate immune system because they are cells that are involved in inflammatory processes with the ability to synthesize and secrete pro and anti-inflammatory cytokines [22]. Cytokines correspond to a diverse group of extracellular, water-soluble proteins, which influence the production and activity of other cytokines by increasing (proinflammatory) or decreasing (anti-inflammatory) the inflammatory response [23].

The human monocyte cell line THP-1 is widely used in research thanks to the ability of monocytes to differentiate into macrophages [24]. THP-1 monocytes have a round shape in suspension; when they differentiate upon stimulation by phorbol 12-myristate-13-acetate (PMA), the cells adhere to the culture plates, gaining phenotypic and functional characteristics similar to primary human macrophages [25,26]. The immune response is assessed by measuring cytokines in the cell culture medium [22].

The inflammatory response of macrophages is activated by invading pathogens, particles, lipopolysaccharides (LPSs), and other stimuli [27]. LPSs are part of the outer membrane of Gram-negative bacteria and can cause tissue damage and the release of multiple pro-inflammatory cytokines [27]. Therefore, when an inflammatory response is induced, pro-inflammatory cytokines, such as interleukin-1 beta (IL-1β), tumor necrosis factor alpha (TNF-α), and interleukin-6 (IL-6), can be released. Likewise, anti-inflammatory cytokines, such as interleukin-10 (IL-10) [28], can be released. Biomaterials, such as high molecular weight polyethylene, can activate macrophages to secrete pro-inflammatory cytokines, including TNF-α and IL-1β, among others, as a response to material implantation [29].

PU applications in biomedicine are diverse due to Pus' various properties. Using aliphatic chains derived from vegetable oils creates flexible PUs, and cyclic diisocyanates provide greater

mechanical strength [30]. Therefore, it is necessary to specifically characterize each synthesized material to determine its functionality and suitability for biomedical devices. The aim of this research was to determine the physicochemical, mechanical, morphological, biodegradability, and in vitro biocompatibility characteristics of the PUs, in addition to the possible inflammatory effects of the materials synthesized with castor oil polyols, depending on segment structure and PU cross-linking density. In this study, different PUs were synthesized with castor oil (chemically modified or not) and isophorone diisocyanate (IPDI) by adding polycaprolactone diol (PCL) (15% *w*/*w*) and chitosan (Ch) (3% *w*/*w*). In vitro degradation was determined in acidic and basic media, and enzymatic degradation was carried out with pig liver esterase. The in vitro cell viability was determined using L929 mouse fibroblasts (ATCC® CCL-1), human fibroblasts (MRC-5) (ATCC® CCL-171™), and adult human dermal fibroblasts (HDFa) (ATCC® PCS-201-012™) with the PUs. The viability was also determined by a live/dead kit for the L929 mouse fibroblasts. Pro- and anti-inflammatory responses were evaluated by cytokine expression (IFN-γ, IL-1β, IL-2, IL-4, IL-5, IL-6, IL-8, IL-10, and TNF-α) of the THP-1 cells with and without stimulation by LPS. The present paper serves as a screening of the immunomodulatory effects of PU materials synthesized with castor oil.

2. Results and Discussion

2.1. Obtaining Polyols

The reaction to obtaining polyols derived from the castor oil is presented in Scheme 1. The hydroxyl number of the polyols transesterified with pentaerythritol was determined. The values of the hydroxyl index for each polyol (P.1, P.2 and P.3) were 160, 191 and 236 mg KOH per g of castor oil sample, respectively. According to the results of the hydroxyl index, it is noted that the chemical modification of the castor oil increases as the pentaerythritol content increases. The increment of the hydroxyl index can be related to the increase of the crosslinking reactions and to the gain of the bulk density of the polymeric materials. An increase in the crosslink density would generate an improvement in the mechanical properties of the polymer matrices.

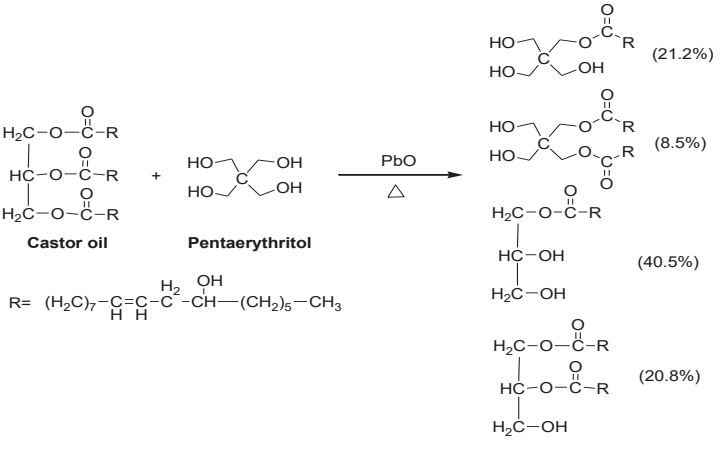

Scheme 1. Reaction scheme for obtaining polyols.

2.2. Mechanical Properties of PUs

Aromatic diisocyanates are the most commonly used in the synthesis of PUs due to their mechanical properties, but they can produce carcinogenic and mutagenic diamines upon degradation [31], therefore, an aliphatic diisocyanate was used in this research to avoid the side effects of the raw materials on living tissues.

Mechanical testing is essential to establish the use of a biomaterial because it allows obtaining the load parameters required for a tissue of interest [32]. The mechanical properties of 12 PU matrices were evaluated by determining the stress-strain curves from which the tensile strength and the elongation at the break were obtained. Figure 1 shows the results of the mechanical properties depending on the polyol used in the synthesis.

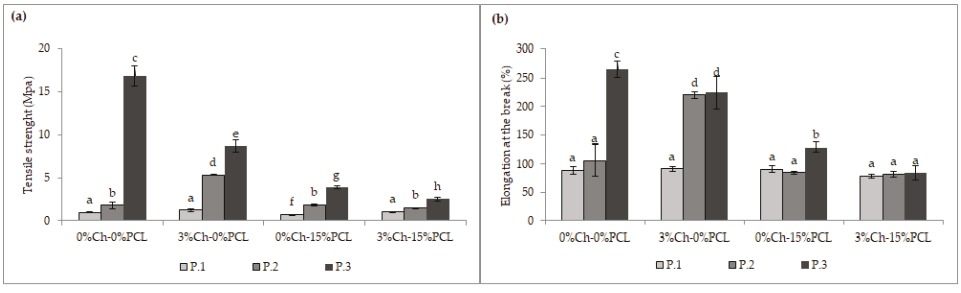

Figure 1. Mechanical properties of the synthesized PUs. (**a**) Maximum stress of PUs; (**b**) Percent elongation of PUs. The data are expressed as the mean ± SD (n = 3). Bars with different letters (a–h) indicate significant differences ($p < 0.05$) between the polyols.

Physical and mechanical properties depend on the atomic and molecular structure of the materials used in the synthesis. The nature of the bonds and subunits of the structure affects the mechanical properties and therefore the stress-strain properties, which are of interest for the evaluation of biomaterials [32]. The highest tensile strength (16.86 MPa) was obtained with polyol P.3 (P.3-0%Ch-0%PCL). Figure 1a shows an increase in the tensile strength of all the materials synthesized with polyol P.3, which has the highest cross-linking. This is how the chemical modification of the polyols increases the maximum stress—via the increase of physical cross-linking of the polymer matrix [33].

The mechanical properties of PUs are attributed to presence of hard and soft segment domains [34]. The hard segment generally refers to the combination of the chain extender and the diisocyanate components, while the soft segments refer to polymeric diols. Depending on the structure of the hard and soft segments, crystalline and amorphous domains can be formed, which determine the stiffness and stability of the material [35]. Hydrogen bond cause strong interactions, so the polar nature of the hard segment causes a strong attraction, forming the domains [36]. Therefore, when using polyol P.3 in the synthesis, the values of the mechanical properties increased because the soft segments had a higher number of hydroxyl groups, increasing the cross-linking density, and the hard segments formed a ring, providing greater resistance.

Regarding the percent elongation at break (Figure 1b), the analysis showed significant differences ($p < 0.05$) of polyol P.1 compared with the other polyols (P.2 and P.3), with the percentage increasing as the polyol was modified. The mechanical properties of PUs depend on many factors, including molecular weight, chemical bonds, cross-linking, crystallinity of the polymer, and the size, shape, and interactions of the hard segment present in the structure [37]. Thus, PUs with a higher degree of cross-linking have higher values of tensile strength and percent elongation at break. Increased cross-linking produces a more compact structure [37]. An increase in strength is attributed to the content of intermolecular hydrogen bonds and cross-linking density [38].

When analyzing the influence of the additives used in the synthesis on the mechanical properties, significant differences are found when 3% Ch was added to polyol P.2 (P.2-3%Ch-0%PCL), obtaining a higher value than the other materials synthesized with P.1 and P.3. For polyol P.3, the additives decreased the maximum stress compared with the material without additives.

Chen et al. (2018) synthesized PUs with PCL as a polyol, IPDI, and polylactic acid (PLA), obtaining tensile strength values between 41 and 60 MPa when using PLA- and PCL-based PU ratios in the

range of 80/20 to 95/5. The authors attributed the decrease in tensile strength as the ratio of PCL increased to the plasticizing effect of certain non-cross-linked PCL polyols and to a possible decrease in compatibility as the PCL content increased [39].

A similar effect was observed for percent elongation at break because it decreased when PCL and Ch were added to polyol P.3 (P.3-3%Ch-15%PCL). The other materials did not differ with the additives used from the material without additives. The flexibility of PU may be due to the long oil hydrocarbon chain present in the polymer chain [37]. This agrees with the results reported by Park et al. (2013), who synthesized PUs with polycaprolactone, hexamethylene diisocyanate, and isosorbide, with silk added, and determined that a higher silk content increased the stiffness and decreased the maximum stress. The authors stated that the design of flexible and soft polymers allows for the production of a wide range of biomaterials to regenerate soft tissues such as muscles and ligaments [6]. Additionally, Vannozzi et al. reported that in general, soft and deformable substrates are key features for skeletal muscle tissue engineering [33].

2.3. Fourier-Transform Infrared Spectroscopy (FTIR)

FTIR was used to determine the efficiency of the synthesis process by the identification of characteristic functional groups of PU and the absence of characteristic peaks of the monomers used in the synthesis process. Figure 2 shows the infrared spectra of the synthesized PUs.

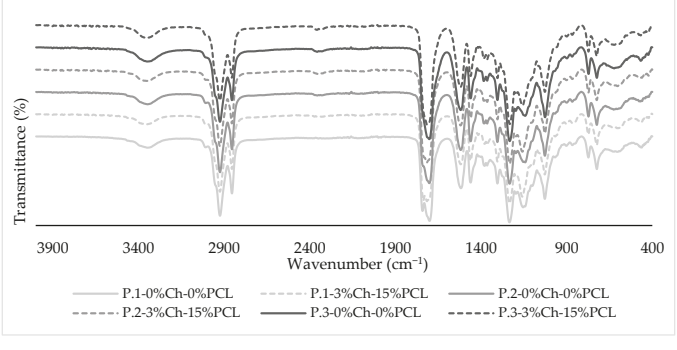

Figure 2. FTIR spectra of the synthesized PUs.

Figure 2 shows that all of the FTIR spectra had similar peaks, independent of the polyol or additive used in the synthesis, and the peaks observed corresponded to the expected PU matrices. The absence of the stretching peak of the −N=C=O bond of the diisocyanates at 2250 cm^{-1} [31], indicates there were no unreacted free isocyanate groups in the synthesized PU matrices, showing that the reaction was complete.

Spectral peaks characteristic of PUs can be seen in the spectra. Thus, around 3330 cm^{-1}, the characteristic bands for the stretching vibrations of the −N–H bonds are observed [40] from which it can be inferred that they correspond to the urethane bonds present in the matrices. Near 2923 cm^{-1}, the stretching peak of the methyl group can be observed, and at around 2855 cm^{-1}, the symmetric stretching of the C–H bond is present. At around 1700 cm^{-1}, an intense band is present due to the C=O bond stretching [40] thus indicating the formation of the urethane group. Around 1250 cm^{-1}, the C–N bond stretching is observed; at about 1140 cm^{-1}, the stretching vibrations of the C–O bond appear [37].

2.4. Thermal Analysis

2.4.1. Thermogravimetric Analysis

Thermogravimetric analysis was performed by producing thermograms of the PUs. Figure 3 shows the results for the synthesized matrices.

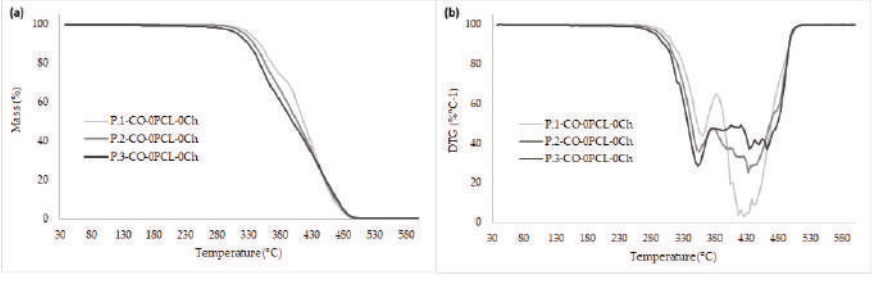

Figure 3. Thermograms of the synthesized PUs. (**a**) Thermogravimetric (TG) curve of PUs; (**b**) Derivative of the thermogravimetric (DTG) curve of PUs.

Figure 3 shows a trend regarding thermal behavior of the synthesized PUs, showing no displacements of the degradation temperatures with the use of modified polyols. When obtaining the curves derived from thermogravimetry, several peaks were observed, which agrees with other authors stating that the mechanism of degradation of PUs is complex due to the formation of various compounds in the process [41].

For each polymer matrix a thermogram was obtained from which the stability of the synthesized PUs in this study were determined. It was observed that the polyol type and additives did not affect the thermal stability of the materials when compared with the synthesized material without additives. The thermograms showed that all PUs were stable at temperatures below 300 °C and showed complete degradation at temperatures near 600 °C, which coincides with the research conducted by Jutrzenka et al. (2018), who synthesized PUs based on a glycerin derivative, polyethylene-butylene, and diphenylmethane diisocyanate. They determined that the materials were stable up to 300 °C [36]. In a study on PUs synthesized with castor oil and isophorone diisocyanate that were proposed as surgical adhesives, the PUs had the same degradation values, and the authors stated that the values related to the degradation temperatures do not affect the biomedical application since physiological temperature is lower (≈37 °C) [42].

Three degradation regions were detected for the polymer matrices. This is consistent with the study performed with polymeric matrices synthesized with castor oil and isophorone diisocyanate by adding different concentrations of PCL and Ch [43]. The first stage of degradation was observed in the range of 250–370 °C and corresponds to the thermal degradation of the urethane bonds formed in the hard segments, characterized by being technically unstable [2]. The second stage was between 375–430 °C and corresponds to the degradation of the soft segments [36]. The last stage was in the range of 425–500 °C and corresponds to the thermal degradation of the double bonds of remaining fatty acids from castor oil [44,45].

2.4.2. Differential Scanning Calorimetry (DSC)

Table 1 shows the glass transition temperature (T_g) values for the synthesized materials, as determined by the DSC curves of the materials. Table 1 shows that the polyol type and the additives significantly influence the T_g value. This agrees with what is understood from the mechanical properties of the molecular structure produced by modifying the polyol derived from castor oil. The values of T_g for P.1, P.2, and P.3 without additives were −14.8 °C, −12.8 °C and 14 °C, respectively. P.1 had the lowest values of T_g (between −14 °C and −25 °C, approximately).

Table 1. DSC thermograms of the synthesized PUs depending on the polyol used.

Polymeric Material	T_g (°C)		
	P.1	P.2	P.3
0%Ch-0%PCL	−14.8	−12.8	14.8
3%Ch-0%PCL	−13.3	−1.0	13.7
0%Ch-15%PCL	−25.3	−10.2	4.7
3%Ch-15%PCL	−25.4	−14.8	2.8

The observed trend is a decrease in T_g as the hydroxyl index decreases, which agrees with the cross-linking of the synthesized PUs, indicating that greater energy is needed for reordering the structure by a change in intermolecular forces. This may be due to secondary interactions resulting from the hyperbranched structure [46]. The thermal properties of PUs depend on the number of urethane bonds present in the structure because they can tolerate a considerable amount of heat [47]. Saénz-Pérez et al. (2016) synthesized PUs with polytetramethylene glycol and diphenylmethane or toluene diisocyanates, and butanediol. In the determination of T_g, they found that the values increased as the amount of chain extender increased. Therefore, the authors state that the increase in T_g was caused by the reduction in the mobility of chain segments due to the increase of hard segments [48].

The ricinoleic acid triglyceride from castor oil used as a polyol contains an ordered structure in which hydroxyl groups are uniformly distributed within the chain, helping to obtain a PU with a uniform cross-linked structure, achieving high mechanical properties and thermal stability [30]. In general, all of the synthesized matrices had a single value of T_g, indicating that all the materials showed homogeneous segment dispersion. The T_g values were similar to those reported for PUs based on polyethylene glycol, poly (ε-caprolactone-co-D,L-lactide), and diurethane diisocyanate (with hexamethylene diisocyanate and butanediol), where the authors found values near −33 °C. Likewise, the authors did not find exothermic peaks because the materials were amorphous [49]. With the above information, it can be generalized that Pus are thermally stable and that they can be used in various biomedical applications, for example, as materials for non-absorbable sutures.

2.5. Hydrophilic Character

2.5.1. Contact Angle

To evaluate the hydrophilic nature of PUs, the water contact angle on their surfaces was determined. Figure 4 shows the results of the synthesized PUs.

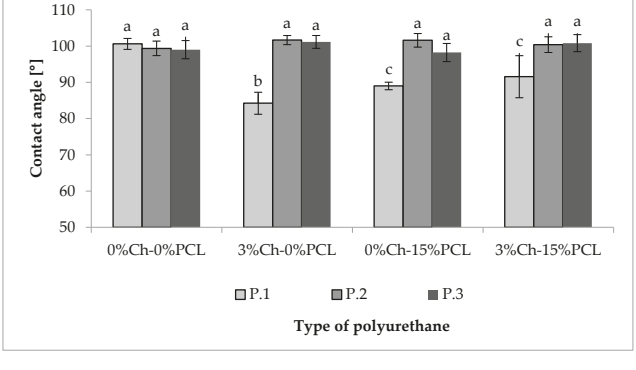

Figure 4. Contact angle of the synthesized PUs. The data are expressed as the mean ± SD (n = 10). Bars with different letters (a–c) indicate significant differences ($p < 0.05$).

According to the statistical analysis in Figure 4, it is observed that for polyols P.2 and P.3, there are no significant differences in contact angle values. For P.1, significant differences are observed by

using additives because there is a reduction of angle values, indicating a decrease in the hydrophilic character. Values near 100 degrees were found, so it can be deduced that the materials tend to be hydrophobic. Mi et al. determined the contact angles of PCL-based thermoplastic PUs and different chain extenders; the values were near 90 degrees. They attributed the results of the contact angle to the hydrophilic functional groups present in the chain extenders that were used. The authors state that although PUs maintain the same chemical structure, monomer variation in the synthesis can affect the wettability and therefore vary the degradation behavior [50].

Likewise, Gossart et al. evaluated the contact angle of PUs synthesized with L-lysine diisocyanate, hydroxyethyl methacrylate, and poly (hexamethylene-carbamate) and found values above 80 degrees. The authors state that the common values reported for PU matrices were in the range of 80 to 90 degrees depending on the structure of the PU and interactions with the surfaces [51]. The results of the contact angle shown in Figure 4 are greater than those reported; this possibly results from the cross-linked network generated by the monomers used in the synthesis, as the materials tended to be hydrophobic.

2.5.2. Water Absorption Rate

Figure 5 shows the rates of water absorption for the synthesized PUs during 72 h of testing.

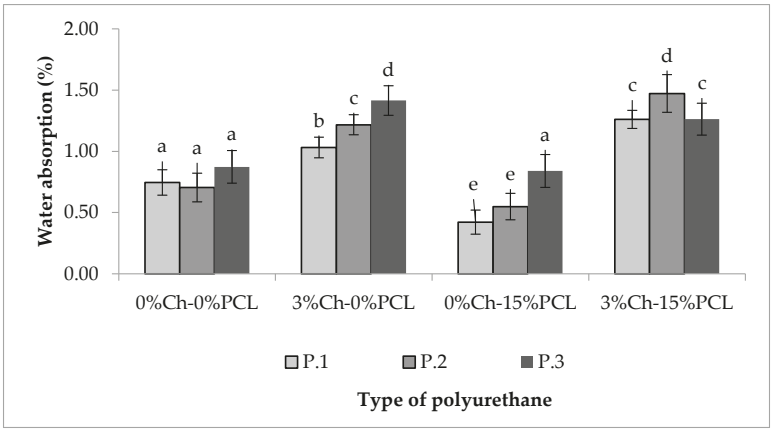

Figure 5. Water absorption rate over 72 h. Absorption results are expressed as the mean ± SD (n = 3). Bars with different letters (a–d) indicate significant differences ($p < 0.05$).

The weights of the materials were monitored until constant weight over 24, 48, 72, and 144 h, but the data are not shown because no significant differences were found after 48 h. The results show that the water absorption rates range between 0.5 and 1.5%. As seen in Figure 5, adding PCL and Ch increases the rate of absorption compared to the material without additives, although the difference in rates was not greater than one. It is likely that by increasing the amount of additive more functional groups became available to interact with the medium, which is also polar. However, by increasing the functionality of the polyol, the effect generated is inverse, showing a reduction in the rate of absorption compared to PUs without the additive. Internal interactions (hydrogen bonds) increase the barrier effect by preventing fluid diffusion. In addition, the additive function causes the chains to reorganize, showing a reduction of volumetric defects or voids in which the water can be deposited [32].

Marques et al. evaluated a bioadhesive synthesized from lactic acid in which the water absorption was 10%. The authors noted that moderate rates of water absorption improved the hemostatic character of the materials [52].

The contact angle and the rate of absorption provide information about hydrophobicity/hydrophilicity and could be an indirect indicator of surface molecular mobility.

Surface wettability can affect protein adsorption on the surface and biocompatibility [53]. This is one reason why it is indispensable to perform a study of material biocompatibility to determine its possible acceptance by the human body. Therefore, the PUs synthesized in this study can be considered suitable for biomedical applications, such as materials for non-absorbable sutures, considering the water absorption rates under the test conditions.

2.6. Density Determination

Figure 6 shows the density of the materials synthesized with IPDI and the additives (PCL and Ch).

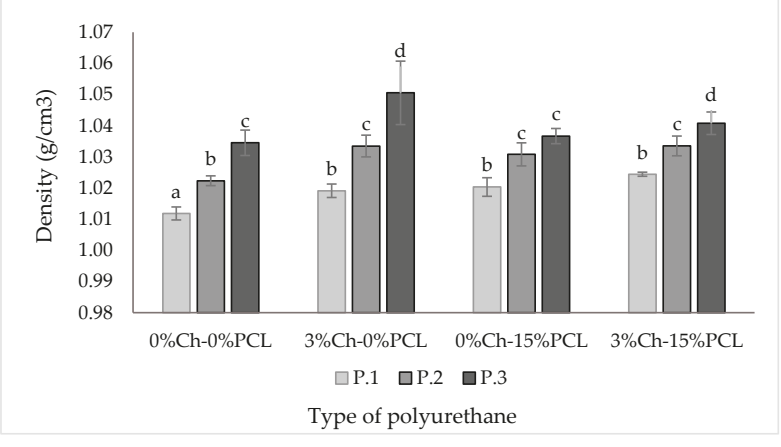

Figure 6. Density of the synthesized PUs. The data are expressed as the mean ± SD (n = 3). Bars with different letters (a–d) indicate significant differences ($p < 0.05$).

As seen in Figure 6, the density of PUs depends on the type of polyol, which agrees with the results shown for the mechanical and thermal properties. As the cross-linking density increased, the density of the resulting polymeric material significantly increased, although the difference between the highest and lowest values was less than 5%. This agrees with the results of Conejero-García et al. who synthesized polyglycerol sebacate, with a different degree of cross-linking, as a material for various applications in tissue engineering. The density values reported by the authors ranged between 1.13 and 1.14 g mL^{-1} [54].

The high densities of polymeric materials can be related to a higher hydroxyl (OH) content due to increased cross-linking reactions [55]. In a study conducted by Carriço et al. they found that increasing the castor oil content in the formulation of foam increased the apparent density, suggesting that the polymer chains were more packed, with less free volume and smaller cells, increasing the stiffness of these materials [55].

2.7. Dynamo-Mechanical Thermal Analysis (DMTA)

Figure 7 shows the dynamic behavior, DMTA, in a tension mode of PUs corresponding to the evolution of the modulus and the loss factor versus temperature. With the variation of the storage modulus and the loss factor, it was possible to observe the displacements suffered by T_g for the evaluated materials. It can be seen that T_g increases when polyols P.2 and P.3 are used; this is probably due to the stiffness of the structure and greater generation of hydrogen bonds because of the high hydroxyl index present in the polyol [38,39]. According to the above results, it can be inferred that material compatibility decreases when the polyol without modifications, and therefore with less cross-linking, is used.

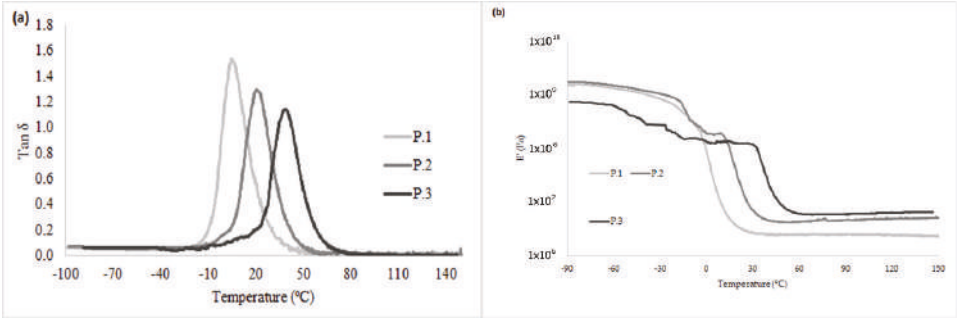

Figure 7. DMTA thermograms of the synthesized PUs. (**a**) Loss factor; (**b**) Storage modulus.

Results with a similar trend were found by Chen et al. on PU matrices synthesized with PCL as a polyol, IPDI, and PLA. The authors reported that when the mobility of the chain decreased, the value of T_g increased. Therefore, they observed that phase compatibility decreased when the PCL content increased due to a possible plasticizing effect of non-cross-linked material [39].

A similar behavior occurred with the modulus results. The lowest values corresponded to the materials synthesized with P.1 (polyol without modification) compared with polyols P.2 and P.3, which have a higher content of hydroxyl groups. An increase in hydroxyl groups results in an increase in cross-linking, hindering polymer chain mobility and thereby increasing the storage modulus. A decrease in polymer chain mobility can limit energy transfer and diffusion, which could decrease the absorption capacity of impact resistance and deformation [39].

The relationship between hard and soft segments is important as they simultaneously act as a physical cross-linking agent and as a high-modulus filler. When there is an organization of the hard and soft segments in the respective domains, pre-polymers tend to have two T_g values. One temperature will be negative corresponding to the soft segments, while the other will be positive, corresponding to the hard segments [38]. When a single event of T_g occurs, it could be inferred that there is a homogeneous phase distribution [38]. According to the results obtained by DSC, it can be observed that the trend of T_g is similar, that is, a single value of T_g is present, increasing as the polyol is modified. The presence of a single transition can be related to the existence of a dominant phase, so it can be inferred that there is a uniform distribution of the components [56]. The differences in T_g between the polyols used may be due to the cross-linking density because this would cause a greater compatibility between hard and soft segments [38].

2.8. Field-Emission Scanning Electron Microscopy (FESEM)

Figure 8 shows the morphology of PUs synthesized with IPDI as a function of the polyol. The FESEM micrographs showed a uniform distribution of PUs, but it was not possible to differentiate the hard segments from the soft segments. Similarly, no differences were observed related to the type of polyol used for the polymeric matrix. These results can be correlated with the calorimetric results because if there is only a single T_g, it is probable that there is a homogeneous phase distribution. This agrees with the results reported by Thakur et al. on PUs synthesized with castor oil and toluene diisocyanate for the coating of materials [47].

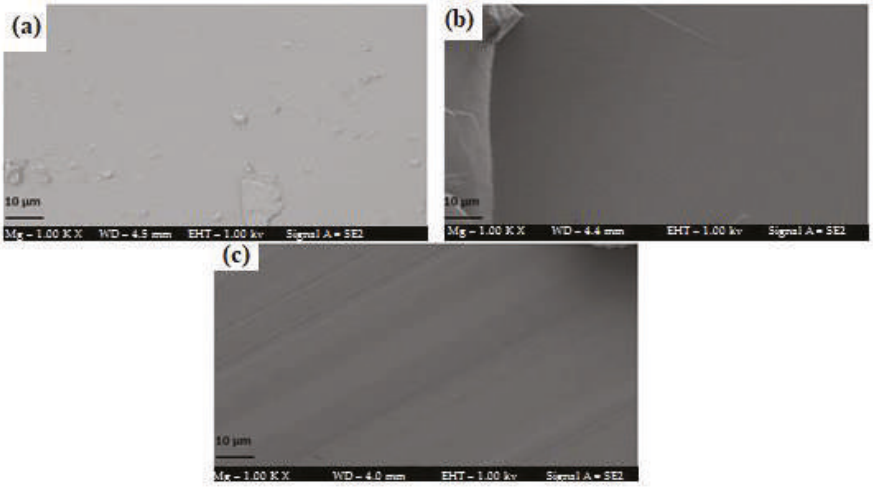

Figure 8. FESEM micrographs of PUs synthesized at 100×. (**a**) P.1; (**b**) P.2; (**c**) P.3.

2.9. In Vitro Biodegradability Assays

The biodegradability of PUs was evaluated in the presence of different media (HCl, NaOH, and enzymatic) over a specific period of time, the results are shown in Figure 9.

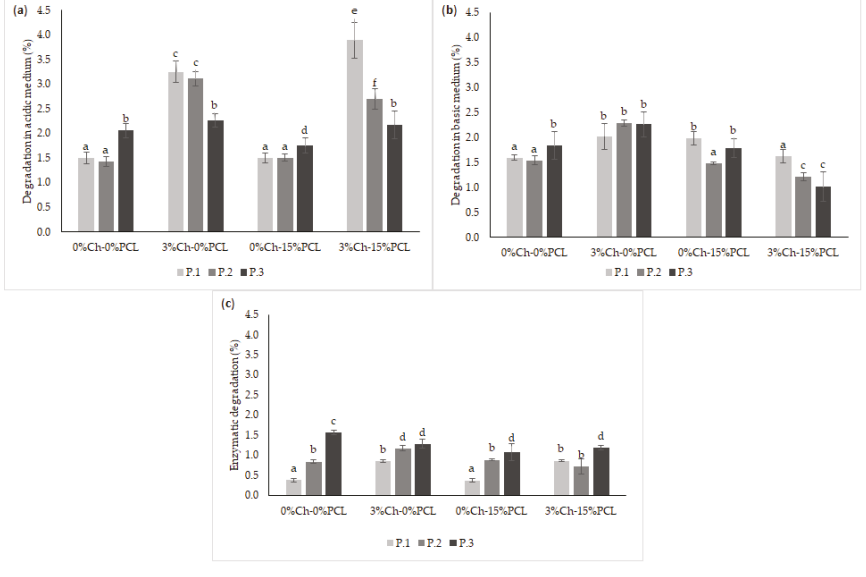

Figure 9. Degradation rate of PUs in different media. (**a**) Acidic medium (0.1 M HCl) for 90 days; (**b**) Basic medium (0.1 M NaOH) for 90 days; (**c**) Enzyme medium (esterase) for 21 days. The data are expressed as the mean ± SD (n = 3). Bars with different letters (a–f) indicate significant differences ($p < 0.05$) between the polyols.

PCL was used as a positive control in enzymatic degradation, showing a degradation of 9.08 ± 0.30% after 21 days. It can be inferred that the linear structure of PCL facilitates the diffusion of the cleaved chains throughout the polymer and their release into the medium, producing a higher

degradation rate. For the synthesized PUs, characterized by being cross-linked materials, the chain mobility is lower, thus hindering the diffusion of the cleaved chains.

The highest value of the degradation rate after 90 days of testing (acidic and basic media) was obtained with the acidic medium under the test conditions for the material synthesized with polyol P.1 by adding the additives (3%Ch-15%PCL). FTIR of the degraded materials (Figure 10) helped determine whether the degradation corresponded to one of the functional groups of the material.

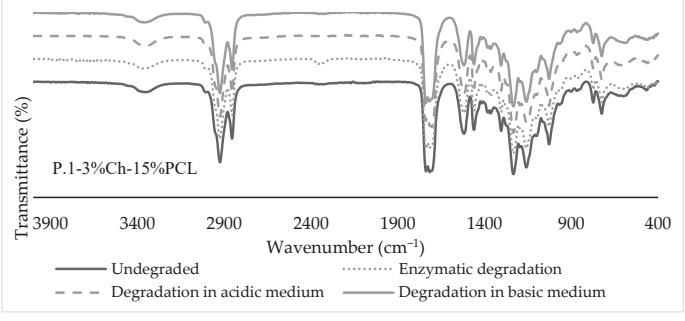

Figure 10. FTIR spectra of PUs degraded in acidic, basic, and enzymatic media.

Figure 10 shows that the functional groups characteristic of PUs are conserved compared with the undegraded material, therefore, it can be inferred that degradation occurs at the surface level. Surface images of the degraded materials were also taken using FESEM, observing a possible surface degradation of the materials (Figure 11). When observing that the degradation rate is less than 4% in the evaluated media, it can be said this is due to the hydrophobic character of PUs, which agrees with the results found for the rate of water absorption and contact angle.

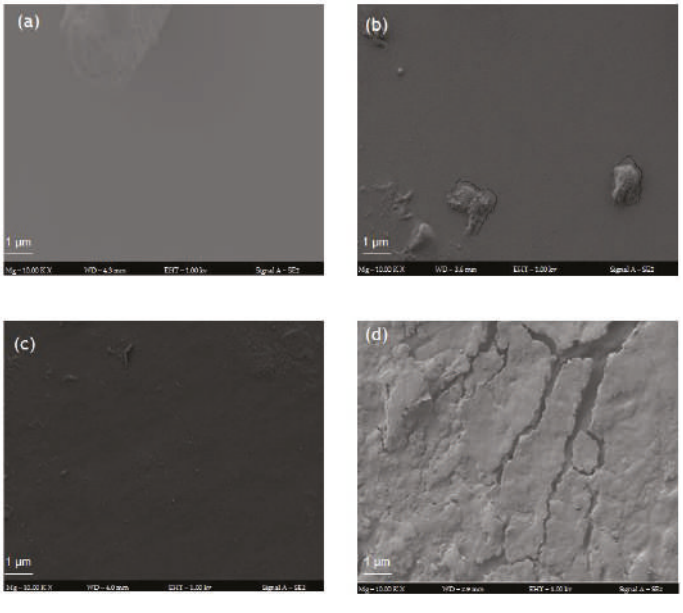

Figure 11. FESEM micrographs of the PU synthesized with P.2-3%Ch-15%PCL after the degradation process in different media (10,000×). (**a**) Undegraded material; (**b**) Acidic medium (0.1 M HCl) after 90 days; (**c**) Basic medium (0.1 M NaOH) after 90 days; (**d**) Enzyme medium (esterase) after 21 days.

The results obtained in this research show a similar trend with those reported by Thakur et al., who evaluated the chemical resistance of PUs in acidic and basic media, finding that in general, PUs show chemical resistance, and PUs based on castor oil showed higher resistance to the basic medium because the oil contains hydrolyzable functional groups [37]. This may be the reason why the biodegradation of the PUs in basic medium was lower than in acidic medium.

The degradation of poly (ester-urethane) occurs mainly by a hydrolytic attack of the ester and urethane bond [31]. Das et al. attributed the degradation in acidic and basic media to different types of strong interactions in the structures of PUs [57]. The authors stated that low resistance to alkalis is due to the hydrolyzable ester bonds in the monoglyceride residues and PCL of polymers [57]. After 90 days of testing, it was observed that the highest values of the degradation rate under the test conditions were relatively low (3.9% in acidic medium and 2.3% in basic medium). These results indicate that the polymeric materials are resistant to degradation due to the structure of PUs, that is, to the cross-linked matrix with high mechanical properties and a hydrophobic character.

Regarding enzymatic degradation (Figure 12c), the highest rate observed was 1.6% after 21 days. This degradation process was greater than those obtained with the other treatments evaluated. This behavior can be attributed to an increase of hydroxyl groups in the polyols, producing an increase in the physical cross-linking of the polymer, and therefore, an increase in urethane groups. Urethane bonds are similar to amides and may be hydrolyzed by enzymes such as the esterase used in this research [58,59]. This agrees with what was stated by Gogoi et al. who reported that amide and urea bonds present in the branched polymer structure facilitate degradation [60]. According to Cherng et al., the degradation of PUs is due to cleavage of the hydrolytically weak bonds that are characteristic of the soft segments; therefore, they concluded that the in vitro degradation rate depends mainly on the type of polyol used in the synthesis due to the ester bonds in the structure [58].

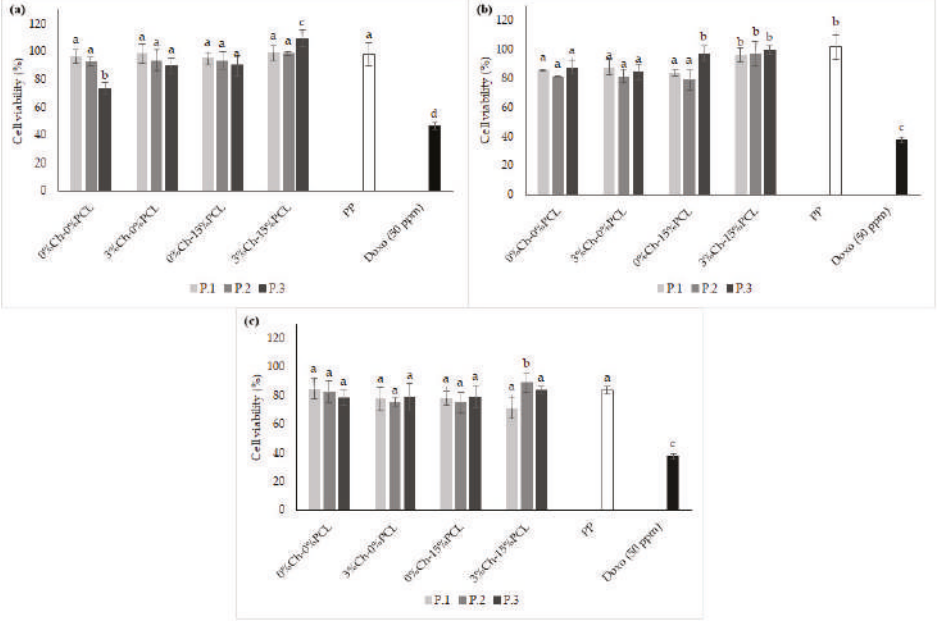

Figure 12. Percentage of cell viability at 24 h. (**a**) L929 Mouse fibroblasts; (**b**) Human fibroblasts (MRC-5); (**c**) Human dermal fibroblasts (HDFa). The data are expressed as the mean ± SD (n = 3). Bars with different letters (a–d) indicate significant differences ($p < 0.05$) between the polyols.

2.10. In Vitro Cell Viability Assay by the MTT Method

As part of the in vitro biological evaluation of PUs, the percentage of cell viability was determined on three fibroblast cell lines. The results are shown in Figure 12.

Figure 12 shows that all polymers had a cell viability of greater than 70% for the three cell types evaluated. According to the ISO/CD 10993-5 standard, values greater than 70% can be considered suitable for biomaterials since they would be non-cytotoxic. As a control material, polypropylene (PP) was used because it is a biocompatible and non-absorbable biomaterial. As a negative control, doxorubicin (Doxo) was used. Figure 12a shows the cell viability results of the PUs on L929 fibroblasts. The percent viability of all matrices, except for the PU synthesized with P.3 without additive, did not show significant differences ($p < 0.05$) compared to PP. For the PU synthesized with P.3, significant differences were observed with the polymer synthesized with P.1 and with the control, but the cell viabilities are suitable to propose the synthesized materials as possible biomaterials. For the L929 fibroblasts, as the cross-linking of PU increased, the percentage of cell viability decreased. It is likely that the high degree of cross-linking produces a low availability of functional groups, such as −OH groups, in the cross-linked polymer. These groups would decrease the cell adhesion to the surface [33] mediated by proteins from the medium.

Bakhshi et al. evaluated PUs synthesized by adding quaternary ammonium salts in the epoxidation of soybean oil and found that PUs show a cell viability between 78–108% with L929 mouse fibroblasts, indicating that there was no toxicity of the synthesized polymers, coinciding with the results of this study [2].

Similar results were found by Calvo-Correas et al. in a preliminary study of in vitro cytotoxicity with murine L929 cells. These authors determined that PUs synthesized from castor oil and lysine diisocyanate had a cell viability greater than 100% in the first 24 h of the assay when following the ISO 10993-12 standard, indicating that the synthesized PUs were non-toxic and could have a potential use in biomedical applications [61]. Likewise, the results from the current study agree with those reported by Reddy et al., who synthesized a PU from lysine diisocyanate, PCL, and 1,4-butane-diamide and found that the polymers did not show toxicity when in contact with NIH/3T3 mouse fibroblasts [62].

Figure 12b shows the cell viability results of the polymers on human fibroblasts (MRC-5). For this cell line, no trend was observed related to the polyol type used in the synthesis of the PUs. The viability was decreased compared to that of the control material (PP); nevertheless, the materials are suitable for use in the design of biomaterials because they show a cell viability of greater than 80%.

Figure 12c shows the cell viability results of PUs on human fibroblasts (HDFa), and the materials show greater than 80% cell viability. Here, there were no statistically significant differences ($p < 0.05$) between the polyols used in the synthesis of PUs. Similarly, there were no significant differences between the synthesized materials and the PP control material; therefore, it can be inferred that the synthesized PUs can be considered suitable for the design of biomaterials for non-absorbable sutures.

The above results are in accordance with those reported by Coakley et al., who evaluated HDFa cells in vitro from a construct derived from porcine urinary bladder as a potential scaffold in tissue engineering. The study demonstrated the viability of the human dermal fibroblasts. The results showed cell viability values of greater than 90% [63].

Cytotoxicity may be related to the relative cell viability of controls, where values lower than 30% indicate severe toxicity of the materials, values between 30 and 60% indicate moderate toxicity, values between 60 and 90% indicate slight toxicity, and values above 90% indicate that the materials are non-toxic [64]. Therefore, the fibroblast cell viability results shown in Figure 12 demonstrate that the PUs are non-toxic for all of the lines evaluated.

2.11. Immunocytochemical Techniques

2.11.1. In Vitro Cell Viability Assay by a Live/Dead Kit

L929 cells that were cultured directly on the material and evaluated by the MTT method showed no toxic effects. When evaluating the cells by a live/dead viability kit, it was possible to observe that the cells adhered to the material, showed viability, and proliferated during the exposure time with the material. This kit allows determination of the number of live and dead cells during the test. In this experiment, viable cells were determined. Figure 13 shows the fluorescence units of the viability results as evaluated by the live/dead kit.

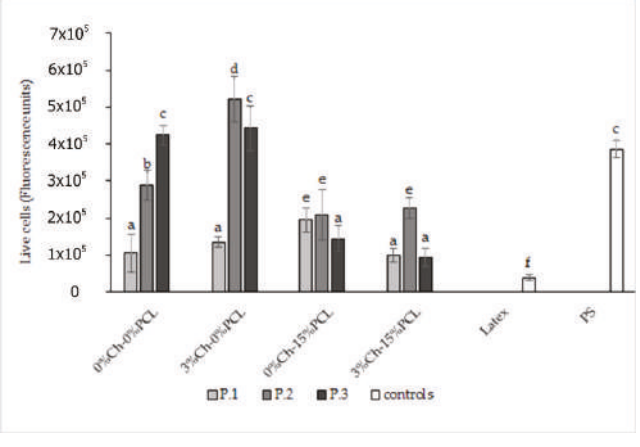

Figure 13. Fluorescence unit results of the in vitro cell viability test after 48 h with the live/dead kit. Polystyrene (PS) positive control; Latex negative control. The data are expressed as the mean ± SD (n = 3). Bars with different letters (a–f) indicate significant differences ($p < 0.05$) between polyols.

The results shown in Figure 13 indicate that PUs synthesized with modified polyols by transesterification with and without the addition of Ch show values of living cells similar to and higher than the material used as a positive control, PS. The materials synthesized with modified polyols by adding Ch showed statistically significant differences compared to the other PUs after 48 h of testing. Likewise, all the materials showed higher values than the negative control used in the test.

All the materials showed statistically significant differences compared to the negative control (latex). When comparing to the results of the positive control (PS), no significant differences were observed between the materials synthesized with P.3 without additive and by adding 3% Ch. This indicated that these materials had a similar cell viability behavior to that obtained with the PS reference material, which is widely used to grow and proliferate cells in vitro. Similarly, it was observed that one material evaluated showed significant differences compared to PS, with the viability values being higher than the positive control. This PU corresponds to the one synthesized with polyol P.2 with 3% Ch. These results indicate that Ch has a positive effect because it improves the biocompatibility of the PU.

Chitosan has a primary amino group and two free hydroxyl groups for each glucose unit, which is beneficial for biomedical applications [15]. The presence of free amino groups causes an increase in the positive charge of the polymer; therefore, there is a greater interaction between Ch and the cells [65].

These results agree with those reported by Laube et al., who performed a live/dead staining assay of NIH/3T3 fibroblasts grown on PU foams that were synthesized with lysine diisocyanate. They found that the cells were viable and proliferated, showing an increased cell density over time. Therefore, the authors proposed these materials as possible substitutes for soft tissue fillers [31].

2.11.2. Fixation and Morphological Analysis with Phalloidin and DAPI

In this assay, the adhesion and proliferation of L929 cells were observed by morphological analysis and were compared to the latex negative control. PS was used as a positive control, which is a common biomaterial used for cell culturing. Figure 14 shows the images obtained from the cells fixed and stained after 24 h of contact with the PUs by polyol type.

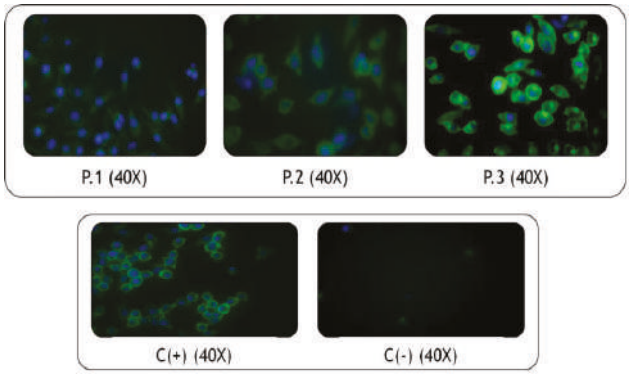

Figure 14. Optical microscopy images of phalloidin (green) and DAPI (blue) staining for representative PUs evaluated on L929 fibroblasts for 24 h. C(+) polystyrene positive control, C(−) latex negative control. Images were analyzed by ImageJ software.

This technique stains the F-actin fibers (a main component of the cytoskeleton) with phalloidin, producing a green color [66], and DAPI staining produces a blue color for the fibroblast nuclei. As observed in the images, the structure of the L929 fibroblasts was conserved when compared with the positive control. Likewise, varying type of polyol or additive did not produce conformational changes in cell structure. As seen in the images, fibroblasts could adhere to the polymeric material, as evaluated after 24 h of contact. Cell morphology can indicate substrate-cell interactions. Flat and extended cell forms indicate strong adhesion from cell to substrate, while a rounded morphology generally means that the cells have difficulty in adhering to the substrate [67]. With the above, it can be inferred that the PUs evaluated in direct contact with cells allow cell proliferation and do not affect the cell morphology after 24 h of testing. Therefore, the synthesized PUs in this research may be suitable as materials for the design of non-absorbable sutures.

2.12. Evaluation of Inflammatory Processes

Twelve materials synthesized with castor oil polyols and IPDI with 3% Ch and 15% PCL were evaluated to determine the in vitro inflammation processes produced after contact with the materials. Inflammation was evaluated by the release of different cytokines to the medium of THP-1 cells that were differentiated into macrophages, with and without LPS stimulation, and in contact with the PUs. Nine inflammatory markers were analyzed, including pro- and anti-inflammatory cytokines (IFN-γ, IL-1β, IL-2, IL-4, IL-5, IL-6, IL-8, IL-10, and TNF-α). The first test group (group A) was used to determine the possible effect of PUs on the inflammatory process of macrophages.

Figure 15 shows the concentrations of anti-inflammatory cytokines expressed by the macrophages after 24 h of exposure to the PUs. Figure 16 shows the concentration of pro-inflammatory cytokines expressed in the culture medium. The reference material was a polypropylene (PP) biomaterial used in non-absorbable biomedical sutures. The control was the culture medium without polymer. Figures 15 and 16 show cytokine expression in the monocytes (the cells not treated with PMA). The second test group (group B) was formed to determine if the synthesized materials had anti-inflammatory activity against cells in which inflammation had been stimulated by LPS before direct contact with the PUs.

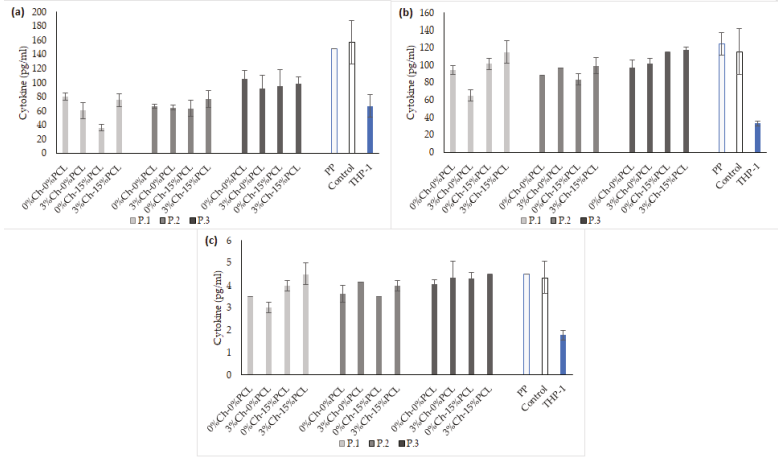

Figure 15. Anti-inflammatory cytokines without LPS stimulation. (**a**) IL-10; (**b**) IL-5; (**c**) IL-4. PP: polypropylene as a reference material; Control: culture medium without PUs; THP-1: monocyte cell line. The concentration of cytokines is expressed as the mean ± SD (n = 3).

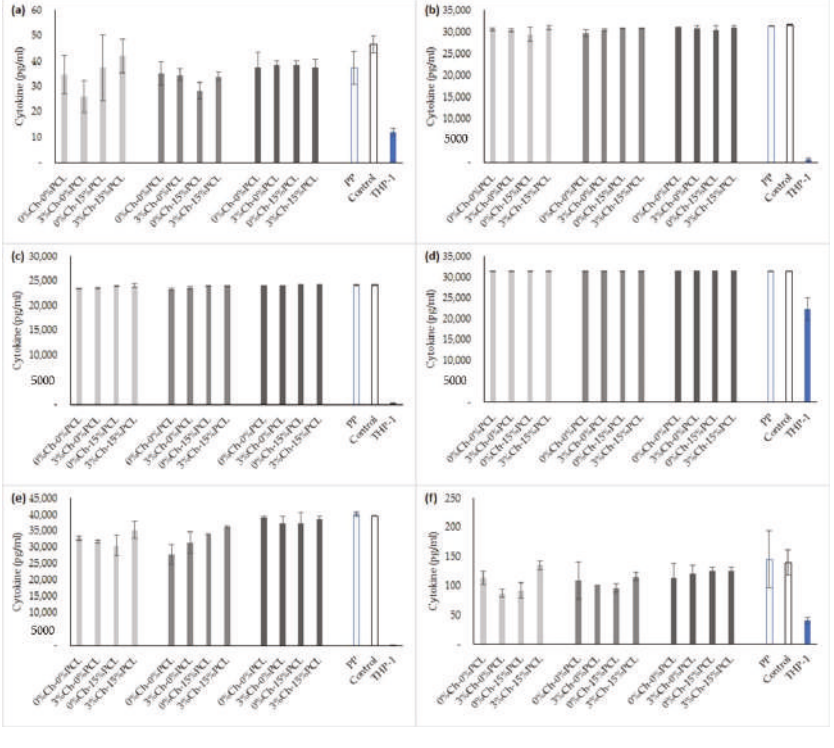

Figure 16. Pro-inflammatory cytokines without LPS stimulation. (**a**) INF-γ; (**b**) TNF-α; (**c**) IL-1β; (**d**) IL-8; (**e**) IL-6; (**f**) IL-2. PP: polypropylene as a reference material; Control: culture medium without PUs; THP-1: monocyte cell line. The concentration of cytokines is expressed as the mean ± SD (n = 3).

The results of the concentration of pro- and anti-inflammatory cytokines from test B are shown in Figures 17 and 18, respectively. PP was tested as a reference material, and culture medium without polymer was used as a control.

As observed in the results of groups A and B, there were no significant differences between the concentrations of the cytokines expressed by the cells that were stimulated with LPS and those that were not stimulated. This may be related to the protocol that was used. A standardized protocol to differentiate THP-1 monocytes into macrophages with PMA is not yet available. Therefore, a wide variation of PMA concentrations is found—between 6 and 600 nM. The time of stimulation with PMA can vary from 3 to 72 h, and the recovery periods vary between 0 and 10 days [25,68]. It is probable that high concentrations of PMA (higher than 100 ng mL^{-1}) increase the levels of expression of genes associated with inflammation and cause an increase in the secretion of pro-inflammatory cytokines, such as TNF or IL-8 [25].

As stated by Park et al. (2007), high concentrations of PMA can induce the expression of some genes during the differentiation process, which can mask the effect of post-differentiation stimuli [69]. The above results indicate that the concentrations of PMA used during the differentiation process of THP-1 monocytes into macrophages triggered the release of pro- and anti-inflammatory cytokines, and this process was prior to exposing the cells to LPS stimulation.

The results obtained for group A (Figures 15 and 16) show that the PUs do not produce an inflammatory process in THP-1 macrophages. This is based on the control results (medium without PU) and the PP reference material, which showed higher values (although not always significant) in the concentrations of the evaluated pro- and anti-inflammatory cytokines.

An acute inflammation in an organism occurs due to a protective response against tissue damage caused by infectious or foreign agents. The first cytokines formed in response to bacterial lipopolysaccharides, tissue injury or infection are TNF-α and IL-1β, which act directly on specific receptors to trigger a cascade of other effectors, such as cytokines and chemokines, among others [23,25,70]. TNF-α and IL-1β have a synergic effect on inflammation, also promoted by IFN-γ through the increase of TNF-α [70]. Tumor necrosis factor (TNF-α) is a pro-inflammatory cytokine that is stimulated early in the inflammatory response [23].

One cytokine evaluated was interleukin-4 (IL-4), characterized by having a potent anti-inflammatory activity and the capacity to inhibit the synthesis of pro-inflammatory cytokines [71]. It acts on activated macrophages to reduce the effects of cytokines IL-1, TNF-α, IL-6, and IL-8 [23]. Therefore, by expressing a pro- or anti-inflammatory cytokine, the expression of its opposite is inhibited. Figure 17 shows IL-4 values near 5 pg mL^{-1}, and its opposites such as TNF-α, IL-6, and IL-8 show values over 20,000 pg mL^{-1}, as observed in Figure 15. Interleukin-10 (IL-10), which exerts anti-inflammatory actions on monocytes or macrophages, was also evaluated [71]. It inhibits the pro-inflammatory cytokines IL-1, TNF-α, and IL-6, stimulating the endogenous production of anti-inflammatory cytokines [23].

TNF-α plays an important role in the inflammatory response of an organism, as previously mentioned. Upon LPS stimulation, a systemic inflammatory state occurs that is characterized by increased levels of the pro-inflammatory cytokines TNF-α and IL-1β, and decreased levels of anti-inflammatory cytokines, such as IL-10 [26]. This behavior was observed in the values obtained from group B because in Figure 18a, the values obtained for TNF-α showed concentrations near 30,000 pg mL^{-1} and IL-1β had values of 25,000 pg mL^{-1}, but for IL-10, mean values of 80 pg mL^{-1} were found.

Other evaluated cytokines were interleukins 2 and 6. Interleukin-2 (IL-2) is a pro-inflammatory cytokine characterized by the generation and propagation of the antigen-specific immune response [23]. Interleukin-6 (IL-6) is a cytokine with pro-inflammatory properties, and high levels are associated with severity in septic processes. IL-6 is sometimes considered an anti-inflammatory cytokine because it can induce beneficial proteins in septic shock [71].

For the two groups (A and B), the cytokines of the THP-1 monocytes that were not transformed to macrophages were evaluated to observe the basal expression levels of each cytokine. According to Chanput et al., the basal levels of cytokines of THP-1 monocytes and macrophages have values near 20 and 30 pg mL^{-1} [22]. For the study performed with PUs, cytokines IFN GAMA, IL-2, IL-5, and IL-6 had values that were within the range mentioned by the study of Chanput et al. for THP-1 monocytes, as observed in Figures 15–18. After the differentiation of monocytes into macrophages, it was observed (Figures 17 and 18) that the expression levels of all cytokines increased compared to the basal levels of the monocytes. Anti-inflammatory cytokines IL-4, IL-5, and IL-10 had increases of 55, 65, and 35%, respectively. Pro-inflammatory cytokines IL-2, IL-6, IL-8, IL-1β, IFN-γ, and TNF-α had increases of 65, 122, 29, 100, 70, and 97%, respectively. Regarding the results of the macrophages stimulated with LPS, the percent increases in the concentrations of the cytokines were similar to these.

According to the results from the reference biomaterial (PP) and the medium without PU, the behavior does not show statistically significant differences of the PUs evaluated in group B. Therefore, it can be inferred that the PUs do not have anti-inflammatory activity.

The results show that, for the differentiation of THP-1 monocytes into macrophages, in vitro standardization and optimization is necessary to achieve adequate cytokine expression results. THP-1 monocytes and macrophages could be an adequate and reliable model to evaluate the inflammatory response before conducting a more detailed study with human-derived cells [22].

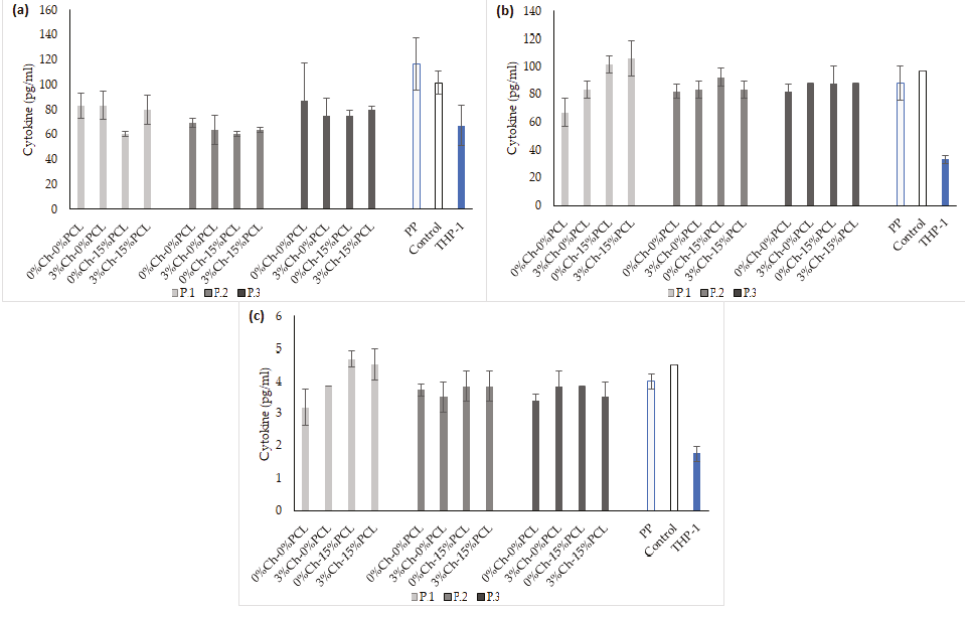

Figure 17. Anti-inflammatory cytokines with LPS stimulation. (**a**) IL-10; (**b**) IL-5; (**c**) IL-4. PP: polypropylene as a reference material; Control: culture medium without PUs; THP-1: monocyte cell line. The concentration of cytokines is expressed as the mean ± SD (n = 3).

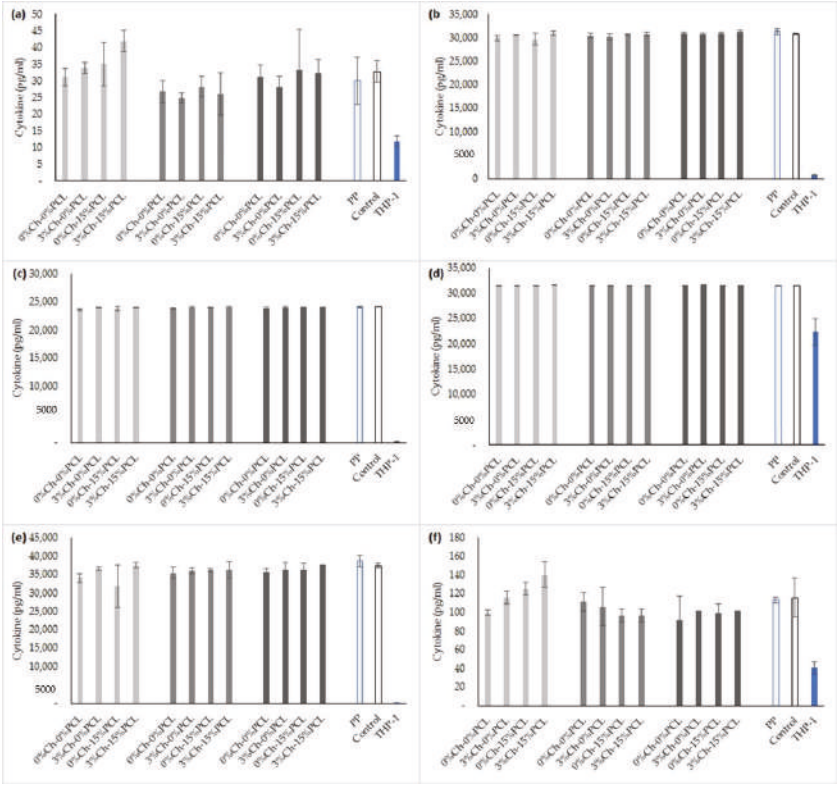

Figure 18. Pro-inflammatory cytokines with LPS stimulation. (**a**) INF-γ; (**b**) TNF-α; (**c**) IL-1β; (**d**) IL-8; (**e**) IL-6; (**f**) IL-2. PP: polypropylene as a reference material; Control: culture medium without PUs; THP-1: monocyte cell line. The concentration of cytokines is expressed as the mean ± SD (n = 3).

3. Materials and Methods

3.1. Reagents

Castor (*Ricinus communis*) oil was purchased from Químicos Campota and Co. Ltd. (Bogotá, Colombia). Isophorone diisocyanate (IPDI), polycaprolactone diol (PCL) (average molecular weight of 2000 g mol^{-1}), low molecular weight chitosan (Ch) (with a percentage of deacetylation between 75–85%), *n*-octane, 0.1 M hydrochloric acid (HCl), 0.1 M NaOH, porcine liver esterase (18 units mg^{-1}), 4′,6-diamidino-2-phenylindole dihydrochloride (DAPI), and phorbol 12-myristate-13-acetate (PMA) were acquired from Sigma-Aldrich Chemical Co. (St. Louis, MO, USA). Pentaerythritol was from Merck KGaA (Darmstadt, Germany). Phosphate-buffered saline (PBS: Dulbecco's phosphate-buffered saline), 3-(4,5-dimethyl-2-thiazolyl)-2,5-diphenyl-2H-tetrazolium bromide (MTT), 2.5% trypsin (10×), penicillin-streptomycin (10,000 units of penicillin and 10,000 µg of streptomycin per milliliter), Dulbecco's modified Eagle medium (DMEM, 1×), Roswell Park Memorial Institute (RPMI) 1640, Live/dead® Viability/Cytotoxicity Kit, Alexa Flour™ 488 phalloidin, and lipopolysaccharide (LPS, *Escherichia coli* 026:B6) were obtained from Gibco/Invitrogen (Paisley, UK). Fetal bovine serum (FBS) was from Eurobio (Les Ulis, France).

3.2. Biological Material

Human acute monocytic leukemia cell line, THP-1 (ATCC® TIB-202™). Mouse subcutaneous connective tissue fibroblasts L929 (ATCC® CCL-1). Human lung fibroblasts MRC-5 (ATCC® CCL-171™). Adult human dermal fibroblast HDFa (ATCC® PCS-201-012™). All biological materials were acquired from the strain library of the Universidad de La Sabana (Chía, Colombia).

3.3. Obtaining Polyols

The polyols were derived from castor oil (P.1, P.2, and P.3). P.1 corresponded to commercial unmodified castor oil. Polyols P.2 and P.3 were obtained by transesterification with pentaerythritol [72]. For the reaction, the castor oil temperature was raised to 120 °C for 10 min. The temperature was then further increased to 210 °C, adding pentaerythritol (1.32% and 2.64% mol pentaerythritol/mol castor oil for P.2 and P.3, respectively) and 0.05% lead oxide as a catalyst. The mixture was maintained at 210 °C for 2 h. After the reaction time, the catalyst was removed by decantation for 24 h and filtration. The hydroxyl number of the polyols were determined according to ASTM D1957-86 [73].

3.4. Synthesis of Polyurethanes

The PUs were synthesized by the pre-polymer method. The polyol was brought to 60 °C, and the diisocyanate was added the reactor at a constant NCO:OH ratio (1:1) [74], and maintained at 300 rpm for 5 min. Them the PCL (15% *w*/*w* of oil polyol weight) and Ch (3% *w*/*w* of oil polyol weight) were then added and maintained at 300 rpm for 5 min additional. The formation of the PU sheets was carried out by pouring the prepolymer into a steel mold. Twelve PU matrices were synthesized in sheets (15 cm × 9 cm × 0.3 cm (length × width × height)). Curing was performed at 110 °C for 12 h [72]. The synthesized PUs are identified with the following nomenclature: Pn-xCh-yPCL, where n represents the polyol used (1 for unmodified castor oil, 2 for castor oil with 1.32% pentaerythritol/mol, and 3 for the castor oil with 2.64% pentaerythritol/mol), and x and y represent the percentage of Ch and PCL, respectively.

3.5. Mechanical Tests

A universal testing machine EZ-LX (Shimadzu, Kyoto, Japan) was used to determine maximum stress, percent elongation, and Young's modulus of the polyurethanes (following the ASTM D638-10 standard). A load cell of 5 kN with a crosshead speed of 25 mm min^{-1} was used [75,76]. Three samples of 40 mm × 6 mm × 3 mm (length × width × thickness) were tested.

3.6. Fourier-Transform Infrared Spectroscopy (FTIR)

Chemical structures were evaluated by an ATR-FTIR spectrometer (Bruker Alpha, Billerica, MA, USA), in the range from 400 to 4000 cm^{-1}. The spectrum corresponds to the average of 24 scans at a spectral resolution of 4 cm^{-1} [40,77].

3.7. Thermal Analysis

3.7.1. Thermogravimetric Analysis

Thermal behavior was evaluated in a TGA/DCS1 thermogravimetric analyzer coupled to DSC (Mettler-Toledo Inc., Schwerzenbach, Switzerland). According to ASTM D6370, the conditions used were as follows: heating speed of 25 °C min^{-1}, a temperature range of 25–600 °C, nitrogen atmosphere, and samples of 15 ± 2 mg [48].

3.7.2. Differential Scanning Calorimetry

Glass transition temperatures were determined by a DSC 3+ analyzer (Mettler-Toledo, Columbus, OH, USA). The conditions were as follows: temperature range from −70 °C to 150 °C, nitrogen atmosphere with 20 mL min^{-1} flow, and sample weights of 10 ± 2 mg [78].

3.8. Hydrophilic Character

3.8.1. Contact Angle

A "Drop Shape Analysis—DSA" device (GH11, Krüss, Hamburg, Germany) was used to measure the contact angle. According to ASTM-D7334-08 (2013), it was measured with the sessile drop method using 10 µL of distilled water at 20 °C [79]. Ten measurements of each material were performed.

3.8.2. Water Absorption Rate

To remove uncross-linked chains and monomer residues after synthesis, the PU materials were washed with ethanol for two days, renewing the ethanol every day. The solvent was then replaced by deionized water for two more days. The materials were dried in a vacuum chamber (0.01 mm Hg) at 37 °C for 24 h [54]. The rate of water absorption was determined by immersing the sample in distilled water until constant weight. The residual water was then removed from the samples with dry filter paper, and the samples were weighed [80]. All tests were performed in triplicate. The rate of water absorption at equilibrium was calculated by comparing the mass of the sample (m_t) after obtaining constant weight with the initial mass (m_i) of the sample using Equation (1):

$$\% \text{ Water absortion of PUs} = (m_i - m_t)/m_i \quad (1)$$

3.9. Determination of Density

The material density was determined using the Archimedes immersion technique using a Mettler AX 205 balance (Mettler-Toledo Inc.) with a sensitivity of 0.01 mg and a Mettler ME-33360 density determination kit. Dry samples of 5 mm × 5 mm × 3 mm were used to calculate the density in triplicate. The PUs were weighed in the air (m_{air}) and then immersed in n-octane with a known density ($\rho_{n\text{-octane}}$), and the immersion weight ($m_{n\text{-octane}}$) was obtained at 20 °C. The density was calculated by the following Equation (2) [54]:

$$\text{Density of PUs} = (m_{aire} \times \rho_{n-octano})/(m_{aire} - m_{n-octano}) \quad (2)$$

3.10. Dynamic Mechanical Thermal Analysis (DMTA)

The effect of temperature on the mechanical properties was evaluated by a DMTA test. A DMA 8000 thermomechanical analyzer (Perkin-Elmer, Waltham, MA, USA) was used at a frequency of 1 Hz, a deformation of 0.1%, and a temperature program between −90 °C and 150 °C, with a heating rate of 5 °C min^{-1}. The storage modulus and the loss factor, tanδ [38], were determined.

3.11. Field Emission Scanning Electron Microscopy (FESEM)

Morphological characterization of the PUs was performed with a field-emission scanning electron microscope (FESEM, ZEISS ULTRA 55 from Oxford Instruments (Abingdon, UK). The PUs were washed with ethanol for two days, renewing the ethanol every day. The solvent was then replaced by deionized water for two more days. The materials were dried in a vacuum chamber (0.01 mm Hg) at 37 °C for 24 h [54]. The samples were coated with platinum to observe the morphology of the materials with an accelerating voltage of 5 kV [81].

3.12. In Vitro Biodegradability Tests

Biodegradability tests were performed in independent tests in triplicate following ASTM F1635-11. To remove uncross-linked chains and monomer residues, the PUs were washed with ethanol for two days, renewing the ethanol each day. The solvent was then replaced by deionized water for two more days. The materials were dried in a vacuum chamber at 37 °C for 24 h [54]. Samples of 5 mm × 5 mm × 3 mm were placed in the biodegradation media and incubated at 37 °C for three months, except for the enzyme medium (10 units mg^{-1} solid), which was for 21 days. After this time, the samples were washed with distilled water, dried in a vacuum chamber, and weighed. The reagents used were: 0.1 M HCl medium, 0.1 M NaOH medium, and porcine liver esterase enzymatic medium. The biodegradation rate was calculated by comparing the dry weight (w_f) of the sample after degradation during the predetermined time with the initial dry weight (w_i) of the sample using Equation (3) [81,82]:

$$\% \text{ Degradation of PUs} = (w_i - w_t)/w_i \quad (3)$$

3.13. In Vitro Cell Viability Assay by the MTT Method

L929 mouse fibroblasts and MRC-5 and HDFa human fibroblasts were cultured in DMEM supplemented with 10% FBS and 1% penicillin-streptomycin in T-75 cell culture flasks. They were grown at 37 °C and 5% CO_2. The cell culture medium was changed every 48 h [83]. At 100% confluence, the cells were trypsinized (trypsin-EDTA) for viability analysis.

The effect of polyurethanes on cell viability was evaluated by the MTT method defined by ISO/CD 10993-5. Cells were seeded in 96-well plates at a concentration of 4.0 × 10^4 cells per well in supplemented medium and cultured at 37 °C and 5% CO_2 for 24 h. Subsequently, PU cylinders of 3 mm × 2 mm (diameter × height) (previously sterilized under ultraviolet UV light (260 nm) for 30 min on each side [33]) were placed in 100 µL of supplemented medium. The materials were left in contact with the polymers for 24 h at 37 °C and 5% CO_2. The supernatant and polymers were then removed, and the MTT solution (12 mM in PBS) was added to a total volume of 100 µL and incubated for 4 h at 37 °C. The supernatant was removed, and 100 µL of dimethyl sulfoxide was added and incubated for 15 min at 37 °C. The optical density was then determined in a plate reader (Bio-Tek ELx800 Microplate Reader, Highland Park, Winooski, VT, USA) at 570 nm. A polypropylene biomaterial (PP) was used as a positive control for cell viability, and doxorubicin (DOXO) was used as a negative control. All tests were performed in triplicate. Cell viability was determined according to Equation (4):

$$\% \text{ Cell viability of PUs} = Abs_{sample}/Abs_{control} \quad (4)$$

where Abs_{sample} corresponds to the absorbance value of the cells after treatment with the PU, and $Abs_{control}$ corresponds to the cells without treatment.

3.14. Immunocytochemical Techniques

In vitro cell viability assay by the live/dead kit. Cell viability was also evaluated by the live/dead kit based on plasmatic membrane integrity and intracellular esterase activity [84]. L929 mouse fibroblasts were cultured in RPMI supplemented with 10% FBS and 1% penicillin-streptomycin in T-75 cell culture flasks at 37 °C and 5% CO_2. The cell culture medium was changed every 48 h [83]. At 100% confluence, the cells were trypsinized (trypsin-EDTA) for viability analysis.

Prior to the assay, the PUs were washed with ethanol and water for 3 days and dried in a vacuum chamber at 37 °C for 24 h [54]. PU sheets with a diameter of 4 mm (previously sterilized under UV light (260 nm) for 30 min on each side) were placed in 96-well plates [33]. Five microliters of cells, at a concentration of 1.0 × 10^4 cells mL^{-1}, were then seeded onto each material using supplemented medium and incubated at 37 °C and 5% CO_2 for 30 min. Next, 95 µL of supplemented medium was added and incubated for 24 h at 37 °C and 5% CO_2 [54]. The supernatant was removed, and 2 µL of calcein AM (live cell marker) staining solution and 4 µL of ethidium homodimer (dead cell marker)

were added and incubated for 20 min in the dark with stirring [84]. Fluorescence measurement was performed for calcein in a Victor 1420 Multilabel Counter spectrophotometer (Perkin-Elmer, Waltham, MA, USA) at 485 nm to determine the concentration of living cells. PS was used as a positive control and latex as a negative control. All tests were performed in triplicate.

Fixation and morphological analysis with phalloidin and DAPI. L929 fibroblasts in contact with the material after 24 h of incubation were washed with PBS and fixed for 20 min with paraformaldehyde 4% w/v at 20 °C. They were then washed twice with PBS at 4 °C. Phalloidin (Alexa Flour™ 488 phalloidin) was added and incubated for 20 min to reveal F-actin. The samples were then washed twice with PBS. The cell nuclei were stained for 5 min with DAPI at a 1/5000 dilution in PBS, followed by washing twice with PBS. Next, 0.05% sodium azide was added. The cell structure was observed using an Eclipse 80i optical microscope (Nikon, Tokyo, Japan) equipped with a Nikon Intensilight Illuminator [54]. The images were analyzed by ImageJ software version 1.45k (Bethesda, MD, USA).

3.15. Differentiation into Macrophages and Inflammation Stimulation

A human acute monocytic leukemia cell line, THP-1, was used. The cells were cultured at 37 °C and 5% CO_2 in RPMI medium supplemented with 10% FBS and 1% penicillin-streptomycin in T-75 cell culture flasks. For cell differentiation into macrophages, the cells were centrifuged at 2000 rpm for 10 min, resuspended in 3 mL of RPMI culture medium and seeded into 24-well plates [69] by adding 200 mM of PMA and incubating for 48 h [27]. The differentiated cells (macrophages) were washed twice with PBS to remove undifferentiated cells [26]. The macrophages that had been differentiated with PMA were stimulated with 700 ng mL^{-1} of LPS for 3 h [22].

3.16. Evaluation of Inflammatory Processes

With the THP-1 cell line and PUs, two independent tests were performed to evaluate the inflammatory processes of the materials in contact with the cells. The first test (group A) consisted in the direct contact of PUs on the cells differentiated into macrophages with PMA, for 24 h, to determine whether the PUs caused inflammation after contact with the cell line. The next test group (group B) consisted of PUs in contact for 24 h with macrophages differentiated with PMA and stimulated with LPS to determine whether the materials had anti-inflammatory activity.

3.17. Immunoassay

The MILLIPLEX® MAP kit for flow cytometry was used to evaluate cytokine production (IFN-γ, IL-1β, IL-2, IL-4, IL-5, IL-6, IL-8, IL-10, and TNF-α) and release to the supernatant of the macrophages cultured in contact with PUs for 24 h, following the instructions provided by the manufacturers. A mixture of beads with different fluorescence intensities, coated with antibodies for the mentioned cytokines, was pre-incubated in the dark for one hour on an orbital shaker. Concentration standards of 3.2, 16, 80, 400, 2000 and 10,000 pg mL^{-1} were used to determine the concentration curve of each analyte. In a 96-well plate, 200 µL of wash buffer was added, the plate was shaken for 10 min, and the supernatant was discarded. Twenty-five microliters of the standards, 25 µL of running buffer, 25 µL of the stock solution, 25 µL of supernatant from cells in the appropriate wells, and 25 µL of the bead mixture were added. The plate was incubated overnight with shaking at 4 °C. The supernatant was then removed, and the samples were washed twice with 200 µL of wash buffer. Next, 25 µL of antibody was added for detection, and the samples were incubated for 1 h in the dark and with shaking. Twenty-five microliters of the streptavidin phycoerythrin binding protein was then added and incubated for 30 min with shaking in the dark. The supernatant was discarded, and the wells were washed twice with 200 µL of wash buffer. One hundred and fifty microliters of the coating liquid were then added, and the plate was read on a MAGPIX flow cytometer from MILLIPLEX MAP (Darmstadt, Germany). The results of the samples were analyzed using the xPONENT MAGPIX software (Madison, WI, USA).

3.18. Statistical Analysis

The results were expressed as mean values ± standard deviation (SD). The data were analyzed by means of an analysis of variance (ANOVA) and the significant differences were determined for $p < 0.05$. For the comparison between samples the *t*-Student test was used with the SPSS Statistics Software v.23 (IBM, Armonk, NY, USA).

4. Conclusions

PUs synthesized with castor oil polyols, isophorone diisocyanate, 15% *w*/*w* polycaprolactone and 3% *w*/*w* chitosan were used to evaluate their mechanical, physicochemical, morphological, biodegradability, and biocompatibility characteristics, along with their possible inflammatory effects. The type of polyol and additive showed a significant impact on the maximum stress, percent elongation, and contact angle of the material. Chemical modification of the polyols improves the evaluated properties due to the increased cross-linking of the resulting materials. The resulting mechanical properties of the PUs verified their dependence on the presence of hydrogen bonds, the number of hydroxyl groups in the polyols, and the interactions between the hard and soft segments of the matrix. The polyol with the highest hydroxyl index showed the highest values for the mechanical and thermal properties. The percent elongation, with a maximum of 265%, can be used to obtain resistant materials with flexibility, which allows designing biomaterials that do not cause injuries to soft tissues. The degradation rates under the study conditions showed values of less than 4%, so it can be inferred that cross-linking of the synthesized PUs hinders the degradation process. In vitro cell viability was determined using L929 mouse fibroblasts, human fibroblasts (MRC-5) and adult human dermal fibroblast (HDFa). The cell viability results of the PUs in contact with the three cell lines demonstrated that there was no effect on cell viability; therefore, it is likely that these materials could be used for direct contact with the skin without causing damage to surrounding cells. Cell viability was also determined by the live/dead kit for the L929 mouse fibroblasts. Due to the biocompatible properties of the PUs evaluated in this study, it can be inferred that they are suitable for use in biomedical applications as materials for non-absorbable biomedical sutures.

Author Contributions: Conceptualization, M.F.V., Y.L.U., L.E.D., J.A.G.-T., and A.V.-L.; Methodology, Y.L.U.; Formal analysis, Y.L.U.; Investigation, Y.L.U., G.V.-F. and M.A.S.; Resources, M.F.V.; Writing—original draft preparation, Y.L.U.; Visualization, Y.L.U.; Supervision, M.F.V. and L.E.D.; Project administration, M.F.V.; Funding acquisition, M.F.V. and L.E.D.

Funding: This research was funded by the UNIVERSIDAD DE LA SABANA, grant number ING-202-2018 and by COLCIENCIAS under scholarship grant 617-2-2014. CIBER-BBN is an initiative funded by the VI National R&D&I Plan 2008–2011, Iniciativa Ingenio 2010, Consolider Program. CIBER Actions are financed by the Instituto de Salud Carlos III with assistance from the European Regional Development Fund. J.A.G.-T. and A.V.-LL. acknowledge the support of the Spanish Ministry of Economy and Competitiveness (MINECO) through project DPI2015-65401-C3-2-R (including FEDER financial support).

Acknowledgments: The authors thank the Universidad de La Sabana for financing research project ING-202-2018 which is part of this research, Colciencias for the doctoral scholarship under grant 617-2 of 2014, and the Universitat Politècnica de València for assistance and advice with the equipment.

Conflicts of Interest: The authors declare no conflict of interest.

References

1. Alishiri, M.; Shojaei, A.; Abdekhodaie, M.J.; Yeganeh, H. Synthesis and characterization of biodegradable acrylated polyurethane based on poly(ε-caprolactone) and 1,6-hexamethylene diisocyanate. *Mater. Sci. Eng. C* **2014**, *42*, 763–773. [CrossRef] [PubMed]
2. Bakhshi, H.; Yeganeh, H.; Yari, A.; Nezhad, S.K. Castor oil-based polyurethane coatings containing benzyl triethanol ammonium chloride: Synthesis, characterization, and biological properties. *J. Mater. Sci.* **2014**, *49*, 5365–5377. [CrossRef]

3. Kucinska-Lipka, J.; Gubanska, I.; Janik, H.; Sienkiewicz, M. Fabrication of polyurethane and polyurethane based composite fibres by the electrospinning technique for soft tissue engineering of cardiovascular system. *Mater. Sci. Eng. C Mater. Biol. Appl.* **2015**, *46*, 166–176. [CrossRef] [PubMed]
4. Tsai, M.-C.; Hung, K.-C.; Hung, S.-C.; Hsu, S. Evaluation of biodegradable elastic scaffolds made of anionic polyurethane for cartilage tissue engineering. *Colloids Surf. B Biointerfaces* **2015**, *125*, 34–44. [CrossRef] [PubMed]
5. Rocco, K.A.; Maxfield, M.W.; Best, C.A.; Dean, E.W.; Breuer, C.K. In vivo applications of electrospun tissue-engineered vascular grafts: A review. *Tissue Eng. Part B* **2014**, *20*, 628–640. [CrossRef]
6. Park, H.; Gong, M.-S.; Park, J.-H.; Moon, S.-I.; Wall, I.B.; Kim, H.-W.; Lee, J.H.; Knowles, J.C. Silk fibroin-polyurethane blends: Physical properties and effect of silk fibroin content on viscoelasticity, biocompatibility and myoblast differentiation. *Acta Biomater.* **2013**, *9*, 8962–8971. [CrossRef]
7. Rajan, K.P.; Al-ghamdi, A.; Parameswar, R.; Nando, G.B. Blends of thermoplastic polyurethane and polydimethylsiloxane rubber: Assessment of biocompatibility and suture holding strength of membranes. *Int. J. Biomater.* **2013**, *2013*. [CrossRef]
8. Rodríguez-Galán, A.; Franco, L.; Puiggal, J. Biodegradable Polyurethanes and Poly(ester amide)s. In *Handbook of Biodegradable Polymers: Synthesis, Characterization and Applications*; Lendlein, A., Sisson, A., Eds.; John Wiley & Sons: Hoboken, NJ, USA, 2011; pp. 133–154.
9. Adolph, E.J.; Pollins, A.C.; Cardwell, N.L.; Davidson, J.M.; Guelcher, S.A.; Nanney, L.B. Biodegradable lysine-derived polyurethane scaffolds promote healing in a porcine full-thickness excisional wound model. *J. Biomater. Sci. Polym. Ed.* **2014**, *25*, 1973–1985. [CrossRef]
10. Shourgashti, Z.; Khorasani, M.T.; Khosroshahi, S.M.E. Plasma-induced grafting of polydimethylsiloxane onto polyurethane surface: Characterization and in vitro assay. *Radiat. Phys. Chem.* **2010**, *79*, 947–952. [CrossRef]
11. Qiu, H.; Li, D.; Chen, X.; Fan, K.; Ou, W.; Chen, K.C.; Xu, K. Synthesis, characterizations, and biocompatibility of block poly(ester-urethane)s based on biodegradable poly(3-hydroxybutyrate-co-4-hydroxybutyrate) (P3/4HB) and poly(ε-caprolactone). *J. Biomed. Mater. Res. A* **2013**, *101*, 75–86. [CrossRef]
12. Morral-Ruíz, G.; Melgar-Lesmes, P.; García, M.L.; Solans, C.; García-Celma, M.J. Polyurethane and polyurea nanoparticles based on polyoxyethylene castor oil derivative surfactant suitable for endovascular applications. *Int. J. Pharm.* **2014**, *461*, 1–13. [CrossRef] [PubMed]
13. Dulińska-Molak, I.; Lekka, M.; Kurzydłowski, K.J. Surface properties of polyurethane composites for biomedical applications. *Appl. Surf. Sci.* **2013**, *270*, 553–560. [CrossRef]
14. Chan-Chan, L.H.; Solis-Correa, R.; Vargas-Coronado, R.F.; Cervantes-Uc, J.M.; Cauich-Rodríguez, J.V.; Quintana, P.; Bartolo-Pérez, P. Degradation studies on segmented polyurethanes prepared with HMDI, PCL and different chain extenders. *Acta Biomater.* **2010**, *6*, 2035–2044. [CrossRef] [PubMed]
15. Usman, A.; Zia, K.M.; Zuber, M.; Tabasum, S.; Rehman, S.; Zia, F. Chitin and chitosan based polyurethanes: A review of recent advances and prospective biomedical applications. *Int. J. Biol. Macromol.* **2016**, *86*, 630–645. [CrossRef] [PubMed]
16. Wu, C.-S. Enhanced antibacterial activity, antioxidant and in vitro biocompatibility of modified polycaprolactone-based membranes. *Int. J. Polym. Mater. Polym. Biomater.* **2016**, *65*, 872–880. [CrossRef]
17. Anirudhan, T.S.; Nair, S.S.; Nair, A.S. Fabrication of a bioadhesive transdermal device from chitosan and hyaluronic acid for the controlled release of lidocaine. *Carbohydr. Polym.* **2016**, *152*, 687–698. [CrossRef]
18. Kaur, G.; Mahajan, M.; Bassi, P. Derivatized Polysaccharides: Preparation, characterization, and application as bioadhesive polymer for drug delivery. *Int. J. Polym. Mater.* **2013**, *62*, 475–481. [CrossRef]
19. Wu, H.; Williams, G.R.; Wu, J.; Wu, J.; Niu, S.; Li, H.; Wang, H.; Zhu, L. Regenerated chitin fibers reinforced with bacterial cellulose nanocrystals as suture biomaterials. *Carbohydr. Polym.* **2018**, *180*, 304–313. [CrossRef]
20. Aranguren, M.I.; González, J.F.; Mosiewicki, M.A. Biodegradation of a vegetable oil based polyurethane and wood flour composites. *Polym. Test.* **2012**, *31*, 7–15. [CrossRef]
21. Guelcher, S.; Srinivasan, A.; Dumas, J. Synthesis, mechanical properties, biocompatibility, and biodegradation of polyurethane networks from lysine polyisocyanates. *Biomaterials* **2008**, *29*, 1762–1775. [CrossRef]
22. Chanput, W.; Mes, J.; Vreeburg, R.A.M.; Savelkoul, H.F.J.; Wichers, H.J. Transcription profiles of LPS-stimulated THP-1 monocytes and macrophages: A tool to study inflammation modulating effects of food-derived compounds. *Food Funct.* **2010**, *1*, 254–261. [CrossRef] [PubMed]
23. Oliveira, C.M.; Sakata, R.K.; Issy, A.M.; Gerola, L.R. Citocinas y dolor. *Rev. Bras. Anestesiol.* **2011**, *61*, 137–142. [CrossRef]

24. Small, A.; Lansdown, N.; Al-Baghdadi, M.; Quach, A.; Ferrante, A. Facilitating THP-1 macrophage studies by differentiating and investigating cell functions in polystyrene test tubes. *J. Immunol. Methods* **2018**, *461*, 73–77. [CrossRef] [PubMed]
25. Lund, M.E.; To, J.; O'Brien, B.A.; Donnelly, S. The choice of phorbol 12-myristate 13-acetate differentiation protocol influences the response of THP-1 macrophages to a pro-inflammatory stimulus. *J. Immunol. Methods* **2016**, *430*, 64–70. [CrossRef] [PubMed]
26. Ballerini, P.; Diomede, F.; Petragnani, N.; Cicchitti, S.; Merciaro, I.; Cavalcanti, M.F.X.B.; Trubiani, O. Conditioned medium from relapsing-remitting multiple sclerosis patients reduces the expression and release of inflammatory cytokines induced by LPS-gingivalis in THP-1 and MO3.13 cell lines. *Cytokine* **2017**, *96*, 261–272. [CrossRef] [PubMed]
27. Dreskin, S.C.; Thomas, G.W.; Dale, S.N.; Heasley, L.E. Isoforms of Jun kinase are differentially expressed and activated in human monocyte/macrophage (THP-1) cells. *J. Immunol.* **2001**, *166*, 5646–5653. [CrossRef] [PubMed]
28. Dash, B.C.; Thomas, D.; Monaghan, M.; Carroll, O.; Chen, X.; Woodhouse, K.; Brien, T.O.; Pandit, A. An injectable elastin-based gene delivery platform for dose- dependent modulation of angiogenesis and inflammation for critical limb ischemia. *Biomaterials* **2015**, *65*, 126–139. [CrossRef] [PubMed]
29. Lin, T.H.; Yao, Z.; Sato, T.; Keeney, M.; Li, C.; Pajarinen, J.; Yang, F.; Egashira, K.; Goodman, S.B. Suppression of wear-particle-induced pro-inflammatory cytokine and chemokine production in macrophages via NF-κB decoy oligodeoxynucleotide: A preliminary report. *Acta Biomater.* **2014**, *10*, 3747–3755. [CrossRef] [PubMed]
30. Zhang, C.; Garrison, T.F.; Madbouly, S.A.; Kessler, M.R. Recent advances in vegetable oil-based polymers and their composites. *Prog. Polym. Sci.* **2017**, *71*, 91–143. [CrossRef]
31. Laube, T.; Weisser, J.; Berger, S.; Börner, S.; Bischoff, S.; Schubert, H.; Gajda, M.; Bräuer, R.; Schnabelrauch, M. In situ foamable, degradable polyurethane as biomaterial for soft tissue repair. *Mater. Sci. Eng. C* **2017**, *78*, 163–174. [CrossRef]
32. Temenoff, J.S.; Mikos, A.G. *Biomaterials: The Intersection of Biology and Materials Science*, 8th ed.; Prentice Hall, Inc.: Upper Saddle River, NJ, USA, 2008.
33. Vannozzi, L.; Ricotti, L.; Santaniello, T.; Terencio, T.; Oropesa-Nunez, R.; Canale, C.; Borghi, F.; Menciassi, A.; Lenardi, C.; Gerges, I. 3D porous polyurethanes featured by different mechanical properties: Characterization and interaction with skeletal muscle cells. *J. Mech. Behav. Biomed. Mater.* **2017**, *75*, 147–159. [CrossRef] [PubMed]
34. Chashmejahanbin, M.R.; Daemi, H.; Barikani, M.; Salimi, A. Noteworthy impacts of polyurethane-urea ionomers as the efficient polar coatings on adhesion strength of plasma treated polypropylene. *Appl. Surf. Sci.* **2014**, *317*, 688–695. [CrossRef]
35. Braun, U.; Lorenz, E.; Weimann, C.; Sturm, H.; Karimov, I.; Ettl, J.; Meier, R.; Wohlgemuth, W.A.; Berger, H.; Wildgruber, M. Mechanic and surface properties of central-venous port catheters after removal: A comparison of polyurethane and silicon rubber materials. *J. Mech. Behav. Biomed. Mater.* **2016**, *64*, 281–291. [CrossRef] [PubMed]
36. Jutrzenka Trzebiatowska, P.; Santamaria Echart, A.; Calvo Correas, T.; Eceiza, A.; Datta, J. The changes of crosslink density of polyurethanes synthesised with using recycled component. Chemical structure and mechanical properties investigations. *Prog. Org. Coat.* **2018**, *115*, 41–48. [CrossRef]
37. Thakur, S.; Karak, N. Castor oil-based hyperbranched polyurethanes as advanced surface coating materials. *Prog. Org. Coat.* **2013**, *76*, 157–164. [CrossRef]
38. Gurunathan, T.; Mohanty, S.; Nayak, S.K. Isocyanate terminated castor oil-based polyurethane prepolymer: Synthesis and characterization. *Prog. Org. Coat.* **2015**, *80*, 39–48. [CrossRef]
39. Chen, H.; Yu, X.; Zhou, W.; Peng, S.; Zhao, X. Highly toughened polylactide (PLA) by reactive blending with novel polycaprolactone-based polyurethane (PCLU) blends. *Polym. Test.* **2018**, *70*, 275–280. [CrossRef]
40. Shah, S.A.A.; Imran, M.; Lian, Q.; Shehzad, F.K.; Athir, N.; Zhang, J.; Cheng, J. Curcumin incorporated polyurethane urea elastomers with tunable thermo-mechanical properties. *React. Funct. Polym.* **2018**, *128*, 97–103. [CrossRef]
41. Cakić, S.M.; Ristić, I.S.; Cincović, M.M.; Nikolić, N.C.; Nikolić, L.; Cvetinov, M.J. Synthesis and properties biobased waterborne polyurethanes from glycolysis product of PET waste and poly (caprolactone) diol. *Prog. Org. Coat.* **2017**, *105*, 111–122. [CrossRef]

42. Ferreira, P.; Pereira, R.; Coelho, J.F.J.; Silva, A.F.M.; Gil, M.H. Modification of the biopolymer castor oil with free isocyanate groups to be applied as bioadhesive. *Int. J. Biol. Macromol.* **2007**, *40*, 144–152. [CrossRef] [PubMed]
43. Arévalo, F.; Uscategui, Y.L.; Diaz, L.; Cobo, M.; Valero, M.F. Effect of the incorporation of chitosan on the physico-chemical, mechanical properties and biological activity on a mixture of polycaprolactone and polyurethanes obtained from castor oil. *J. Biomater. Appl.* **2016**, *31*, 708–720. [CrossRef] [PubMed]
44. Corcuera, M.A.; Rueda, L.; Fernandez d'Arlas, B.; Arbelaiz, A.; Marieta, C.; Mondragon, I.; Eceiza, A. Microstructure and properties of polyurethanes derived from castor oil. *Polym. Degrad. Stab.* **2010**, *95*, 2175–2184. [CrossRef]
45. Uscátegui, Y.L.; Arévalo-Alquichire, S.J.; Gómez-Tejedor, J.A.; Vallés-Lluch, A.; Díaz, L.E.; Valero, M.F. Polyurethane-based bioadhesive synthesized from polyols derived from castor oil (*Ricinus communis*) and low concentration of chitosan. *J. Mater. Res.* **2017**, *32*, 3699–3711. [CrossRef]
46. Saikia, A.; Karak, N. Renewable resource based thermostable tough hyperbranched epoxy thermosets as sustainable materials. *Polym. Degrad. Stab.* **2017**, *135*, 8–17. [CrossRef]
47. Thakur, S.; Hu, J. Polyurethane: A Shape Memory Polymer (SMP). In *Aspects of Polyurethanes*; Yilmaz, F., Ed.; InTechOpen: London, UK, 2017; pp. 53–71.
48. Sáenz-Pérez, M.; Lizundia, E.; Laza, J.M.; García-Barrasa, J.; Vilas, J.L.; León, L.M. Methylene diphenyl diisocyanate (MDI) and toluene diisocyanate (TDI) based polyurethanes: Thermal, shape-memory and mechanical behavior. *RSC Adv.* **2016**, *6*, 69094–69102. [CrossRef]
49. Hou, Z.; Zhang, H.; Qu, W.; Xu, Z.; Han, Z. Biomedical segmented polyurethanes based on polyethylene glycol, poly(ε-caprolactone-co-D,L-lactide), and diurethane diisocyanates with uniform hard segment: Synthesis and properties. *Int. J. Polym. Mater. Polym. Biomater.* **2016**, *65*, 947–956. [CrossRef]
50. Mi, H.Y.; Jing, X.; Hagerty, B.S.; Chen, G.; Huang, A.; Turng, L.S. Post-crosslinkable biodegradable thermoplastic polyurethanes: Synthesis, and thermal, mechanical, and degradation properties. *Mater. Des.* **2017**, *127*, 106–114. [CrossRef]
51. Gossart, A.; Battiston, K.G.; Gand, A.; Pauthe, E.; Santerre, J.P. Mono vs multilayer fibronectin coatings on polar/hydrophobic/ionic polyurethanes: Altering surface interactions with human monocytes. *Acta Biomater.* **2018**, *66*, 129–140. [CrossRef]
52. Marques, D.S.; Santos, J.M.C.; Ferreira, P.; Correia, T.R.; Correia, I.J.; Gil, M.H.; Baptista, C.M.S.G. Photocurable bioadhesive based on lactic acid. *Mater. Sci. Eng. C* **2016**, *58*, 601–609. [CrossRef]
53. Sheikh, Z.; Khan, A.S.; Roohpour, N.; Glogauer, M.; Rehman, I.U. Protein adsorption capability on polyurethane and modified-polyurethane membrane for periodontal guided tissue regeneration applications. *Mater. Sci. Eng. C* **2016**, *68*, 267–275. [CrossRef]
54. Conejero-García, Á.; Gimeno, H.R.; Sáez, Y.M.; Vilariño-Feltrer, G.; Ortuño-Lizarán, I.; Vallés-Lluch, A. Correlating synthesis parameters with physicochemical properties of poly(glycerol sebacate). *Eur. Polym. J.* **2017**, *87*, 406–419. [CrossRef]
55. Carriço, C.S.; Fraga, T.; Pasa, V.M.D. Production and characterization of polyurethane foams from a simple mixture of castor oil, crude glycerol and untreated lignin as bio-based polyols. *Eur. Polym. J.* **2016**, *85*, 53–61. [CrossRef]
56. Fuentes, L.E.; Pérez, S.; Martínez, S.I.; García, Á.R. Redes poliméricas interpenetradas de poliuretano a partir de aceite de ricino modificado y poliestireno: Miscibilidad y propiedades mecánicas en función de la composición. *Revisata Ion.* **2011**, *24*, 45–50.
57. Das, B.; Konwar, U.; Mandal, M.; Karak, N. Sunflower oil based biodegradable hyperbranched polyurethane as a thin film material. *Ind. Crops Prod.* **2013**, *44*, 396–404. [CrossRef]
58. Cherng, J.Y.; Hou, T.Y.; Shih, M.F.; Talsma, H.; Hennink, W.E. Polyurethane-based drug delivery systems. *Int. J. Pharm.* **2013**, *450*, 145–162. [CrossRef] [PubMed]
59. Spontón, M.; Casis, N.; Mazo, P.; Raud, B.; Simonetta, A.; Ríos, L.; Estenoz, D. Biodegradation study by Pseudomonas sp. of flexible polyurethane foams derived from castor oil. *Int. Biodeterior. Biodegradation* **2013**, *85*, 85–94. [CrossRef]
60. Gogoi, S.; Barua, S.; Karak, N. Biodegradable and thermostable synthetic hyperbranched poly(urethane-urea)s as advanced surface coating materials. *Prog. Org. Coat.* **2014**, *77*, 1418–1427. [CrossRef]

61. Calvo-Correas, T.; Santamaria-Echart, A.; Saralegi, A.; Martin, L.; Valea, Á.; Corcuera, M.A.; Eceiza, A. Thermally-responsive biopolyurethanes from a biobased diisocyanate. *Eur. Polym. J.* **2015**, *70*, 173–185. [CrossRef]
62. Reddy, T.T.; Kano, A.; Maruyama, A.; Takahara, A. Synthesis, characterization and drug release of biocompatible/biodegradable non-toxic poly(urethane urea)s based on poly(epsilon-caprolactone)s and lysine-based diisocyanate. *J. Biomater. Sci. Polym. Ed.* **2010**, *21*, 1483–1502. [CrossRef] [PubMed]
63. Coakley, D.N.; Shaikh, F.M.; O'Sullivan, K.; Kavanagh, E.G.; Grace, P.A.; McGloughlin, T.M. In vitro evaluation of acellular porcine urinary bladder extracellular matrix—A potential scaffold in tissue engineered skin. *Wound Med.* **2015**, *10–11*, 9–16. [CrossRef]
64. Shahrousvand, M.; Sadeghi, G.M.M.; Shahrousvand, E.; Ghollasi, M.; Salimi, A. Superficial physicochemical properties of polyurethane biomaterials as osteogenic regulators in human mesenchymal stem cells fates. *Colloids Surf. B Biointerfaces* **2017**, *156*, 292–304. [CrossRef] [PubMed]
65. Aranaz, I.; Mengíbar, M.; Harris, R.; Paños, I.; Miralles, B.; Acosta, N.; Galed, G.; Heras, Á. Functional characterization of chitin and chitosan. *Curr. Chem. Biol.* **2009**, *3*, 203–230.
66. Ortuno-Lizarán, I.; Vilarino-Feltrer, G.; Martinez-Ramos, C.; Pradas, M.M.; Vallés-Lluch, A. Influence of synthesis parameters on hyaluronic acid hydrogels intended as nerve conduits. *Biofabrication* **2016**, *8*, 1–12. [CrossRef] [PubMed]
67. Jing, X.; Mi, H.Y.; Huang, H.X.; Turng, L.S. Shape memory thermoplastic polyurethane (TPU)/poly(ε-caprolactone) (PCL) blends as self-knotting sutures. *J. Mech. Behav. Biomed. Mater.* **2016**, *64*, 94–103. [CrossRef] [PubMed]
68. Starr, T.; Bauler, T.J.; Malik-Kale, P.; Steele-Mortimer, O. The phorbol 12-myristate-13-acetate differentiation protocol is critical to the interaction of THP-1 macrophages with Salmonella Typhimurium. *PLoS ONE* **2018**, *13*, 1–13. [CrossRef] [PubMed]
69. Park, E.K.; Jung, H.S.; Yang, H.I.; Yoo, M.C.; Kim, C.; Kim, K.S. Optimized THP-1 differentiation is required for the detection of responses to weak stimuli. *Inflamm. Res.* **2007**, *56*, 45–50. [CrossRef] [PubMed]
70. Gómez Estrada, H.A.; González Ruiz, K.N.; Medina, J.D. Actividad antiinflamatoria de productos naturales. *Bol. Latinoam. Caribe Plantas Med. Aromat.* **2011**, *10*, 182–217.
71. González, R.; Zamora, Z.; Alonso, Y. Citocinas anti-inflamatorias y sus acciones y efectos en la sepsis y el choque séptico. *REDVET Rev. Electrónica Vet.* **2009**, *10*, 1–11.
72. Valero, M.F.; Ortegón, Y. Polyurethane elastomers-based modified castor oil and poly(e-caprolactone) for surface-coating applications: Synthesis, characterization, and in vitro degradation. *J. Elastomers Plast.* **2015**, *47*, 360–369. [CrossRef]
73. Valero, M.F.; Pulido, J.E.; Ramírez, Á.; Cheng, Z. Determinación de la densidad de entrecruzamiento de poliuretanos obtenidos a partir de aceite de ricino modificado por transesterificación. *Polímeros* **2009**, *19*, 14–21. [CrossRef]
74. Valero, M.F. Poliuretanos elastoméricos obtenidos a partir de aceite de ricino y almidón de yuca original y modificado con anhidrido propiónico: Síntesis, propiedades fisicoquímicas y fisicomecánicas. *Quim. Nov.* **2010**, *33*, 850–854. [CrossRef]
75. Simón-Allué, R.; Pérez-López, P.; Sotomayor, S.; Peña, E.; Pascual, G.; Bellón, J.M.; Calvo, B. Short- and long-term biomechanical and morphological study of new suture types in abdominal wall closure. *J. Mech. Behav. Biomed. Mater.* **2014**, *37*, 1–11. [CrossRef] [PubMed]
76. Yoshida, K.; Jiang, H.; Kim, M.J.; Vink, J.; Cremers, S.; Paik, D.; Wapner, R.; Mahendroo, M.; Myers, K. Quantitative evaluation of collagen crosslinks and corresponding tensile mechanical properties in mouse cervical tissue during normal pregnancy. *PLoS ONE* **2014**, *9*. [CrossRef] [PubMed]
77. Mekewi, M.A.; Ramadan, A.M.; ElDarse, F.M.; Abdel Rehim, M.H.; Mosa, N.A.; Ibrahim, M.A. Preparation and characterization of polyurethane plasticizer for flexible packaging applications: Natural oils affirmed access. *Egypt. J. Pet.* **2017**, *26*, 9–15. [CrossRef]
78. Hormaiztegui, M.E.V.; Aranguren, M.I.; Mucci, V.L. Synthesis and characterization of a waterborne polyurethane made from castor oil and tartaric acid. *Eur. Polym. J.* **2018**, *102*, 151–160. [CrossRef]
79. Kanmani, P.; Rhim, J.-W. Physical, mechanical and antimicrobial properties of gelatin based active nanocomposite films containing AgNPs and nanoclay. *Food Hydrocoll.* **2014**, *35*, 644–652. [CrossRef]
80. Członka, S.; Bertino, M.F.; Strzelec, K. Rigid polyurethane foams reinforced with industrial potato protein. *Polym. Test.* **2018**, *68*, 135–145. [CrossRef]

81. Basak, P.; Adhikari, B. Effect of the solubility of antibiotics on their release from degradable polyurethane. *Mater. Sci. Eng. C* **2012**, *32*, 2316–2322. [CrossRef]
82. Wang, Y.; Yu, Y.; Zhang, L.; Qin, P.; Wang, P. One-step surface modification of polyurethane using affinity binding peptides for enhanced fouling resistance. *J. Biomater. Sci. Polym. Ed.* **2015**, *26*, 459–467. [CrossRef]
83. Rezvanain, M.; Ahmad, N.; Mohd Amin, M.C.I.; Ng, S.F. Optimization, characterization, and in vitro assessment of alginate-pectin ionic cross-linked hydrogel film for wound dressing applications. *Int. J. Biol. Macromol.* **2017**, *97*, 131–140. [CrossRef]
84. Vilariño Feltrer, G.; Martínez Ramos, C.; Monleon De La Fuente, A.; Vallés Lluch, A.; Moratal Pérez, D.; Barcia Albacar, J.; Monleón Pradas, M. Schwann-cell cylinders grown inside hyaluronic-acid tubular scaffolds with gradient porosity. *Acta Biomater.* **2016**, *30*, 199–211. [CrossRef] [PubMed]

Sample Availability: Samples of the compounds are not available from the authors.

molecules

MDPI

Article

Immobilizing Polyether Imidazole Ionic Liquids on ZSM-5 Zeolite for the Catalytic Synthesis of Propylene Carbonate from Carbon Dioxide

Liying Guo [1,*], Xianchao Jin [1], Xin Wang [2], Longzhu Yin [1,2], Yirong Wang [1] and Ying-Wei Yang [2,*]

[1] School of Petrochemical Engineering, Shenyang University of Technology, Liaoyang 111003, China; xcjin1993@163.com (X.J.); yinlz18@mails.jlu.edu.cn (L.Y.); yrwang2000@163.com (Y.W.)

[2] State Key Laboratory of Inorganic Synthesis and Preparative Chemistry, International Joint Research Laboratory of Nano-Micro Architecture Chemistry (NMAC), College of Chemistry, Jilin University, 2699 Qianjin Street, Changchun 130012, China; xinwangjlu@163.com

* Correspondence: lyguo1981@163.com (L.G.); ywyang@jlu.edu.cn (Y.-W.Y.); Tel.: +86-151-4099-8399 (L.G.); +86-431-8516-8468 (Y.-W.Y.)

Received: 21 September 2018; Accepted: 20 October 2018; Published: 21 October 2018

Abstract: Traditional ionic liquids (ILs) catalysts suffer from the difficulty of product purification and can only be used in homogeneous catalytic systems. In this work, by reacting ILs with co-catalyst ($ZnBr_2$), we successfully converted three polyether imidazole ionic liquids (PIILs), i.e., HO-[Poly-epichlorohydrin-methimidazole]Cl (HO-[PECH-MIM]Cl), HOOC-[Poly-epichlorohydrin-methimidazole]Cl (HOOC-[PECH-MIM]Cl), and H_2N-[Poly-epichlorohydrin-methimidazole]Cl (H_2N-[PECH-MIM]Cl), to three composite PIIL materials, which were further immobilized on ZSM-5 zeolite by chemical bonding to result in three immobilized catalysts, namely ZSM-5-HO-[PECH-MIM]Cl/[$ZnBr_2$], ZSM-5-HOOC-[PECH-MIM]Cl/[$ZnBr_2$], and ZSM-5-H_2N-[PECH-MIM]Cl/[$ZnBr_2$]. Their structures, thermal stabilities, and morphologies were fully characterized by Fourier-transform infrared spectroscopy (FT-IR), X-ray diffractometry (XRD), thermogravimetric analysis (TGA), and scanning electron microscopy (SEM). The amount of composite PIIL immobilized on ZSM-5 was determined by elemental analysis. Catalytic performance of the immobilized catalysts was evaluated through the catalytic synthesis of propylene carbonate (PC) from CO_2 and propylene oxide (PO). Influences of reaction temperature, time, and pressure on catalytic performance were investigated through the orthogonal test, and the effect of catalyst circulation was also studied. Under an optimal reaction condition (130 °C, 2.5 MPa, 0.75 h), the composite catalyst, ZSM-5-HOOC- [PECH-MIM]Cl/[$ZnBr_2$], exhibited the best catalytic activity with a conversion rate of 98.3% and selectivity of 97.4%. Significantly, the immobilized catalyst could still maintain high heterogeneous catalytic activity even after being reused for eight cycles.

Keywords: catalyst; CO_2; heterogeneous catalysis; molecular sieve; polyether imidazole ionic liquid

1. Introduction

Carbon dioxide (CO_2) is a rich carbon resource in nature. Over the years, experts and scholars around the world have been working on the catalytic conversion and utilization of CO_2 [1–5]. Although research results have shown that the chemically speaking CO_2 is extremely inactive, careful selection of proper catalysts could make CO_2 become a low-cost and widely used resource. Therefore, the development of efficient catalysts is the key to achieve chemical fixation and conversion of CO_2 under mild conditions.

Ionic liquids (ILs), as environmentally friendly chemical materials, have been widely used in various fields including organic synthesis, biomass dissolution, catalysis, and composite materials

preparation due to their unique properties [6–10]. In recent years, studies on the conversion of CO_2 to cyclic carbonate using ILs as catalysts have been widely reported [11–13], demonstrating that the catalytic performance of ILs as a single component in catalysts is unfavorable, and the addition of Lewis acids or other co-catalysts in the catalysts is necessary to achieve better catalytic activity. However, these studies are still associated with several disadvantages including limitation of the intermittent tank reaction system, catalyst separation, and product purification [14]. These defects make ILs difficult to be applied in industrial processes. To solve these problems, a structural design concept based on ILs-immobilized catalysts has gained considerable attention. Yin and coworkers [15] immobilized 3-(2-hydroxyethyl)-1-propylimidazolium bromide ILs on SBA-15, Al-SBA-15, and SiO_2, but the yield declined obviously after three cycles of catalysis. Zhang's group [16] and Xiong's group [17] immobilized ILs on chitosan and coconut shell activated carbon supporter, respectively. However, gradual loss of active components in the immobilized catalysts also occurred in the catalytic process. Therefore the utilization of chemical bonding between ILs and supporters is key to realize the resource transformation of CO_2. Compared with other catalytic systems, such as metal [18], metal complexes [19], and imidazolium salt [20], ILs with the advantages of low energy consumption, high recycling efficiency, and less corrosion to equipment have become a hotspot [16]. Polyether polymer catalysts contain macromolecular chains that can form a synergistic and base barrier effect to enhance catalytic activity [21].

In this work, three polyether imidazole ionic liquids (PIILs) were selected to react with co-catalyst ($ZnBr_2$) to obtain three composite PIILs, followed by further immobilization on ZSM-5 zeolite to result in three immobilized PIILs catalysts (Figure 1 and Supplementary Materials). The chemical bonding between the composite PIILs and ZSM-5 was determined and the phase transitions of PIILs were also achieved. The immobilization is stable, so that the prepared catalyst can still maintain high catalytic activity after eight cycles.

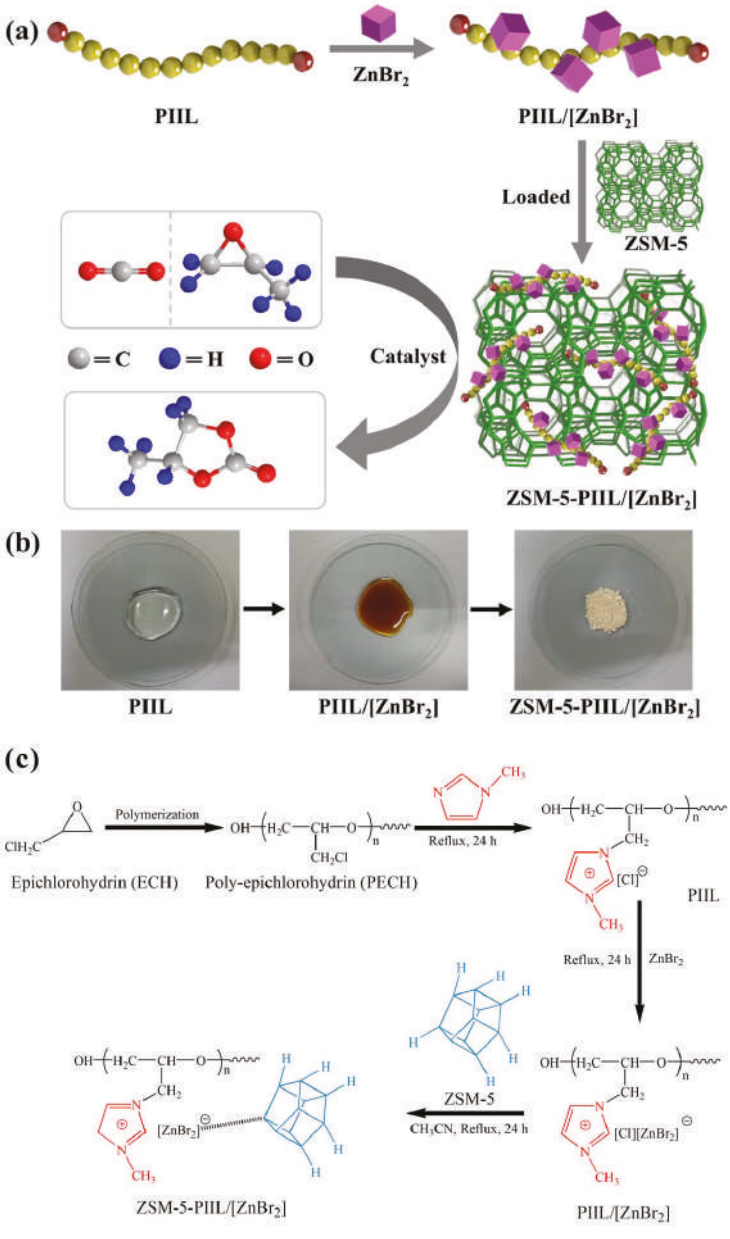

Figure 1. (**a**) The diagram for the preparation of immobilized catalysts for the synthesis of propylene carbonates from carbon dioxide; (**b**) the photos of the synthesized materials showing the color change and phase transition; and (**c**) the chemical structure of the catalyst and its synthesis process, taking ZSM-5-HO-[PECH-MIM]Cl/[$ZnBr_2$] as an example.

2. Results and Discussion

2.1. Fourier-Transform Infrared Spectroscopy (FT-IR)

FT-IR studies on zeolite ZSM-5 and its immobilized catalysts were carried out (Figure 2). As in pattern (a), the peak at 1066 cm^{-1} corresponds to the Si–O characteristic peak of ZSM-5 [22]. Patterns (b, c, d) contain all the characteristic absorption peaks of pattern (a), and meanwhile, the characteristic peaks at ca. 1655 cm^{-1} and 626 cm^{-1}, which are associated with the stretching frequency of the imidazole ring, were also found. The peaks at ca. 1275 cm^{-1} in patterns (b, c, d) could be assigned to the enhanced stretching vibration of C–O–C. The strong absorption peak at 3386 cm^{-1} of pattern (b) corresponds to the stretching vibration of the hydroxyl group. When polyether imidazole molecular chains are linked to ZSM-5, hydrogen chloride is released [15,23,24]. However, a small portion of HOOC-[PECH-MIM]Cl/[$ZnBr_2$] still exists as deduced from the peak at 1720 cm^{-1} with low intensity in pattern (c), which is due to the physical adsorption on the surface of ZSM-5. In the immobilization process of H_2N-[PECH-MIM]Cl/[$ZnBr_2$], there are hydrogen atoms on the surface and inside of the molecular sieve [25]. A part of hydrogen on ZSM-5 reacted with the chloride ions of H_2N-[PECH-MIM]Cl/[$ZnBr_2$] thus releasing hydrogen chloride, and the other part of the hydrogen easily forms a hydrogen bond with oxygen in the polyether chain [15,23]. The hydrogen bonds caused the appearance of a wide and strong hydroxyl peak at 3396 cm^{-1} in pattern (d), thus the low amino peak was covered. The above results indicated the successful anchorage of composite PIILs on ZSM-5.

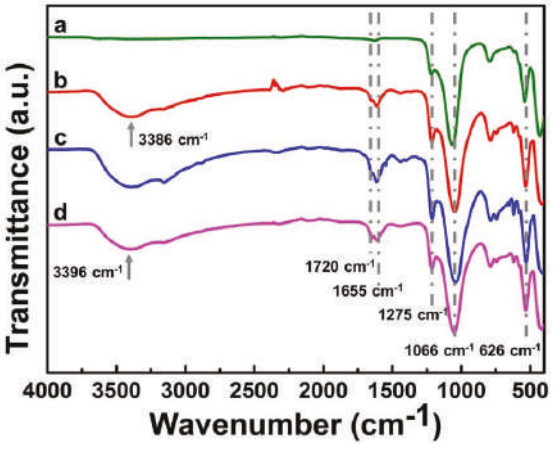

Figure 2. FT-IR spectra of zeolite ZSM-5 and its immobilized catalysts: (**a**) ZSM-5; (**b**) ZSM-5-HO-[PECH-MIM]Cl/[$ZnBr_2$]; (**c**) ZSM-5-HOOC-[PECH-MIM]Cl/[$ZnBr_2$]; and (**d**) ZSM-5-H_2N-[PECH-MIM]Cl/[$ZnBr_2$].

2.2. Scanning Electron Microscopy (SEM)

SEM images of ZSM-5 and its immobilized catalysts are provided in Figure 3. After the immobilization, the surfaces of the catalysts (b, c, d) were covered with a white translucent substance, and the surfaces became smoother. The particles became larger in size and their profiles became clearer, indicating that a part of the PIILs was immobilized on the surface of ZSM-5. SEM results further suggest the successful immobilization of PIILs catalysts on ZSM-5 and the solid state of the obtained immobilized catalysts. See Figure 1b for ordinary photos of the phase transition.

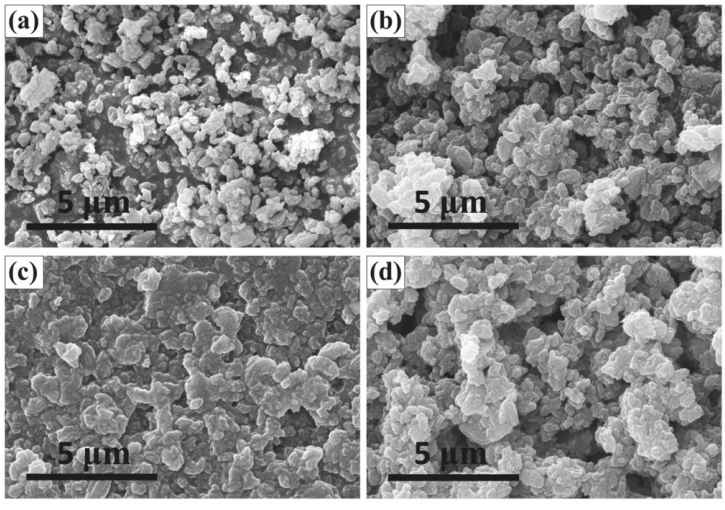

Figure 3. SEM images of zeolite ZSM-5 and its immobilized catalysts: (**a**) ZSM-5; (**b**) ZSM-5-HO-[PECH-MIM]Cl/[$ZnBr_2$]; (**c**) ZSM-5-HOOC-[PECH-MIM]Cl/[$ZnBr_2$]; and (**d**) SM-5-H_2N-[PECH-MIM]Cl/[$ZnBr_2$].

2.3. X-Ray Diffractometry (XRD)

The XRD patterns of ZSM-5 and its immobilized catalysts are shown in Figure 4. In pattern (a), the peaks of high intensity at 23.1°, 23.9°, and 24.4° are the characteristic diffraction peaks of ZSM-5, indicating good crystallinity of our synthesized ZSM-5. Compared with pattern (a), patterns (b, c, d) exhibit all the diffraction peaks of ZSM-5, and the shape and intensity of the diffraction peaks have negligible changes, indicating that the prepared catalysts maintained the good crystallinity of ZSM-5 after immobilization of the three composite PIILs onto ZSM-5.

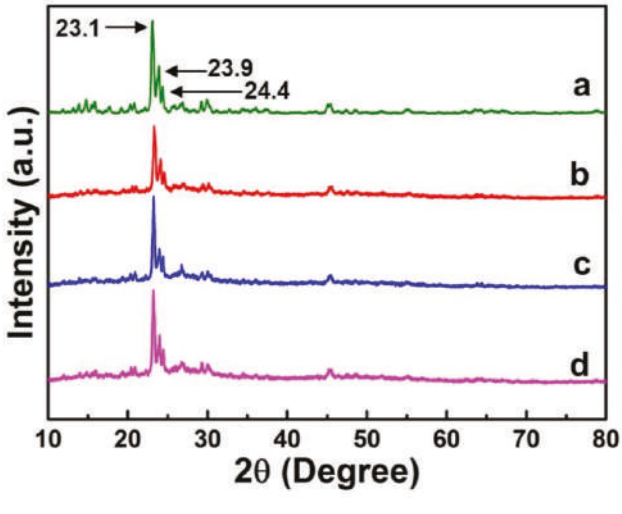

Figure 4. XRD patterns of zeolite ZSM-5 and its immobilized catalysts: (**a**) ZSM-5; (**b**) ZSM-5-HO-[PECH-MIM]Cl/[$ZnBr_2$]; (**c**) ZSM-5-HOOC-[PECH-MIM]Cl/[$ZnBr_2$]; and (**d**) ZSM-5-H_2N-[PECH-MIM]Cl/[$ZnBr_2$].

2.4. Thermogravimetry (TG) and Derivative Thermogravimetry (DTG)

Molecular sieve ZSM-5 and its immobilized catalysts were further characterized by thermogravimetric analyzer (TGA) to explore their thermal stability with a heating rate of 10 °C/min. TG and DTG results are shown in Figure 5. As seen in Figure 5a, ZSM-5 and the three catalysts have slight weight loss before 150 °C, which is caused by the evaporation of water. As the temperature rises, the curve of ZSM-5 in Figure 5b approximates to a straight line, where the weight loss rate does not change and ZSM-5 does not break down. From Figure 5a, the three immobilized catalysts were broken down in two steps. The first loss (230–550 °C) is attributed to the loss of grafted composite PIILs [26–28], and the second slight loss (550–700 °C) is due to the decomposition of some molecular sieve [29–31]. The three catalysts with functional groups of –OH, –COOH, and $–NH_2$ have maximum decomposition rate at 490 °C, 460 °C, and 475 °C, respectively, and their residual rates are maintained above 50%. The decomposition speed and thermal stability of the three immobilized catalysts with different functional groups are different, and among them, ZSM-5-HOOC-[PECH-MIM]Cl/[$ZnBr_2$] possesses the fastest decomposition and the highest residual rate. The thermal stability of the other two immobilized catalysts shows little difference, and the weight loss processes are similar. TG and DTG results suggest that the immobilized catalysts have good thermal stability, and that the immobilized catalysts would not decompose under 230 °C.

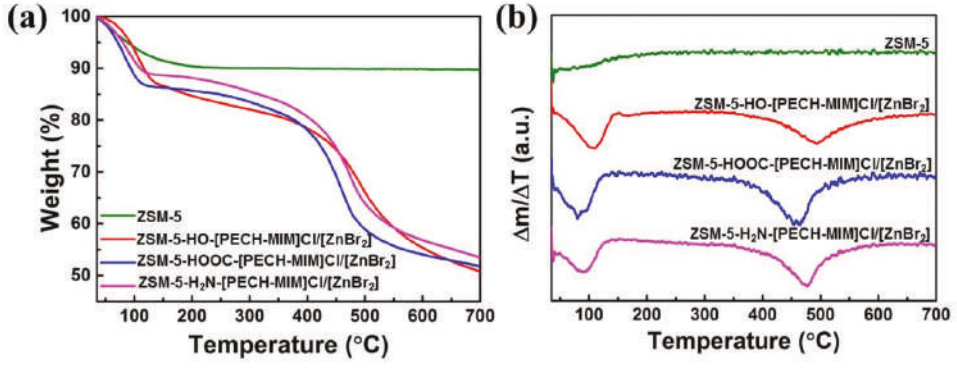

Figure 5. (**a**) TG and (**b**) DTG of zeolite ZSM-5 and its immobilized catalysts: ZSM-5-HO-[PECH-MIM]Cl/[$ZnBr_2$]; ZSM-5-HOOC-[PECH-MIM]Cl/[$ZnBr_2$]; and ZSM-5-H_2N-[PECH-MIM]Cl/[$ZnBr_2$].

2.5. Effects of Different Catalysts on the Catalytic Performance

The catalytic performance of the above mentioned three PIILs, three composite PIILs, ZSM-5, and three immobilized catalysts for the synthesis of propylene carbonate (PC) from CO_2 and propylene oxide (PO) was investigated (Table 1). Three PIILs showed catalytic activity (entries 1–3), among them, HOOC-[PECH-MIM]Cl has the best catalytic performance because the terminal carboxyl group has acidity and can also act as donor of a hydrogen bond, which could add a synergistic effect with the anion. The synergistic effect contributes to the activation and ring opening of PO and improves the catalytic activity [15,24]. Zinc bromide has a catalytic effect when used alone as a co-catalyst (entry 4). The catalytic performance of PIILs were further improved after addition of zinc bromide (entries 5–7) [26,27], where the conversion rate reached 100%, and the selectivity and yield both reached above 97%. The improvement of the catalytic performance can be attributed to the addition of zinc bromide that increased the amount of bromide ions. The Br^- attacked the β-carbon atom of PO, and therefore increased the conversion rate. The polyether macromolecular chain has a basic isolation effect and an infinite dilution effect, which could not only inhibit the formation of by-products but also improve the selectivity [32,33]. The catalytic activity of ZSM-5

is poor (entry 8). The excellent catalytic performance of the three immobilized catalysts is very promising, although there is no big difference between them (entries 9–11). This is because the structures of the immobilized catalysts were similar after three composite PIILs were immobilized on the molecular sieve by chemical bonding. The chemical bonding occurs through the covalent bond formation by condensation between the chlorine of PIILs and the hydrogen on ZSM-5 [25]. All of the three immobilized catalysts have polyether macromolecular chains as the main chains and imidazole rings as the branched chains. ZSM-5-HOOC-[PECH-MIM]Cl/[$ZnBr_2$] has better catalytic activity than the other two immobilized catalysts, because there is still a small amount of HOOC-[PECH-MIM]Cl/[$ZnBr_2$] physically adsorbed on the surface of ZSM-5. It still has acidity, which is good for ring opening [15,24], consistent with the FT-IR study. The catalytic activity of the immobilized catalysts is slightly lower than that of the composite PIILs since the amount of composite PIILs is reduced after immobilization. However, the conversion rate and selectivity both reached 95%. Experimental results showed an excellent catalytic performance of the three immobilized catalysts, among which ZSM-5-HOOC-[PECH-MIM]Cl/[$ZnBr_2$] represents the best.

Table 1. Effects of different catalysts on catalytic performance [1].

	Catalyst	Conversion Rate (%)	Selectivity (%)	Yield (%)	Purity (%)
1	HO-[PECH-MIM]Cl	90.4	96.4	87.1	99.1
2	HOOC-[PECH-MIM]Cl	95.1	96.8	92.1	99.4
3	H_2N-[PECH-MIM]Cl	93.3	95.3	88.9	98.9
4	$ZnBr_2$	40.8	68.2	27.8	95.2
5	HO-[PECH-MIM]Cl/[$ZnBr_2$]	100	97.1	97.1	99.5
6	HOOC-[PECH-MIM]Cl/[$ZnBr_2$]	100	98.9	98.9	99.7
7	H_2N-[PECH-MIM]Cl/[$ZnBr_2$]	100	97.6	97.6	99.4
8	ZSM-5	9.4	41.2	3.87	96.4
9	ZSM-5-HO-[PECH-MIM]Cl/[$ZnBr_2$]	95.8	96.5	92.4	98.3
10	ZSM-5-HOOC-[PECH-MIM]Cl/[$ZnBr_2$]	96.3	96.8	93.2	99.2
11	ZSM-5-H_2N-[PECH-MIM]Cl/[$ZnBr_2$]	96.1	96.4	92.6	99.0

[1] Reaction condition: catalyst, 2.5 wt%, temperature, 120 °C; pressure, 2.5 MPa; time, 1 h.

2.6. Effects of Reaction Conditions on the Catalytic Performance

The effect of reaction conditions on the catalytic performance of ZSM-5-HOOC-[PECH-MIM]Cl/[$ZnBr_2$] was studied. To define the optimal reaction conditions, the orthogonal test of L9 (3^4) was used to investigate the effects of reaction pressure, temperature, and time on the conversion rate and selectivity (Table 2). K_{nj} (n = 1,2,3) indicated the sums of three conversion rates or selectivity when the values of the corresponding factors were the same for each time. R was the range. The results show that reaction pressure has the greatest effect on conversion rate and selectivity, followed by reaction temperature and time. When the reaction pressure is 2.5 MPa, the temperature is 130 °C, and the time is 0.75 h, the immobilized catalyst exhibited the best catalytic performance with a conversion rate of 98.3% and a selectivity of 97.4%. When the reaction pressure is increased, more CO_2 can be dissolved in PO, therefore, the conversion rate and selectivity can be increased. If the pressure was too high or the reaction time prolonged, the selectivity declined, which is consistent with the previous literature reports [16,34–36]. Excessive temperature could cause a decrease in selectivity due to the exothermic nature of the cycloaddition reaction that could lead to the production of some byproduct such as from the polymerization of PC [15,37].

Table 2. Orthogonal test-effects of reaction conditions on catalytic performance.

	Factor			Conversion Rate (%)	Selectivity (%)
	Pressure (MPa)	Temperature (°C)	Time (h)		
1	2.0	110	0.75	82.3	92.4
2	2.0	120	1.0	90.6	90.1
3	2.0	130	1.25	95.4	85.2
4	2.5	110	1.0	95.9	98.2
5	2.5	120	1.25	97.6	97.5
6	2.5	130	0.75	98.3	97.4
7	3.0	110	1.25	92.1	94.6
8	3.0	120	0.75	97.9	90.3
9	3.0	130	1.0	99.5	84.2
K_{1j}	268.3/267.7	270.3/285.2	278.5/280.1	—	—
K_{2j}	291.8/293.1	286.1/277.9	286.0/272.5	—	—
K_{3j}	289.5/269.1	293.2/266.8	285.1/277.3	—	—
R	23.5/25.4	22.9/18.4	7.5/7.6	—	—

2.7. Effect of the Catalyst Circulation on the Catalytic Performance

The effect of catalyst circulation on catalytic performance was investigated under an optimized reaction condition (2.5 MPa, 130 °C, 0.75 h), with ZSM-5-HOOC-[PECH-MIM]Cl/[$ZnBr_2$] as the catalyst. As in Figure 6, the experimental results suggest an excellent reusability of the immobilized catalyst. The conversion rate and yield are 98.3% and 97.4%, respectively, in the first use. In the next two cycles, the catalytic performance decreased. Elemental analysis was used to measure the fresh catalyst, three and eight cycle catalysts, respectively (Table 3). The results showed that the grafted rate of composite PIILs catalyst decreased over 1 to 3 cycles, and there was negligible change after three cycles. The reason is that a small amount of physically adsorbed PIILs is easily falls off from ZSM-5 zeolite during the 1st to 3rd cycles. From the 4th cycle, the grafted rate of PIILs, conversion rate and yield showed small changes, which indicate that the chemical bonding between the composite PIILs and the zeolite is steady, and therefore the catalytic performance of the immobilized catalyst remains stable. The conversion rate is 86.7% and the yield is 77.9% after the 8th cycle. The results in Figure 6 are consistent with those in Table 3. The amount of the grafted PIIL is 1.121 mmol/g, the chemical graft is about 0.803 mmol/g, and physical graft is about 0.318 mmol/g.

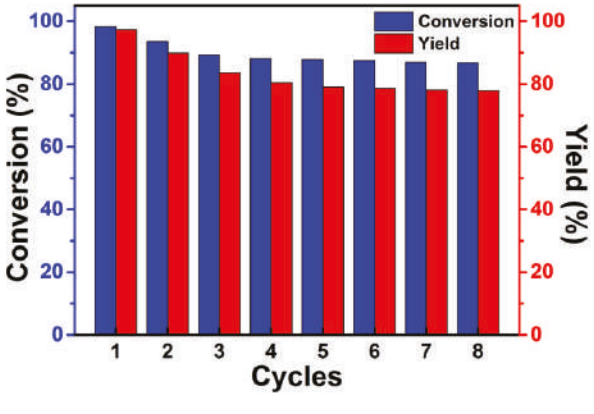

Figure 6. Effect of the catalyst circulation on catalytic performance.

Table 3. Elemental analysis results of the catalysts.

Catalyst	N (wt%)	C (wt%)	H (wt%)	PIILgrafted (mmol/g)	Standard Error (mmol/g)
ZSM-5-HOOC-[PECH-MIM]Cl/[$ZnBr_2$] [1]	3.149	7.744	2.000	1.121	1.780×10^{-3}
ZSM-5-HOOC-[PECH-MIM]Cl/[$ZnBr_2$] [2]	2.275	7.131	1.694	0.810	1.472×10^{-3}
ZSM-5-HOOC-[PECH-MIM]Cl/[$ZnBr_2$] [3]	2.256	7.059	1.681	0.803	1.633×10^{-3}

[1] Fresh catalyst; [2] Catalyst reused 2 times; [3] Catalyst reused 8 times.

3. Materials and Methods

3.1. Reagents and Instruments

Three PIILs, i.e., HO-[PECH-MIM]Cl, HOOC-[PECH-MIM]Cl, and H_2N-[PECH-MIM]Cl, were prepared according to our published procedures [26–28]. Zinc bromide was purchased from Tianjin Guangfu chemical reagents factory (Tianjin, China). Acetonitrile was received from Tianjin Guangfu Fine Chemical Research Institute and used without further purification. PO was obtained from Jiangsu Yonghua fine chemicals Research Company (Suzhou, China). ZSM-5 zeolite, CO_2, and nitrogen were supplied by Liaoyang Petrochemical Industries Company (Liaoning, China).

Instruments used in this study included a MAGNA-IR750 Fourier Transform Infrared Spectrometer (FT-IR, Thermo Nicolet Corporation, Markham, ON, Canada); TM3000 Scanning Electron Microscope (SEM, Keyence, Osaka, Japan); D/max-2400 Automatic X-ray Diffractometer (XRD, RKC Instrument Inc., Tokyo, Japan); TGA4000 Thermogravimetric Analyzer (TGA, PerkinElmer, Waltham, MA, USA); PerkinElmer-2400 Element Analyzer (EA, PerkinElmer, Waltham, MA, USA); PARR4523 Catalytic Device (PARR, Moline, IL, USA); 1790F Gas Chromatograph (GC) (Agilent Technologies, Inc., Santa Clara, CA, USA); D08-8C Carbon Dioxide Flowmeter (Beijing Sevenstar Electronics Co., Ltd., Beijing, China); DF-101S Magnetic Stirrer (Gongyi Yuhua Instrument Co., Ltd., Gongyi, China); SFX-2L Rotary Evaporator (Taiwan Xinyue Instrument and Meter Co., Ltd., Xiamen, China); DZF-6050 Vacuum Drying box (Gongyi Yuhua Instrument Co., Ltd., Gongyi, China); 2-XZ-4 rotary vane vacuum pump (Wenling City Yangan Electromechanical Co., Ltd., Wenling, China).

3.2. Preparation of Immobilized Catalysts

Three PIILs, i.e., HO-[PECH-MIM]Cl, HOOC-[PECH-MIM]Cl, and H_2N-[PECH-MIM]Cl, were prepared according to our published procedures [26–28]. Briefly, epichlorohydrin (ECH) was polymerized to form poly-epichlorohydrin (PECH) possessing –OH groups, then chloroacetic acid and ammonia were used to react with PECH to obtain products with –COOH and $–NH_2$ groups, respectively. Then three types of PECH samples with –OH, –COOH, and $–NH_2$ were reacted with imidazole to obtain three PIILs. Next, a given amount of $ZnBr_2$ was added into the three PIILs, respectively, and the resulting mixtures were heated at reflux under stirring for 24 h. As the reaction proceeded, the mixtures became more viscous with a dark color change. When the reactions were complete, three reddish brown liquids were obtained, namely three composite PIILs, i.e., HO-[PECH-MIM]Cl/[$ZnBr_2$], HOOC-[PECH-MIM]Cl/[$ZnBr_2$], and H_2N-[PECH-MIM]Cl/[$ZnBr_2$]. Then, the composite PIILs were added, respectively, to the suspension of ZSM-5 in acetonitrile, and the resulting mixtures were stirred at 70 °C for 24–36 h to obtain milk-white liquids. Acetonitrile was removed from the obtained liquids by rotary evaporation at 65 °C. The afforded three samples of white powder were then dried in vacuum at 65 °C for 24 h under 0.08 MPa to remove residual acetonitrile, leading to the final products of immobilized PIILs catalysts, i.e., ZSM-5-HO-[PECH-MIM]Cl/[$ZnBr_2$], ZSM-5-HOOC-[PECH-MIM]Cl/[$ZnBr_2$] and, ZSM-5-H_2N-[PECH-MIM]Cl/[$ZnBr_2$] (Figure 1c).

3.3. Typical Procedure for the Synthesis of PC from PO and CO_2

The immobilized catalyst (2.5% mass fraction of PO) was added in the stainless-steel autoclave. After the atmosphere was replaced by nitrogen, PO and CO_2 were filled into the autoclave. When the

flow of CO_2 was 0, the reaction was complete. The crude product was purified to obtain the refined PC, and its purity was determined by gas chromatography. Specific steps refer to our reported papers [26,27].

4. Conclusions

Three immobilized PIILs catalysts were newly developed, and their catalytic performance studied. The results showed that the immobilization of composite PIILs on ZSM-5 was mainly based on chemical bonding, while a small amount of physical adsorption also existed. ZSM-5-HOOC-[PECH-MIM]Cl/[$ZnBr_2$] exhibited the highest catalytic activity in the synthesis of PC under the optimized condition: reaction temperature of 130 °C, pressure of 2.5 MPa, and time of 0.75 h, where the conversion rate reached 98.3% and the selectivity 97.4%. Significantly, the catalyst still maintained a good catalytic activity after eight cycles. We envisage that the newly prepared catalysts can solve the problems of traditional ILs catalysts including the difficulty in production purification and short service life in the catalytic process. We believe that our research can provide industrial continuous conversion of CO_2 in a packed bed reactor with acceptable performance.

Supplementary Materials: The supplementary materials are available online.

Author Contributions: Conceptualization, L.G.; Investigation, L.G., X.J., X.W., L.Y., and Y.W.; Supervision, L.G. and Y.-W.Y.; Writing—original draft, L.G. and X.J.; Writing—review and editing, L.G. and Y.-W.Y.

Funding: This work was supported by the National Natural Science Foundation of China (21706163), Department of Education of Liaoning Province (LQGD2017020), and Jilin Province-University Cooperative Construction Project—Special Funds for New Materials (SXGJSF2017-3).

Conflicts of Interest: The authors declare no conflict of interest. The funding sponsors had no role in the design of the study; in the collection, analyses, or interpretation of data; in the writing of the manuscript, and in the decision to publish the results.

References

1. Rulev, Y.A.; Gugkaeva, Z.; Maleev, V.I.; North, M.; Belokon, Y.N. Robust bifunctional aluminium-salen catalysts for the preparation of cyclic carbonates from carbon dioxide and epoxides. *Beilstein J. Org. Chem.* **2015**, *11*, 1614–1623. [CrossRef] [PubMed]
2. Kember, M.R.; Buchard, A.; Williams, C.K. Catalysts for CO_2/epoxide copolymerisation. *Chem. Commun.* **2011**, *47*, 141–163. [CrossRef] [PubMed]
3. Yang, L.H.; Wang, H.M. Recent advances in carbon dioxide capture, fixation, and activation by using N-heterocyclic carbenes. *ChemSusChem* **2014**, *7*, 962–998. [CrossRef] [PubMed]
4. Chen, S.M.; Liu, Y.; Guo, J.P.; Li, P.Z.; Huo, Z.Y.; Ma, P.T.; Niu, J.Y.; Wang, J.P. A multi-component polyoxometalate and its catalytic performance for CO_2 cycloaddition reactions. *Dalton Trans.* **2015**, *44*, 10152–10155. [CrossRef] [PubMed]
5. Li, Z.X.; Na, W.; Wang, H.; Gao, W.G. Direct syntheses of Cu-Zn-Zr/SBA-15 mesoporous catalysts for CO_2 hydrogenation to methanol. *Chem. J. Chin. Univ.* **2014**, *35*, 2616–2623.
6. Agatemor, C.; Ibsen, K.N.; Tanner, E.E.L.; Mitragotri, S. Ionic liquids for addressing unmet needs in healthcare. *Bioeng. Transl. Med.* **2018**, *3*, 7–25. [PubMed]
7. Earle, M.J.; Seddon, K.R. Ionic liquids. Green solvents for the future. *Pure Appl. Chem.* **2009**, *72*, 1391–1398. [CrossRef]
8. Sheldon, R. Catalytic reactions in ionic liquids. *Chem. Commun.* **2001**, *23*, 2399–2407. [CrossRef]
9. Seddon, K.R. Ionic liquids for clean technology. *J. Chem. Technol. Biotechnol.* **1997**, *68*, 351–356. [CrossRef]
10. Shi, F.; Gu, Y.L.; Zhang, Q.H.; Deng, Y.Q. Development of ionic liquids as green reaction media and catalysts. *Catal. Surv. Asia* **2004**, *8*, 179–186. [CrossRef]
11. Peng, J.J.; Deng, Y.Q. Formation of propylene carbonate catalyzed by room temperature ionic liquids. *Chin. J. Catal.* **2001**, *22*, 598–600.
12. Li, F.W.; Xiao, L.F.; Xia, C.G. Synthesis of cyclic carbonates catalyzed by ionic liquid mediated $ZnBr_2$ catalytic system. *Chem. J. Chin. Univ.* **2005**, *26*, 343–345.

13. Guo, L.Y.; Deng, L.L.; Jin, X.C.; Wu, H.; Yin, L.Z. Composite ionic liquids immobilized on MCM-22 as efficient catalysts for the cycloaddition reaction with CO_2 and propylene oxide. *Catal. Lett.* **2017**, *147*, 2290–2297. [CrossRef]
14. Wang, Y.H.; Li, W.; Luo, S.; Liu, S.X.; Ma, C.H.; Li, J. Research advances on the applications of immobilized ionic liquids functional materials. *Acta Chim. Sin.* **2018**, *76*, 85–94. [CrossRef]
15. Dai, W.L.; Chen, L.; Yin, S.F.; Luo, S.L.; Au, C.T. 3-(2-Hydroxyl-Ethyl)-1-propylimidazolium bromide immobilized on SBA-15 as efficient catalyst for the synthesis of cyclic carbonates via the coupling of carbon dioxide with epoxides. *Catal. Lett.* **2010**, *135*, 295–304. [CrossRef]
16. Sun, J.; Wang, J.Q.; Cheng, W.G.; Zhang, J.X.; Li, X.H.; Zhang, S.J.; She, Y.B. Chitosan functionalized ionic liquid as a recyclable biopolymer-supported catalyst for cycloaddition of CO_2. *Green Chem.* **2012**, *14*, 654–660. [CrossRef]
17. Zhang, Y.L.; Tan, Z.T.; Liu, B.L.; Mao, D.S.; Xiong, C.R. Coconut shell activated carbon tethered ionic liquids for continuous cycloaddition of CO_2 to epichlorohydrin in packed bed reactor. *Catal. Commun.* **2015**, *68*, 73–76. [CrossRef]
18. Zhuo, C.W.; Qin, Y.S.; Wang, X.H.; Wang, F.S. Temperature-responsive catalyst for the coupling reaction of carbon dioxide and propylene oxide. *Chin. J. Chem.* **2018**, *36*, 299–305. [CrossRef]
19. Della Monica, F.; Maity, B.; Pehl, T.; Buonerba, A.; De Nis, A.; Monari, M.; Grassi, A.; Rieger, B.; Cavallo, L.; Capacchione, C. [OSSO]-type iron(III) complexes for the low-pressure reaction of carbon dioxide with epoxides: Catalytic activity, reaction kinetics, and computational study. *ACS Catal.* **2018**, *8*, 6882–6893. [CrossRef]
20. Bobbink, F.D.; Vasilyev, D.; Hulla, M.; Chamam, S.; Menoud, F.; Laurenczy, G.; Katsyuba, S.; Dyson, P.J. Intricacies of cation–anion combinations in imidazolium salt-catalyzed cycloaddition of CO_2 into epoxides. *ACS Catal.* **2018**, *8*, 2589–2594. [CrossRef]
21. Wang, G.J.; Wang, D.H.; Qiu, J.; Zhao, L.Q. *Functional Polymer Materials*, 1st ed.; East China University of Science and Technology Press: Shanghai, China, 2006; pp. 283–285.
22. Sang, Y.; Liu, H.X.; He, S.C.; Li, H.S.; Jiao, Q.Z.; Wu, Q.; Sun, K.N. Catalytic performance of hierarchical H-ZSM-5/MCM-41 for methanol dehydration to dimethyl ether. *J. Energy Chem.* **2013**, *22*, 769–777. [CrossRef]
23. Valkenberg, M.H.; deCastro, C.; Hölderich, W.F. Immobilisation of ionic liquids on solid supports. *Green Chem.* **2002**, *4*, 88–93. [CrossRef]
24. Cheng, W.G.; Chen, X.; Sun, J.; Wang, J.Q.; Zhang, S.J. SBA-15 supported triazolium-based ionic liquids as highly efficient and recyclable catalysts for fixation of CO_2 with epoxides. *Catal. Today* **2013**, *200*, 117–124. [CrossRef]
25. Mao, D.S.; Guo, Q.S.; Meng, T. Effect of magnesium oxide modification on the catalytic performance of nanoscale HZSM-5 zeolite for the conversion of methanol to propylene. *Acta Phys-Chim. Sin.* **2010**, *26*, 2242–2248.
26. Guo, L.Y.; Ma, X.Y.; Li, C.Y.; Deng, L.L.; Bai, S.Y. Preparation and catalytic properties of chloride 1-carboxyl polyether-3-mtthyl imidazole ionic liquid. *Acta Pet. Sin. (Pet. Process Sect.)* **2017**, *33*, 342–348.
27. Guo, L.Y.; Ma, X.Y.; Wang, L.Y.; Deng, L.L.; Jin, X.C. Preparation and catalytic properties of chloride 1-amino polyether-3-methyl imidazole ionic liquid. *Chem. Ind. Eng. Prog.* **2017**, *36*, 581–587.
28. Guo, L.Y.; Zhang, B.; Li, C.Y.; Ma, X.Y.; Chang, X.T.; Gao, X. Synthesis of polyether ionic liquids and its influence on properties of phenolic resin. *Plastics.* **2015**, *44*, 57–59.
29. Yuan, S.B.; She, L.Q.; Liu, X.Y.; Li, X.W.; Pang, L.; Huang, H.Z.; Zhou, Y. Characterization and aromazization activity of gallium modified HZSM-5 catalysts. *Chin. J. Catal.* **1988**, *1*, 25–31.
30. Leng, Y.; Lu, D.; Jiang, P.P.; Zhang, C.J.; Zhao, J.W.; Zhang, W.J. Highly cross-linked cationic polymer microspheres as an efficient catalyst for facile CO_2 fixation. *Catal. Commun.* **2016**, *74*, 99–103. [CrossRef]
31. Saptal, V.B.; Bhanage, B.M. Bifunctional ionic liquids for the multitask fixation of carbon dioxide into valuable chemicals. *ChemCatChem* **2016**, *8*, 244–250. [CrossRef]
32. Han, L.; Li, H.Q.; Choi, S.J.; Park, M.S.; Lee, S.M.; Kim, Y.J.; Park, D.W. Ionic liquids grafted on carbon nanotubes as highly efficient heterogeneous catalysts for the synthesis of cyclic carbonates. *Appl. Catal. A* **2012**, *429*, 67–72. [CrossRef]
33. Fujita, S.; Nishiura, M.; Arai, M. Synthesis of styrene carbonate from carbon dioxide and styrene oxide with various zinc halide-based ionic liquids. *Catal. Lett.* **2010**, *135*, 263–268. [CrossRef]

34. Kim, M.I.; Choi, S.J.; Kim, D.W.; Park, D.W. Catalytic performance of zinc containing ionic liquids immobilized on silica for the synthesis of cyclic carbonates. *J. Ind. Eng. Chem.* **2014**, *20*, 3102–3107. [CrossRef]
35. Takahashi, T.; Watahiki, T.; Kitazume, S.; Yasuda, H.; Sakakura, T. Synergistic hybrid catalyst for cyclic carbonate synthesis: Remarkable acceleration caused by immobilization of homogeneous catalyst on silica. *Chem. Commun.* **2006**, *37*, 1664–1666. [CrossRef] [PubMed]
36. Sun, J.; Cheng, W.G.; Fan, W.; Wang, Y.H.; Meng, Z.Y.; Zhang, S.J. Reusable and efficient polymer-supported task-specific ionic liquid catalyst for cycloaddition of epoxide with CO_2. *Catal. Today* **2009**, *148*, 361–367. [CrossRef]
37. Appaturi, J.N.; Adam, F. A facile and efficient synthesis of styrene carbonate via cycloaddition of CO_2 to styrene oxide over ordered mesoporous MCM-41-Imi/Br catalyst. *Appl. Catal. B* **2013**, *136*, 150–159. [CrossRef]

Sample Availability: Samples of the PIILs and the immobilized catalysts are available from the authors.

molecules

MDPI

Article

Structure Characterization and Otoprotective Effects of a New Endophytic Exopolysaccharide from Saffron

Juan Li [1], Guimei Wu [1], Cuiying Qin [1], Wuhai Chen [1], Gang Chen [1,2,3,*] and Lu Wen [1,*]

[1] School of Pharmacy, Guangdong Pharmaceutical University, Guangzhou 510006, China; smilewinnie@126.com (J.L.); gdpuwgm@126.com (G.W.); gdpuwen@126.com (C.Q.); gdpucwh@126.com (W.C.)

[2] Guangdong Provincial Key Laboratory of Advanced Drug Delivery, Guangdong Pharmaceutical University, Guangzhou 510006, China

[3] Guangdong Provincial Engineering Center of Topical Precise Drug Delivery System, Guangdong Pharmaceutical University, Guangzhou 510006, China

* Correspondence: cg753@126.com (G.C.); gdpuwen@gdpu.edu.cn (L.W.)

Received: 28 January 2019; Accepted: 18 February 2019; Published: 19 February 2019

Abstract: Saffron, a kind of rare medicinal herb with antioxidant, antitumor, and anti-inflammatory activities, is the dry stigma of *Crocus sativus* L. A new water-soluble endophytic exopolysaccharide (EPS-2) was isolated from saffron by anion exchange chromatography and gel filtration. The chemical structure was characterized by FT-IR, GC-MS, and 1D and 2D-NMR spectra, indicating that EPS-2 has a main backbone of (1→2)-linked α-D-Manp, (1→2, 4)-linked α-D-Manp, (1→4)-linked α-D-Xylp, (1→2, 3, 5)-linked β-D-Araf, (1→6)- linked α-D-Glcp with α-D-Glcp-(1→ and α-D-Galp-(1→ as sidegroups. Furthermore, EPS-2 significantly attenuated gentamicin-induced cell damage in cultured HEI-OC1 cells and increased cell survival in zebrafish model. The results suggested that EPS-2 could protect cochlear hair cells from ototoxicity exposure. This study could provide new insights for studies on the pharmacological mechanisms of endophytic exopolysaccharides from saffron as otoprotective agents

Keywords: hearing loss; saffron; endophytic exopolysaccharide; gentamicin; cochlear hair cell

1. Introduction

Hearing loss is a global problem. To date, more than 466 million people have moderate to severe or greater hearing loss, and one-third of them are over 65 years old. As the world's population ages, it is estimated that approximately 900 million people (or one in every 10 people) will suffer hearing loss by 2050. World Health Organization (WHO) estimates that an annual global cost of hearing loss will be US $750 billion, including health sector costs (excluding hearing equipment), education support costs, productivity losses and social costs [1]. Unfortunately, hearing loss has not received sufficient attention by the pharmaceutical industry, and until now there have been few Food and Drug Administration (FDA)-approved drugs to treat or prevent different types of hearing loss [2]. Most hearing loss is caused by permanent loss of hair cells in the inner ear. One of the most likely causes of hair cell death is exposure to ototoxic agents, including aminoglycoside antibiotics such as gentamicin (GM) and neomycin, and cisplatin anticancer agents [3,4]. Additionally, it is estimated that aminoglycoside antibiotics generate hearing thresholds of almost 50% [5]. However, these aminoglycoside drugs also continue to be used in view of their cost and effectiveness, and their ototoxicity usually limits the dose range of drugs [4,6]. GM is a cationic aminoglycoside that enters cells via endocytosis and forms a complex with iron, which drives the formation of free radicals and directly promotes the formation of ROS [7]. Recent reports show that antioxidant drugs can benefit patients with hearing loss, because hearing loss is produced by excessive generation of reactive oxygen species (ROS) in cells

of the cochlea [8,9]. Therefore, it is highly possible to find potential drugs in antioxidants to prevent hair cell loss due to ototoxicity exposure and attenuate hearing loss.

With today's interest in new renewable sources of polymers, polysaccharides are macromolecular carbohydrates that play a vital role in the growth and development of living organisms, and serve as important biological response modifiers. Furthermore, it is well known that the polysaccharides can be used in various pharmaceutical formulations due to their sustainability, biodegradability, and biosafety [10–12]. Polysaccharides are widely distributed in plants, animals, and microorganisms. Endophytic fungi symbiotically live in plant tissues and all or part of their entire life cycles is spent in and/or between plant cells, often without causing apparent symptoms of diseases. Moreover, these microorganisms play important roles as components of plant ecosystems [13]. Endophytic fungi benefit their hosts by enhancing resistance to disease, abiotic stress and plant growth, and they have been widely recognized as a rich, potential and novel source of natural bioactive substances in agricultural, pharmaceutical and food industries [14]. Nowadays, endophytic fungi, as a renewable resource, are of growing interest. They often produce exopolysaccharides with unique structures and diverse biological activities, which have become the most promising group of antioxidants [15,16].

Saffron (*Crocus sativus* L.) is a perennial stemless herb of the Iridaceae family grown in Turkey, Iran, and China, and it has a variety of biological activities, such as antitumor, antioxidant, and anti-inflammatory effects [17,18]. As the main medicinal part of saffron, the stigma extract has antioxidant properties, which can scavenge oxygen radicals and effectively inhibit the activity of oxygen radicals [19]. Our previous studies have shown that crude exopolysaccharide extracted from fermentation mycelia of saffron exhibited excellent scavenging activities against 1, 1-diphenyl-2-picrylhydrazyl, hydroxyl and superoxide anion radicals [20]. However, the purification of exopolysaccharide and its further activity have not been researched. The present research describes the purification and characterization of a water-soluble exopolysaccharide (EPS-2) from the fermentation culture of endophytic fungus *Penicillium citreonigrum* CSL-27 of saffron and investigates its protective role in the damaged cochlear hair cells.

2. Results and Discussion

2.1. Isolation and Purification of Exopolysaccharide

The main exopolysaccharide fraction EPS-2 was collected according to the detection curve of phenol-sulphuric acid colorimetry. After purification with a DEAE-52 cellulose column (Figure 1a), one major fractional peak was obtained. According to Figure 1b, the fraction appeared as a single and symmetrical peak after being further purified by Sephadex G-75 column chromatography. EPS-2 appeared as a single and symmetrical peak in the high performance gel permeation chromatography (HPGPC) (Figure 1c), indicating homogeneity. By comparison of the retention times of EPS-2 with the molecular standards, the molecular weight of EPS-2 was estimated to be 40.4 kDa. The colorimetric analysis has shown that EPS-2 contains 88.9% total carbohydrate, and no sulfate ester, protein, or uronic acid is detected. Monosaccharide composition analysis indicated that EPS-2 was mainly composed of mannose, glucose, galactose, xylose, and arabinose with a molar ratio of 51.77:36.76:5.76:3.16:6.94. The results of SEM have shown that EPS-2 has a frizzy shape, and the surface has a scaly texture. The irregular aggregation has determined that EPS-2 is an amorphous solid. The molecular aggregation may be attributed to a repulsive force between the polysaccharides and the side chains.

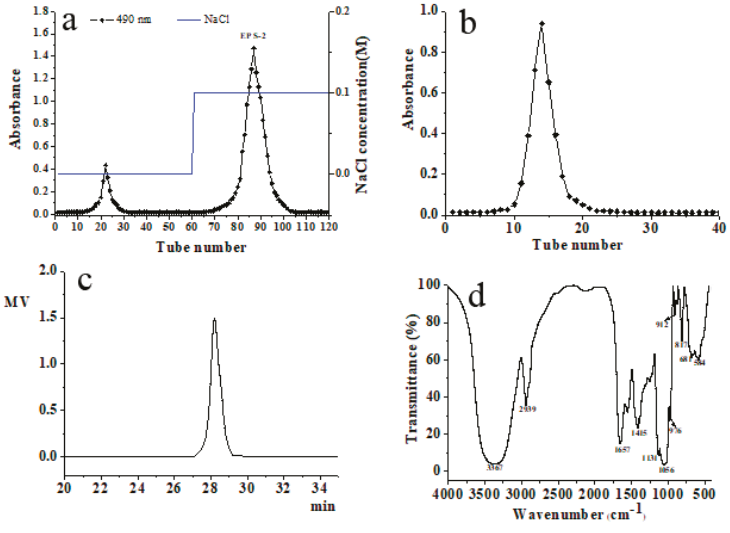

Figure 1. Chromatograms of EPS-2 from *P. citreonigrum* CSL-27 from (**a**) DEAE-52 cellulose column chromatography, (**b**) Sephadex G-75 chromatography, (**c**) HPGPC, and (**d**) FT-IR spectrum.

2.2. Fourier Transformed Infrared (FT-IR) Spectroscopy Analysis

The IR spectrum of EPS-2 displayed the characteristic peaks of polysaccharide (Figure 1d). The strong and broad absorption peak at 3367 cm^{-1} was related to the stretch vibration of O–H (hydroxyl group) bond existing in all polymers. The strong peak at 2939 cm^{-1} was due to the C–H stretching vibration in the sugar ring and the strong absorption peak at 1657 cm^{-1} represented the stretching vibration of C=O and carboxyl group. Another peak at 1418 cm^{-1} could be attributed to the symmetric stretching of the COO-group [21]. The presence of strong absorbance in the region 1200–950 cm^{-1} indicated the polysaccharide nature of EPS-2. The strong absorption at 1131 and 1056 cm^{-1} in the range of 1200–1000 cm^{-1}, which is anomeric region, was attributed to C–O–C and C–O groups in the polysaccharide, suggesting that the monosaccharide in the EPS-2 has a pyranose ring [22]. Moreover, the band at 912 cm^{-1} indicated the pyranose form of the glucosyl residue and absorption peak at 817 cm^{-1} as well as the existence of glycosidic linkages of the EPS-2. Moreover, the weak absorption at 912 and 817 cm^{-1} was assigned to the coexistence of α and β glycosidic bonds [23].

2.3. Methylation Analysis

Methylation is an essential method to analyze linkages that form methoxyl groups on the free hydroxyl groups of polysaccharides [24]. After methylation of EPS-2, a series of methylated derivatives were identified based on a gas chromatography coupled with mass spectrometry (GC-MS) analysis. According to the retention time and the ion fragment characteristics in the GC-MS spectra, 1,2,5-tri-*O*-acetyl-3,4,6-tri-*O*-methyl-mannitol (residue A), 1,2,4,5-tri-*O*-acetyl-3,6-tri-*O*-methyl-mannitol (residue B), 1,5-di-*O*-acetyl-2,3,4,6-tetra-*O*-methyl-D-glucitol (residue C), 1,5,6-tri-*O*-acetyl-2,3, 4-tri-*O*-methyl-D-glucitol (residue D), 1, 5-di-*O*-acetyl-2, 3, 4, 6-tetra-*O*-methyl-galactitol (residue E), 1,4,5-tri-*O*-acetyl-2, 3-di-*O*-methyl-D-xylitol (residue F), and 2,3,4,5-tetra-*O*-acetyl-D-arabinitol (residue G) were detected (summarized in Table 1), indicating the presence of →2)–Manp-(1→, →2, 4)–Manp-(1→, Glc-(1→, →6)-Glcp-(1→, Gal-(1→, →4)–α-D-Xyl-(1→ and →2, 3, 5)–Ara-(1→, respectively. The molar ratio was 7.2:2.3:3.3:1.2:1.0:1.1:1.1, which was in agreement with the results of the GC analysis of monosaccharide components.

Table 1. Glycosidic linkage composition of methylated EPS-2.

PMAA	Mass Fragments (*m*/*z*)	Molar Ratio	Linkage Type
3,4,6-Me_3-Manp [a]	87, 101, 117, 129, 161, 189, 233	7.2	→2)-D-Manp-(1→
3,6-Me_2-Manp	43, 71, 87, 129, 173, 189, 233	2.3	→2, 4)-D-Manp-(1→
2,3,4,6-Me_4-Glcp	45, 71, 87, 101, 117, 129, 145, 161, 205	3.3	D-Glcp-(1→
2,3,4-Me_3-Glcp	58, 71, 87, 99, 101, 117, 129, 161, 189, 233	1.2	→6)-D-Glcp-(1→
2,3,4,6-Me_4-Galp	87, 101, 117, 129, 189, 233	1.0	D-Galp-(1→
2,3-Me_2-Xylp	43, 87, 101, 117, 129, 189	1.1	→4)-D-Xylp-(1→
Araf	73, 85, 115, 145, 158, 187, 217	1.1	→2, 3, 5)-D-Araf-(1→

[a] 3, 4, 6-Me_3-Manp = 1, 2, 5-Tri-*O*-acetyl-3,4,6-tri-*O*-methyl-mannitol.

2.4. Nuclear Magnetic Resonance (NMR) Spectroscopy Analysis

The structure of EPS-2 was further analyzed by NMR spectroscopy. The ^{1}H, ^{13}C, HSQC, and HMBC spectra of EPS-2 are shown in Figure 2. Several anomeric proton signals (5.31–5.03 ppm) appeared in the ^{1}H-NMR spectrum. Other proton signals were located in the region of about 4.25–3.36 ppm, which were attributed to the protons of the C-2–C-6 of hexosyl glycosidic ring. The corresponding anomeric carbon signals (102.4–98.2 ppm) were identified in the ^{13}C-NMR and HSQC spectra of EPS-2. These signals corresponded to seven types of residues (residue A–G, respectively), and this result was consistent with the GC-MS result.

The carbon and proton signals of residues A-G were grouped by comprehensive analysis, comparison of the NMR spectra, GC-MS data of EPS-2 and published literature [25–28]. The α/β configurations of residues were judged by the chemical shift and coupling constant of the anomeric proton [29,30]. In the HSQC spectrum, the anomeric signals at 100.5/5.30, 98.2/5.16, 98.3/5.07,102.4/5.10, 102.1/5.06, 102.0/5.03, and 102.3/5.07 ppm corresponded to residues A–G, respectively, which belonged to →2)–α-D-Manp-(1→, →2, 4)–α-D-Manp-(1→, α-D-Glcp-(1→, →6)-α-D-Glcp-(1→, α-Galp-(1→, →4)–α-D-Xylp-(1→, and →2, 3, 5)–β-D-Araf-(1→, respectively. Additionally, the adjacent carbon and hydrogen signals of each residue were assigned according to the HMBC spectrum. The data on carbon and hydrogen for EPS-2 are shown in Table 2.

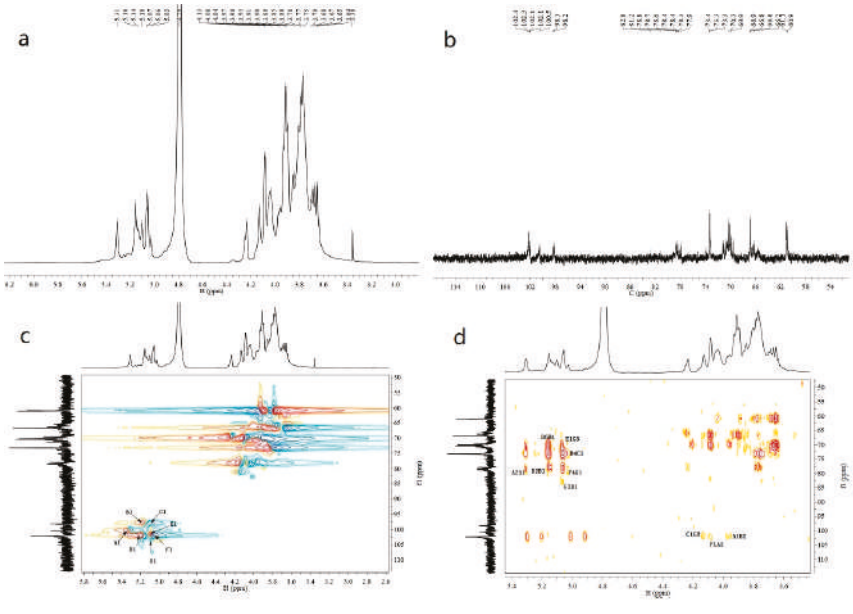

Figure 2. *Cont*.

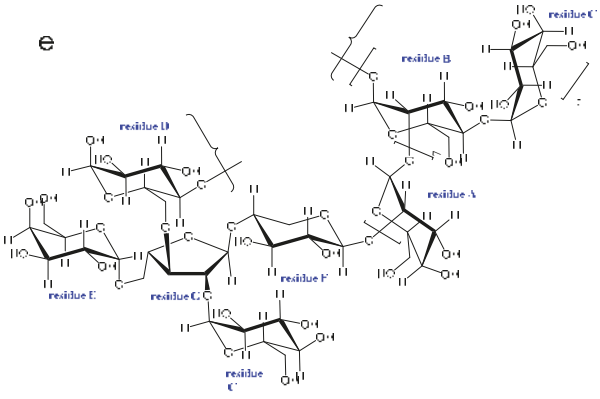

Figure 2. ^{1}H-NMR (**a**), ^{13}C-NMR (**b**), HSQC (**c**), HMBC spectrum (**d**), and predicted repetitive structural unit (**e**) of EPS-2.

Table 2. Assignment of ^{13}C-NMR and ^{1}H-NMR chemical shifts of EPS-2.

No.	Glycosyl Residues	Chemical Shifts, δ (ppm)					
		C1/H1	C2/H2	C3/H3	C4/H4	C5/H5	C6/H6
A	→2)–α-D-Manp-(1→	100.5 5.30	78.5 4.11	70.6 3.97	66.8 3.65	73.9 3.80	63.4 3.91
B	→2, 4)–α-D-Manp-(1→	98.2 5.16	78.3 3.96	70.1 4.07	70.3 3.89	73.6 3.76	66.9 3.85, 3.77
C	α-D-Glcp-(1→	98.3 5.07	70.4 3.80	73.3 3.85	76.7 4.08	70.1 3.90	61.0 3.81, 3.75
D	→6)-α-D-Glcp-(1→	102.4 5.10	73.3 3.36	73.5 3.60	70.4 3.62	76.8 4.08	66.2 3.75
E	α-D-Galp-(1→	102.1 5.06	70.2 3.82	73.2 4.13	71.2 4.02	73.3 4.04	61.1 3.72
F	→4)–α-D-Xylp-(1→	102.0 5.03	75.3 3.82	76.3 3.95	78.4 3.73	65.5 3.65	
G	→2, 3, 5)–β-D-Araf-(1→	102.3 5.07	81.1 4.25	82.8 4.02	81.1 4.23	66.6 3.96, 3.88	

Some points existed in HSQC and also showed in HMBC were removed, and the remained linkage sites between the residues were determined by analyzing the HMBC spectrum of EPS-2. In the HMBC spectrum, the peak at *δ* 78.5/5.30 ppm (AC2/AH1) suggested that there is a recurring C-2 linked O-1 of residue A structure in EPS-2. The signal at *δ* 78.3/5.16 ppm (B C2/B H1) has shown that C-2 is linked to O-1 of residue B, and the signal at *δ* 100.5/3.96 ppm (A C1/B H2) has indicated that C-2 of residue B is linked to O-1 of recurring residue A. Likewise, the linkages of residue F O-1 with residue A C-2, residue C O-1 with residue B C-4, and residue B O-1 with residue D C-6 were deduced by the signals at *δ* 102.0/4.11 ppm (FC1/AH2), 70.3/5.07 ppm (BC4/CH1), 66.2/5.16 ppm (DC6/BH1), respectively. In addition, signals at *δ δ*98.3/4.25 ppm (CC1/GH2), *δ* 82.8/5.10 ppm (GC3/DH1), *δ* 66.6/5.06 ppm (GC5/EH1), and *δ* 78.4/5.07 ppm (FC4/GH1) illustrate that O-1, C-2, C-3 and C-5 of residue G were linked to the C-4 of residue F, O-1 of residue C, O-1 of residue D, O-1 of residue E, respectively. The possible repetitive structure unit of EPS-2 was inferred and is shown in Figure 2e.

2.5. Effects of EPS-2 on the Viability of House Ear Institute-Organ of Corti 1 (HEI-OC1) Cells Treated with GM

As evidenced by the MTT assay, the exposure to GM for 24 h decreased the cell viability in a dose-dependent manner. Cell viability was reduced by ca. 50% by 10 mM GM (Figure 3a).

Thus, 10 mM GM was used subsequently. Cells were pretreated with 50, 100, 200, 400, and 800 μg/mL EPS-2 for 1 h before adding 10 mM GM. Control cells were treated with a vehicle (0.1% DMSO). Cell survival was determined after 24 h. In the control group, no cytotoxicity was observed at 0.1% DMSO. The exposure of HEI-OC1 cells to GM resulted in a significant reduction of cell viability, but cell pretreatment with EPS-2 significantly inhibited GM-mediated cytotoxicity in a dose-dependent manner, as shown in Figure 3b. In cells treated with GM only, EPS-2 at 50 μg/mL increased cell viability by 50% EDA (40 μM), a positive control also significantly increased cell survival.

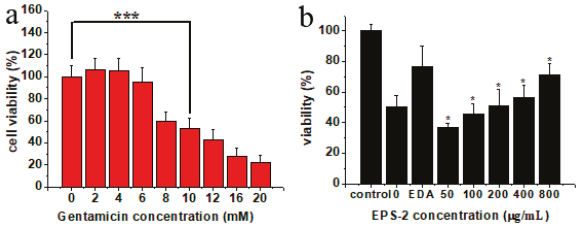

Figure 3. Effect of EPS-2 on GM-mediated decrease in viability of HEI-OC1 cells. (**a**) GM decreased cell viability dose dependently. GM (10 mM) treatment for 24 h decreased the cell viability by ca. 50%. (**b**) EPS-2 protected HEI-OC1 cells following GM (10 mM) treatment. * $p < 0.05$, *** $p < 0.001$ vs. control group. Results are shown as the mean ± SD ($n = 6$).

2.6. Protective Effect of EPS-2 on Hair Cells in Neuromasts

Using the zebrafish lateral line as a model of hair cell death, we tested EPS-2 prevented GM-induced hair cell death. DASPEI was performed to stain mitochondria, and the mean number of hair cells in the four neuromasts (SO1, SO2, O1, and OC1) of the zebrafish larvae was calculated to quantitatively assess the changes. Aminoglycoside treatment caused nuclear fragmentation and reduced neuromast fluorescence, while protective compound could prevent fragmentation and preserve labeling intensity.

From two independent screens, we found that EPS-2 protected hair cells from GM (Figure 4). We first determined whether 1 h of exposure to EPS-2 alone caused hair cell death, and the 400 μg/mL concentration of EPS-2 was revealed to have toxicity for hair cells compared to negative control, whereas 200 μg/mL EPS-2 had no toxicity for hair cells compared to the negative control group. Therefore, EPS-2 at a concentration of 200 μg/mL was expected to be applied as a maximal concentration in the following study. Pretreatment with 25, 50, 100, and 200 μg/mL EPS-2 resulted in significant protection of hair cells exposed to 100 μM GM compared to GM alone. The mean (± SD) number of hair cells in the neuromasts in the negative control group was 36.62 ± 1.85, and the viability of hair cells was set to 100%. In the model group (100 μM GM), the viability of hair cells was 50%; in the positive control group (0.5 μM EDA), the viability of hair cells was 82%; the protective effect of pre-treated EPS-2 increased in a dose-dependent manner until 200 μg/mL (the viability of hair cells was up to 72%) of concentration with a significantly large number of viable hair cells than that in the model group.

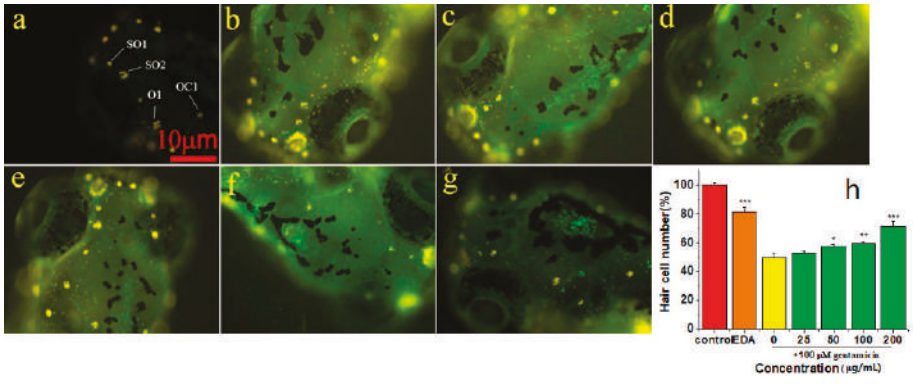

Figure 4. Analysis of hair cell damage by DASPEI assay (×10). (**a**) negative control: 36.62 ± 1.85 cells; (**b**) GM 100 μM treatment: 18.37 ± 2.26 cells; (**c**) EPS-2 25 μg/mL + GM 100 μM treatment: 19.37 ± 1.41 cells; (**d**) EPS-2 50 μg/mL + GM 100 μM treatment: 21.00 ± 1.85cells; (**e**) EPS-2 100 μg/mL + GM 100 μM treatment: 21.87 ± 1.55 cells; (**f**) EPS-2 200 μg/mL + GM 100 μM treatment: 26.25 ± 3.01 cells; (**g**) positive control: 30.00 ± 3.16 cells; and (**h**) EPS-2 protected hair cells following GM (100 μM) treatment. * $p < 0.05$, ** $p < 0.01$, *** $p < 0.001$ vs. control group). Results are shown as the mean ± SD (n = 8 fish per treatment). Scale bar = 10 μm.

3. Experimental

3.1. Chemicals and Reagents

3-Aminobenzoic acid ethyl ester methanesulfonate (MS-222, CAS no. 886-86-2), 3-methy-1-pheny-2-pyrazoline-5-one (EDA, CAS no. 89-25-8), 2-(4-(dimethylamino)styryl)-*N*- ethylpyridinium iodide (DASPEI, CAS no. 3785-01-1) and 3-(4, 5-dimethylthiazol-2-yl)-2, 5-diphenyltetrazolium bromide (MTT, CAS no. 298-93-1) were obtained from Sigma-Aldrich (St Louis, MO, USA). Gentamycin (GM, CAS no.1405-41-0) was purchased from Dalilan Meilun Biotechnology Co., Ltd. (Dalian, China). The Hepes-buffered DMEM solution (pH 7.4, Gibco, 1×, sterile, CAS no. 21063-029) used in this study contained neither phenol red nor sodium pyruvate was purchased from Life Technologies Co. (Grand Island, NY, USA). High-glucose Dulbecco's modified Eagle medium (DMEM) and Fetal bovine serum (FBS) were purchased from Thermo Fisher Scientific (Waltham, MA, USA). DEAE-cellulose 52 was purchased from Beijing Dingguo Changsheng Biotechnology Co., Ltd. (Beijing, China). Sephadex G-75 gel filtration medium was purchased from Shanghai Lanji Biotechnology Co., Ltd. (Shanghai, China). Trifluoroacetic acid (TFA), 1-phenyl-3-methyl-5-pyrazolone (PMP), standard monosaccharides (D-mannose, L-rhamnose, D-glucuronic acid, D-galacturonic acid, D-glucose, D-galactose, D-xylose, L-arabinose, and D-fucose), T-series dextrans of different molecular weights (T-5.2, T-11.6, T-23.8, T-48.6, T-148, T-273, T-410, T-668, and T-1400) and dialysis tubing (molecular weight cut off, 8000–14,000 Da) were obtained from Sigma-Aldrich (St. Louis, MO, USA). The reagents used in high-performance liquid chromatography (HPLC) and GC-MS were of chromatograph grade, and all other chemicals and reagents used were of analytical grade (AR).

3.2. Fungal Material Microbial Strain and Culture Conditions

The strain CSL-27 was isolated from the corm of saffron and identified as *Penicillium citreonigrum* by Beijing Dingguo Changsheng Biotechnology Co. Ltd. The strain was stored at China Center for Type Culture Collection (CCTCC) (Wuhan, China). The strain was activated on potato dextrose agar (PDA) slants, and then cultivated on a rotary shaker (TCYQ, Taicang Laboratory Equipment Factory, Jiangsu Province, China) constantly at 120 rpm and 28 °C for 14 days. The liquid culture medium contained 10 g/L glucose, 2 g/L peptone, 1 g/L yeast extract and 1 g/L NaCl with a pH of 6.5.

3.3. Cell Culture

HEI-OC1 cell line, derived from the organ of Corti was obtained from the House Ear Institute (Los Angeles, CA, USA). Cells were cultured in high-glucose DMEM, supplemented with 10% FBS at 33 °C and 10% CO_2 in a humidified atmosphere without antibiotics. The cell incubator (HERAcell 150i) was derived from Thermo Fisher Scientific (Waltham, MA, USA).

3.4. Zebrafish Husbandry

Zebrafish (*Danio rerio*) embryos were produced by paired matings of AB wild-type adult fish from School of Pharmaceutical Sciences, Sun Yat-sen University and maintained in zebrafish facilities at School of Pharmacy, Guangdong Pharmaceutical University. Experiments were performed on 5–6 day old larval zebrafish maintained at 28 °C in a defined embryo medium (EM) containing 1 mM $MgSO_4$, 120 μM KH_2PO_4, 74 μM Na_2HPO_4, 1 mM $CaCl_2$, 500 μM KCl, 15 mM NaCl, and 500 μM $NaHCO_3$ in distilled water at pH 7.2. This age range was selected due to the fact that hair cells in 5 day-old fish show mature responses to ototoxic insult, and the small fish size allows for high throughput screening of compounds in small volumes [31]. All procedures were approved by the appropriate Institutional Animal Care and Use Committee at Guangdong Pharmaceutical University.

3.5. Isolation and Purification of EPS-2

The supernatant from the culture of strain CSL-27 was collected and concentrated by a vacuum rotary evaporator (EYELA, Japan). The concentrated solution was treated with four volumes of cold 95% EtOH and kept overnight at 4 °C. The precipitate was separated and collected by centrifugation at 3000 rpm for 20 min and dissolved in distilled water and deproteinated by the Sevag method [32]. Finally, the precipitate was dialyzed in distilled water for 48 h at 4 °C and then freeze-dried to obtain a crude polysaccharide. The sugar content in the EPS was analyzed using phenol-sulfuric acid method with glucose as the standard [33].

The crude exopolysaccharide was purified using a column (2.6 × 95 cm) packed with Macroporous resin AB-8. Distilled water was employed as the mobile phase. The flow rate was 2 mL/min. Each fraction (10 mL) was collected and analyzed with the phenol-sulfuric acid reagent at 490 nm using a spectrophotometer [33]. The fractions, which coincided with the major peak, were collected together, concentrated at 60 °C with a rotary evaporator under vacuum, dialyzed (Mw cut off: 8000 Da) and lyophilized. The exopolysaccharide samples obtained by lyophilizing were dissolved in distilled water and fractionated on a pre-equilibrated DEAE-52 cellulose column (2.6 × 60 cm) equilibrated with distilled water and then eluted with aqueous NaCl solution (0.1 mol/L) at a flow rate of 1 mL/min. All the fractions were assayed for carbohydrate content by the phenol-sulfuric acid method and the fraction representing only one sharp peak was collected, dialyzed, concentrated and further purified using a Sephadex G-75 gel-filtration column (1.6 × 70 cm) by eluting with distilled water at a flow rate of 0.2 mL/min. Consequently, a fine exopolysaccharide, named EPS-2, was obtained. After freeze-drying, EPS-2 was available for use in the subsequent experiments.

3.6. Analysis of Physicochemical Characteristics

The molecular weight of EPS-2 was assessed by HPGPC on TSK-5000PWXL and TSK G-3000 PWXL gel columns (1.8 × 300 mm) in series (Tosoh Biosep, Tokyo, Japan). The columns were calibrated with dextran standards and a refractive index detector (Waters 2414, Milford, MA, USA), and eluted with 0.02 M KH_2PO_4 solution at a flow rate of 0.6 mL/min and column temperature of 35 °C. The molecular weight was estimated by reference to a calibration curve made by a set of standards dextran (*M*w: 1400, 668, 410, 273, 148, 48.6, 23.8, and 5.2 kDa) [34]. The sample was dissolved in 1 mL of distilled water and mixed with an equal volume of 4.0 M TFA. The sample was allowed to stand still for 4 h at 100 °C and the acid-hydrolyzed sample was filtered through a 0.45 μm syringe filter and the residual acid was removed through decompression and distillation

with methanol for thrice [35]. The resulting monosaccharide compositions were determined by HPLC after precolumn derivatization with PMP using a Shimadzu HPLC system fitted with Phenomenex GEMINI-NX C_{18} HPLC column (4.6 nm × 250 mm) and Shimadzu prominence diode array detector. The sugar was identified by comparison with reference sugars (L-rhamnose, L-arabinose, D-fucose, D-xylose, D-mannose, D-galactose, D-glucose, D-glucuronic acid, and D-galacturonic acid). Calculation of the molar ratio of the monosaccharide was carried out on the basis of the peak area of the monosaccharide [24].

The morphology of EPS-2 was observed under a low vacuum scanning electron microscope (SEM, Philips Quanta-400, Netherlands). The dried exopolysaccharide powder was placed on a specimen holder with the help of double-sided adhesive tapes and then sputtered with the gold powder using a sputter coater. The sample was observed at magnifications of 800× and 1600× at an accelerating potential of 20 kV under low vacuum conditions.

3.7. FT-IR Analysis

FT-IR spectroscopy was used to determine the functional groups of the purified EPS. Infrared spectra of the purified EPS fraction were recorded in the 4000–400 cm^{-1} region using a FT-IR system (Perkin Elmer Spectrometer 100, Wellesley, MA, USA). The sample (10 mg) was mixed with 100 mg of dried potassium bromide (KBr) and compressed to prepare as a salt disc (10 mm diameter) for reading the spectrum further. The determinations were performed in two independent replicates and are reported as the mean with standard deviations.

3.8. Methylation Analysis

A methylation analysis was performed by the method of Hakomori with some modifications [15]. In brief, polysaccharide in dimethyl sulfoxide (DMSO) was methylated using NaH and iodomethane. After 6 h total hydrolysis with 2 M TFA at 105 °C, the methylated sugar residues were converted to partially methylated alditol acetates by reduction with $NaBH_4$, followed by acetylation with acetic anhydride. The derived sugar residues were dissolved in 100 μL chloroform. Subsequently, partial methylated alditol acetates (PMAAs) were analyzed by GC-MS on the Shimadzu NTST system equipped with a TG WAXMS capillary column (30.0 m × 0.25 mm × 0.25 μm) (ThermoFinnigan, Silicon valley, CA, USA). The temperature was set to 50 °C, maintained for 3 min, then increased to 240 °C at a rate of 15 °C/min, and maintained at 240 °C for 20 min. Helium acted as the carrier gas, with the flow rate maintained at 1.0 mL/min. PMAAs were identified by the retention times and fragmentation patterns.

3.9. NMR Spectroscopy Analysis

^{1}H-NMR and ^{13}C-NMR spectra were recorded using a Bruker AVANCE IIIT600 NMR spectrometer at 25 °C. The sample (35 mg) was deuterium-exchanged by lyophilization two times with 99.97% D_2O, and then was dissolved in 1.0 mL of 99.97% D_2O. Acetone was taken as the internal standard (2.225 ppm for ^{1}H and 31.07 ppm for ^{13}C). ^{1}H-NMR, ^{13}C-NMR, ^{1}H-^{1}H COSY, HSQC, and HMBC were performed using the standard Agilent software.

3.10. Protection Assay

Hair cells act as sensory receptors for the auditory and vestibular systems in all vertebrates. Conventional vertebrate experimental animal models are well suited to detect and solve problems related to hair cell death and survival, but they are not suitable for drug screening. This is mainly because the inner ear is inaccessible and the alive time of inner ear cochlear tissue is very short in vitro [36]. As present, HEI-OC1 cell line is a mature and immortalized cell lines derived from the cochlea and vestibular tissue that has been shown to be sensitive to some known ototoxins, such as GM and cisplatin [37]. In addition, Hair cells in the inner ear of mammals are similarity with the pathway activated by ototoxicity exposure in zebrafish lateral line, but hair cells in zebrafish regenerate

following ototoxicity exposure unlike mammals. Therefore, the zebrafish lateral line is an excellent model for drug screening that modulates hair cell survival, an intractable approach in mammalian systems [3]. In this experiment, HEI-OC1 cell line and zebrafish model were effectively combined for the activity assay of EPS-2.

3.10.1. Cell Viability Assay

Cell viability was measured using the MTT assay as described previously [38]. HEI-OC1 cells were seeded at a density of 1×10^4 cells/well in a 96-well plate and cultured overnight. To investigate the effect of EPS-2 on cell viability, HEI-OC1 cells were treated with 50, 100, 200, 400, and 800 μg/mL EPS-2 for 1 h, before being exposed to GM. When the cells were confluent, the culture medium was replaced with medium containing GM, which was the calculated half-maximal inhibitory concentration (IC_{50}). After one day of incubation, 100 μL MTT was added to each culture well and the 96-well plate was incubated at 33 °C in an atmosphere of 10% CO_2 for 4 h. EDA (40 μM) was used as a positive control. The effect of EPS-2 on viability at each concentration was calculated as a percentage of the control activity from the absorbance values. Absorbance at 490 nm was measured using a Microplate spectrophotometer (RT-2100C, Shenzhen Rayto Life Science Co., Ltd., China) for cell viability and the average OD in control cells was taken as 100% of viability. A final concentration of 10 mM GM was selected to damage the HEI-OC1 cells in the following experiments.

$$\text{Cell relative viability (\%)} = OD_{experiment}/OD_{control} \times 100\% \ (OD_{blank} \text{ was used to zero})$$

Six wells were used for each EPS-2 concentration and three independent experiments were performed.

3.10.2. Assay of Zebrafish Neuromast Hair Cell Protection

At 5–6 days post-fertilization (dpf) AB zebrafish larvae were raised at 28.5 °C in Petri dishes and transferred to cell culture baskets placed in 96-well culture plates in groups of 3–4 fish per basket. The larvae were exposed to EPS-2 at the following concentrations: 25, 50, 100, 200, and 400 μg/mL for 1 h for the experimental group. A negative control group with no additional sample was also established. The larvae were then washed with the EM three times and anesthetized using 40 μg/mL MS-222 for 5 min as described in previous publications [39]. The mean count of hair cells was calculated within four neuromasts (SO1, SO2, O1, and OC1) on one side of each fish at a 10× magnification using a Zeiss inverted fluorescence microscope (Carl ZEISS AG, Germany) for each group (n = 8). All zebrafish were alive and no abnormal developments were observed.

Then the 5–6 dpf zebrafish larvae were pretreated with EPS-2 for 1 h at concentrations of 25, 50, 100, and 200 μg/mL followed by treatment with 100 μM GM, respectively. Following 1 h GM exposure, the larvae were rinsed briefly with EM, and incubated in a staining agent (0.005% DASPEI) for 15min, rinsed three times with fresh EM and anesthetized in 40 μg/mL MS-222 for 5 min. The hair cells within the above-mentioned four neuromasts were examined. Each neuromast was scored for presence of a normal compliment of hair cells, with reduced or absent DASPEI staining indicating a reduction in the number of hair cells. Composite scores were calculated for the larvae in each treatment group, normalized to the control group and expressed as % hair cell survival. Negative controls were treated with GM while positive controls were treated with 0.5 μM EDA.

3.10.3. Statistical Analysis

All data were presented as the mean ± standard deviation. One-way analysis of variance (ANOVA) was used for multiple comparisons; $p < 0.05$ was considered statistically significant. Statistical analysis was performed with IBM SPSS 21.0 for Windows (IBM, Armonk, NY, USA).

4. Conclusions

Hearing loss is the one of the most common sensory disorders in humans, and a large number of cases are due to hair cell damage caused by ototoxicity drugs such as GM. Therefore, it is great significance to identify agents and their mechanisms that protect hair cells from ototoxicity damage [40]. Saffron has strong biological activities, and the active part is concentrated in the stigma, and the amount is too small to be detrimental to further research. Thus, endophytic fungus is a good substitute for studying saffron. Moreover, many literatures have reported that endophytic exopolysaccharides have unique charms and effective activities. We previously reported the antioxidant activity of crude exopolysaccharide extracted from fermentation mycelia of saffron. The characterization of polysaccharides of the endophytic fungus had great significance for the further structure-function relationship study, and the development and application of the endophytic polysaccharide. Therefore, we purified the polysaccharide with DEAE-52 cellulose and Sephadex G-75 columns, and a new water-soluble endophytic polysaccharide EPS-2 with a molecular weight of 40.4 kDa was obtained. The results of monosaccharide composition, FT-IR spectroscopy, GC-MS and NMR analyses suggested that EPS-2 is composed of →2)–Manp-(1→, →2, 4)–Manp-(1→, Glc-(1→, →6)- Glcp-(1→, Gal-(1→, →4)–α-D-Xyl-(1→, and →2, 3, 5)–Ara-(1→. The possible repetitive structural unit of EPS-2 was inferred. The most effective concentration of EPS-2 for attenuating GM-induced HEI-OC1 cell damage was 200 μg/mL (50% cell viability), and EPS-2 protected hair cells from a concentration of 25 μg/mL (50% hair cell number) in a zebrafish model. In conclusion, the study reports the systematic purification, structural identification, and the in-vitro testing of its protective effects on hair cells against GM toxicity of EPS-2 and notes its potential as a natural candidate lead for new drugs to combat hearing loss that can be utilized in the pharmaceutical and healthcare industries.

Author Contributions: L.W. and G.C. conceived, designed the experiment and elaborated the manuscript; J.L. performed activity assays and analyzed the data; G.W. performed structure elucidation and provided 1D- and 2D-NMR spectra; C.Q. cultured the fungus, prepared a crude fungal extract and assisted in structure elucidation; W.C. isolated and purified the exopolysaccharide; and all authors approved the final paper.

Funding: This research was financially supported by the National Natural Science Foundation of China (Nos. 81502944 and 81573618).

Conflicts of Interest: The authors declare no conflicts of interest.

References

1. WHO Media centre. Deafness and hearing loss. World Health Organization. Available online: http://www.who.int/mediacentre/factsheets/fs300/en/ (accessed on 15 March 2018).
2. Thomas, A.J.; Wu, P.; Raible, D.W.; Rubel, E.W.; Simon, J.A.; Ou, H.C. Identification of small molecule inhibitors of cisplatin-induced hair cell death: Results of a 10,000 compound screen in the zebrafish lateral line. *Otol. Neurotol.* **2015**, *36*, 519–525. [CrossRef] [PubMed]
3. Kruger, M.; Boney, R.; Ordoobadi, A.J.; Sommers, T.F.; Trapani, J.G.; Coffin, A.B. Natural bizbenzoquinoline derivatives protect zebrafish lateral line sensory hair cells from aminoglycoside toxicity. *Front Cell Neurosci.* **2016**, *10*, 83–98. [CrossRef]
4. Esterberg, R.; Coffin, A.B.; Ou, H.; Simon, J.A.; Raible, D.W.; Rubel, E.W. Fish in a dish: drug discovery for hearing habilitation. *Drug Discov. Today* **2013**, *10*, 23–29. [CrossRef] [PubMed]
5. Fausti, S.A.; Henry, J.A.; Schaffer, H.I.; Olson, D.J.; Frey, R.H.; McDonald, W.J. High-frequency audiometric monitoring for early detection of aminoglycoside ototoxicity. *J. Infect. Dis.* **1992**, *165*, 1026–1032. [CrossRef] [PubMed]
6. Noack, V.; Pak, K.; Jalota, R.; Kurabi, A.; Ryan, A.F. An antioxidant screen identifies candidates for protection of cochlear hair cells from gentamicin toxicity. *Front Cell Neurosci.* **2017**, *11*, 242–252. [CrossRef]
7. Draz, E.I.; Abdin, A.A.; Sarhan, N.I.; Gabr, T.A. Neurotrophic and antioxidant effects of silymarin comparable to 4-methylcatechol in protection against gentamicin-induced ototoxicity in guinea pigs. *Pharmacol. Rep.* **2015**, *67*, 317–325. [CrossRef] [PubMed]

8. Oishi, N.; Kendall, A.; Schacht, J. Metformin protects against gentamicin-induced hair cell death in vitro but not ototoxicity in vivo. *Neurosci. Lett.* **2014**, *583*, 65–69. [CrossRef] [PubMed]
9. Le Prell, C.G.; Ojano-Dirain, C.; Rudnick, E.W.; Nelson, M.A.; DeRemer, S.J.; Prieskorn, D.M.; Miller, J.M. Assessment of nutrient supplement to reduce gentamicin-induced ototoxicity. *J. Assoc. Res. Oto.* **2014**, *15*, 375–393. [CrossRef] [PubMed]
10. Zhang, Y.; Wang, F.; Li, M.; Yu, Z.; Qi, R.; Ding, J.; Zhang, Z.; Chen, X. Self-stabilized hyaluronate nanogel for intracellular codelivery of doxorubicin and cisplatin to osteosarcoma. *Adv. Sci.* **2018**, *5*, 1700821. [CrossRef]
11. Chen, J.; Ding, J.; Xu, W.; Sun, T.; Xiao, H.; Zhuang, X.; Chen, X. Receptor and microenvironment dual-recognizable nanogel for targeted chemotherapy of highly metastatic malignancy. *Nano Lett.* **2017**, *17*, 4526–4533. [CrossRef]
12. Li, D.; Han, J.; Ding, J.; Chen, L.; Chen, X. Acid-sensitive dextran prodrug: A higher molecular weight makes a better efficacy. *Carbohydr. Polym.* **2017**, *161*, 33–41. [CrossRef] [PubMed]
13. Rodriguez, R.J.; White, J.F., Jr.; Arnold, A.E.; Redman, R.S. Fungal endophytes: diversity and functional roles. *New Phytol.* **2009**, *182*, 314–330. [CrossRef] [PubMed]
14. Park, Y.H.; Chung, J.Y.; Ahn, D.J.; Kwon, T.R.; Lee, S.K.; Bae, I.; Yun, H.K.; Bae, H. Screening and characterization of endophytic fungi of *Panax ginseng* Meyer for biocontrol activity against *Ginseng pathogens*. *Biol. Control* **2015**, *91*, 71–81. [CrossRef]
15. Yan, M.X.; Mao, W.J.; Liu, X.; Wang, S.Y.; Xia, Z.; Cao, S.J.; Li, J.; Qin, L.; Xian, H.L. Extracellular polysaccharide with novel structure and antioxidant property produced by the deep-sea fungus *Aspergillus versicolor* N2bc. *Carbohydr. Polym.* **2016**, *147*, 272–281. [CrossRef]
16. Kavitake, D.; Devi, P.B.; Singh, S.P.; Shetty, P.H. Characterization of a novel galactan produced by *Weissella confusa* KR780676 from an acidic fermented food. *Int. J. Biol. Macromol.* **2016**, *86*, 681–689. [CrossRef] [PubMed]
17. Hatziagapiou, K.; Kakouri, E.; Lambrou, G.I.; Bethanis, K.; Tarantilis, P.A. Antioxidant properties of *Crocus sativus* L. and its constituents and relevance to neurodegenerative diseases; focus on Alzheimer's and Parkinson's disease. *Curr. Neuropharmacol.* **2018**, *16*, 1–26. [CrossRef] [PubMed]
18. Lopresti, A.L.; Drummond, P.D.; Inarejos-García, A.M.; Prodanov, M. Affron®, a standardised extract from saffron (*Crocus sativus* L.) for the treatment of youth anxiety and depressive symptoms: a randomised, double-blind, placebo-controlled study. *J. Affect Disorders* **2018**, *232*, 349–357. [CrossRef] [PubMed]
19. Christodoulou, E.; Kadoglou, N.P.E.; Stasinopoulou, M.; Konstandi, O.A.; Kenoutis, C.; Kakazanis, Z.I.; Rizakou, A.; Kostomitsopoulos, N.; Valsami, G. *Crocus sativus* L. aqueous extract reduces atherogenesis, increases atherosclerotic plaque stability and improves glucose control in diabetic atherosclerotic animals. *Atherosclerosis* **2018**, *268*, 207–214. [CrossRef] [PubMed]
20. Wen, L.; Xu, Y.; Wei, Q.; Chen, W.; Chen, G. Modeling and optimum extraction of multiple bioactive exopolysaccharide from an endophytic fungus of *Crocus sativus* L. *Pharmacogn. Mag.* **2018**, *14*, 36–43.
21. Zhao, M.; Yang, N.; Yang, B.; Jiang, Y.; Zhang, G. Structural characterization of water-soluble polysaccharides from *Opuntia monacantha* cladodes in relation to their anti-glycated activities. *Food Chem.* **2007**, *105*, 1480–1486. [CrossRef]
22. Vijayabaskar, P.; Babinastarlin, S.; Shankar, T.; Sivakumar, T.; Anandapandian, K.T.K. Quantification and characterization of exopolysaccharides from *Bacillus subtilis* (MTCC 121). *Adv. Biol. Res.* **2011**, *5*, 71–76.
23. Lim, J.M.; Joo, J.H.; Kim, H.O.; Kim, H.M.; Kim, S.W.; Hwang, H.J.; Yun, J.W. Structural analysis and molecular characterization of exopolysaccharides produced by submerged mycelial culture of *Collybia maculata* TG-1. *Carbohydr. Polym.* **2005**, *61*, 296–303. [CrossRef]
24. Zhang, Y.; Zhou, T.; Wang, H.; Cui, Z.; Cheng, F.; Wang, K.P. Structural characterization and *in vitro*, antitumor activity of an acidic polysaccharide from *Angelica sinensis*, (Oliv.) Diels. *Carbohydr. Polym.* **2016**, *147*, 401–408. [CrossRef] [PubMed]
25. Jeff, I.B.; Li, S.; Peng, X.; Kassim, R.M.; Liu, B.; Zhou, Y. Purification, structural elucidation and antitumor activity of a novel mannogalactoglucan from the fruiting bodies of *Lentinus edodes*. *Fitoterapia* **2013**, *84*, 338–346. [CrossRef] [PubMed]
26. Xia, Y.G.; Liang, J.; Yang, B.Y.; Wang, Q.H.; Kuang, H.X. Structural studies of an arabinan from the stems of *Ephedra sinica* by methylation analysis and 1D and 2D-NMR spectroscopy. *Carbohydr. Polym.* **2015**, *121*, 449–456. [CrossRef] [PubMed]

27. Sen, I.K.; Mandal, A.K.; Chakraborty, R.; Behera, B.; Yadav, K.K.; Maiti, T.K.; Islam, S.S. Structural and immunological studies of an exopolysaccharide from *Acinetobacter junii* BB1A. *Carbohydr. Polym.* **2014**, *101*, 188–195. [CrossRef]
28. Jeff, I.B.; Yuan, X.; Sun, L.; Kassim, R.M.; Foday, A.D.; Zhou, Y. Purification and in vitro anti-proliferative effect of novel neutral polysaccharides from *Lentinus edodes*. *Int. J. Biol. Macromol.* **2013**, *52*, 99–106. [CrossRef] [PubMed]
29. Gong, Y.J.; Zhang, J.; Gao, F.; Zhou, J.W.; Xiang, Z.N.; Zhou, C.G.; Wan, L.S.; Chen, J.C. Structure features and in vitro hypoglycemic activities of polysaccharides from different species of Maidong. *Carbohydr. Polym.* **2017**, *173*, 215–222. [CrossRef] [PubMed]
30. Fang, T.T.; Zirrolli, J.; Bendiak, B. Differentiation of the anomeric configuration and ring form of glucosyl-glycolaldehyde anions in the gas phase by mass spectrometry: isomeric discrimination between m/z 221 anions derived from disaccharides and chemical synthesis of *m/z* 221 standards. *Carbohydr Res.* **2007**, *342*, 217–235. [CrossRef] [PubMed]
31. Coffin, A.B.; Rubel, E.W.; Raible, D.W. Bax, Bcl2, and P53 differentially regulate neomycin- and gentamicin-induced hair cell death in the zebrafish lateral line. *J. Assoc. Res. Oto.* **2013**, *14*, 645–659. [CrossRef]
32. Wilkinson, J.F.; Dudman, W.F.; Aspinall, G.O. The extracellular polysaccharide of *Aerobacter aerogenes* A3 (S1) (*Klebsiella* type 54). *Biochem. J.* **1955**, *59*, 446–451. [CrossRef]
33. Dubois, M.; Gilles, K.A.; Rebers, P.A.; Smith, F. Colorimetric method for determination of sugar and related substances. *Anal. Chem.* **1956**, *28*, 350–356. [CrossRef]
34. Chen, Y.; Mao, W.; Wang, B.; Zhou, L.; Gu, Q.; Chen, Y.; Zhao, C.; Li, N.; Wang, C.; Shan, J.; et al. Preparation and characterization of an extracellular polysaccharide produced by the deep-sea fungus *Penicillium griseofulvum*. *Bioresource Technol.* **2013**, *132*, 178–181. [CrossRef] [PubMed]
35. Seedevi, P.; Moovendhan, M.; Viramani, S.; Shanmugam, A. Bioactive potential and structural chracterization of sulfated polysaccharide from seaweed (*Gracilaria corticata*). *Carbohydr. Polym.* **2017**, *155*, 516–524. [CrossRef] [PubMed]
36. Ou, H.C.; Santos, F.; Raible, D.W.; Simon, J.A.; Rubel, E.W. Drug screening for hearing loss: using the zebrafish lateral line to screen for drugs that prevent and cause hearing loss. *Drug Discov. Today* **2010**, *15*, 265–271. [CrossRef] [PubMed]
37. Kalinec, G.M.; Webster, P.; Lim, D.J.; Kalinec, F. A cochlear cell line as an in vitro system for drug ototoxicity screening. *Audiol. Neurootol.* **2003**, *8*, 177–189. [CrossRef] [PubMed]
38. Song, J.J.; Lee, J.D.; Lee, B.D.; Chae, S.W.; Park, M.K. Effect of diesel exhaust particles on human middle ear epithelial cells. *J. Assoc. Res. Oto.* **2012**, *76*, 334–338. [CrossRef]
39. Rah, Y.C.; Choi, J.; Yoo, M.H.; Yum, G.; Park, S.; Oh, K.H.; Lee, S.H.; Kwon, S.Y.; Cho, S.H.; Kims, S.; et al. Ecabet sodium alleviates neomycin-induced hair cell damage. *Free Radical Bio. Med.* **2015**, *89*, 1176–1183. [CrossRef]
40. Li, H.; Song, Y.; He, Z.; Chen, X.; Wu, X.; Li, X.; Bai, X.; Liu, W.; Li, B.; Wang, S.; et al. Meclofenamic acid reduces reactive oxygen species accumulation and apoptosis, inhibits excessive autophagy, and protects hair cell-like HEI-OC1 cells from cisplatin-induced damage. *Front Cell Neurosci.* **2018**, *12*, 139. [CrossRef]

Sample Availability: Samples of the compounds are not available from the authors.

molecules

MDPI

Article

Rare Earth Hydroxide as a Precursor for Controlled Fabrication of Uniform β-$NaYF_4$ Nanoparticles: A Novel, Low Cost, and Facile Method

Lili Xu [1], Man Wang [1], Qing Chen [1], Jiajia Yang [1], Wubin Zheng [1], Guanglei Lv [1,*], Zewei Quan [2,*] and Chunxia Li [1,*]

[1] Key Laboratory of the Ministry of Education for Advanced Catalysis Materials, Zhejiang Normal University, Jinhua 321004, China; 18329016701@163.com (L.X.); 15500100396@zjnu.edu.cn (M.W.); 1369976191@zjnu.edu.cn (Q.C.); 1547533672@zjnu.edu.cn (J.Y.); 13636130@zjnu.edu.cn (W.Z.)

[2] Department of Chemistry, Southern University of Science and Technology, Shenzhen 518055, China

* Correspondence: guanglei@zjnu.edu.cn (G.L.); quanzw@sustc.edu.cn (Z.Q.); cxli@zjnu.edu.cn (C.L.); Tel.: +86-0579-82282269 (G.L. & C.L.); +86-0755-88018399 (Z.Q.)

Received: 31 December 2018; Accepted: 17 January 2019; Published: 19 January 2019

Abstract: In recent years, rare earth doped upconversion nanocrystals have been widely used in different fields owing to their unique merits. Although rare earth chlorides and trifluoroacetates are commonly used precursors for the synthesis of nanocrystals, they have certain disadvantages. For example, rare earth chlorides are expensive and rare earth trifluoroacetates produce toxic gases during the reaction. To overcome these drawbacks, we use the less expensive rare earth hydroxide as a precursor to synthesize β-$NaYF_4$ nanoparticles with multiform shapes and sizes. Small-sized nanocrystals (15 nm) can be obtained by precisely controlling the synthesis conditions. Compared with the previous methods, the current method is more facile and has lower cost. In addition, the defects of the nanocrystal surface are reduced through constructing core–shell structures, resulting in enhanced upconversion luminescence intensity.

Keywords: β-$NaYF_4$; rare earth upconversion nanoparticles; core–shell structure

1. Introduction

In recent years, Lanthanide (Ln^{3+})-doped upconversion nanoparticles (UCNPs) that convert low energy photons into high energy photons through a two- or multi-photon absorption mechanism have extensively attracted researchers' attention due to their potential applications in a variety of fields, such as bioimaging [1–8], biosensing [9,10], drug delivery [11,12], and cancer therapy [13–16]. Compared with traditional fluorescent probes, such as organic fluorescent dyes and semiconductor quantum dots, UCNPs possess some unique advantages, including weak background fluorescence, large anti-Stokes shift, high photochemical stability, narrow emission bandwidth, long luminescent lifetime, high penetration depth, and low toxicity, among others [17–24]. Among reported UCNPs, hexagonal phase (β-) sodium yttrium fluoride has been shown to be one of most efficient host materials owing to its low photon cutoff energy (~350 cm^{-1}) and high chemical stability, which are able to effectively reduce non-radiative energy losses at the intermediate states of lanthanide ions [25]. So far, several methods have been reported to synthesize lanthanide-doped β-$NaYF_4$ nanoparticles with controlled crystalline phase, shape, and size. Solvothermal method and thermal decomposition methods are two of the most frequently used techniques to synthesize monodisperse lanthanide-doped β-$NaYF_4$ nanoparticles. For example, Haase reported the synthesis of β-$NaYF_4$ by using expensive rare earth chlorides as precursors [26]. Capobianco and co-workers synthesized β-$NaYF_4$ nanocrystals co-doped with Yb^{3+}/Er^{3+} or Yb^{3+}/Tm^{3+} via the thermal decomposition of rare earth trifluoroacetate

precursors where octadecene (ODE) and oleic acid (OA) were chosen as a solvent and ligand, respectively [27]. However, there are disadvantages in this method, such as the high synthetic temperature, the complicated decomposition process, and the uncontrollable experimental conditions. More importantly, the heating of trifluoroacetate would produce toxic fluorinated and oxyfluorinated carbon gases.

In this paper, we developed a novel method by using cheap rare earth hydroxide as a precursor to synthesize monodisperse hexagonal $NaYF_4$:Yb^{3+}/Ln^{3+} core and $NaYF_4$:Yb^{3+}/Ln^{3+}@$NaGdF_4$ (Ln = Er, Tm, and Ho) core–shell nanoparticles with well-defined shapes. Compared with the previous methods, this method is low-cost and more facile. Moreover, during the reaction process no toxic gases are produced. In addition, the size of nanocrystals can be tuned by controlling the reaction conditions, such as the molar ratio of Na^+/Ln^{3+}/F^-, the volume ratio of OA and ODE, and the amount of sodium oleate (NaOA). Under 980 nm laser excitation, these core–shell nanoparticles showed intense upconversion emissions relative to $NaYF_4$:Yb/Ln (Ln = Er, Tm, and Ho) core nanoparticles.

2. Results and Discussion

It is well known that for the synthesis of nanomaterials, sodium sources and fluorine sources are two important factors in affecting the morphology and size of nanocrystals. In our experiments, we explored the effects of sodium hydroxide (NaOH), sodium oleate (NaOA), sodium trifluoroacetate (CF_3COONa), and sodium fluoride (NaF) on the morphology and size of nanocrystals. It can be easily seen that the particle size was uneven when CF_3COONa (Figure 1A) and NaF (Figure 1B) were used as sodium sources. Moreover, their powder X-ray diffraction (XRD) patterns were in line with the standard cubic one of JCPDS 06-0342 (Figure 1E). The broader width (red pentagram) of the XRD was ascribed to the peak of silica from the slide. However, $NaYF_4$:Yb^{3+}/Er^{3+} nanoparticles obtained with NaOH (Figure 1C) or NaOA (Figure 1D) as sodium sources had a uniform size and a crystal phase that matched well the standard JCPDS 16-0334 of β-$NaYF_4$ (Figure 1E). In addition, the size of the upconverting nanoparticles synthesized with NaOA was smaller than that of NaOH. This means NaOA can effectively inhibit the growth of $NaYF_4$ because of extra OA–ligands from NaOA. Taken together, the sodium source has a great influence on the size and crystal phase of the nanocrystals.

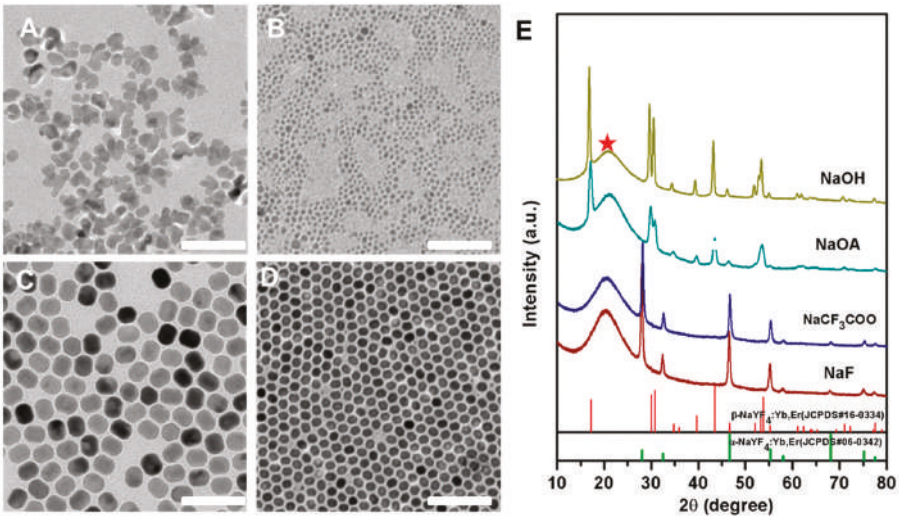

Figure 1. TEM images of $NaYF_4$:Yb^{3+}/Er^{3+} nanocrystals synthesized with NaOH (**A**), NaOA (**B**), CF_3COONa (**C**), and NaF (**D**) as well as the corresponding XRD patterns (**E**). The red pentagram represents the peak of silica from the slide. The standard diffraction patterns of the α-$NaYF_4$ (JCPDS 06-0342) and the β-$NaYF_4$ (JCPDS 16-0334) are displayed at the bottom for reference. Scale bars, 100 nm.

Based on the above results, we firstly used NaOH as sodium sources to explore the effect of $Na^+/Ln^{3+}/F^-$ on the size and morphology of nanocrystals. A series of $NaYF_4$:Yb^{3+}/Er^{3+} nanocrystals were synthesized with different ratios of $Na^+/Ln^{3+}/F^-$ when the volume ratio of OA/ODE was fixed. Figure 2 presents the TEM images and size distributions of the $NaYF_4$:Yb^{3+}/Er^{3+} nanocrystals. It can be clearly seen that when the molar ratio $Na^+/Ln^{3+}/F^-$ increased, the particle size of the products decreased accompanied by the shape evolution from rod to sphere. When the molar ratio of $Na^+/Ln^{3+}/F^-$ was 2.5:1:4, the nanoparticles are regular rods with good monodispersity. Their lengths and widths are 32 nm and 27 nm (Figure 2A,B and Figure S1, Supporting Information), which are obtained by randomly measuring more than 150 particles. When the ratio of $Na^+/Ln^{3+}/F^-$ was increased from 2.5:1:4 to 4:1:4, the size of the nanocrystals was reduced from 32.7 to 27.7 nm. It has been reported that the simultaneous addition of Na^+ and F^- in the solution can produce small β-phase seeds, thereby the final growth of small-sized nanocrystals can be controlled easily [28]. Moreover, the size of the nanocrystals was decreased from 25 to 23 nm when the molar ratio of $Na^+/Ln^{3+}/F^-$ was increased to be 6:1:6 (Figure 2G,H). When the molar ratio was further increased to 8:1:8 (Figure 2I,J), the size of the nanocrystals was reduced to 22 nm.

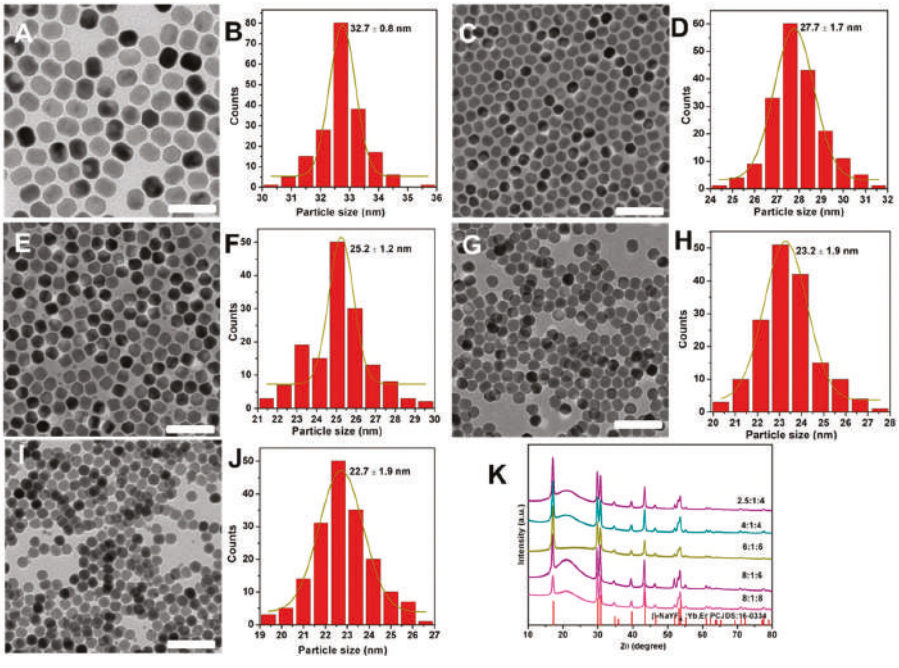

Figure 2. TEM images and size histograms of $NaYF_4$:Yb^{3+}/Er^{3+} nanocrystals synthesized with NaOH by using $Na^+/Ln^{3+}/F^-$ with a molar ratio of 2.5:1:4 (**A**,**B**), 4:1:4 (**C**,**D**), 6:1:6 (**E**,**F**), 8:1:6 (**G**,**H**), and 8:1:8 (**I**,**J**), respectively, as well as the corresponding XRD patterns (**K**); the standard diffraction pattern of the β-$NaYF_4$ (JCPDS 16-0334) is depicted at the bottom for reference. Scale bars, 100 nm.

To clarify the role of NaOA, we further studied the effect of its amount on the synthesis of $NaYF_4$:Yb^{3+}/Er^{3+} nanocrystals. Herein, we used NaOA substitute for NaOH to synthesize diverse nanoparticles with different molar ratios of $Na^+/Ln^{3+}/F^-$. Figure 3 shows the TEM images of as-synthesized $NaYF_4$:Yb^{3+}/Er^{3+} nanocrystals, which exhibited the morphology and size evolution. As expected, the morphology of the nanocrystals changed from rods to spheres. Meanwhile, the size was reduced from about 24 to 16 nm. As the amount of NaOA increased from 1.5 to 2.5 mmol, the size of the nanocrystals decreased to 20 nm (Figure 3A–D). Then the size of $NaYF_4$:Yb^{3+}/Er^{3+} nanocrystals

was further decreased to about 17 nm when the amount of NaOA increased to 6 mmol (Figure 3E,F) and 8 mmol (Figure 3G,H), respectively. It was possible that oxygen moiety in the OA–ligands had a much stronger binding affinity to Y^{3+} ions when there were adequate OA–ligands with the increased of NaOA.

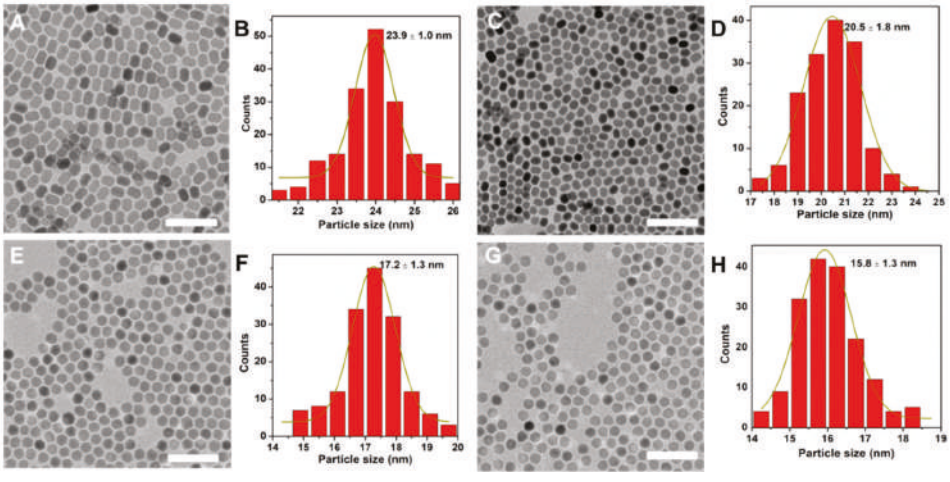

Figure 3. TEM images and size histograms of $NaYF_4$:Yb^{3+}/Er^{3+} nanocrystals synthesized with NaOA by using Na^+/Ln^{3+}/F^- withmolar ratios of 1.5:1:4 (**A**,**B**), 2.5:1:4 (**C**,**D**), 6:1:4 (**E**,**F**), and 8:1:4 (**G**,**H**), respectively. Scale bars, 100 nm.

The OA–ligands can effectively induce the orderly arrangement of Y^{3+} ions during the formation process of $NaYF_4$ [29]. Additionally, when the amount of OA–ligands was adequate, they would cover the surface of the nanoparticles to inhibit the growth of nanocrystals, which is an effective method to obtain the nanocrystals with a smaller size. Figure S2 (Supporting Information) shows the XRD patterns of the as-prepared $NaYF_4$:Yb^{3+}/Er^{3+} core nanoparticles. All the XRD patterns of samples could be matched with the pure hexagonal-phases $NaYF_4$ (JCPDS 16-0334), and no trace of other phases or impurities were observed, which clearly suggests the high crystallinities of these as-prepared nanoparticles. It has been reported that the presence of oleic acid in the solvent plays an important role in tuning the size and morphology of $NaYF_4$:Yb^{3+}/Er^{3+} nanocrystals [30]. Figure 4 shows the TEM images and size distributions of $NaYF_4$:Yb^{3+}/Er^{3+} nanoparticles prepared at different ratios of OA/ODE of 4/15 (Figure 4A,B), 8/15 (Figure 4C,D), 10/15 (Figure 4E,F), and 15/15 (Figure 4H,I). As can be seen, the resulting $NaYF_4$:Yb^{3+}/Er^{3+} nanoparticles with the ratio of OA/ODE (4/15) were hexagonal in shape with an average diameter of about 26 nm. With the increased volume ratio of OA/ODE, the particle size of $NaYF_4$:Yb^{3+}/Er^{3+} nanoparticles gradually increased, and the average diameter of nanoparticles was found to be approximately 40 nm at 8/15 of OA/ODE. The XRD of all as-prepared samples are shown in Figure S3 (Supporting Information). The same procedure was used to further synthesize $NaYF_4$ nanoparticles doped with other lanthanide elements such as 40% Yb^{3+}/0.5%Tm^{3+} (Figure S3A,B) and 18% Yb^{3+}/2% Ho^{3+} (Figure S3C,D, Supporting Information), respectively. It was observed that the size and morphology of the nanoparticles closely resembled those of the Yb^{3+}/Er^{3+} co-doped $NaYF_4$ counterpart (Figure S1, Supporting Information). These results indicate that the change of dopant ions in low doping concentrations does not alter the particle growth process [31].

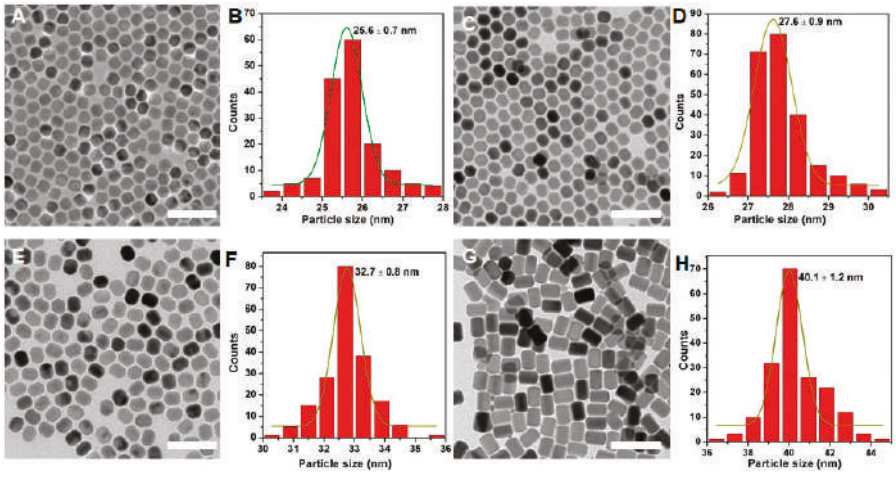

Figure 4. TEM images and size histograms of $NaYF_4$:Yb^{3+}/Er^{3+} nanocrystals synthesized at varied amounts of oleic acid (OA). The volume ratios of OA and octadecene (ODE) are 4:15 (**A**,**B**), 8:15 (**C**,**D**), 10:15 (**E**,**F**), and 15:15 (**G**,**H**), respectively. Scale bars, 100 nm.

More importantly, the emission intensity of Ln^{3+} doped UCNPs depends on dopant–host combination, particle size, shape, and phase [32–38]. The emission intensity of $NaYF_4$ core was relatively weak due to the surface defects. However, in recent years, the construction of core–shell structure has been one of the effective ways to improve the efficiency of upconversion luminescence [26,39–42]. This is because the inert shell coating can protect the luminescent activators in the core nanoparticles from the surface quenching of excitation energy [42]. In this paper, we prepared $NaYF_4$:Yb^{3+}/Ln^{3+}@$NaGdF_4$ and studied their upconversion optical properties. Figure 5A–F displays the TEM images and the corresponding size distribution of $NaYF_4$:Yb^{3+}/Ln^{3+}@$NaGdF_4$ core–shell nanoparticles. The $NaYF_4$:Yb^{3+}/Er^{3+} core-only nanoparticles with an average diameter of about 27 nm are shown in Figure S1. After coating an inert shell layer of $NaGdF_4$, the average diameter of $NaYF_4$:Yb^{3+}/Er^{3+}@$NaGdF_4$ core–shell was determined to be about 42 nm, which means a thick shell layer (thickness ~7.5 nm) was coated around the $NaYF_4$:Yb^{3+}/Er^{3+} core nanoparticles (Figure 5A,B). Similar TEM image and size distribution were obtained for $NaYF_4$:Yb^{3+}/Tm^{3+}@$NaGdF_4$ (Figure 5C,D) and $NaYF_4$:Yb^{3+}/Ho^{3+}@$NaGdF_4$ (Figure 5E,F) core–shell nanoparticles. The corresponding shell thickness was determined to be about 11 nm and 9 nm, respectively. Figure 5G depicts the upconversion emission spectra for the $NaYF_4$:Yb^{3+}/Er^{3+} core nanoparticles and the $NaYF_4$:Yb^{3+}/Er^{3+}@$NaGdF_4$ core–shell nanoparticles. As can be seen, there were two green emission bands centered at 520 nm and 540 nm, which were attributed to the electronic transition of $^2H_{11/2} \rightarrow {}^4I_{15/2}$, $^4S_{3/2} \rightarrow {}^4I_{15/2}$ of Er^{3+}. In addition, there was a red emission at 654 nm, which corresponded to the $^4F_{9/2} \rightarrow {}^4I_{15/2}$ transition of Er^{3+}. For the $NaYF_4$:Yb^{3+}/Er^{3+} core, after coating 7.5 nm $NaGdF_4$ shell, the fluorescence intensity of $NaYF_4$:Yb^{3+}/Er^{3+}@$NaGdF_4$ core–shell nanoparticles was about 100 times higher than that of $NaYF_4$:Yb^{3+}/Er^{3+} core nanoparticles at 540 nm. In contrast, for the $NaYF_4$:Yb^{3+}/Tm^{3+} core nanoparticles, the blue emissions, the ultraviolet emission, and red emission corresponded to the ($^1I_6 \rightarrow {}^3F_4$, 342 nm, $^1D_2 \rightarrow {}^3H_6$, 360 nm), ($^1D_2 \rightarrow {}^3F_4$, 450 nm, $^1G_4 \rightarrow {}^3H_6$, 475 nm), ($^1G_4 \rightarrow {}^3F_4$, 647 nm) transitions of Tm^{3+} ions, respectively. Due to the $NaGdF_4$ (~11 nm) shell coating, the emission intensity was remarkably enhanced to about 120 times at 475 nm (Figure 5G). Figure 5H shows the upconversion emission spectra of the $NaYF_4$:Yb^{3+}/Ho^{3+} core nanoparticles and the $NaYF_4$:Yb^{3+}/Ho^{3+}@$NaGdF_4$ core–shell nanoparticles. When excited at 980 nm, three upconversion fluorescence bands with maxima at green (540 nm), red (645 nm), and 750 nm regions could be observed from optimized $NaYF_4$:Yb^{3+}/Ho^{3+} nanophosphors, which corresponded to $^5S_2 \rightarrow {}^5I_8$, $^5F_3 \rightarrow {}^5I_8$, and $^5S_2 \rightarrow {}^5I_7$ transitions of Ho^{3+} ions. Similarly, when the ~9 nm $NaGdF_4$ shell was covered on the surface

of the $NaYF_4$:Yb^{3+}/Ho^{3+} core, the luminescence intensity was also significantly improved. The emission intensity of $NaYF_4$:Yb^{3+}/Ho^{3+}@$NaGdF_4$ core–shell nanoparticles was determined to be about 80 times as strong as that of $NaYF_4$:Yb^{3+}/Ho^{3+} core nanoparticles.

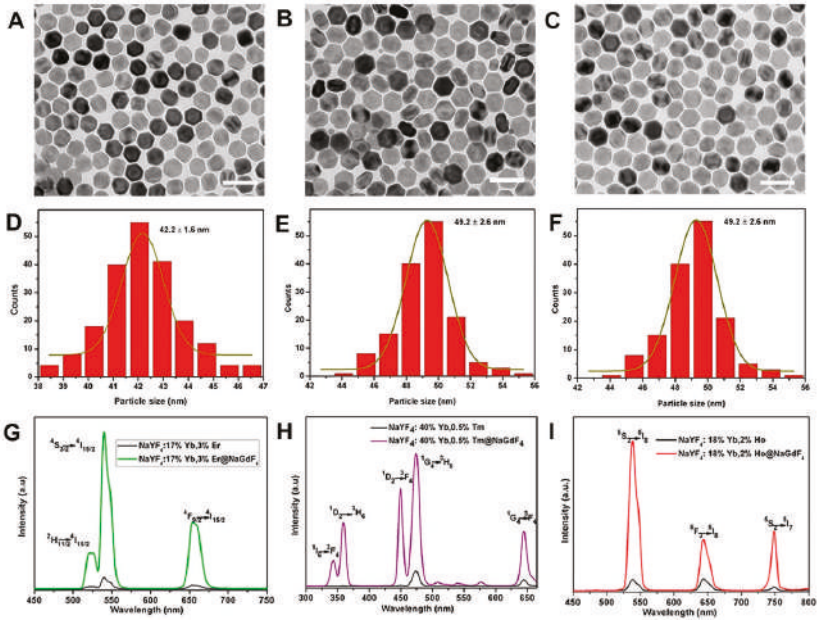

Figure 5. TEM images, size histograms, and the corresponding upconversion spectra of core–shell structured $NaYF_4$:Yb^{3+}/Er^{3+}@$NaGdF_4$ (**A**,**D**,**G**), $NaYF_4$: Yb^{3+}/Tm^{3+}@$NaGdF_4$ (**B**,**E**,**H**), and $NaYF_4$:Yb^{3+}/Ho^{3+}@$NaGdF_4$ (**C**,**F**,**I**), respectively. Scale bars, 100 nm.

3. Materials and Methods

3.1. Materials

Materials Y_2O_3 (99.99%), Yb_2O_3 (99.99%), Er_2O_3 (99.99%), Tm_2O_3 (99.99%), Ho_2O_3 (99.99%), Y_2O_3 (99.99%), $GdCl_3{\cdot}6H_2O$ (99.99%), NH_4F (98%), NaF (98%), and CF_3COONa (97%) were purchased from Aladdin (Shanghai, China). Oleic acid (OA, 90%), 1-octadecene (ODE, 90%), and sodium oleate (Na-OA, >97%) were purchased from Sigma-Aldrich (Darmstadt, Germany). Other chemical reagents, such as NaOH (90%), ethyl alcohol (99.7%), methanol (99.5%), and *n*-hexane (97%), were obtained from Shanghai Lingfeng Chemical Reagent Co., Ltd. All chemicals were used as received without further purification.

Rare earth chloride ($LnCl_3$) stock solutions of 1 M (Ln = Y, Yb) and 0.1 M (Ln = Er, Tm, and Ho) were prepared by dissolving the corresponding metal oxides in hydrochloric acid at elevated temperature. The final solutions were adjusted to pH ~6.

3.2. Synthesis of β-$NaYF_4$:Yb^{3+}/Ln^{3+} (Ln = Er, Tm and Ho) Core Nanoparticles

First, $Ln(OH)_3$ (Ln = Y^{3+}, Yb^{3+}, and Er^{3+}/Tm^{3+}/Ho^{3+}) complexes were prepared by adding NaOH of 2 M to the rare earth chloride solution, and then the obtained product was washed twice. Rare earth hydroxide was added to a 100 mL flask containing 10 mL of OA and 15 mL of ODE. The mixture was heated at 140 °C for 1 h under stirring in order to form the lanthanide–oleate complexes. After cooling down to 40 °C naturally, 8 mL of methanol solution containing NH_4F (4 mmol) and NaOH (2.5 mmol) was added. Subsequently, the resulting mixture solution was heated at 70 °C for 10 min to evaporate

the methanol under magnetic stirring. After the temperature was raised up to 110 °C under vacuum for 30 min, the reaction mixture was heated to 300 °C under argon for 1 h and then cooled down to room temperature. The resulting nanoparticles were precipitated by adding excess ethanol, separated by centrifugation at 4000 rpm for 4 min, washed with a mixture of *n*-hexane and ethanol several times, and finally dispersed in *n*-hexane for further use.

3.3. Synthesis of β-$NaYF_4$:Yb/Ln@$NaGdF_4$ (Ln = Er, Tm, and Ho) Core–Shell Nanoparticles

In a typical procedure for the synthesis of $NaYF_4$:Yb^{3+}/Er^{3+} (17/3%)@$NaGdF_4$ nanoparticles, the $NaGdF_4$ inert shell precursor was prepared by mixing 0.5 mmol of $GdCl_3$ with 6 mL of OA and 15 mL of ODE in a 100 mL flask followed by heating at 150 °C for 40 min. Then, the obtained $NaGdF_4$ inert shell precursor was cooled down to room temperature. Subsequently, the $NaYF_4$:Yb^{3+}/Er^{3+} (17/3%) core-only nanoparticles dispersed in 3 mL of cyclohexane along with 8 mL of methanol solution of NH_4F (2 mmol) and NaOH (1.25 mmol) was added. Subsequently, the resulting mixture solution was heated at 70 °C for 10 min under magnetic stirring to evaporate the methanol. After the resulting solution for 30 min at 110 °C under vacuum, the reaction mixture was heated to 310 °C under argon for 1.5 h and then cooled down to room temperature. Finally, the obtained core–shell nanoparticle products were precipitated by the addition of ethanol, collected by centrifugation at 4000 rpm for 4 min, washed with a mixture of *n*-hexane and ethanol several times, and finally dispersed in *n*-hexane.

3.4. Instrumentation

Transmission electron microscopy (TEM) images (Hitachi, Tokyo, Japan) were acquired on a HT7700 transmission electron microscopy at an acceleration voltage of 100 kV. X-ray diffraction (XRD) patterns were recorded on an X-ray diffraction (RigakuSmartLab, Tokyo, Japan) with Cu Kαradiation (λ = 0.15418 nm) at a voltage of 45 kV and a current of 20 mA. Upconversion luminescence spectra were detected by a spectrophotometer (FluoroMax-4, Shanghai, China) equipped with a 980 nm diode laser.

4. Conclusions

In summary, we developed a novel, facile, and low-cost method to synthesize Yb^{3+}/Ln^{3+} (Ln = Er, Tm, and Ho) co-doped β-$NaYF_4$ nanocrystals. The size and morphology of the products were manipulated through the precise tuning of the ratio of Na^+/Ln^{3+}/F^-, the ratio of OA/ODE, and the quantity of the NaOA. As the ratio of Na^+/Ln^{3+}/F^- and the amount of NaOA increased, the size of the nanocrystals gradually decreased and the corresponding morphologies evolved from nanospheres to nanorods. Finally, this method can also apply to the fabrication of core–shell structured nanomaterials. The uniform $NaYF_4$:Yb^{3+}/Ln^{3+}@$NaGdF_4$ core–shell nanoparticles were prepared successfully, and their emission intensity was remarkably enhanced, which could provide prospect applications in the biomedical fields. Particularly, some photosensitizers or chemotherapy drugs could be conjugated with these UCNPs to achieve NIR-triggered drug delivery and controlled release to ameliorate the therapy efficiency of tumors.

Supplementary Materials: The following are available online, Figure S1: TEM image (A) and the corresponding size histogram (B) of $NaYF_4$:Yb^{3+}/Er^{3+} nanocrystals synthesized with NaOH as sodium source, Figure S2: XRD patterns of the as-synthesized $NaYF_4$:Yb^{3+}/Er^{3+} nanocrystals with NaOA at varied molar ratios of Na^+/Ln^{3+}/F^-. The standard diffraction patterns of the β-$NaYF_4$ (JCPDS 16-0334) depicted at the bottom for reference, Figure S3: XRD patterns of the as-synthesized $NaYF_4$:Yb^{3+}/Er^{3+} nanocrystals at varied amounts of oleic acid. The volume ratios of oleic acid and octadecene are 15:15, 10:15, 8:15, and 4:15, respectively. The diffraction pattern at the bottom is the literature reference for hexagonal $NaYF_4$ nanocrystal (JCPDS 16-0334), Figure S4: TEM images and size histograms of the $NaYF_4$:Yb^{3+}/Er^{3+} (A, B), and $NaYF_4$: Yb^{3+}/Ho^{3+} (C, D), respectively.

Author Contributions: Conceptualization, L.X. and G.L.; investigation and data curation, M.W. and Q.C.; writing and original draft preparation, L.X. and J.Y.; writing, reviewing, and editing, W.Z., C.L. and G.L.; and supervision, G.L., Z.Q. and C.L.

Funding: This research was funded by the National Natural Science Foundation of China (51572258, 51872263 and 51772142), Zhejiang Provincial Natural Science Foundation of China (LZ19E020001 and LQ19B050003), the Key Construction Project (2017XM022) of Zhejiang Normal University and Open Research Fund of Key Laboratory of the Ministry of Education for Advanced Catalysis Materials, and Zhejiang Key Laboratory for Reactive Chemistry on Solid Surfaces, Zhejiang Normal University.

Conflicts of Interest: The authors declare no conflict of interest.

References

1. Park, I.; Lee, K.T.; Suh, Y.D.; Hyeon, T. Upconverting nanoparticles: A versatile platform for wide-field two-photon microscopy and multi-modal in vivo imaging. *Chem. Soc. Rev.* **2015**, *44*, 1302–1317. [CrossRef] [PubMed]
2. Dong, H.; Sun, L.D.; Wang, Y.F.; Ke, J.; Si, R.; Xiao, J.W.; Lyu, G.M.; Shi, S.; Yan, C.H. Efficient Tailoring of Upconversion Selectivity by Engineering Local Structure of Lanthanides in Na_xREF_{3+x} Nanocrystals. *J. Am. Chem. Soc.* **2015**, *137*, 6569–6576. [CrossRef] [PubMed]
3. Wolfbeis, O.S. An overview of nanoparticles commonly used in fluorescent bioimaging. *Chem. Soc. Rev.* **2015**, *44*, 4743–4768. [CrossRef]
4. Wei, Z.W.; Sun, L.N.; Liu, J.L.; Zhang, J.Z.; Yang, H.R.; Yang, Y.; Shi, L.Y. Cysteine modified rare-earth up-converting nanoparticles for in vitro and in vivo bioimaging. *Biomaterials* **2014**, *35*, 387–392. [CrossRef] [PubMed]
5. Zhang, H.; Wu, Y.; Wang, J.; Tang, Z.M.; Ren, Y.; Ni, D.L.; Gao, H.B.; Song, R.X.; Jin, T.; Li, Q.; et al. In Vivo MR Imaging of Glioma Recruitment of Adoptive T-Cells Labeled with NaGdF4-TAT Nanoprobes. *Small* **2017**, *14*, 1702951–1702959. [CrossRef] [PubMed]
6. Deng, M.L.; Wang, L.Y. Unexpected luminescence enhancement of upconverting nanocrystals by cation exchange with well retained small particle size. *Nano Res.* **2014**, *7*, 782–793. [CrossRef]
7. Xu, S.; Yu, Y.; Gao, Y.F.; Zhang, Y.Q.; Li, X.P.; Zhang, J.S.; Wang, Y.F.; Chen, B.J. Mesoporous silica coating $NaYF_4$:Yb,Er@$NaYF_4$ upconversion nanoparticles loaded with ruthenium(II) complex nanoparticles: Fluorometric sensing and cellular imaging of temperature by upconversion and of oxygen by downconversion. *Microchim. Acta* **2018**, *185*, 454–463. [CrossRef] [PubMed]
8. Lei, X.L.; Li, R.F.; Tu, D.T.; Shang, X.Y.; Liu, Y.; You, W.W.; Sun, C.X.; Zhang, F.; Chen, X.Y. Intense near-infrared-II luminescence from $NaCeF_4$:Er/Yb nanoprobes for in vitro bioassay and in vivo bioimaging. *Chem. Sci.* **2018**, *9*, 4682–4988. [CrossRef] [PubMed]
9. Liu, J.; Liu, Y.; Bu, W.; Bu, J.; Sun, Y.; Du, J.; Shi, J. Ultrasensitive Nanosensors Based on Upconversion Nanoparticles for Selective Hypoxia Imaging in vivo upon Near-Infrared Excitation. *J. Am. Chem. Soc.* **2014**, *136*, 9701–9709. [CrossRef] [PubMed]
10. Zheng, W.; Tu, D.T.; Huang, P.; Zhou, S.Y.; Chen, Z.; Chen, X.Y. Time-resolved luminescent biosensing based on inorganic lanthanide-doped nanoprobes. *Chem. Commun.* **2015**, *51*, 4129–4143. [CrossRef] [PubMed]
11. Jalani, G.; Tam, V.; Vetrone, F.; Cerruti, M. Seeing, Targeting and Delivering with Upconverting Nanoparticles. *J. Am. Chem. Soc.* **2018**, *140*, 10923–10931. [CrossRef] [PubMed]
12. Zhang, Y.; Yu, Z.Z.; Li, J.Q.; Ao, Y.X.; Xue, J.W.; Zeng, Z.P.; Yang, X.L.; Tan, T.T.Y. Ultrasmall-Superbright Neodymium-Upconversion Nanoparticles via Energy Migration Manipulation and Lattice Modification: 808 nm-Activated Drug Release. *ACS Nano* **2017**, *11*, 2846–2857. [CrossRef] [PubMed]
13. Zhang, C.; Chen, W.H.; Liu, L.H.; Qiu, W.X.; Yu, W.Y.; Zhang, X.Z. An O_2 Self-Supplementing and Reactive-Oxygen-Species-Circulating Amplifed Nanoplatform via H_2O/H_2O_2 Splitting for Tumor Imaging and Photodynamic Therapy. *Adv. Funct. Mater.* **2017**, *27*, 1700626–1700639. [CrossRef]
14. Lu, S.; Tu, D.T.; Hu, P.; Xu, J.; Li, R.F.; Wang, M.; Chen, Z.; Huang, M.D.; Chen, X.Y. Multifunctional Nano-Bioprobes Based on Rattle-Structured Upconverting Luminescent Nanoparticles. *Angew. Chem. Int. Ed.* **2015**, *54*, 7915–7919. [CrossRef] [PubMed]
15. Zhu, X.J.; Li, J.C.; Qiu, X.C.; Liu, Y.; Wang, F.; Li, F.Y. Upconversion nanocomposite for programming combination cancer therapy by precise control of microscopic temperature. *Nat. Commun.* **2018**, *9*, 2176–2186. [CrossRef] [PubMed]
16. Zhang, C.; Zhao, K.L.; Bu, W.B.; Ni, D.L.; Liu, Y.Y.; Feng, J.W.; Shi, J.L. Marriage of Scintillator and Semiconductor for Synchronous Radiotherapy and Deep Photodynamic Therapy with Diminished Oxygen Dependence. *Angew. Chem. Int. Ed.* **2015**, *54*, 1770–1774. [CrossRef]

17. Yang, D.M.; Ma, P.A.; Hou, Z.Y.; Cheng, Z.Y.; Li, C.X.; Lin, J. Current advances in lanthanide ion (Ln^{3+})-based upconversion nanomaterials for drug delivery. *Chem. Soc. Rev.* **2015**, *44*, 1416–1448. [CrossRef]
18. Liu, Y.S.; Tu, D.T.; Zhu, H.M.; Chen, X.Y. Photon upconversion nanomaterials. *Chem. Soc. Rev.* **2015**, *44*, 1299–1301. [CrossRef]
19. Zeng, S.J.; Wang, H.B.; Lu, W.; Yi, Z.G.; Rao, L.; Liu, H.R.; Hao, J.H. Dual-modal upconversion fluorescent/X-ray imaging using ligand-free hexagonal phase $NaLuF_4$:Gd/Yb/Er nanorods for blood vessel visualization. *Biomaterials* **2014**, *35*, 2934–2941. [CrossRef]
20. Wang, C.; Yao, W.X.; Wang, P.Y.; Zhao, M.Y.; Li, X.M.; Zhang, F. A catalase-loaded hierarchical zeolite as an implantable nanocapsule for ultrasound-guided oxygen self-sufficient photodynamic therapy against pancreatic cancer. *Adv. Mater.* **2018**, *30*, 1704833–1704840.
21. Chen, D.Q.; Chen, Y.; Lu, H.W.; Ji, Z.G. A Bifunctional Cr/Yb/Tm:$Ca_3Ga_2Ge_3O_{12}$ Phosphor with Near-Infrared Long-Lasting Phosphorescence and Upconversion Luminescence. *Inorg. Chem.* **2014**, *53*, 8638–8645. [CrossRef] [PubMed]
22. Shi, Z.L.; Duan, Y.; Zhu, X.J.; Wang, Q.W.; Li, D.D.; Hu, K.; Feng, W.; Li, F.Y.; Xu, C.X. Dual functional $NaYF_4$:Yb^{3+},Er^{3+}@$NaYF_4$:Yb^{3+}, Nd^{3+} core–shell nanoparticles for cell temperature sensing and imaging. *Nanotechnology* **2018**, *29*, 094001–094009. [CrossRef] [PubMed]
23. Dai, Y.L.; Xiao, H.H.; Liu, J.H.; Yuan, Q.H.; Ma, P.A.; Yang, D.M.; Li, C.X.; Cheng, Z.Y.; Hou, Z.Y.; Yang, P.P.; et al. In vivo multimodality imaging and cancer therapy by near-infrared light-triggered trans-platinum pro-drug-conjugated upconverison nanoparticles. *J. Am. Chem. Soc.* **2013**, *135*, 18920–18929. [CrossRef] [PubMed]
24. Yu, Z.S.; Xia, Y.Z.; Xing, J.; Li, Z.H.; Zhen, J.J.; Jin, Y.H.; Tian, Y.C.; Liu, C.; Jiang, Z.Q.; Li, J.; Wu, A.G. Y1-receptor–ligand-functionalized ultrasmall upconversion nanoparticles for tumortargeted trimodality imaging and photodynamic therapy with low toxicity. *Nanoscale* **2018**, *10*, 17038–17052. [CrossRef] [PubMed]
25. Wang, F.; Liu, X.G. Recent advances in the chemistry of lanthanide-doped upconversion nanocrystals. *Chem. Soc. Rev.* **2009**, *38*, 976–989. [CrossRef] [PubMed]
26. Homann, C.; Krukewitt, L.; Frenzel, F.; Grauel, B.; Wgrth, C.; Resch-Genger, U.; Haase, M. NaYF4:Yb,Er/NaYF4 Core/Shell Nanocrystals with High Upconversion Luminescence Quantum Yield. *Angew. Chem. Int. Ed.* **2018**, *57*, 8765–8769. [CrossRef]
27. Boyer, J.C.; Vetrone, F.; Cuccia, L.A.; Capobianco, J.A. Synthesis of colloidal upconverting $NaYF_4$ nanocrystals doped with Er^{3+}, Yb^{3+} and Tm^{3+}, Yb^{3+} via thermal decomposition of lanthanide trifluoracetate precursors. *J. Am. Chem. Soc.* **2006**, *128*, 7444–7445. [CrossRef]
28. Li, H.; Xu, L.; Chen, G.Y. Controlled Synthesis of Monodisperse Hexagonal $NaYF_4$:Yb/Er Nanocrystals with Ultrasmall Size and Enhanced Upconversion Luminescence. *Molecules* **2017**, *22*, 2113. [CrossRef]
29. Liu, D.M.; Xu, X.X.; Du, Y.; Qin, X.; Zhang, Y.H.; Ma, C.S.; Wen, S.H.; Ren, W.; Goldys, E.M.; Piper, J.A.; et al. Three-dimensional controlled growth of monodisperse sub-50 nm heterogeneous nanocrystals. *Nat. Commun.* **2016**, *7*, 10254–10261. [CrossRef]
30. Huang, X.Y. Synthesis, multicolour tuning, and emission enhancement of ultrasmall LaF_3:Yb^{3+}/Ln^{3+} (Ln = Er, Tm, and Ho) upconversion nanoparticles. *J. Mate. Sci.* **2016**, *51*, 3490–3499. [CrossRef]
31. Chen, G.Y.; Ågren, H.; Ohulchanskyy, T.Y.; Prasad, P.N. Light upconverting core–shell nanostructures: Nanophotonic control for emerging applications. *Chem. Soc. Rev.* **2015**, *44*, 1680–1713. [CrossRef] [PubMed]
32. Han, S.Y.; Deng, R.R.; Xie, X.J.; Liu, X.G. Enhancing Luminescence in Lanthanide-Doped Upconversion Nanoparticles. *Angew. Chem. Int. Ed.* **2014**, *53*, 11702–11715. [CrossRef] [PubMed]
33. Wang, F.; Han, Y.; Lim, C.S.; Lu, Y.H.; Wang, J.; Xu, J.; Chen, H.Y.; Zhang, C.; Hong, M.H.; Liu, X.G. Simultaneous phase and size control of upconversion nanocrystals through lanthanide doping. *Nature* **2010**, *463*, 1061–1065. [CrossRef] [PubMed]
34. Chen, X.; Jin, L.M.; Kong, W.; Sun, T.Y.; Zhang, W.F.; Liu, X.H.; Fan, J.; Yu, S.F.; Wang, F. Confining energy migration in upconversion nanoparticles towards deep ultraviolet lasing. *Nat. Commun.* **2016**, *7*, 10304–10309. [CrossRef] [PubMed]
35. Das, A.; Mao, C.; Cho, S.; Kim, K.; Park, W. Over 1000-fold enhancement of upconversion luminescence using water-dispersible metalinsulator-metal nanostructures. *Nat. Commun.* **2018**, *9*, 4828–4839. [CrossRef] [PubMed]
36. Cheng, T.; Marin, R.; Skripka, A.; Vetrone, F. Small and Bright Lithium-Based Upconverting Nanoparticles. *J. Am. Chem. Soc.* **2018**, *140*, 12890–12899. [CrossRef]

37. Moon, B.S.; Kim, H.E.; Kim, D.H. Ultrafast Single-Band Upconversion Luminescence in a Liquid-Quenched Amorphous Matrix. *Adv. Mater.* **2018**, *30*, 1800008. [CrossRef]
38. Cheng, X.W.; Pan, Y.; Yuan, Z.; Wang, X.W.; Su, W.H.; Yin, L.S.; Xie, X.J.; Huang, L. Er^{3+} Sensitized Photon Upconversion Nanocrystals. *Adv. Funct. Mater.* **2018**, *28*, 1800208–1800213. [CrossRef]
39. Xia, M.; Zhou, D.C.; Yang, Y.; Yang, Z.W.; Qiu, J.B. Synthesis of Ultrasmall Hexagonal $NaGdF_4$: $Yb^{3+}Er^{3+}$@$NaGdF_4$:Yb^{3+}@$NaGdF_4$: Nd^{3+} Active-Core/Active-Shell/Active-Shell Nanoparticles with Enhanced Upconversion Luminescence. *ECS J. Solid State Sci. Technol.* **2017**, *6*, R41–R46. [CrossRef]
40. Yi, G.S.; Chow, G.M. Water-soluble $NaYF_4$: Yb, Er(Tm)/$NaYF_4$/polymer core/shell/shell Nanoparticles with Significant Enhancement of Upconversion Fluorescence. *Chem. Mater.* **2007**, *19*, 341–343. [CrossRef]
41. Shi, R.K.; Ling, X.C.; Li, X.N.; Zhang, L.; Lu, M.; Xie, X.J.; Huang, L.; Huang, W. Tuning hexagonal $NaYbF_4$ nanocrystals down to sub-10 nm for enhanced photon upconversion. *Nanoscale* **2017**, *9*, 13739–13746. [CrossRef] [PubMed]
42. Liu, Y.; Tu, D.; Zhu, H.; Chen, X. Lanthanide-doped luminescent nanoprobes: Controlled synthesis, optical spectroscopy, and bioapplications. *Chem. Soc. Rev.* **2013**, *42*, 6924–6958. [CrossRef] [PubMed]

Sample Availability: Not available.

molecules

MDPI

Article

Fluoropolymer-Containing Opals and Inverse Opals by Melt-Shear Organization

Julia Kredel [1], Christian Dietz [2] and Markus Gallei [1,*]

[1] Ernst-Berl Institute of Technical and Macromolecular Chemistry, Technische Universität Darmstadt, Alarich-Weiss-Straße 4, 64287 Darmstadt, Germany; j.kredel@mc.tu-darmstadt.de

[2] Institute of Materials Science, Physics of Surfaces, Technische Universität Darmstadt, Alarich-Weiss-Str. 2, D-64287 Darmstadt, Germany; dietz@pos.tu-darmstadt.de

* Correspondence: m.gallei@mc.tu-darmstadt.de

Received: 22 December 2018; Accepted: 16 January 2019; Published: 17 January 2019

Abstract: The preparation of highly ordered colloidal architectures has attracted significant attention and is a rapidly growing field for various applications, e.g., sensors, absorbers, and membranes. A promising technique for the preparation of elastomeric inverse opal films relies on tailored core/shell particle architectures and application of the so-called melt-shear organization technique. Within the present work, a convenient route for the preparation of core/shell particles featuring highly fluorinated shell materials as building blocks is described. As particle core materials, both organic or inorganic (SiO_2) particles can be used as a template, followed by a semi-continuous stepwise emulsion polymerization for the synthesis of the soft fluoropolymer shell material. The use of functional monomers as shell-material offers the possibility to create opal and inverse opal films with striking optical properties according to Bragg's law of diffraction. Due to the presence of fluorinated moieties, the chemical resistance of the final opals and inverse opals is increased. The herein developed fluorine-containing particle-based films feature a low surface energy for the matrix material leading to good hydrophobic properties. Moreover, the low refractive index of the fluoropolymer shell compared to the core (or voids) led to excellent optical properties based on structural colors. The herein described fluoropolymer opals and inverse opals are expected to pave the way toward novel functional materials for application in fields of coatings and optical sensors.

Keywords: fluoropolymers; melt-shear organization; chemical resistance; solvent responsiveness; hydrophobicity; core/shell particles; emulsion polymerization; particle processing

1. Introduction

Fluor-containing polymers represent a unique class of functional materials combining different interesting properties, and such polymers have attracted significant attention in the recent past. Some of these properties are their remarkable resistance toward chemicals, high thermal stability, wetting behavior, and repellent capabilities, as well as their low refractive indices compared to other polymer materials [1–3]. Therefore, the field of applications for fluoropolymers is widespread and range over coatings, membranes, optical applications, and high performance elastomers [4–8]. Designing novel fluoropolymer and hierarchical architectures is relevant for the development of improved and new applications, for instance, in the field of three-dimensionally ordered porous coatings and photonic materials. In general, the control and understanding of surface properties is crucial for the development of advanced materials with well-defined wetting properties. Such so-called *smart surfaces* have already been used in applications such as self-cleaning surfaces, tunable optical lenses, lab-on-chip systems, microfluidic devices, and many different textile applications [9–14]. Considerable effort has been carried out on understanding the influence of designed, rough surfaces on the wetting properties, initiated by the pioneering works of Wenzel, Cassie, and Baxter long

ago [15,16]. Hierarchical particle-based architectures, such as colloidal crystals and inverse opals with adjustable dimensions, have gained considerable attention due to their tremendous potential for various applications in catalysis, separation, sensors, optics, and biomedicine [17–27]. In the case of porous materials, different templating approaches have been used for the design of the final materials after removal of the template material [28–33]. Colloidal crystals can be prepared by various techniques such as particle deposition or spin coating of respective particle dispersions [21,34]. For example, Kim et al. developed omniphobic inverse opals for the preparation of omniphobic porous materials some years ago [35]. Vogel et al. reported on the infiltration of inverse opals with lubricants for gaining access to highly repellent surfaces toward many different liquids [36]. By this elegant approach, the adsorption of liquid-borne contaminants could be prevented, and reduction of ice adhesion could be accomplished. Single and dual inverse opal structures of fluoropolymer-containing materials have been developed by Wu and co-workers [37]. All these materials were obtained by the vertical deposition method or via spin-coating of particles. Another technique for the precise arrangement of polymer-based particles can be accomplished in flow fields by, e.g., combinations of melting and shear-ordering methods leading to so-called polymer opal films [27,38,39]. This so-called *melt-shear organization* technique requires core-shell particles and features the major advantage of fully solvent- and dispersion-free material processing. The hard core/soft shell particles are compressed between the plates of a moderately hot press, and the hard core particles can merge into the colloidal crystal structure yielding free-standing polymer opal films in one single step. Only recently, the feasibility of this technique was shown for inorganic core particles featuring a polymer or hybrid soft and meltable shell was reported [40–44]. This melt-shear organization technique allows for the facile preparation of almost perfectly ordered core/shell particles embedded in an elastomeric polymer matrix, and it can be applied on industrially relevant length scales [45]. The combination of fluoropolymers with this technique has not been reported for the preparation of functional opal films or inverse opals films yet. Within the present study, we report for the first time the incorporation of fluoropolymers into core/shell particle architectures, which can be advantageously used for the melt-shear organization technique. Both organic particle cores and inorganic silica core particles featuring a comparably soft fluoropolymer shell are prepared. Application of the melt-shear organization technique yield free-standing fluoropolymer opal and inverse films with remarkably distinct reflection colors and hydrophobic properties. Moreover, these novel opal and inverse opal films were investigated with respect to their optical properties, swelling capability in water, and chemical resistance toward acids and bases.

2. Results and Discussion

The following chapter is divided into six sections, starting with the design of fluorine-containing core/shell particles, followed by the preparation of opal and inverse opal films based on these particles by application of the melt-shear organization technique. Finally, the feasibility of herein investigated fluorine-containing opals and inverse opals will be elucidated with respect to their optical properties, chemical resistance, and solvent-induced structural color changes.

2.1. Bottom-Up Fabrication of Fluorine-Containing Opal and Inverse Opal Films

For the preparation of fluorine-containing opal films as well as inverse opal films the tailored design of monodisperse core interlayer shell particles is a basic prerequisite. For this purpose, the complex particle architecture was developed by a step-wise emulsion polymerization as given in Figure 1. In the case of filled opal films (Figure 1a), the hard organic core particles were generated by the polymerization of styrene, combined with the cross-linker butandiol diacrylate (BDDA), followed by a starved feed addition of an emulsion consisting of styrene and allylmethacrylate (ALMA). The particle sizes were analyzed by means of dynamic light scattering (DLS) and transmission electron microscopy (TEM), as described in detail in the following. For the next synthesis step, an additional cross-linked interlayer consisting of *n*-butylacrylate (*n*BuA) and ALMA was introduced. Herein,

the residual allyl-moieties of ALMA were capable of acting as grafting anchors for the soft shell material. As already mentioned in the introduction, this step is important to ensure preservation of the spherical shape of the particle cores during processing and during the application of mechanical stress during the melt-shear-organization [27,46,47]. The major part of the outer soft shell consisted of poly(1*H*,1*H*,2*H*,2*H*-nonafluorohexylmethacrylate) (PNFHMA) (60 wt%) as a fluorine-containing polymer. For maintaining a soft and processable polymer mass for the intended extrusion step, a softer comonomer was additionally introduced as shell material. For this purpose, *n*BuA (20 wt%) and trifluoroethylacrylate (TFEA) (20 wt%) as comonomers were copolymerized with an NFHMA monomer. The intermediate glass transition temperature (T_g) decreased up to 14 °C for the copolymer, compared to the respective T_g of the respective PNFHMA homopolymers (T_g = 25 °C) (Figure S1 of the Supporting Information) [48]. These three monomers were used for the formation of the—compared to the hard core material—soft and functional fluorine-containing particle shell material. The successful formation of the core/interlayer/shell-particles was followed by DLS measurements (Figure S2a of the Supporting Information), proving an increase in the diameter after every synthesis step. In detail, the average hydrodynamic diameter of the particles were 206 ± 2 nm for the PS core particles, 211 ± 2 nm for the core/interlayer, and 246 ± 1 nm for the final fluorine-containing core/interlayer/shell particles. It can be concluded from these results that rather monodisperse particles were accessible, which will be important for the optical properties of the opal films (see next sections). The fluorine-containing particles were additionally investigated by using transmission electron microscopy (TEM) (Figure S2b–d), confirming the monodisperse and spherical character of the fluoropolymer-containing core/shell particles. These findings were essential for the fabrication of soft colloid crystal films as described in the next section. Both the DLS and TEM measurements revealed the successful formation of the core/interlayer/shell architecture and sizes of each particles were found to be in excellent agreement with expectations based on monomer consumption and the recipe for emulsion polymerization (*cf.* Experimental Section).

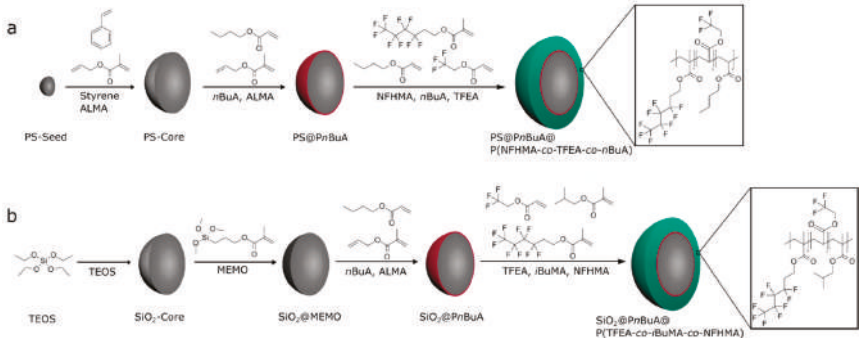

Figure 1. (**a**) Stepwise synthesis of organic fluorine-containing PS@P(NFHMA-*co*-TFEA-*co*-*n*BuA) core/interlayer/shell particles; (**b**) stepwise synthesis of inorganic/organic fluorine-containing SiO2@P(TFEA-*co*-NFHMA-*co*-*i*BuMa) core/interlayer/shell particles. Abbreviations: polystyrene (PS), allylmethacrylate (ALMA), *n*-butylacrylate (*n*BuA), 1*H*,1*H*,2*H*,2*H*-nonafluorohexylmethacrylate (NFHMA), trifluoroethylacrylate (TFEA), tetraethoxysilane (TEOS), 3-methacryloxypropyltrimethoxysilane (MEMO), and *i*-butylmethacrylate (*i*BuMA).

Core/interlayer/shell particles were also synthesized for the preparation of the corresponding inverse opal films. For this purpose, silica (SiO_2) particles were used as hard core particles. Pristine SiO_2-particles were synthesized according to the literature by van Blaaderen et al. [49], applying a sol-gel process (Stöber process). For the preparation of monodisperse SiO_2 particles, tetraethoxysilane (TEOS) in ethanol was used as a precursor, followed by a functionalization of the particle surface with 3-methacryloxypropyltrimethoxysilane (MEMO) [39]. For transferring the particles into the emulsion

polymerization, ethanol was substituted by deionized water by azeotropic distillation. In the next step, the MEMO-functionalized SiO_2-particles were used for the preparation of the interlayer, consisting of poly(*n*BuA-*co*-ALMA). Finally, the polymerization of the outer shell was performed by copolymerizing TFEA (60 wt%), NFHMA (20 wt%), and *iso*-butylmethacrylate (*i*BMA) (20 wt%) as monomers. These inorganic core particles featuring an organic interlayer/shell polymer were examined with respect to morphology and average size by DLS measurements and TEM (Figure 2). All data on the different particles are compiled in Table 1.

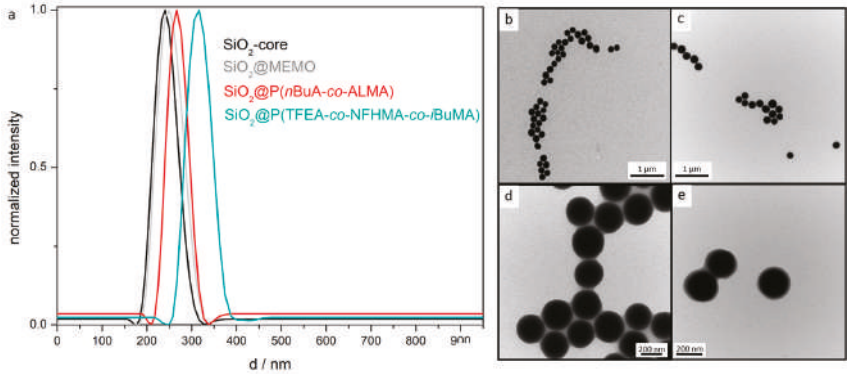

Figure 2. (**a**) DLS measurements of SiO_2 core particles, MEMO-functionalized SiO_2 particles, SiO_2 core/P(*n*BuA-*co*-AMLA)-interlayer particles, and SiO_2 core/P(*n*BuA-*co*-ALMA)interlayer/P(TFEA-*co*-NFHMA-*co*-*i*BuMA)-shell particles; (**b**) TEM image of SiO_2-core particles; (**c**) TEM image of MEMO-functionalized SiO_2 particles; (**d**) TEM image of SiO_2 core/interlayer particles; (**e**) TEM image of SiO_2 core interlayer shell particles.

Table 1. Average hydrodynamic diameter of particles measured by means of DLS and average diameters of the dried particle, as determined by TEM. In the case of TEM analysis, 50 particles were measured with respect to their size.

Particle	DLS (d/nm)	TEM (d/nm)
PS	206 ± 2	192 ± 10
PS@P(*n*BuA-*co*-ALMA)	211 ± 2	202 ± 6
PS@P(NFHMA-*co*-TFEA-*co*-*n*BuA)	246 ± 1	238 ± 11
SiO_2	240 ± 1	232 ± 6
SiO_2@MEMO	249 ± 4	234 ± 11
SiO_2@P(*n*BuA-*co*-ALMA)	271 ± 1	261 ± 8
SiO_2@P(TFEA-*co*-NFHMA-*co*-*i*BuMa)	315 ± 9	303 ± 4

In summary, the DLS and TEM measurements again evidenced the successful preparation of well-defined spherical particles and a continuously increasing particle size for each synthesis step. While the particles in Figure 2b,c were still clearly separated from each other, the particles in Figure 2d,e are obviously connected by a soft polymer shell. DLS measurements in general give a larger diameter for particle systems compared to the TEM images, because the hydrodynamic diameters of the particles is determined, which is larger compared to particles in the dried state. For gaining insights into the composition and the thermal properties of the designed functional particles comprising the PS core, the PS@P(NFHMA-*co*-TFEA-*co*-*n*BuA) as well as the SiO_2@P(TFEA-*co*-NFHMA-*co*-*i*BuMA) core/interlayer/shell particles, differential scanning calorimetry (DSC) measurements were performed. The measured glass transition temperature of the (NFHMA-*co*-TFEA-*co*-*n*BuA)-polymer shell was found to be 14 °C, which was significantly lower than the T_g value found for the PS core, i.e., 100 °C (Figure S1). Moreover, the T_g value of the shell was found to be in between the T_gs of the pure

components, i.e., 25 °C for PNFHMA [48], −54 °C for P*n*BuA [50], and −10 °C for PTFEA, confirming the successful copolymerization of the corresponding monomers.

Compared to this organic particle system, the glass transition temperature for the SiO_2@P(TFEA-*co*-NFHMA-*co*-*i*BuMA) core/shell particles was found to be 27 °C (Figure S3) due to the content of P*i*BuMA, which featured a glass transition temperature of 53 °C for the homopolymers [50]. Hence, successful copolymerization of the respective monomers was evidenced by the presence of the intermediate glass transition temperature. Moreover, these moderate values for the glass transition temperatures should enable processing by means of melt-shear organization of the core/shell particles, which will be described in the following.

For preparation of the elastomeric opal films using the melt-shear organization technique, the core/interlayer/shell particles were precipitated from their dispersion followed by drying at 40 °C. For homogenization of the obtained particle mass as well as for the addition of UV-cross-linking reagents (Irgacure 184, benzophenone, and 1,4-butanedioldiacrylate (BDDA)), the sticky particle mass was mixed using a microextruder at 90 °C (see Experimental Section). During this step, the addition of cross-linking reagents is important for subsequent UV-induced cross-linking reaction of the opal film. For this reason, cross-linking reagents that do not initiate chemical reactions during the melt-shear organization process but can initiate a posteriori are necessary. A cross-linked network, generated by the UV irradiation of the opal films, enhances the mechanical—and therefore the optical—properties of the opal films [46,47,51]. In order to additionally enhance the reflection colors of the opal films, 0.05 wt% carbon black (special black 4, Degussa) powder as an absorber was added during the extrusion. In general, carbon black powder has been found to dramatically enhance the perceived reflection color due to spectrally resonant scattering inside the opal structure without affecting the lattice quality [52]. Moreover, because of the small amount of added carbon black, it is not expected that the refractive index of the fluoropolymer-containing matrix material will be significantly increased. In the next step, the extruded polymer strands were subjected to the melt-shear organization process (Figure 3), allowing the core/shell particles to merge into a colloid crystal structure.

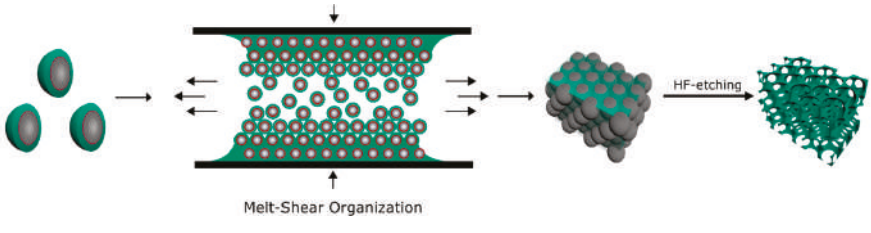

Figure 3. Fabrication of opal films using the melt-shear organization technique and preparation of an inverse opal by HF etching of the SiO_2 core particles.

For this purpose, the particle mass was placed between the plates of a press followed by increasing the temperature and applying a pressure up to 100 bar (*cf.* Experimental Section). Within this film formation step, the soft shells generated a continuous matrix embedding the hexagonally arranged hard core particles. The latter formed the final colloidal crystal structure. In order to gain elastomeric properties and to maintain the stability upon etching for the preparation of an inverse opal film, the opal film was irradiated with UV-light to initiate the cross-linking reaction inside the polymer matrix. In this way, an elastomeric fluorine-containing opal film with iridescent reflection colors was prepared as studied in detail in the next section.

2.2. Optical Properties and Morphology of the PS@P(NFHMA-co-TFEA-co-nBuA) Opal Film

For the preparation of the elastomeric fluorine-containing opal films, some basic requirements must be fulfilled: (i) a periodic close-packed arrangement of the hard spheres, (ii) the monodispersity

of the core particles, and (iii) a refractive index contrast between the hard core, respectively the voids, and the matrix material.

According to Bragg´s law of diffraction combined with Snell´s law (Equation (1)), the perceived wavelength of reflection (λ_{111}) is influenced by the average refractive index n_{eff}, which can be calculated by considering the refractive index n_i and the volume fractions ϕ_i for all ingredients of the opal (Equation (2)). The wavelength of reflection depends also on the periodicity α_{111} and the angle of incident light θ [24].

$$\lambda_{111} = 2\alpha_{111}\left(n_{eff}^2 - \sin^2\theta\right)^{1/2} \quad (1)$$

$$n_{eff} = \sum n_i \phi_i \quad (2)$$

For this purpose, an organic core-particle consisting of polystyrene ($n_{eff} \cong 1.59$) [53] and a shell material containing a high content of poly(NFHMA) ($n_{eff} \cong 1.35$) [54] was used. Compared to previously reported organic core/shell opal films, this combination featured a higher refractive index contrast ($\Delta n_{eff} \leq 0.24$). From the photographs obtained by scanning electron microscopy (SEM) (Figure 4a), it can be concluded that the particle-based film consists of closely packed and hexagonally aligned layers of particles. Additional to these findings, transmission electron microscopy (TEM) images obtained for ultra-thin slices prepared from the opal film are shown in Figure 4b, revealing the individual PS particles embedded in a lighter appearing matrix. The lighter matrix corresponded to the fluoropolymer shell material, having less electron contrast compared to the aromatic PS core particles. However, in the case of the TEM images, the core particles appeared to be more distorted. This can be explained by the fact that the spherical domains having a size of 192 ± 10 nm are much larger than the microtomed thin slices, which are approximately 50–70 nm in thickness. During ultramicrotoming of the bulk polymer films with spherical domains inside a soft matrix, the probability for perfect cutting of spherical objects is reduced, which is a known problem for spherical domains during sample preparation by using ultramicrotomy [55].

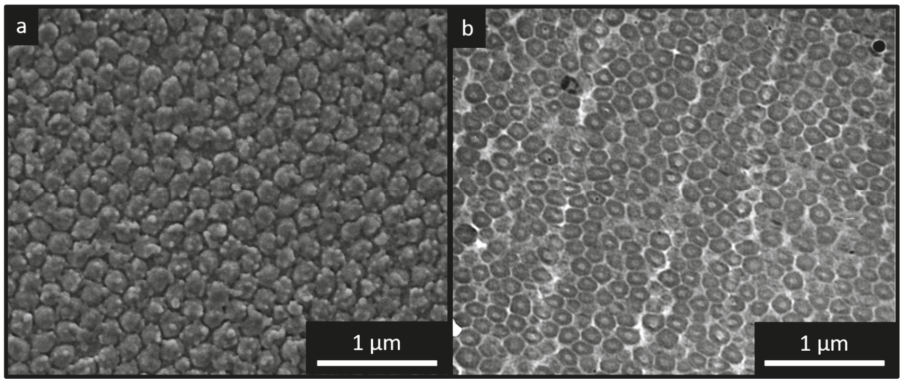

Figure 4. (**a**) SEM image: surface of PS@P(NFHMA-*co*-TFEA-*co*-*n*BuA) opal film; (**b**) TEM image: ultra-thin cut of the cross-section of a PS@P(NFHMA-*co*-TFEA-*co*-*n*BuA) opal film.

To determine the position of the Bragg peak and evidencing a good optical performance based on the ordered particles, angle-dependent UV/Vis measurements were performed (Figure 5). The measurements were recorded for angles of incident between 90° and 60°. Within the corresponding spectra, a distinct Bragg peak at a wavelength of 558 nm was observed. At lower angles of incidence, the value for the reflected light, i.e., the Bragg peak was blue-shifted from 558 nm at 90° to 486 nm at 60° according to Bragg´s law of diffraction. This finding proved the existence of a structural color for the herein designed fluorine-containing opal films. Moreover, it can be concluded that the

melt-shear organization of the PS@P(NFHMA-*co*-TFEA-*co*-*n*BuA) particles leads to a regularly ordered particle-based film with brilliant reflection colors.

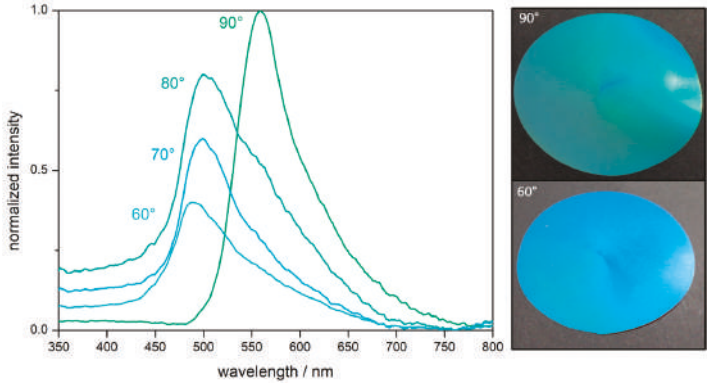

Figure 5. Angle-dependent UV/Vis reflection spectra of the opal film prepared from PS@P(NFHMA-*co*-TFEA-*co*-*n*BuA) core/interlayer/shell particles and corresponding photographs of the opal film at an angle of view of 90° and 60°. The final opal discs featured a diameter of 8 cm.

2.3. Chemical Resistance of the PS@P(NFHMA-co-TFEA-co-nBuA) Opal Film

In general, polymers having a high content of fluorine-containing monomers feature a good chemical resistance toward acids or bases [56]. In order to investigate the chemical resistance, the here prepared opal films were exposed to a strong acid (hydrochloric acid pH = 1) and base (potassium hydroxide pH = 13), followed by subsequent UV/Vis measurements of the samples. In Figure S4, UV/Vis spectroscopy measurements of the opal films treated with potassium hydroxide solution and hydrochloric acid are shown. The untreated film featured a reflection color maximum at a wavelength of approximately 525 nm. When the fluorine-containing opal film was treated with deionized water, the reflection peak of the opal film slightly shifted to 544 nm, which was due to the swelling capability of the matrix material. However, treatment of the swollen opal films with concentrated acid or concentrated base did not lead to a significant change of the optical properties. In more detail, the reflection color of the opal film treated for 20 min with potassium hydroxide was shifted only toward 6 nm and Bragg peak maximum was finally located at a wavelength of 550 nm at an angle of view of 90°. When the opal film was treated for 20 min with hydrochloric acid, the peak was located at a wavelength of 540 nm, i.e., only with a shift of 4 nm. Therefore, UV/Vis measurements proved the excellent order and resistance of the opal films under harsh conditions.

2.4. Hydrophobicity and Solvent Response of the PS@P(NFHMA-co-TFEA-co-nBuA) Opal Film

The hydrophobic character of the fluorine-containing opals was determined by contact angle measurements. A contact angle between the opal film surface and a sessile drop of deionized water of 106 ± 3° was obtained, which categorized the surface hydrophobic (see Figure S5a). As described in the introduction, fluoropolymers have already found an extensive application as a low surface energy material for water repellency applications [37,57]. In general, the wettability of surfaces with liquid depends on two factors: (i) the chemical factor based on the low surface energy and (ii) the geometrical factors mainly given by roughness and tailored architecture of the surface. As can be concluded from the SEM image in Figure 4a, the surface of the opal film is not exceptional rough or structured, and the water repellency effect is therefore considered to stem from the chemical factor, i.e., the used fluorine-containing polymers. Despite the high chemical resistance and water repellency, the domain sizes of the opal film could be influenced upon treatment with various organic solvents. When the distance between the spheres forming the colloidal crystal stack is in the range of half the wavelength

of visible light, structural colors can be observed, as described by Bragg´s law of diffraction. Solvent treatment caused a swelling-induced volume change of the matrix polymer, resulting in the increase of surface plane spacing of the closely packed PS spheres embedded in the cross-linked opal film. Moreover, the Bragg conditions for the respective colors was also influenced by the refractive index of the solvent used for matrix swelling, which has been described in earlier works [23,24,58]. Typically, the swelling behavior of the matrix materials leads to a shift of the reflection peak maximum toward a higher wavelength. In other words, the volume expansion of the polymer matrix induced by solvent treatment leads to a red-shift of the reflection peak maxima. Exemplarily, the peak maximum shifted from 525 nm for the untreated opal film to 808 nm after treatment with THF (Figure 6). Depending on the swelling capability, the used media (water, ethanol, acetonitrile, acetone, ethyl methyl ketone (EMK), and THF) will lead to a more pronounced reflection peak maximum shift within this order. Noteworthy, after complete evaporation of the used solvents, the fluorine-containing opals reached the original peak maximum value after repeated solvent treatment-evaporation cycles, at least three times.

In summary, the convenient preparation of fluoropolymer-containing opal films featuring angle-dependent reflection colors and solvent-responsive behavior were prepared. Moreover, the reflection peak position of the fluorine-containing opal films were not altered by treatment with concentrated acids and bases.

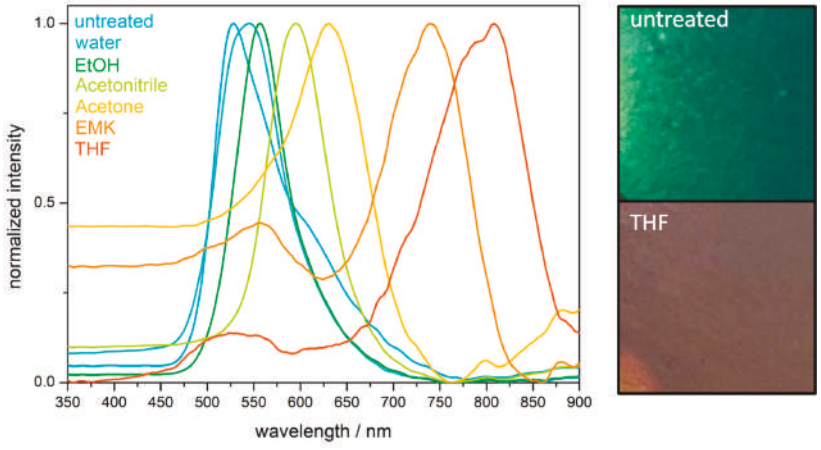

Figure 6. UV/Vis reflection spectra of a solvent-treated opal film based on PS@P(NFHMA-*co*-TFEA-*co*-*n*BuA) core/interlayer/shell particles (**left**) and exemplary photographs of the opal film prior to and after treatment with THF (**right**). Abbreviations: ethanol (EtOH), ethyl methyl-ketone (EMK), and tetrahydrofurane (THF).

2.5. Optical and Structural Properties of the SiO_2@P(TFEA-co-NFHMA-co-iBuMA) Inverse Opal Film

For the preparation of fluoropolymer inverse opal films, SiO_2 core particles with a comparably soft fluorine-copolymer shell were subjected to the melt-shear-organization technique. The silica-core particles were etched by HF treatment in a subsequent step in order to gain access to the inverted opal structure (see Experimental Section). The opal films prior to the etching process featured no bright reflection color, since the refractive index contrast Δn_{eff} between the silica core particles (n_{eff} = 1.43) [59] and the fluoropolymer matrix ($n_{eff} \leq 1.41$) was rather low [57]. However, after removal of the silica core particles, the ordered pores inside the fluoropolymer matrix led to a more pronounced refractive index contrast and therefore to the appearance of iridescent structural colors. Figure 7a shows photographs of the opal film filled with SiO_2 cores featuring no reflection colors, while in Figure 7b the inverted opal film is given showing structural colors.

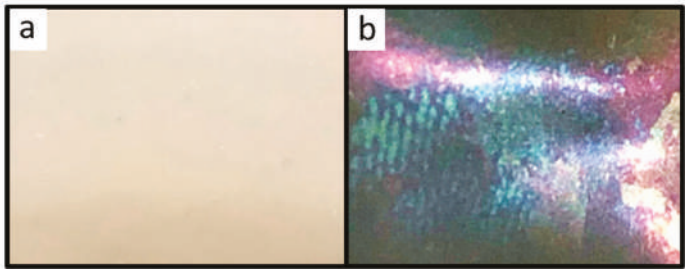

Figure 7. (**a**) Photographic picture of the filled opal film based on SiO_2@P(TFEA-*co*-NFHMA-*co*-*i*BuMA) core/interlayer/shell particles, without reflection colors; (**b**) photographic picture of the inverse opal film based on SiO_2@P(TFEA-*co*-NFHMA-*co*-*i*BuMA) core/interlayer/shell particles, with reflection colors. The cutout of the inverse opal discs featured a diameter of 2 cm.

In order to obtain more intensive reflection colors, a higher content of pores was of utmost importance. Therefore, the film was treated with hydrofluoric acid for full removal of the SiO_2 cores after several days. Corresponding SEM studies revealed that the surface of the inverse fluoropolymer opal film is open-porous with a uniform diameter of the pores of 175 ± 5 nm (Figure 8a). The corresponding cross-section (Figure 8b) revealed that the SiO_2 core particles were also removed in the interior of the opal film. It has to be mentioned that the pore order and pore size distribution seemed to be influenced with respect to their spherical shape within the SEM photographs for the cross-section compared to the film topography. This might be caused by sample preparation using freeze-fracturing for the comparably soft inverse opal films. Moreover, for the preparation of the fluoropolymer inverse opal films, a slightly different polymer composition was chosen. In comparison to the opal films described in Section 2.2, a lower fraction of NFHMA (20 wt%) and a higher amount of TFEA (60 wt%) was used. The reason for changing the composition and for additionally introducing *i*BuMA (20 wt%) instead of *n*BuA was the softness of the final inverse opal film leading to a pore collapse after the etching process. While using a fluropolymer copolymer with P*i*BMA, the glass transition temperature could be increased to 25 °C, suitable for convenient core/shell particle processing and for the preparation of a free-standing inverse opal film. The T_g was determined to be 25 °C, as studied by DSC measurements (Figure S3).

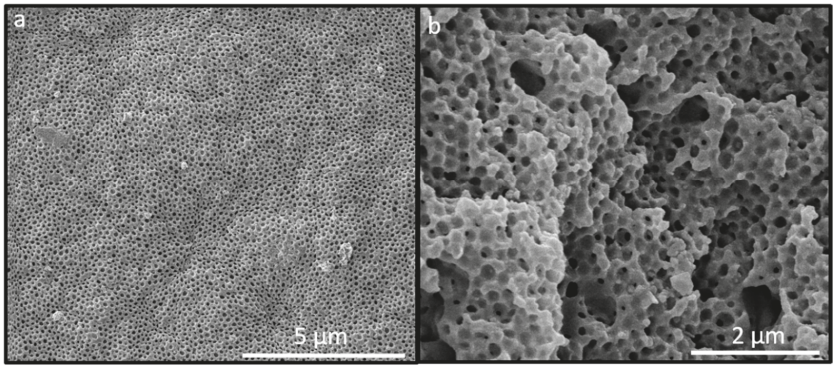

Figure 8. SEM photograph of the topography (**a**) and corresponding cross-section SEM photograph (**b**) of an inverse opal film based on SiO_2@P(TFEA-*co*-NFHMA-*co*-*i*BuMA) core/interlayer/shell particles after melt-shear organization and subsequent HF etching.

To further investigate the pore order and to visualize influence on the morphology upon water treatment, atomic force microscopy (AFM) studies were additionally carried out. Corresponding AFM

measurements for the dried film and for the inverse opal film in water are given in Figure 9. In good accordance with the SEM images in Figure 8, AFM studies confirmed the presence of well-ordered hexagonally aligned pores. The average pore size in the dried state was determined to be 179 ± 8 nm, which was in good agreement with the pore size determined in the corresponding SEM image (175 ± 5 nm). Figure 9b give the results for AFM measurement of the same inverse opal film in water. As a finding, the average pore size was found to 153 ± 10 nm in diameter, which reflects a slight swelling capability of the water-treated inverse opal matrix material.

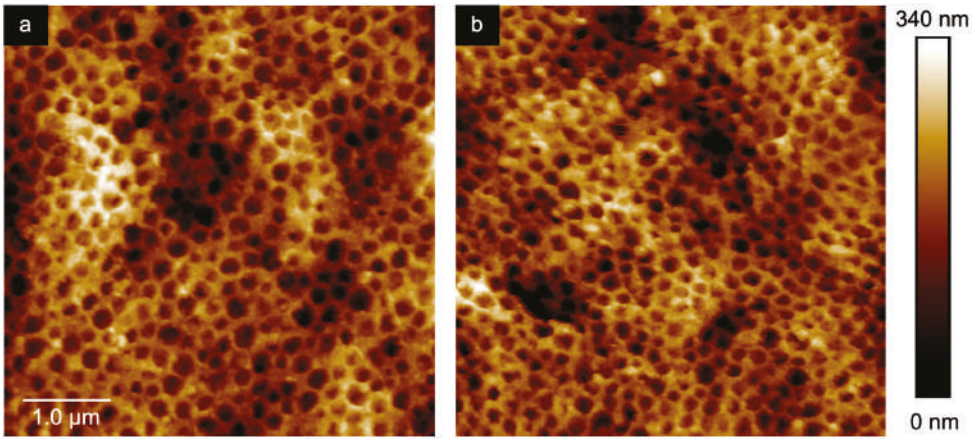

Figure 9. AFM image of the dried inverse opal film obtained after etching of the SiO_2@P(TFEA-*co*-NFHMA-*co*-*i*BuMA)-based particle films (**a**) and the same film measured in water (**b**) Scale bars correspond to 1 µm (see text).

2.6. Chemical Resistance and Solvent-Responsivness of the Inverse Opal Film

As already mentioned in the previous section, the hydrophobic character of the fluoropolymer-based opal materials was proven by contact angle measurements. Here, contact angle measurements for the inverse opal film derived after etching of SiO_2@P(TFEA-*co*-NFHMA-*co*-*i*BuMA)-based particle films, resulted in a contact angle of 102 ± 2° (Figure S5b). Along with the results obtained from the AFM measurements, a slight swelling of the inverse opal film upon water treatment was observed, which also led to a shift of the maximum peak position during UV/Vis spectroscopy measurements (Figure 10). In detail, the dried inverse opal film featured a reflection color peak at a wavelength of 518 nm, while the peak shifted to a wavelength of 570 nm upon water treatment. This was found to be a remarkable difference compared to the results obtained for the filled opals as shown in Figure 6, revealing a peak maximum shift of only 16 nm. This finding underpins the more pronounced sensing capability for water (and other media) for the inverse opal structures compared to the filled opal films. This effect is even more pronounced while using organic solvents (Figure 10). The peak maxima shifted in polar media, such as water (peak maximum at 570 nm) or ethanol (612 nm), tetrahydrofuran (704 nm), and acetonitrile (836 nm), respectively. This observation can be explained by the swelling capability induced by the different solvents for the fluorine-containing matrix. In contrast, the appearance of the structural colors is only slightly affected by the change of the refractive index contrast, since the different refractive indices of the used solvents are similar, i.e., 1.33 for water, 1.36 for ethanol, 1.37 for ethyl methyl ketone, 1.40 for THF, and 1.34 for acetonitrile [60,61].

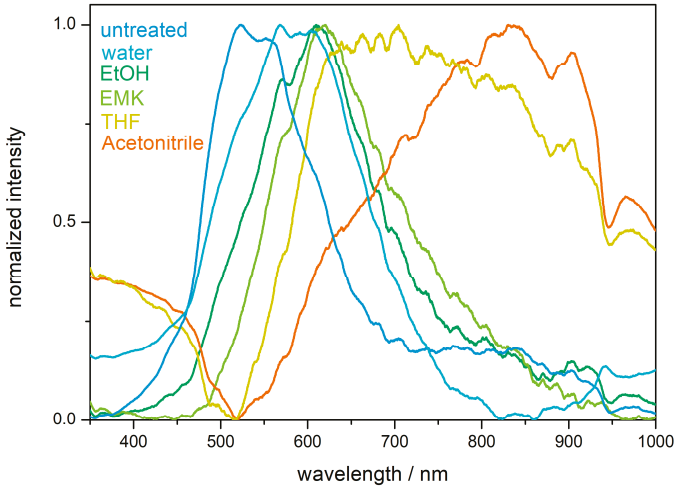

Figure 10. UV/Vis reflection spectra of solvent-treated inverse opal film based on P(TFEA-*co*-NFHMA-*co*-*i*BuMA). Abbreviations: ethanol (EtOH), ethyl methyl ketone (EMK), and tetrahydrofuran (THF).

Finally, the chemical resistance of the inverse opal film caused by fluorine-containing matrix was also examined by treatment with a strong acid (hydrochloric acid pH = 1) and base (potassium hydroxide pH = 13) by UV/Vis spectroscopy measurements (Figure S6). Despite the slightly reduced fluorine-content inside the inverse opal matrix, only a small shift of the reflection peak maximum of approximately 10 nm was obtained from the corresponding spectra. This finding proved the high chemical resistance also for the inverse opal films upon potassium hydroxide and hydrochloric acid treatment.

3. Experimental

3.1. Materials and Methods

1*H*,1*H*,2*H*,2*H*-Nonafluorohxylmethacrylate (NFHMA, 95%) was obtained from ABCR (Karlsruhe, Germany), trifluoroethylacrylat (TFEA, >98%) from TCI (Eschborn, Germany), Butandioldiacrylate (BDDA), and Irgacure 184 from BASF (Ludwigshafen, Germany). Dowfax 2A1, a surfactant having a dual polar head group and a non-polar alkyl chain was obtained from Dow Chemicals (Midland, MI, USA), carbon black (Special Black 4) by Degussa GmbH (Essen, Germany), and benzophenon, the UV-initiator, was donated by Merck Chemicals (Darmstadt, Germany). All other chemicals were purchased from VWR (Radnor, PA, USA), Acros Organics, Fisher Scientific (Schwerte, Germany), and Sigma Aldrich (St. Louis, MO, USA) and used as received, if not otherwise mentioned. Prior to use for the polymerization, inhibitors were removed from the monomers *n*BuA, *i*BuMA, and styrene by passing through an alumina column (basic, 50–200 µm, Acros Organics).

Dynamic light scattering (DLS) measurements of the particle dispersions were performed with a Zetasizer ZS90 (Malvern Instruments, Malvern, UK). The measurements were carried out at 25 °C at an angle of 90°. For the evaluations, the z-weight average hydrodynamic diameter was used. Transmission electron microscopy (TEM) was realized on a Zeiss EM 10 electron microscope (Oberkochen, Germany) operating at 60 kV. The images were recorded in bright field mode with a slow scan CCD camera obtained from TRS Tröndle (Morrenweis, Germany). The control of the camera was computer-assisted using ImageSP from TRS. Scanning electron microscopy (SEM) was performed on a Philips XL30 FEG (Amsterdam, Netherlands) with an operating voltage of 5–10 kV. The samples were previously coated for 100 s at 30 mA with a thin gold layer, using a Quorum Q300T D sputter coater (Lewes,

UK). Angle dependent reflection measurements were performed using a custom built goniometer setup measured in steps of 10° of scattering angle. All other reflection spectra were recorded using a Vis/-NIR fiber spectrometer USB 2000, Ocean Optics (Ostfildern, Germany). For the measurements, a deuterium/tungsten halogen lamp DT mini 2, Ocean Optics was used. Measurements in water or solvents were carried out at normal light incidence (90°). Thermal properties of the core interlayer shell particles were characterized using a differential scanning calorimeter (DSC) from Mettler Toledo (Columbus, OH, USA) DSC-1 in the temperature range from −50 °C to 150 °C with a heating rate of 20 K min^{-1} in a nitrogen atmosphere. Atomic force microscopy measurements were accomplished in the PeakForce Tapping mode with an Icon Dimension Bruker AXS (Santa Barbara, CA, USA). Images with dimensions of 5 × 5 μm^2 (512 × 512 pixel) were taken in air and deionized water at a scan rate of 1 Hz using a maximum force of 2 nN. The inverse optical sensitivity of the laser detection system was calibrated by pushing the cantilever with the tip onto a stiff substrate (sapphire) and relating the deflection of the laser spot on the photosensitive diode with the movement of the z-piezo. The cantilever spring constant was 0.8 nN/nm measured by the thermal noise method [62]. The contact angle (CA) was measured using the sessile-drop-method with a Contact angle system DATAPhysics OCA 15 EC (Filderstadt, Germany) using 2 µL droplets of deionized water. The measurements were conduced in a controlled climatic chamber at a temperature of 23 ± 2 °C and a relative humidity of 40%. Contact angles were determined geometrically using the SCA20 software by aligning a tangent from the surficial contact point along the droplet profile.

3.2. Synthesis of PS@PBuA@P(NFHMA-co-TFEA-co-nBuA) Core/Interlayer/Shell-Particles

The stepwise generation of fluorine-containing polymer based particles is illustrated in Figure 1a. The corresponding monodisperse PS particles were synthesized according to starved feed emulsion polymerization protocols. A 1 L reactor under an argon stream, equipped with a reflux condenser and a stirrer, was heated up to 80 °C and filled with a dispersion of 3.6 g of styrene, 0.4 g of BDDA, 0.1 g of SDS, and 280 g of degassed water. The polymerization was initiated by adding solutions of 70 mg of sodiummetabisulfite (SBS) in 5 g of water and 500 mg of sodiumperoxodisulfate (SPS) in 5 g of water. After 20 min, a monomer emulsion containing 3.5 g of ALMA, 31.5 g of styrene, 180 mg of KOH, 164 mg of SDS 105 mg of Igepal, and 40.9 g of water was added continuously with a flow rate of 0.5 mL/min. After one hour of reaction time, the polystyrene particles with an average diameter of 206 nm were characterized and stored for further use.

The core-shell particle featuring a copolymer of P*n*BuA, PNFHMA, and PTFEA as a soft shell was synthesized in a 100 mL double-wall reactor equipped with a stirrer and reflux condenser in an argon atmosphere at 80 °C. For this purpose, 60 g of the PS-particle dispersion with a solid content of 8.4 wt% was filled into the reactor, and the emulsion polymerization was initiated by the addition of 14 mg of SBS and 77 mg of SPS dissolved in 2 mL of deionized water. After 20 min reaction time, a monomer emulsion (ME1) consisting of 75 mg of ALMA, 425 mg of *n*BuA, 10 mg of Dowfax 2A1, 5 mg of SDS, and 2.5 g of deionized water was added with a flow rate of 0.2 mL min^{-1} using a rotary piston pump. After the complete addition of ME1, a solution of 12 mg of SPS in 2 g of water was added and a second monomer emulsion (ME2) consisting of 2.7 g of NFHMA, 0.9 g of TFEA, 0.9 g of *n*BuA, 45 mg of KOH, 16 mg of SDS, 13 mg of Dowfax 2A1, and 5.22 g of water were continuously added with a flow rate of 0.2 mL min^{-1}. After complete addition of the ME2, the temperature of polymerization was maintained for an additional hour prior to cooling the vessel to room temperature. The average particle diameter of the core shell particle was determined to be 246 ± 1 nm (DLS).

3.3. Synthesis of SiO_2@PBuA@P(TFEA-co-NFHMA-co-iBuMA) Core/Interlayer/Shell-Particles

Silica particle dispersion with a solid content of 2.5 wt% in ethanol were prepared using a sol-gel process (Stöber process) according to the protocol described by van Blaaderen [49]. A mixture of 1.3 L of ethanolic silica dispersion with 1.6 mL of 3-methacryloxypropyltrimethoxysilane (MEMO) was heated to 60 °C and stirred for 2 h. After functionalization, ammonia was carefully removed

by azeotropic distillation at 60 °C under reduced pressure, while the volume was kept constant by tcontinuous addition of ethanol. When the dispersion was free of ammonia, the volume was reduced to 300 mL at 60 °C. For transferring the silica particle dispersion into an aqueous medium for the intended emulsion polymerization, a solution of 50 mg of SDS in 100 mL of deionized water was added, and ethanol was removed by azeotropic distillation. The volume was kept constant by continuous addition of water. The final MEMO-functionalized aqueous dispersion featured a silica solid content of 8.83 wt%. The average particle diameter of the particles after functionalization was 249 ± 4 nm, as determined by DLS measurements.

For synthesis of the hybrid core-shell particles, 70 g of the pristine SiO_2 particle dispersion was filled in a 100 mL double wall reactor. The emulsion polymerization was initiated at 80 °C by the addition of a solution of 16 mg of SBS and 94 mg of SPS in 2 mL of deionized water. After 20 min, a monomer emulsion (ME1) consisting of 83 mg of ALMA, 0.47 g of *n*BuA, 11 mg of Dowfax 2A1, 6 mg of SDS, and 2.77 g of water were added by a rotary piston pump with a flow rate of 0.2 mL min^{-1}. After a 15 min reaction time, 15 mg of SPS in 2 mL of water was added and another monomer emulsion (ME2) composed of 3.55 g of TFEA, 0.9 g of NFHMA, 0,9 g of *i*BuMA, 7 mg of KOH, 16 mg of SDS, 12 mg of Dowfax 2A1, and 5.2 g of water was continuously added with a flow rate of 0.2 mL min^{-1}. After an additional hour, the product was cooled to room temperature. The diameter of the core/shell particle was 315 ± 9 nm, as determined by DLS measurements.

3.4. Particle Processing and Preparation of Opal and Inverse Opal Films

For the preparation of elastomeric opal films, the obtained PS@P*n*BuA@P(NFHMA-*co*-TFEA-*co*-*n*BuA) particles were precipitated in methanol containing 20% of saturated sodium chloride solution. The precipitate was filtered, washed with water, and dried under vacuum at 40 °C. For homogenization, the precursor powder was mixed with 7.25 wt% BDDA, 1 wt% benzophenone, 1 wt% Irgacure 184, and 0.05 wt% carbon black (special black 4, Degussa) in a microextruder (HAAKE Minilab II350, Thermo Scientific, Waltham, MA, USA) at 90 °C. For opal film formation, a 2 g portion of the polymeric mass was covered by two PET foils and heated between two steel-plates in a Collin laboratory press (Dr. Collin GmbH, Ebersberg, Germany). The particle mass was transduced into an opal disc film of approximately 8 cm in size by using the melt-shear organization technique at 90 °C and 100 bar. Subsequently, the opal films were irradiated with a mercury lamb (UVA Cube 2000, Dr Hoenle AG, Gräfelfing, Germany) with an output power of 1000 W at a distance of 10 cm for 3 min at both sides, for cross-linking reactions. For conversion of the opal film containing SiO_2 core particles into an inverse opal film, the cores were removed by etching with hydrofluoric acid (HF, 10 wt% in water) for 4 days. The films were washed with plenty of deionized water several times.

4. Conclusions

In conclusion, the current work demonstrated an efficient protocol for preparation of fluorine-containing core/interlayer/shell particles. For the hard core particle preparation, inorganic SiO_2 or PS particles were used, whereas the soft shell was formed by a stepwise emulsion polymerization of highly fluorinated monomers, i.e., 1*H*,1*H*,2*H*,2*H*-nonafluorohexylmethacrylate (NFHMA) and trifluoroethylacrylate (TFEA), leading to well-defined fluorine-containing core/shell particles. The melt-shear organization technique was applied for the preparation of easily scalable fluoropolymer opal disc films. The opal film based on SiO_2 core particles were subjected to an etching protocol using hydrofluoric acid to gain access to fluoropolymer inverse opal structures. Characterization of the particles, opal films, and inverse opal films was carried out using DLS, TEM, SEM, AFM, DSC, UV/Vis spectroscopy, and contact angle measurements, evidencing the size, uniformity, and order after the melt-shear organization and subsequent etching. The feasibility of fluorine-containing polymers as functional matrix materials, leading to opal films featuring brilliant reflection colors, was shown by the good refractive index contrast compared to the PS core material (or air voids in the case of the inverse opals). Finally, swelling capability and stimuli-responsiveness

upon treatment with different solvents were investigated, and the reversible switching behavior of the optical properties was shown. Moreover, the inverse opals revealed good hydrophobic properties and excellent chemical resistance toward strong acids and bases. Along with the good structural colors, we envisage the herein investigated fluorine-containing opal and inverse opal films as promising candidates in the field of robust coatings and switchable optical sensing devices.

Supplementary Materials: The following information are available online, Figure S1: DSC thermogram of PS based core/shell particles; Figure S2: DLS measurements and TEM images of PS based core/shell particles; Figure S3: DSC thermogram of SiO_2 based core/shell particles; Figure S4: UV/Vis spectra of an opal film; Figure S5: Photograph of drops of water on opal and invers opal films; Figure S6: UV/Vis spectra of an inverse opal film.

Author Contributions: Conceptualization: J.K. and M.G.; methodology: J.K. and M.G.; validation: J.K. and M.G.; AFM analysis: C.D.; investigation: J.K.; writing—original draft preparation: M.G. and J.K.; writing—review and editing: J.K. and M.G.; supervision: M.G.; project administration: M.G.; funding acquisition: M.G.

Funding: This research received no external funding.

Acknowledgments: The authors thank the company Merck KGaA for the scientific collaboration.

Conflicts of Interest: The authors declare no conflict of interest.

References

1. Drobny, J.G. *Technology of Fluoropolymers*, 2nd ed.; CRC Press: New York, NY, USA, 2009.
2. Munekata, S. Fluoropolymers as coating material. *Progr. Org. Coat.* **1988**, *16*, 113–134. [CrossRef]
3. Smith, D.W.; Iacono, S.T.; Iyer, S.S. *Handbook of Fluoropolymer Science and Technology*, 1st ed.; Wiley: Hoboken, NJ, USA, 2014.
4. Cui, Z.; Drioli, E.; Lee, Y.M. Recent progress in fluoropolymers for membranes. *Progr. Polym. Sci.* **2014**, *39*, 164–198. [CrossRef]
5. Ameduri, B.; Boutevin, B. *Well-Architectured Fluoropolymers: Synthesis, Properties and Applications*; Elsevier: Amsterdam, The Netherlands, 2004.
6. Gardiner, J. Fluoropolymers: Origin, Production, and Industrial and Commercial Applications. *Aust. J. Chem.* **2015**, *68*, 13–22. [CrossRef]
7. Moore, A.L. *Fluoroelastomers Handbook: The Definitive User's Guide and Databook*; William Andrew Publishing: Norwich, NY, USA, 2005.
8. Dams, R.; Hintzer, K. Chapter 1 Industrial Aspects of Fluorinated Oligomers and Polymers. In *Fluorinated Polymers: Volume 2: Applications*; The Royal Society of Chemistry: London, UK, 2017; Volume 2, pp. 1–31.
9. Sun, W.; Zhou, S.; You, B.; Wu, L. A facile method for the fabrication of superhydrophobic films with multiresponsive and reversibly tunable wettability. *J. Mater. Chem. A* **2013**, *1*, 3146–3154. [CrossRef]
10. Shi, F.; Song, Y.; Niu, J.; Xia, X.; Wang, Z.; Zhang, X. Facile Method to Fabricate a Large-Scale Superhydrophobic Surface by Galvanic Cell Reaction. *Chem. Mater.* **2006**, *18*, 1365–1368. [CrossRef]
11. Feng, C.L.; Zhang, Y.J.; Jin, J.; Song, Y.L.; Xie, L.Y.; Qu, G.R.; Jiang, L.; Zhu, D.B. Reversible Wettability of Photoresponsive Fluorine-Containing Azobenzene Polymer in Langmuir-Blodgett Films. *Langmuir* **2001**, *17*, 4593–4597. [CrossRef]
12. Pei, Y.; Travas-Sejdic, J.; Williams, D.E. Reversible electrochemical switching of polymer brushes grafted onto conducting polymer films. *Langmuir* **2012**, *28*, 8072–8083. [CrossRef]
13. Hu, J.; Meng, H.; Li, G.; Ibekwe, S.I. A review of stimuli-responsive polymers for smart textile applications. *Smart Mater. Struct.* **2012**, *21*, 053001. [CrossRef]
14. Drelich, J.; Chibowski, E.; Meng, D.D.; Terpilowski, K. Hydrophilic and superhydrophilic surfaces and materials. *Soft Matter* **2011**, *7*, 9804–9828. [CrossRef]
15. Wenzel, R.N. Resistance of Solid Surfaces to Wetting by Water. *Ind. Eng. Chem. Res.* **1936**, *28*, 988–994. [CrossRef]
16. Cassie, A.B.D.; Baxter, S. Wettability of porous surfaces. *Trans. Faraday Soc.* **1944**, *40*, 546–550. [CrossRef]
17. Whitesides, G.M. Nanoscience, nanotechnology, and chemistry. *Small* **2005**, *1*, 172–179. [CrossRef] [PubMed]
18. Piao, Y.; Burns, A.; Kim, J.; Wiesner, U.; Hyeon, T. Designed Fabrication of Silica-Based Nanostructured Particle Systems for Nanomedicine Applications. *Adv. Funct. Mater.* **2008**, *18*, 3745–3758. [CrossRef]

19. Phillips, K.R.; Vogel, N.; Hu, Y.; Kolle, M.; Perry, C.C.; Aizenberg, J. Tunable Anisotropy in Inverse Opals and Emerging Optical Properties. *Chem. Mater.* **2014**, *26*, 1622–1628. [CrossRef]
20. Huang, X.; Chen, J.; Lu, Z.; Yu, H.; Yan, Q.; Hng, H.H. Carbon inverse opal entrapped with electrode active nanoparticles as high-performance anode for lithium-ion batteries. *Sci. Rep.* **2013**, *3*, 2317. [CrossRef] [PubMed]
21. Schäfer, C.G.; Vowinkel, S.; Hellmann, G.P.; Herdt, T.; Contiu, C.; Schneider, J.J.; Gallei, M. A polymer based and template-directed approach towards functional multidimensional microstructured organic/inorganic hybrid materials. *J. Mater. Chem. C* **2014**, *2*, 7960–7975. [CrossRef]
22. Schäfer, C.G.; Gallei, M.; Zahn, J.T.; Engelhardt, J.; Hellmann, G.P.; Rehahn, M. Reversible Light-, Thermo-, and Mechano-Responsive Elastomeric Polymer Opal Films. *Chem. Mater.* **2013**, *25*, 2309–2318. [CrossRef]
23. Schäfer, C.G.; Biesalski, M.; Hellmann, G.P.; Rehahn, M.; Gallei, M. Paper-supported elastomeric opal films for enhanced and reversible solvatochromic response. *J. Nanophotonics* **2013**, *7*. [CrossRef]
24. Schäfer, C.G.; Winter, T.; Heidt, S.; Dietz, C.; Ding, T.; Baumberg, J.J.; Gallei, M. Smart polymer inverse-opal photonic crystal films by melt-shear organization for hybrid core–shell architectures. *J. Mater. Chem. C* **2015**, *3*, 2204–2214. [CrossRef]
25. Schaffner, M.; England, G.; Kolle, M.; Aizenberg, J.; Vogel, N. Combining Bottom-Up Self-Assembly with Top-Down Microfabrication to Create Hierarchical Inverse Opals with High Structural Order. *Small* **2015**, *11*, 4334–4340. [CrossRef]
26. Phillips, K.R.; England, G.T.; Sunny, S.; Shirman, E.; Shirman, T.; Vogel, N.; Aizenberg, J. A colloidoscope of colloid-based porous materials and their uses. *Chem. Soc. Rev.* **2016**, *45*, 281–322. [CrossRef]
27. Gallei, M. Functional Polymer Opals and Porous Materials by Shear-Induced Assembly of Tailor-Made Particles. *Macromol. Rapid Commun.* **2018**, *39*, 1700648. [CrossRef] [PubMed]
28. Schüth, F.; Schmidt, W. Microporous and Mesoporous Materials. *Adv. Mater.* **2002**, *14*, 629–638. [CrossRef]
29. Stein, A. Advances in Microporous and Mesoporous Solids—Highlights of Recent Progress. *Adv. Mater.* **2003**, *15*, 763–775. [CrossRef]
30. Thomas, A.; Goettmann, F.; Antonietti, M. Hard Templates for Soft Materials: Creating Nanostructured Organic Materials. *Chem. Mater.* **2008**, *20*, 738–755. [CrossRef]
31. Llusar, M.; Sanchez, C. Inorganic and Hybrid Nanofibrous Materials Templated with Organogelators. *Chem. Mater.* **2008**, *20*, 782–820. [CrossRef]
32. Joshi, R.K.; Schneider, J.J. Assembly of one dimensional inorganic nanostructures into functional 2D and 3D architectures. Synthesis, arrangement and functionality. *Chem. Soc. Rev.* **2012**, *41*, 5285–5312. [CrossRef] [PubMed]
33. Scheid, D.; Cherkashinin, G.; Ionescu, E.; Gallei, M. Single-source magnetic nanorattles by using convenient emulsion polymerization protocols. *Langmuir* **2014**, *30*, 1204–1209. [CrossRef]
34. Galisteo-López, J.F.; Ibisate, M.; Sapienza, R.; Froufe-Pérez, L.S.; Blanco, Á.; López, C. Self-assembled photonic structures. *Adv. Mater.* **2011**, *23*, 30–69. [CrossRef]
35. Kang, H.; Lee, J.S.; Chang, W.S.; Kim, S.H. Liquid-impermeable inverse opals with invariant photonic bandgap. *Adv. Mater.* **2015**, *27*, 1282–1287. [CrossRef]
36. Vogel, N.; Belisle, R.A.; Hatton, B.; Wong, T.S.; Aizenberg, J. Transparency and damage tolerance of patternable omniphobic lubricated surfaces based on inverse colloidal monolayers. *Nat. Commun.* **2013**, *4*, 2167. [CrossRef]
37. Wu, Y.; Zhou, S.; Wu, L. Fabrication of Robust Hydrophobic and Super-Hydrophobic Polymer Films with Onefold or Dual Inverse Opal Structures. *Macromol. Mater. Eng.* **2016**, *301*, 1430–1436. [CrossRef]
38. Ruhl, T.; Spahn, P.; Hellmann, G.P. Artificial opals prepared by melt compression. *Polymer* **2003**, *44*, 7625–7634. [CrossRef]
39. Finlayson, C.E.; Baumberg, J.J. Generating Bulk-Scale Ordered Optical Materials Using Shear-Assembly in Viscoelastic Media. *Materials* **2017**, *10*, 688. [CrossRef] [PubMed]
40. Scheid, D.; Stock, D.; Winter, T.; Gutmann, T.; Dietz, C.; Gallei, M. The pivotal step of nanoparticle functionalization for the preparation of functional and magnetic hybrid opal films. *J. Mater. Chem. C* **2016**, *4*, 2187–2196. [CrossRef]

41. Winter, T.; Su, X.; Hatton, T.A.; Gallei, M. Ferrocene-Containing Inverse Opals by Melt-Shear Organization of Core/Shell Particles. *Macromol. Rapid Commun.* **2018**, *39*. [CrossRef]
42. Vowinkel, S.; Schäfer, C.G.; Cherkashinin, G.; Fasel, C.; Roth, F.; Liu, N.; Dietz, C.; Ionescu, E.; Gallei, M. 3D-ordered carbon materials by melt-shear organization for tailor-made hybrid core–shell polymer particle architectures. *J. Mater. Chem. C* **2016**, *4*, 3976–3986. [CrossRef]
43. Vowinkel, S.; Malz, F.; Rode, K.; Gallei, M. Single-source macroporous hybrid materials by melt-shear organization of core-shell particles. *J. Mater. Sci.* **2017**, *52*, 11179–11190. [CrossRef]
44. Vowinkel, S.; Boehm, A.; Schäfer, T.; Gutmann, T.; Ionescu, E.; Gallei, M. Preceramic Core-Shell Particles for the Preparation of Hybrid Colloidal Crystal Films by Melt-Shear Organization and Conversion into Porous Ceramics. *Mater. Des.* **2018**, *160*, 926–935. [CrossRef]
45. Zhao, Q.; Finlayson, C.E.; Snoswell, D.R.E.; Haines, A.; Schäfer, C.; Spahn, P.; Hellmann, G.P.; Petukhov, A.V.; Herrmann, L.; Burdet, P.; et al. Large-scale ordering of nanoparticles using viscoelastic shear processing. *Nat. Commun.* **2016**, *7*, 11661. [CrossRef]
46. Schäfer, C.G.; Smolin, D.A.; Hellmann, G.P.; Gallei, M. Fully Reversible Shape Transition of Soft Spheres in Elastomeric Polymer Opal Films. *Langmuir* **2013**, *29*, 11275–11283. [CrossRef] [PubMed]
47. Schäfer, C.G.; Viel, B.; Hellmann, G.P.; Rehahn, M.; Gallei, M. Thermo-cross-linked Elastomeric Opal Films. *ACS Appl. Mater. Interfaces* **2013**, *5*, 10623–10632. [CrossRef] [PubMed]
48. Jiang, J.; Zhang, G.; Wang, Q.; Zhang, Q.; Zhan, X.; Chen, F. Novel Fluorinated Polymers Containing Short Perfluorobutyl Side Chains and Their Super Wetting Performance on Diverse Substrates. *ACS Appl. Mater. Interfaces* **2016**, *8*, 10513–10523. [CrossRef] [PubMed]
49. Graf, C.; van Blaaderen, A. Metallodielectric Colloidal Core-Shell Particles for Photonic Applications. *Langmuir* **2002**, *18*, 524–534. [CrossRef]
50. Schneider, H.A. Polymer class specificity of the glass temperature. *Polymer* **2005**, *46*, 2230–2237. [CrossRef]
51. Viel, B.; Ruhl, T.; Hellmann, G.P. Reversible Deformation of Opal Elastomers. *Chem. Mater.* **2007**, *19*, 5673–5679. [CrossRef]
52. Pursiainen, O.L.J.; Baumberg, J.J.; Winkler, H.; Viel, B.; Spahn, P.; Ruhl, T. Nanoparticle-tuned structural color from polymer opals. *Opt. Express* **2007**, *15*, 9553–9561. [CrossRef]
53. Katritzky, A.R.; Sild, S.; Karelson, M. Correlation and Prediction of the Refractive Indices of Polymers by QSPR. *J. Chem. Inf. Comp. Sci.* **1998**, *38*, 1171–1176. [CrossRef]
54. Yao, W.; Li, Y.; Huang, X. Fluorinated poly(meth)acrylate: Synthesis and properties. *Polymer* **2014**, *55*, 6197–6211. [CrossRef]
55. Gleinser, W.; Maier, D.; Schneider, M.; Weese, J.; Friedrich, C.; Honerkamp, J. Estimation of sphere-size distributions in two-phase polymeric materials from transmission electron microscopy data. *J. Appl. Polym. Sci.* **1994**, *53*, 39–50. [CrossRef]
56. De Francisco, R.; Tiemblo, P.; Hoyos, M.; González-Arellano, C.; García, N.; Berglund, L.; Synytska, A. Multipurpose Ultra and Superhydrophobic Surfaces Based on Oligodimethylsiloxane-Modified Nanosilica. *ACS Appl. Mater. Interfaces* **2014**, *6*, 18998–19010. [CrossRef]
57. García-Domenech, R.; de Julián-Ortiz, J.V. Prediction of Indices of Refraction and Glass Transition Temperatures of Linear Polymers by Using Graph Theoretical Indices. *J. Phys. Chem. B* **2002**, *106*, 1501–1507. [CrossRef]
58. Schäfer, C.G.; Lederle, C.; Zentel, K.; Stuhn, B.; Gallei, M. Utilizing stretch-tunable thermochromic elastomeric opal films as novel reversible switchable photonic materials. *Macromol. Rapid Commun.* **2014**, *35*, 1852–1860. [CrossRef] [PubMed]
59. Hart, S.J.; Terray, A.V. Refractive-index-driven separation of colloidal polymer particles using optical chromatography. *Appl. Phys. Lett.* **2003**, *83*, 5316–5318. [CrossRef]
60. Aralaguppi, M.I.; Jadar, C.V.; Aminabhavi, T.M. Density, Viscosity, Refractive Index, and Speed of Sound in Binary Mixtures of Acrylonitrile with Methanol, Ethanol, Propan-1-ol, Butan-1-ol, Pentan-1-ol, Hexan-1-ol, Heptan-1-ol, and Butan-2-ol. *J. Chem. Eng. Data* **1999**, *44*, 216–221. [CrossRef]

61. Awwad, A.M.; Al-Dujaili, A.H. Density, Refractive Index, Permittivity, and Related Properties for N-Formylmorpholine + Ethyl Acetate and + Butanone at 298.15 K. *J. Chem. Eng. Data* **2001**, *46*, 1349–1350. [CrossRef]
62. Butt, H.J.; Jaschke, M. Calculation of thermal noise in atomic force microscopy. *Nanotechnology* **1995**, *6*, 1. [CrossRef]

Sample Availability: Samples of the compounds (particles, opals and inverse opals) are available from the authors.